Experimental, numerical and analytical investigations on the segmented post-tensioned hybrid steel-glass beams TVT

TESI

SCUOLA DI INGEGNERIA

SCUOLA DI DOTTORATO IN INGEGNERIA "LEONARDO DA VINCI"

PROGRAMMA DI DOTTORATO IN SCIENZE E TECNICHE DELL'INGEGNERIA CIVILE

UNIVERSITÀ DI PISA

TESI PER IL CONSEGUIMENTO DEL TITOLO DI DOTTORE DI RICERCA

[SSD: ICAR/09]

Vincenzo MAMONE

Italia
2015

Experimental, numerical and analytical investigations on the segmented post-tensioned hybrid steel-glass beams TVT

TESI

SCUOLA DI INGEGNERIA

SCUOLA DI DOTTORATO IN INGEGNERIA "LEONARDO DA VINCI"

PROGRAMMA DI DOTTORATO IN SCIENZE E TECNICHE DELL'INGEGNERIA CIVILE

UNIVERSITÀ DI PISA

TESI PER IL CONSEGUIMENTO DEL TITOLO DI DOTTORE DI RICERCA

[SSD: ICAR/09]

Ph.D. CANDIDATE

Vincenzo MAMONE

SUPERVISOR

Prof. ing Maurizio Froli

University of Pisa

SUPERVISOR

Dr. ir. Christian Louter

EPFL, Lausanne, Switzerland

Experimental, numerical and analytical investigations on the segmented post-tensioned hybrid steel-glass beams TVT

SCUOLA DI INGEGNERIA

SCUOLA DI DOTTORATO IN INGEGNERIA "LEONARDO DA VINCI"

PROGRAMMA DI DOTTORATO IN SCIENZE E TECNICHE DELL'INGEGNERIA CIVILE

UNIVERSITÀ DI PISA

TESI PER IL CONSEGUIMENTO DEL TITOLO DI DOTTORE DI RICERCA

[SSD: ICAR/09]

Signature of the Author:

Vincenzo Mamone
Ph.D. Candidate
Doctoral School of Engineering "Leonardo da Vinci"
University of Pisa, Pisa, Italy

Certified by:

Maurizio Froli
Associate Professor of Building Technology
University of Pisa, Pisa, Italy
Tutor and thesis supervisor

Certified by:

Christian Louter
Post-doctoral researcher
ICOM, ENAC, EPFL, Lausanne, Switzerland
Supervisor at EPFL

Accepted by:

Stefano Pagliara
Associate Professor of Hydraulics
University of Pisa
Chair of the Doctoral Program

Accepted by:

Stefano Bennati
Professor of Solid and Structural Mechanics
University of Pisa, Pisa, Italy
Chair of the Doctoral School of Engineering

Ai miei genitori,

ai miei fratelli.

Acknowledgements

Foremost, I wish to express my gratitude to my tutor Prof. Maurizio Froli for providing me the opportunity to work on this fascinating and interesting PhD research.

I would like to thank Christian Louter for his comments and hospitality at the Steel Structures Laboratory ICOM of the Ecole Polytechnique Fédérale de Lausanne (EPFL) where I developed the numerical modelling and performed the numerical analyses.

A special thanks goes to the technician Michele Di Ruscio for his flexibility and capability in performing the experiments and all the laboratory work.

Last but not the least, I would like to thank my family and my friends who have been always of great support to me.

Vincenzo Mamone

Pisa, Italy, May 2015

Abstract

The use of glass as a structural load-bearing material is a relatively new concept in civil engineering and architecture. It started in the 1980s and 1990s, but it has only recently been used to create various structural glass components such as columns, beams and walls for footbridges, as well as conservatories, roof structures, canopies and facades.

Its transparency makes it particularly appealing but, as a structural building material, glass is essentially unsafe. Needless to say, glass is notoriously brittle. It does not show ductile deformation before ultimate failure occurs and it fails suddenly without warning, leaving sharp and harmful fragments. Due to this inherent inability to deform in a ductile manner by redistributing stresses through plastic deformation, glass is highly sensitive to impact and stress concentration. This causes it to break suddenly.

Its weakness in tension and the difficulties in predicting its failure limit its applicability as a tension component. However, glass is strong in compression. For this reason, when using glass as a load-bearing material, specific design measures should be taken to avoid and reduce any unpredictable consequence in case of breakage.

The purpose of this PhD research was to examine a specific safety concept for structural segmented post-tensioned hybrid steel-glass beams introduced by Maurizio Froli. This technique consists in using small laminated glass segments and assembling them together using post-tensioned steel bars. The absence of glued connection, mechanical fixings and holes in the glass is designed to avoid tensile stress. Steel bars transfer the tensile forces, while the compressive forces are in the compression zone in the glass. As a result, the beam will no longer fail in a brittle manner because its failure is now ductile due to the presence of steel bars. This concept enhances the safety performance of the beam and provides a ductile breakage response.

This safety concept was already partially investigated in previous studies leaded by M. Froli at the University of Pisa. This PhD research builds upon these studies, researching the basic safety concept in more detail. The research is based on laboratory tests made on the 12 m segmented post-tensioned hybrid steel-glass beam prototype named TVTɣ which has been designed and built to investigate its static and dynamic structural response. The experimental investigations are compared with the numerical and analytical models which have been developed to describe the structural response of the prototype, the experimental tests and the numerical and analytical modelling give rather matching results.

The experimental investigations performed on the 12 m prototype, together with the numerical and analytical models have investigated in more detail the structural behaviour of this kind of glass beams and the parameters which affect its breakage and post-breakage response. The experimental investigations have demonstrated that the breakage of the beam is ductile due to the plastic deformation of tensile steel bars. The numerical modelling provides a good method for describing the behaviour of the post-tensioned hybrid steel-glass beams. The analytical model represents the most important result of this research because it allows to calculate the axial forces in steel bars, the compressive forces in the triangular glass panels and the deformations of the beams. Furthermore, the analytical modelling gives a clear explanation of the internal mechanical behaviour of the beam.

Starting from the results of this research it is recommended to perform additional studies into the effects of the parameter interlayer type and the parameter glass type, and into the effects of the size parameter of the beam on its structural response. In addition, it is recommended to investigate the influence of the bar sizes on the

response of beams in terms of stiffness and strength, and especially the relation between the diameter of bars and the dimensions, sizes and thickness of laminated glass panels.

Keywords

Structural glass

Glass beam

Post-tensioned glass beam

Hybrid steel-glass beam

Hybrid glass strucutres

Riassunto

La crescente domanda di trasparenza proveniente dal mondo dell'architettura contemporanea ha portato nel corso degli ultimi decenni ad un crescente impiego del vetro come materiale strutturale. Parallelamente si è assistito al proliferare di ricerche scientifiche aventi per oggetto lo studio e lo sviluppo di nuovi elementi portanti in vetro in particolare travi, pilastri e pareti.

È ben noto che il vetro è un materiale fragile e questa sua caratteristica lo rende in linea di principio non adatto ad essere utilizzato nella realizzazione di elementi portanti. La rottura di un elemento in vetro si verifica in modo improvviso ed istantaneo producendo schegge e frammenti taglienti e molto pericolosi, pertanto l'impiego del vetro impone che siano adottate e soddisfatte specifiche misure di progettazione onde evitare catastrofiche conseguenze in caso di rottura.

Il dottorato di ricerca ha avuto come oggetto lo studio analitico, numerico e sperimentale del comportamento meccanico di una particolare tipologia di travi post-tese in sistema misto vetro-acciaio. L'idea di base concepita e sviluppata da M. Froli, consiste nel realizzare le travi mediante l'assemblaggio di pannelli in vetro laminato di piccole dimensioni tenuti insieme ed irrigiditi da un sistema di barre o funi metalliche post-tese. L'assenza di collegamenti incollati, fissaggi meccanici e fori nel vetro limita drasticamente l'insorgenza di tensioni di trazione in esso, le barre metalliche trasferiscono le forze di trazione mentre le forze di compressione interessano il vetro. Di conseguenza il collasso della trave non si verifica per rottura fragile degli elementi in vetro bensì per rottura duttile dovuta allo snervamento delle barre metalliche tese.

L'idea di base è stata già parzialmente studiata in precedenti attività di ricerca condotte presso l'Università di Pisa sotto la guida di M. Froli. Il dottorato di ricerca riprende e sviluppa ulteriormente le conoscenze scientifiche attorno all'idea originaria attraverso uno studio teorico più dettagliato di tipo numerico ed analitico. Il comportamento statico e dinamico è stato indagato sperimentalmente effettuando prove di laboratorio su un prototipo di trave segmentata in sistema misto vetro-acciaio di luce 12 metri precompressa mediante cavi post-tesi in acciaio.

Parallelamente alle prove sperimentali sono stati sviluppati opportuni modelli numerici ed analitici della trave che ne descrivono fedelmente il comportamento sperimentale. In particolare, i risultati delle prove sperimentali hanno evidenziato un comportamento a rottura della trave di tipo duttile che si verifica per snervamento delle barre longitudinali tese. Dai risultati ottenuti si può affermare che il modello numerico costituisce un valido strumento per la progettazione, mentre il modello analitico permette di calcolare in modo semplice e sufficientemente preciso lo sforzo assiale nelle barre metalliche, lo sforzo di compressione nei pannelli triangolari in vetro e la deformazione della trave.

Parole chiave

Vetro strutturale

Travi in vetro di grande luce

Travi post-tese in sistema misto vetro-acciaio

Contents

List of Figures

List of Tables

Chapter 1 Introduction to the research

This chapter provides an introduction to the research. It briefly introduces the research topic, the research approach, the research methodology and the objectives.

1.1 Introduction

In contemporary architecture there has been a growing demand for complete building transparency. Because of this demand, glass is now being used as a load-bearing material. This research focuses on a specific safety concept ideated and developed by M. Froli for segmented post-tensioned hybrid steel-glass beams, which allow to overcome the structural problems of glass, namely its brittleness and its unpredictable failure. This safety concept combines the transparency and compressive strength of glass with the tensile strength and the elastic-plastic behaviour of steel. The result is a hybrid steel-glass beam composed of small laminated glass segments and post-tensioned steel bars. Steel bars transfer the tensile forces while the compressive forces are in the compression zone in glass. The beam is composed of multiple laminated glass segments that are joined by contact without bolted connections, glued connections or other mechanical fixings. No internal tensile forces or cracks occur in glass due to glass segmentation. Because of the steel bars' yielding and the ensuing plastic deformations, the breakage and post-breakage response is ductile.

The current research started from previous systematic experimental and numerical investigations performed at the University of Pisa under the guide of M. Froli which already demonstrated the potentiality of this concept.

This safety concept was already researched in previous studies at the University of Pisa (Froli & Lani, 2010) (Froli & Mamone, 2013a) (Froli & Mamone, 2013b). The basic idea had been found and developed by Maurizio Froli who patented it for the University of Pisa [Italian patent certificate - PI/2006/A/000017 del 13/2/2006]. Currently, all rights for a commercial use of the patents have been acquired and owned exclusively by the Spin-off Society TVT s.r.l.

The current research consists of experimental investigations on the structural response of a 12 m prototype and on the numerical and analytical modelling of its response.

1.2 Problem definition

In the last few decades, besides the traditional use of glass as an infill material, we have seen an increase in the application of glass as a load-bearing material. Glass columns, glass beams and glass walls are applied in several structures such as footbridges, roof structures, canopy structures and facade structures.

The current research focuses on the use of glass for bending components; it focuses on the investigations of the aforementioned specific safety concept used to obtain longer beams. Manufacturing processes, such as glass production and glass lamination, limit the maximum possible length of beams made of one continuous element of laminated glass to 6 - 7.5 meters. Even though at present glass sheets can be tempered up to 9 meters, in actual fact the fabrication and installation tolerances limit their maximum length to 6 m.

At present, two categories of structural beams have been applied to span lengths greater than 6 meters; namely segmented glass beams and splice-laminated glass beams. Segmented glass beams are composed of laminated glass elements joined using mechanical fixings or bolted connections. Splice-laminated glass beams are composed of multiple glass sheets laminated in overlap. The result is a glass beam with a length larger than the length of single glass sheet. Examples of applications of segmented glass beams and splice-laminated glass beam are provided in *Chapter 2*.

In this PhD research we studied a new method and a new safety concept designed to achieve greater beam lengths. We have researched the structural response of the segmented post-tensioned hybrid steel-glass beam so as to overcome limitations imposed by unexpected stress concentrations observed in segmented glass beams and to overcome size restrictions in transport, as well as fabrication tolerances required by splice-laminated beams.

1.2.1 Segmented post-tensioned hybrid steel-glass beam concept

The current research focuses on the structural response and functioning of segmented post-tensioned hybrid steel-glass beams, which are composed of small laminated glass elements with no mechanical fixings or glued connections. The compressive forces in glass are generated by the physical contact; no tensile force or tensile stress is applied to the glass. To obtain this result, a post-tensioned system of steel bars is necessary, since it defines the steel reinforcement of the beam and increases its stiffness.

The segmentation of glass, the absence of mechanical fixings in glass and the presence of steel bars avoid tensile forces. These aspects, combined with a precise glass thickness design and a precise measurement of the steel bars' diameter, ensure ductile breakage and a good post-breakage response.

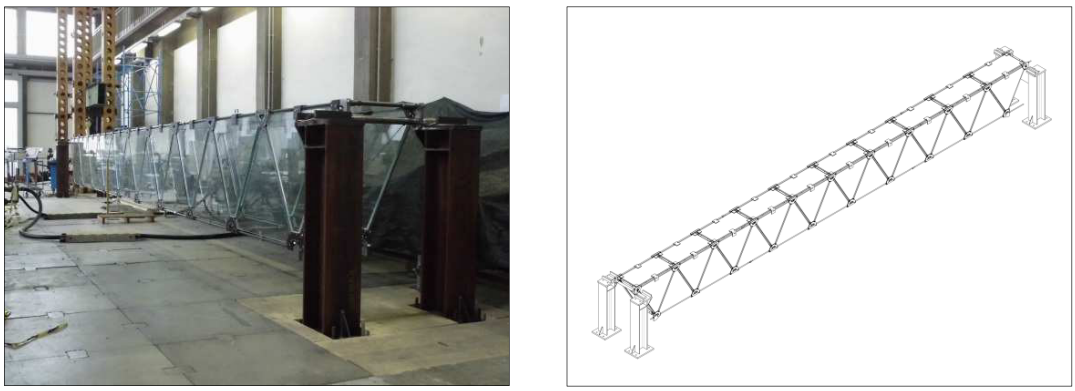

(a) Photograph of beam prototype. (b) Isometric view.

Figure 1.1 The 12 m post-tensioned hybrid steel-glass beam on its supports

The basic concept of segmented post-tensioned hybrid steel-glass beam has been studied since 2006 at the University of Pisa where Froli & Lani constructed and tested the first two specimens of hybrid steel-glass beams composed of triangular double-layer PVB-laminated chemically tempered glasses, steel joints and steel tendons, named TVTα and TVTβ (Froli & Lani, 2008) (Froli & Lani, 2010).

1.3 Research methodology

The research methodology is focused on the dynamic and static functioning of the 12 m prototype named TVTγ. The objective is to validate the safety concept of post-tensioned hybrid steel-glass beams by means of experimental investigations and by comparing the experimental results with the results of analytical and numerical modelling. The following sub-sections briefly describe the experimental, analytical and numerical analyses performed.

1.3.1 Experimental investigations

A 12 m segmented post-tensioned hybrid steel-glass beam was designed, constructed and tested at the University of Pisa in the research programme started by M. Froli since 2006 with the first TVTα and TVTβ prototypes funded by the Italian Ministry of Education, University and Research (MIUR) with the funding PRIN 2005 "Affidabilità di elementi in vetro strutturale: indagini teoriche e sperimentali sulla risposta termomeccanica di strutture trasparenti di tipo innovative", national coordinator M. Froli.

The construction of the 12 m prototype TVTɣ has been funded by the Italian Ministry of Education, University and Research (MIUR) with the funding PRIN 2008 "*Progettazione e comportameto meccanico di giunzioni incollate per travi in vetro e di innovative travi in vetro in sistema misto presollecitate mediante cavi in acciaio*", local coordinator M. Froli (Univ. of Pisa).

Two kind of of experimental analyses have been performed on the 12 m prototype to determine its dynamic and static response.

The aim of the dynamic experimental investigations was to determine the 12 meter beam's natural frequencies and mode shapes under free vibrations.

The static experimental investigations have been performed to determine its structural functioning, its breakage and post-breakage behaviour. A four-point bending test was carried out to investigate stiffness, strength, horizontal and vertical displacement and the load-bearing capacity of the 12 m beam. The tensile forces and deformations in steel bars have also been determined. The four-point bending test proved that the beam's breakage is ductile due to the plastic deformation of the steel bars followed by the buckling of a glass element.

The results of the experimental investigations are compared with numerical and analytical findings and used as a reference to validate them.

1.3.2 Numerical investigations

A 3D numerical model was made with ABAQUS® Finite Element software, using solid continuum elements and beam elements to investigate and describe the structural static response of the 12 m beam. Geometric nonlinearities, friction and material nonlinearities have been implemented in the model, and various analyses have been performed to investigate the effects of friction, post-tensioning forces and mechanical properties of the interlayer.

The numerical model was validated by comparing numerical results with the results of static experimental investigations. The numerical findings are accurate and in good agreement with experimental results.

1.3.3 Analytical investigations

An analytical model was developed to calculate the deformations and the axial forces in steel bars and to determine the deformation of the beam. The analytical model takes account of the material nonlinearities and of the effects of friction on the deformations and on the tensile forces of the steel bars. Even though rather coarse assumptions were made in the analytical modelling, these can be validated by comparing the analytical results with the experimental and numerical results.

The analytical model data is largely in agreement with the experimental results.

1.4 Objective

The objective of this research is to increase understanding of the structural response of the segmented post-tensioned hybrid steel-glass beams thanks to experimental investigations performed on the 12 m prototype TVTɣ through analytical and numerical modelling. Not all the structural aspects of this safety concept have been investigated and understood.

1.4.1 Conclusions

From the experimental investigations, we can conclude that the post-tensioning forces applied to steel bars affect just slightly the stiffness of the beam. The breakage of the beam is ductile due to the plastic deformation of tensile steel bars, and subsequently its final collapse is brought about by the buckling of a laminated glass segment in compression. The numerical and analytical modellings thoroughly describe the experimental structural behaviour of the beam.

1.4.2 Recommendations

From the experimental investigations and numerical and analytical modelling performed in this research, several recommendations for future research can be made.

It is recommended to carry out additional studies on the effects of various parameters on the structural response of segmented post-tensioned hybrid steel-glass beams, especially on the effects of the parameter interlayer type and the parameter glass type on the final buckling collapse of the laminated glass panels in compression.

It is recommended to investigate the effects of the size parameter of the beam on the structural response and on its breakage and post-breakage response. It would also be interesting to investigate the exact effects of the bar size on the beams' response in terms of stiffness and strength, and especially the relation between the bars' diameter and the dimensions, sizes and thickness of laminated glass panels.

It is recommended to further develop the analytical model taking into account the effects of shear forces and its relation with the bending moment in glass elements and the steel bars.

Finally, it is also recommended to further investigate the possibilities of embedded reinforcement in glass panels, which could offer a structural benefit in terms of ultimate strength.

1.5 Outline of the dissertation

The following list provides an outline of the dissertation, which consists of 9 chapters and 2 appendices:

- Chapter 1: the current chapter. It provides a brief "*Introduction to the research*".
- Chapter 2: provides "*An overview of structural glass beam*"; it illustrates some applications of structural glass beams and explains briefly their safety concepts.
- Chapter 3: presents "*The segmented post-tensioned hybrid steel-glass beam concept*" that illustrates the safety concept.
- Chapter 4: focuses on the "*Materials*"; it provides an overview of the mechanical properties of the materials applied to construct the 12 m segmented post-tensioned hybrid steel-glass beam.
- Chapter 5: presents the "*Experimental investigations*" performed on the 12 m segmented post-tensioned hybrid steel-glass beam.
- Chapter 6: provides the "*Numerical modelling"* of the structural response of the 12 m segmented post-tensioned hybrid steel-glass beam.
- Chapter 7 provides the "*Analytical modelling"* of the structural response of the 12 m segmented post-tensioned hybrid steel-glass beam.
- Chapter 8 provides a "*Comparison of the experimental results and of the numerical and analytical findings"* of the structural response of the 12 m segmented post-tensioned

hybrid steel-glass beam.

- Chapter 9 gives an overall "*Conclusions"* of the PhD research.
- Appendix I provides the diagrams of the experimental, numerical and analytical results.
- Appendix II provides photographs of the 12 m segmented post-tensioned hybrid steel-glass beam.
- Appendix III lists the technical drawings appended to the dissertation.

Chapter 2 An overview of structural glass beams

This chapter illustrates some applications of structural glass beams and briefly explains their safety concepts.

2.1 Introduction

Due to its brittnless, its weakness in tension and its unpredictable failure behaviour, glass is essentially an unsafe load-bearing material. For this reason, tempered and laminated glass elements are used in structural applications to provide sufficient tensile strength and redundancy.

The tempering process increases the tensile strength of glass by creating a residual field of compressive stresses on the glass surface and tensile stresses in the core. The residual compressive stress on the surface has a positive effect and, as long as the tensile stress on the surface is not bigger than residual compressive stress, no fracture-crack growth can occur. The result is an increase in resistence to the tensile stress of the glass sheet.

The lamination process improves the structural capacity of glass. Laminated glass elements consist of two or more glass layers bonded together by some plastic film or resin interlayer so that the cross section responds mechanically with composite effect. Laminated glass improves the structural capacity of glass. If one or more glass panes should break, the glass fragments adhere to the interlayer, thus improving the residual structural post-breakage capacity. The laminated glass ensures robustness and redundancy of glass structural elements, both in terms of increased tensile strenght of glass and in terms of adequate of post-breakage stability level.

2.2 Structural glass beams design process

The design procedure for structural glass elements is an iterative process combining rules of thumb, analytical modelling and prototype testing.

As with any structural material, the design process determines the ultimate limit state requirements and serviceability limit states requirements. The ultimate limit state performance requirements include and ensure adequate material strength, structural stability, structural robustness, and adequate breakage and post-breakage structural behaviour of glass elements. Serviceability limit state requirements ensure and limit deflections, vibrations and movements.

The brittleness of glass and its inability to redistribute local stress concentrations by yielding are critical in the design process of glass elements and connections. In order to prevent and to avoid stress concentrations, great attention to design, detailing, fabrication tolerances and construction tolerances are required. Structural glass design requires an assessment of glass properties, actions, geometry, temperature differences, imposed deformations as well as constraints, fabrication and installation tollerances, stiffness and kind of connections.

2.3 Examples of glass beams

The following sub-sections illustrate some applications of structural glass beams by also providing a brief description of the rather new research on glass beams. Six categories of glass beams are defined (Louter, 2011):

continuous glass beams, segmented glass beams, splice-laminated glass beams, reinforced glass beams, hybrid glass beams and pre-stressed glass beams.

The reinforced glass beams consist of metal reinforced glass beams, carbon fibre reinforced glass beams, and glass fibre reinforced glass beams.

The hybrid glass beams consist of hybrid steel-glass beams, hybrid concrete-glass beams and hybrid timber-glass beams.

2.3.1 Continuous glass beams

Continuous glass beams are made of two or more glass layers laminated using polymer interlayers. All the glass layers are of the same length, and span the full length of the beam. This means that the span of continuous glass beams is limited to the maximum available manufactured size.

Continuous glass beams are loaded in bending about their strong axis, generating bending moment which creates linearly distributed tensile and compressive bending stresses across the section. Bending stresses depend on the span and the type of support of the beam. The width and the height of the cross section increase the moment of inertia and the beam resists the bending moment.

The load-bearing capacity of a continuous glass beams is limited by local buckling, lateral torsional buckling and by tensile bending stresses. Fort this reason, in the case of slender-beams, an accurate design is required because of their low torsional stiffness which makes them prone to suffer lateral deformation whilst twisting; in the case of non-slender beams, the design is determined by stress concentrations and by the strength in the tensile bending stress zone. Some early applications of continuous structural glass beams are provided in the following figures.

(a) Exterior view. (b) Detail of a connection.

Figure 2.1 Glass extension, Hampstead (United Kingdom), Eng.: L. Dewhurst & T. Macfarlane, Arch.: R. Mather, 1989-1992.

(a) Exterior view.

(b) Interior view.

Figure 2.2 Broadfield House Glass Museum (United Kingdom), Eng.: Dewhurst Macfarlane & Partner, Arch.: Design Antenna, 1994.

The safety concept of continuous glass beams derives from overdimensioning; for this reason, in order to minimize the chances of a total collapse of the laminated glass beam, outer glass layers are added to protect the inner glass layers. The failure of outer layers due to impact does not affect the load bearing capacity of the beam because the remaining layers are able to carry the load.

Nevertheless, a total collapse cannot be excluded since failure of all glass layers might still occur due to unforeseen stress concentrations caused by assembly errors, or nickel sulphide inclusions in case of tempered glass layers.

2.3.2 Segmented glass beams

Segmented glass beams are made of small laminated glass elements joined together by using mechanical connections, namely through bolt connections and friction grip connections. In segmented glass beams, point connections transfer internal forces, consequently a critical aspect of structural detailing consists in avoiding or reducing high stress concentrations and direct steel-to-glass contact. This is achieved mainly by using intermediate materials that should be strong and stiff enough to transfer internal forces to glass but, at the same time, sufficiently soft to redistribute stress concentration.

An early application of segmented glass beam is the Yurakucho canopy (Macfarlene, 1999). Three cantilevering beams support the glass roof; each one of them is assembled from seven triangular laminated glass segments bolted together. Each segment is fabricated from two sheets of fully tempered glass, laminated using an acrylic resin.

(a) Frontal view.

(b) Lateral view.

Figure 2.3 Yurakucho glass canopy, Tokyo (Japan), Eng.: Dewhurst Macfarlane, Arch.: R Viñoly, 1996.

Friction grip connections are used in the 8 m glass cube built in 1998 for the reading room of the Arab Urban Development Institute - AUDI - in Riyad.

Figure 2.4 Arab Urban Development Institute Reading Room, Riyadh (Saudi Arabia), Eng.: Dewhurst Macfarlane, Arch.: N Fanous, 1998.

(a) Interior view.

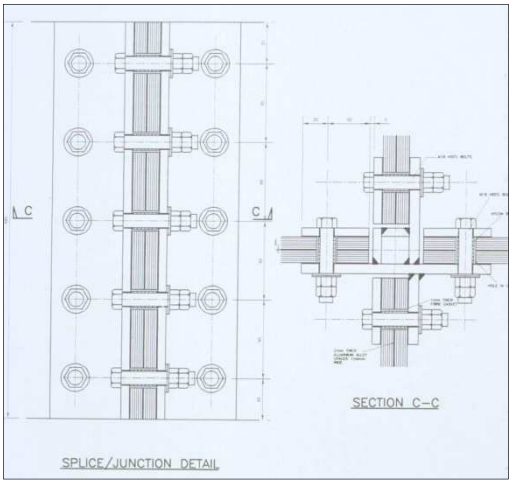

(b) Detail of a joint.

Figure 2.5 Details of Arab Urban Development Institute Reading Room, Riyadh (Saudi Arabia), Eng.: Dewhurst Macfarlane, Arch.: N Fanous, 1998.

Other examples of application of segmented glass beams are the courtyard roof covering of the IHK in Munich and the atrium roof covering of the Medical School in Glasgow.

In the courtyard roof covering in Munich, the 12 m glass beams are composed of triangular laminated glass segments joined by bolted connections.

In the atrium roof covering of the Medical School in Glasgow, each glass beam is composed of four laminated glass segments joined by friction grip connectors with soft aluminium inserts.

(a) Interior view.

(b) Detail of a joint.

Figure 2.6 Courtyard roof covering IHK München, Munich (Germany), Eng.: Ludwing & Weiler, Arch.: Betsch & Betsch, 2001.

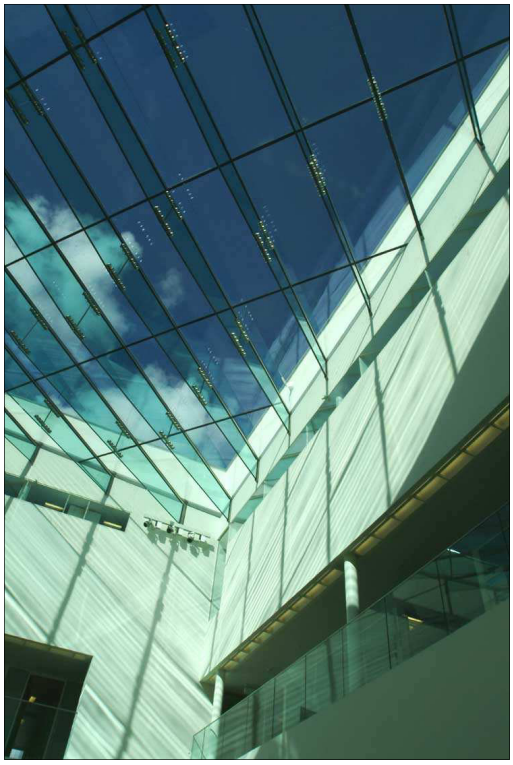

(a) Interior view.

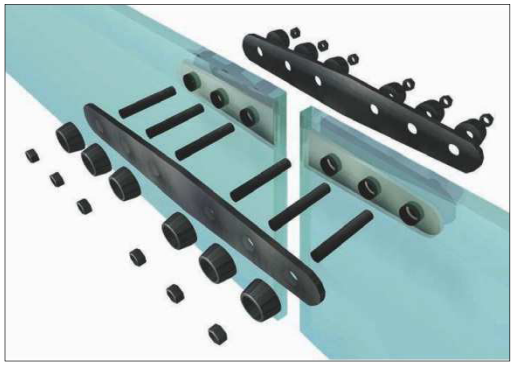

(b) Detail of a joint.

Figure 2.7 Wolson Medical School, University of Glasgow, Glasgow (United Kingdom), Eng.: Arup Façade Engineering, Arch.: Reiach & Hall, 2001.

2.3.3 Splice-laminated glass beams

Splice-laminated glass beams are composed of multiple glass layers bonded in overlap for the creation of one single glass beam or fin that is greater in length than the single glass sheet. An early example of an application that features splice-laminated glass fins was the Apple store glass Cube, built in 2006, in 5th Avenue, New York City. In this project, 6 m glass sheets were spliced together in five-ply laminates to achieve an overall length of 10 meters.

In 2011, the Apple store glass Cube built in 2006 was rebuilt. The high transparency of the new Cube is due to the advances in fabrication and design. The structure is the result of the possibility to maximize the glass panel sizes and to minimize the number of the connection fittings (O'Callaghan, 2012).

In 2010, Glas Trösch showcased his 21 m long splice laminated glass beam. Experimental investigations were performed together with numerical and analytical modelling (Trösch & Kassnel-Henneberg, 2013).

(a) Glass Cube built in 2006.

(b) Glass Cube rebuilt in 2011.

Figure 2.8 Apple Glass Cube 5th Avenue, New Jork City (USA), Eng.: Eckersley O'Callaghan, 2006 & 2011 (O'Callaghan, 2012).

2.3.4 Reinforced glass beams

Over the last few decades, several research projects have focused on the use of glass combined with other materials. The safety concept of reinforced glass beam is to increase the strength of glass beam and to generate a ductile response at failure (Louter, 2011). This behaviour is achieved by bonding a small reinforcement made of steel, carbon fiber, glass fiber or steel fiber to the tensile edge of the beam.

In case of glass fracture, the crack propagation at tensile edge is limited due to elastic-plastic deformation of the reinforcement. The reinforcement transfers the tensile forces, bridges cracks in glass and, together with a compressive internal force in the uncracked compression zone of the beam, it generates an internal couple. In fact, the reinforcement ensures load-bearing capacity in case of glass fracture by generating an internal moment capacity that enables the beam to carry load in analogy with reinforced concrete. This increases the safety performance of the beam, even if all glass layers are cracked (Louter, 2011).

Steel reinforced glass beams

The first studies and investigations on the structural response of steel reinforced glass beams were performed at the TU Delft starting in, 2003 when Veer introduced the reinforced glass beam concept by developing and testing glass-polycarbonate laminated beams with an L-shaped stainless steel reinforcement bonded at the tensile edge (Veer, et al., 2003).

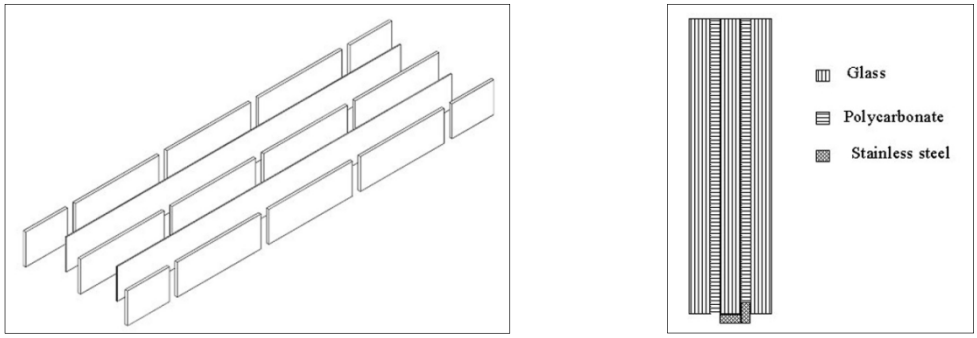

(a) Configuration of segmented laminated specimen. (b) Cross section.

Figure 2.9 Glass-polycarbonate beam with reinforcement (Veer, et al., 2003).

In 2003 Veer and Gross designed and constructed an 8 m long glass box aquarium. The aquarium consists of annealed float glass with two stainless steel box reinforcements bonded at the tensile edge. Due to its length, the glass layers were bounded in overlap to create the full 8 m span (Veer, et al., 2003).

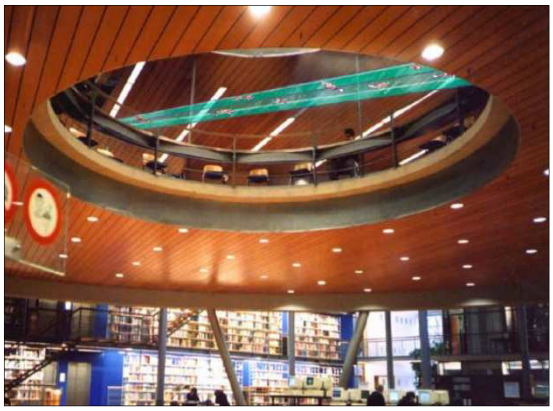

Figure 2.10 8 m reinforced glass box aquarium (Veer, et al., 2003).

Louter performed further investigations on reinforced glass box-section beams; he designed and tested a 3 m prototype of a box-section reinforced glass beam composed of annealed float glass and stainless steel box sections at the tensile edge (Louter, 2011).

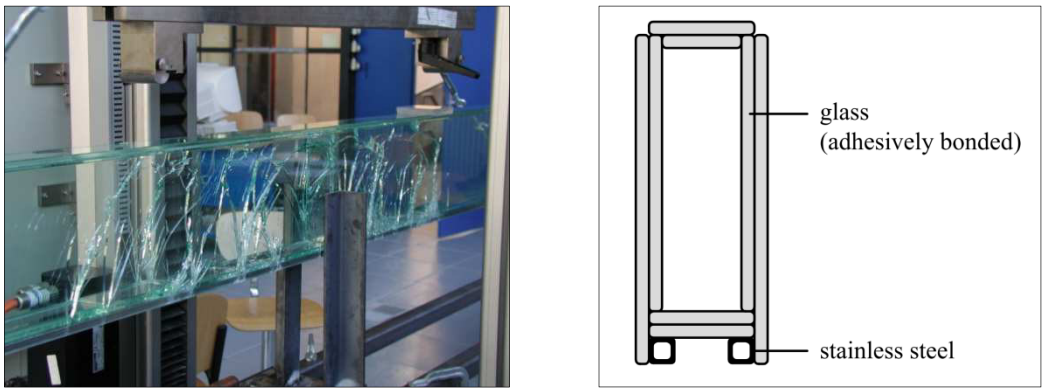

(a) Beam during the test. (b) Cross section.

Figure 2.11 Reinforced glass box-section beam researched by Louter (Louter, 2011).

Subsequently Louter designed and built a 3 m prototype of a T-section glass beam which was both reinforced and post-tensioned. The web and flange were segmented and bonded in overlap, and a curved stainless steel box reinforcement was integrated in the tensile edge of the web (Louter, 2011).

(a) Beam prototype. (b) Cross section.

Figure 2.12 Post-tensioned T-section glass beam investigated by Louter (Louter, 2011).

In 2004, an all transparent pavillon was designed and built at TU Delft. The beams were 7.2 m reinforced glass full section beams which spanned 4.8 m and cantilevered 1.2 meters. The beams consisted of 4 annealed float glass layers bonded in overlap with two stainlsess box reinforcements integrated at the top and bottom edge of the section (Louter, et al., 2005) (Bos, et al., 2005) (Bos, et al., 2005).

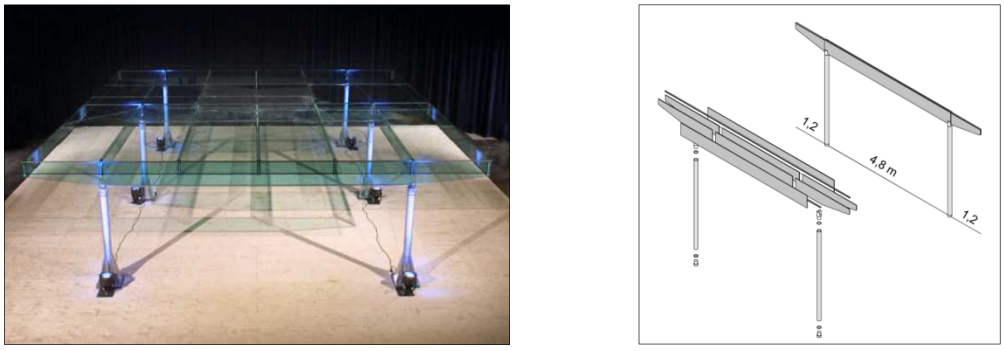

(a) Glass pavilion. (b) Exploded view of cantilever beam.

Figure 2.13 All Transparent Pavilion (Louter, 2011) (Bos, et al., 2005).

Louter has further researched the safety concept of reinforced glass beams. Through experimental investigations, and analytical and numerical modelling, Louter focused on the effects of the following parameters: bond system, temperature, thermal cycling, humidity, load duration, reinforcement material, reinforcement percentage and beam size on the structural response of reinforced glass beams. He also performed pull-out tests to investigate the pull-out strength of the reinforcement, and bending tests to investigate the structural response of glass reinforced beams (Louter, 2011).

Carbon fiber reinforced glass beams and steel fiber reinforced glass beams

Carbon fiber reinforced polymer (CFRP) glass beams have been investigated by Palumbo et al. (Palumbo, et al., 2005) who applied the concept in the restoration of the roof "Loggia de Vicari" in Italy. A carbon fibre strip was adhesively bonded to the bottom tensile edge of the laminated glass beam, made of four annealed float glass layers.

Figure 2.14 Loggia de Vicari, 2005 (Palumbo, et al., 2005).

Cagnacci et al. studied the structural performances of glass beams reinforced with FRP pultruded bars (Cagnacci, et al., 2009). They performed experimental investigations on glass beams composed of three-layer laminated glass sheets and FRP bars bonded using structural resin at the beam edges. The research included 4-point bending tests and analytical and numerical modelling.

(a) Beam during the test.

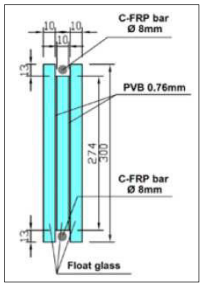

(b) Cross section.

Figure 2.15 Glass beam reinforced with FRP pultruded bars (Cagnacci, et al., 2009).

Agnetti & Speranzani (Agnetti & Speranzani, 2014) investigated steel fiber reinforced glass beams by perfoming a campaign of 4-point bending tests on several glass beam specimens. The glass beams were made of multiple annealed float glass, laminated with resin or PVB interlayers with steel fiber reinforcement bonded at the tensile edge.

2.3.5 Hybrid steel-glass beams

Hybrid steel-glass beams were investigated by Wellershoff at the Institute of Steel Construction at RWTH Aachen (Wellershoff & Sedlacek, 2003) (Wellershoff, et al., 2004). The cross-section of the beam consisted of a glass web, adhesively bonded to steel angles screwed to steel rectangular flanges. Four point bending test was performed on a prefabricated 3.6 m long I-shaped hybrid beam.

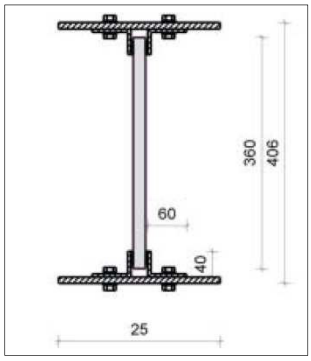

Figure 2.16 Cross section of the steel-glass beam investigated by Wellershoff & Sedlacek (Wellershoff & Sedlacek, 2003).

Furhter research on hybrid steel-glass beams has been performed by Ungermann at the Institute of Steel Construction at Dortmund University (Ungermann & Preckwinkel, 2010). The steel flanges were bonded directly to the glass web. 4.0 m long beams were built and tested in four-point bending. The specimens consisted of steel flanges and of two 12 mm toughened glass layers laminated together.

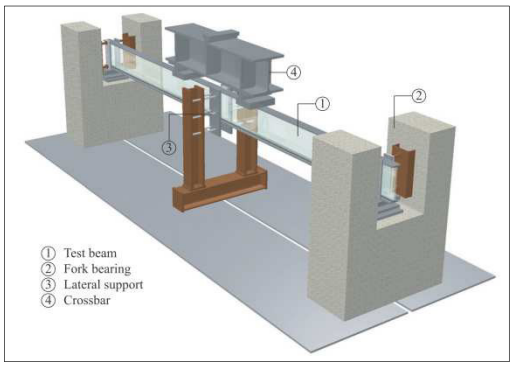

(a) Test setup.

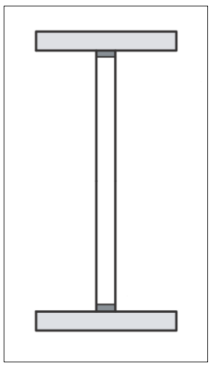

(b) Cross section.

Figure 2.17 Hybrid steel-glass beam investigated by Ungerman & Preckwinker (Ungermann & Preckwinkel, 2010).

Many other researchers have studied hybrid I-section steel-glass beams, among which Bucak et al., Feldmann et al., Netusil & Eliasova (Bucak, et al., 2009) (Feldmann, et al., 2010) (Netusil & Eliasova, 2010).

Ølgaard et al. investigated steel-glass beams composed of a glass web and a solid steel section bonded at the tensile edge (Ølgaard, et al., 2009). The glass webs consisted of annealed float glass, single layered or laminated.

Belis et al. investigated an interesting example of hybrid steel-glass beams (Belis, et al., 2009). The beams consisted of a double-layer fully tempered laminated glass web and a steel framing bondend to the glass using a structural sealant.

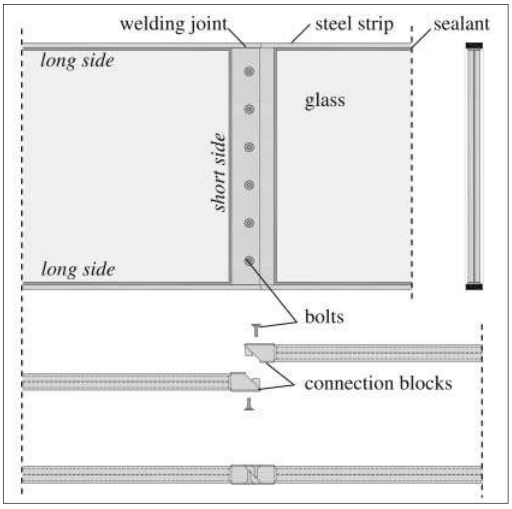

Figure 2.18 Cross section of the steel-glass beam and details of the connection (Belis, et al., 2009).

Also Weller et al. investigated composite steel-glass beams by performing experimental investigations on beams composed of three annealed float glass layers laminated together and various steel reinforcements bonded at both edges (Weller, et al., 2010).

2.3.6 Hybrid concrete-glass beams

Freytag investigated glass-concrete composite beams at Graz University of Technology (Freytag, 2004). He performed experimental investigations on specimens composed of three 8 mm tempered glass layers laminated together and of two high-performance concrete flanges. A direct continuous connection between glass and concrete was achieved through pouring concrete.

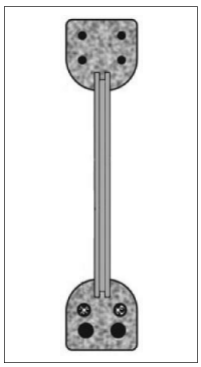

Figure 2.19 Cross section of the concrete-glass beam investigated by Freytag (Freytag, 2004).

2.3.7 Hybrid timber-glass beams

Hamm and Kreher researched timber-glass composite beams at École Polytechnique Fédérale de Lausanne. The tested beams were made of a single layer glass beam web and wooden flanges glued at the top and bottom edge of the glass web. An example of the application of timber-glass composite beams is the project for the roof structure of the Palafitte Hotel in Switzerland (Hamm, 2001) (Kreher, et al., 2004).

Figure 2.20 Timber-glass beams in the Palafitte Hotel in Switzerland (Kreher, et al., 2004).

Further studies have been carried out by Cruz & Pequeno, who tested several timber-glass composite beams having different lengths and different cross-section geometries. All beams are made of double layer float glass web and timber flanges, bounded to glass using various adhesives (Cruz & Pequeno, 2008a) (Cruz & Pequeno, 2008b).

Also Kozlowsky et al. investigated timber-glass composite beams (Kozlowski, et al., 2014). The glass webs of their timber-glass composite specimens are adhesively bonded to the timber flanges using three different adhesives: epoxy, acrylate and silicone. For the webs, two types of 8 mm thick glass were used; annealed float and heat-strengthened glass.

2.3.8 Pre-stressed glass beams

Jordão et al. performed numerical investigations to study the behaviour of laminated glass beams reinforced externally with twin steel rods (Jordão, et al., 2014).

Weller & Engelmann investigated the deformation behaviour of two meter long glass beams with four different post-tensioned cable layouts (Weller & Engelmann, 2014).

2.4 Conclusions

From this brief overview of structural glass beams it is concluded that the brittleness of glass and its inability to redistribute local stress concentrations by yielding are critical in the design process of glass elements and connections.

To overcome this unsafe behaviour, in all structural applications glass beams are always made of two or more tempered glass layers laminated together. The tempering process increases the strength of the glass layers; the lamination process ensures robustness and redundancy if one of the layers breaks. Furthermore, additional measures or solutions are recommended to enhance redundancy in case of an unforeseen complete failure of the structural glass element.

Chapter 3 The segmented post-tensioned hybrid steel-glass beam concept

This chapter illustrates the safety concept of segmented post-tensioned hybrid steel-glass beam. It provides an overview of the evolution of the concept explored in previous research at the University of Pisa. Furthermore, it focuses on an accurate description of a 12 m prototype constructed and investigated in this research.

3.1 Introduction

The segmented post-tensioned hybrid steel-glass beam concept has already been researched in preceding research at the University of Pisa (Froli & Lani, 2008) (Froli & Lani, 2010). The following sub-sections briefly describe the segmented post-tensioned hybrid steel-glass beams investigated prior to this research and present the evolution of the concept (Froli & Mamone, 2013a) (Froli & Mamone, 2013b). The current research builds upon this preceding study and has investigated the structural response of a 12 m prototype.

The basic idea of the safety concept is to avoid any tensile force in glass generated by either mechanical fixings, bolted connections or glued connections. The beam consists of small double-layer PVB laminated glass segments, steel joints and post-tensioned steel tendons (rods or bars).

The small laminated glass segments only transfer compressive force, whereas the steel tendons transfer the tensile forces. The tensile tendons and the compression zone in the glass generate an internal couple which enables the segmented beam to carry load. The post-tensioning system increases the beam's stiffness. Because the glass segments are detached from the joints at tensile zone, no fracture can be caused by tensile stresses.

3.2 The evolution of the segmented post-tensioned hybrid steel-glass beam concept at the University of Pisa

The following sub-sections briefly present the beams investigated prior to this research and describe the evolution of the basic concept.

3.2.1 The first prototype: TVTα

The first prototype of segmented post-tensioned hybrid steel-glass beam, namely TVTα, had a length of 2970 mm and consisted of multiple triangular laminated glass panels, stainless steel joints and stainless steel rods. The equilateral triangular laminated glass panels had sides of 330 mm and consisted of two 5 mm thick chemically tempered glass sheets laminated with a PVB interlayer (thickness of 1.52 mm) (Froli & Lani, 2008).

Some defects in the post-tensioning system of the diagonal rods had generated an incomplete post-tensioning of the beam with a lack of stiffness, therefore bending tests performed on the specimen showed a low lateral stability; lateral torsional buckling of the beam occurred before the yielding of steel rods and before glass failure.

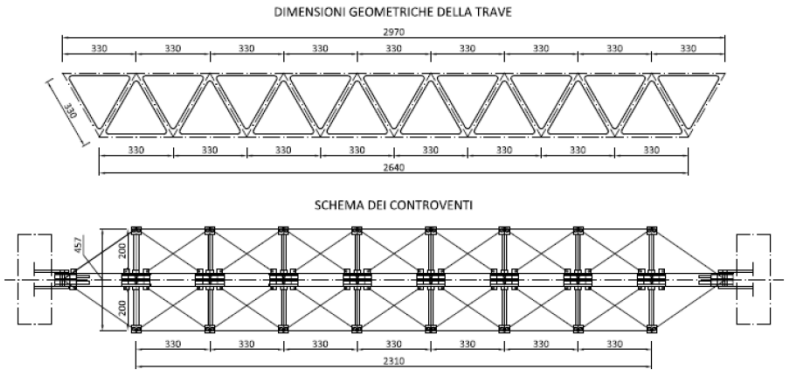

Figure 3.1 Engineering drawings of the prototype TVTα (Froli & Lani, 2008).

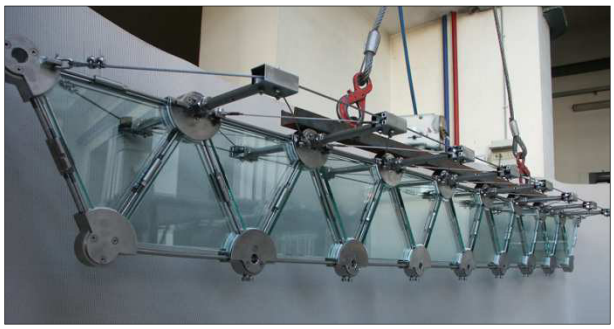

Figure 3.2 Photograph of the prototype TVTα (Froli & Lani, 2008).

3.2.2 The second prototype: TVTβ

The second prototype of segmented post-tensioned hybrid steel-glass beam, namely TVTβ, had a length of 3300 mm (Froli & Lani, 2008) (Froli & Lani, 2010). The beam consisted of 18 triangular laminated glass panels, 22 stainless steel joints and stainless steel rods.

The second prototype was improved by enlarging the size of the triangular laminated panels, by doubling the vertical glass webs and by improving the post-tensioning technique. The equilateral triangular laminated glass panels had side of 660 mm and were made of two 5 mm thick chemically tempered glass sheets laminated with a PVB interlayer (thickness of 1.52 mm). The beams had two vertical glass webs put at a distance of 171 mm from each other and a horizontal bracing system to increase its global lateral buckling strength.

Experimental dynamic and static investigations were performed and the experimental structural response was compared with 2D and 3D numerical modelling. The laboratory tests were a success and the mechanical response of the beam occurred as expected, the beam was very stiff, it didn't crack under sustained loads and the final failure occurred in a ductile manner.

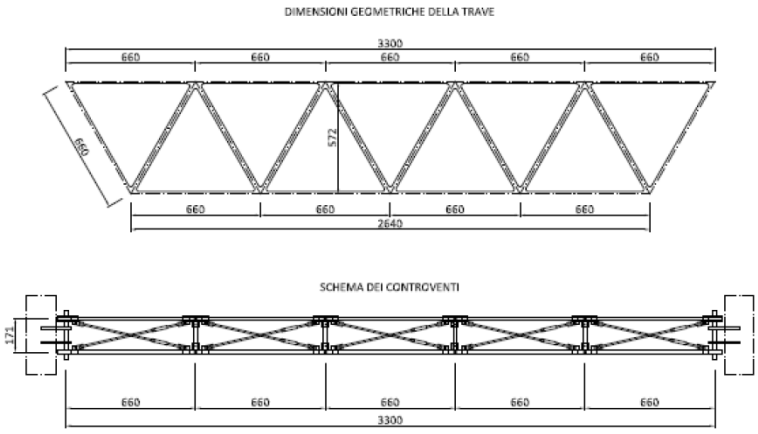

Figure 3.3 Engineering drawings of the prototype TVTβ (Froli & Lani, 2008).

Figure 3.4 Photograph of the prototype TVTβ (Froli & Lani, 2010).

3.3 The segmetend post-tensioned hybrid steel-glass beam investigated in this research

3.3.1 Geometric description

The basic aim of the TVT segmented post-tensioned hybrid steel-glass beam is to avoid any crack initiation and propagation in glass caused by tensile force that might occur in glass bending components. This result is achieved by subdividing the glass webs and the glass flange in multiple rectangular and equilateral triangular laminated segments and by connecting them together with a system of post-tensioned steel bars.

The laminated glass panels are connected to each other at their corners with of steel joints that exert just contact pressure on glass. There are no mechanical fixings or glued connections between steel joints and glass panels, as they could generate tensile stresses and failure of glass. Only contact pressures can be transferred to glass, due to the unilateral restraint between laminated glass panels, steel joints and the post-tensioned steel bars.

In order to avoid local and dangerous contact peaks on glass, all glass panels have round corners and aluminium elements between steel and glass.

The segmentation, the post-tensioning, glass panels' thickness and the steel bars' diameter ensure ductile breakage of the beam (Froli & Mamone, 2013a) (Froli & Mamone, 2013b). The beam breakage shows large deformations and displacements and it is due to the yielding of the steel bars and not to the buckling of glass in compression.

The prototype TVTɣ has been designed, constructed, tested and investigated at the University of Pisa. It has a length of 12000 mm, a height of 1039 mm, a width of 600 mm and it weights about 18 kN.

The length of the beam - 12000 mm - is the distance between the beam supports. The height of the beam - 1039 mm - is the distance between the axis of the top longitudinal bar and the axis of the bottom longitudinal bar. The cross-section is an inverted U composed of two vertical twin glass webs put at a distance of 600 mm from each other and a top horizontal glass flange; the bottom side of the beam is open. Each of the two twin webs consists of 19 identical equilateral triangular laminated glass panels, 21 steel joints located at the corners of the equilateral triangular panels, 20 diagonal steel bars, 1 top longitudinal steel bar and 1 bottom longitudinal steel bar.

All steel joints of each web are connected to the opposite joints of the opposite twin web by means of circular hollow profiles.

The top of the beam consists of 10 rectangular laminated glass panels pinned to steel joints. Furthermore, a grip joint connects the longer side of the rectangular glass panels to the horizontal edge of the triangular panels, in order to reduce the buckling length of glass panels in compression.

Furthermore, an X type torsional bracing system composed of steel bars increases the lateral torsional buckling strength of the beam.

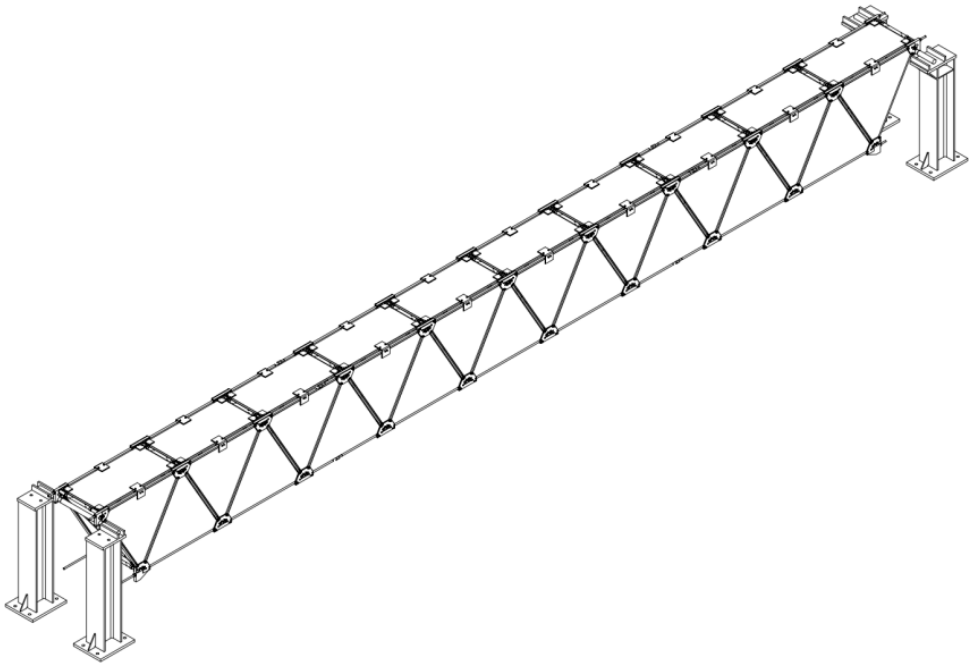

Figure 3.5 Isometric drawing of the 12 m prototype TVTɣ.

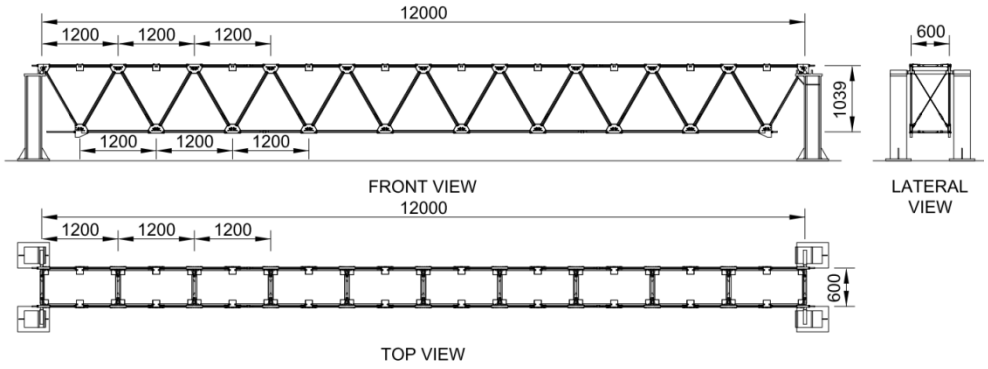

Figure 3.6 Engineering drawings of the 12 m prototype TVTɣ.

Figure 3.7 Photograph of the 12 m prototype.

3.3.2 Laminated glass panels

The two identical webs are composed of 38 identical equilateral triangular laminated glass panels. All of them have 1128 mm long sides and round corners - radius of 28mm.

Each glass panel is composed of two 10 mm thick heat-strengthened glass sheets laminated with a 1.52 mm thick foil of PVB interlayer.

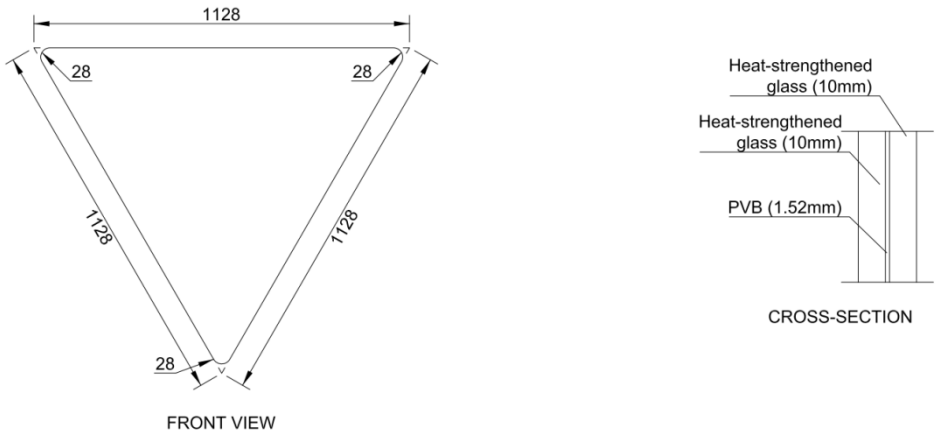

Figure 3.8 Triangular laminated glass panel.

The top flange consists of 10 identical rectangular laminated glass panels having sides of 1126 by 524 mm; all panels have round corners - radius of 28mm.

Each glass panel is composed of two 10 mm thick heat-strengthened glass sheets laminated with a 1.52 mm thick foil of PVB interlayer.

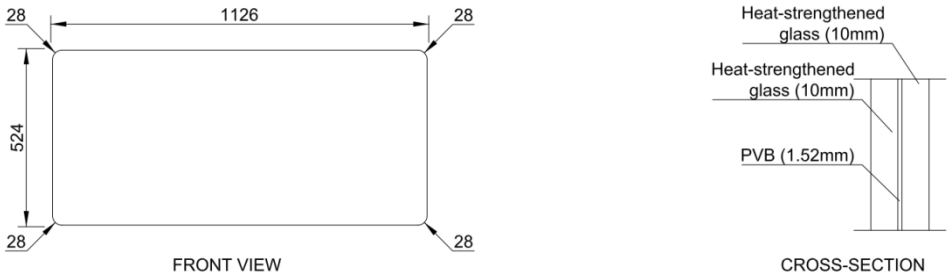

Figure 3.9 Rectangular laminated glass panel.

An aluminium element is put between each glass corner and the steel joints to avoid any local dangerous contact tension peak in glass. Moreover, polyethylene elements are put at glass corner between the lateral glass surfaces of laminated glass panels and steel to avoid a direct contact glass-steel, see *paragraph 3.3.9*.

3.3.3 Steel components

The beam's steel components are listed below and a brief description is provided in the following sub-sections:

- steel joints
- steel pinned connections
- steel joint-to-joint connections
- steel friction – grip connections
- steel bars

3.3.4 Steel joints

Steel joints transfer the internal forces and stress between steel bars and glass panels, and between contiguous glass panels. Depending on their geometry, their shape and place in the beam, three kind of steel joints are defined:

- top-end joints
- bottom-end joints
- central joints

Steel joints exert just a unilateral contact restrain, transferring compression force to the glass. There are no tensile forces in the glass, thanks to the detachment of glass corners from the joints.

Top-end joints

The four top-end joints transfer the loads applied on the beam to the supporting columns. The four-top end joints are named: Joint A1, Joint A2, Joint B1 and Joint B2.

All the four top-end joints have the same geometry and shape but they do present some differences due to their position in the beam and the symmetry of the beam.

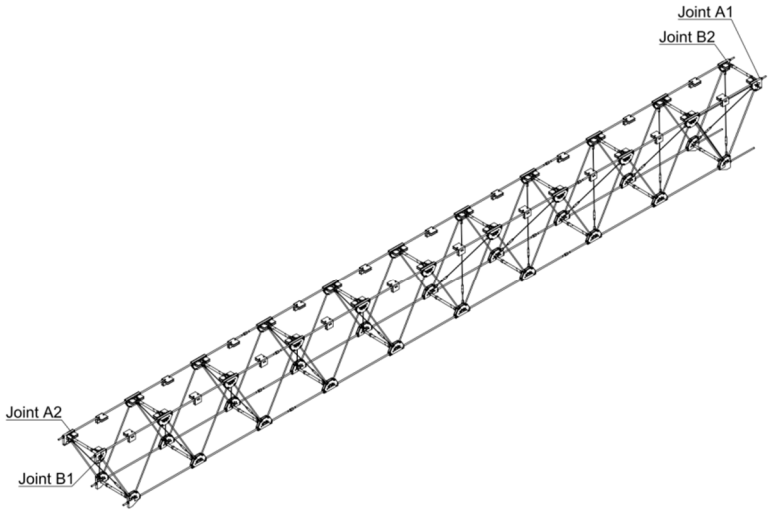

Figure 3.10 Position of the four top-end joints in the beam.

Each top-end joint consists of a main steel body, an inner lateral steel plate, an outer lateral steel plate and a bottom U-shaped steel element.

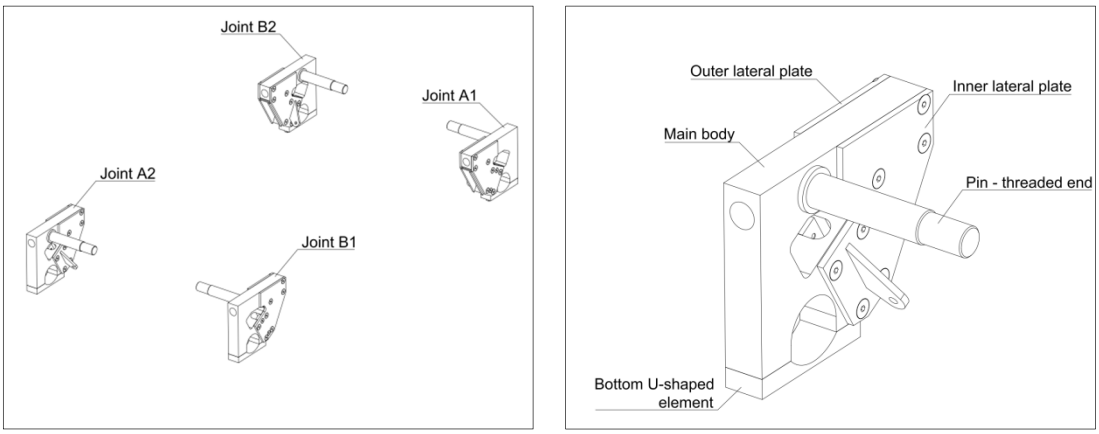

(a) Isometric view of the four top-end joints. (b) Components of the top-end joint A2.

Figure 3.11 The four top-end joints and their components.

(a) Photograph of the top-end joint B2.

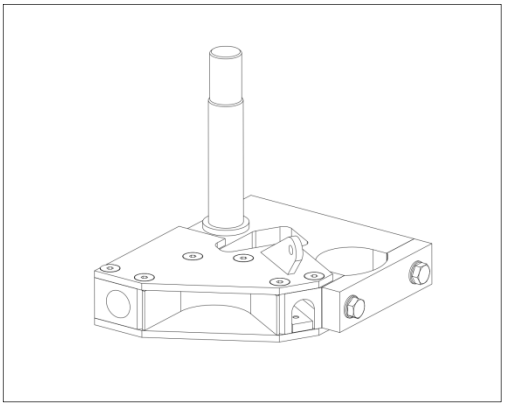

(b) Engineering drawing of the top-end joint B2.

Figure 3.12 The top-end joint B2.

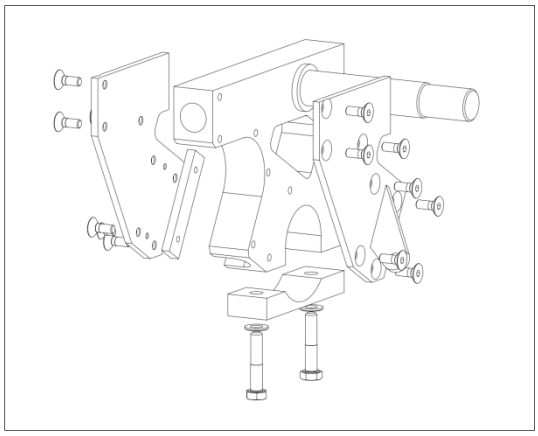

(a) First exploded view.

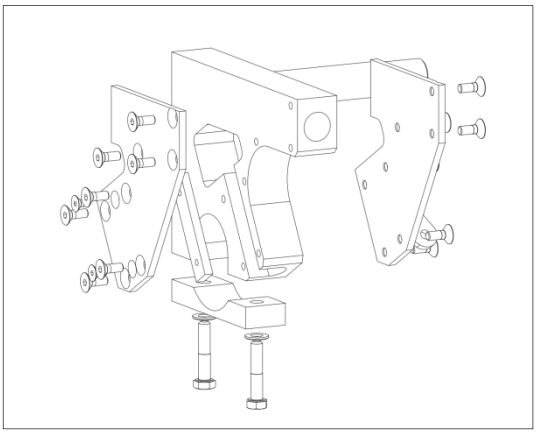

(b) Second exploded view.

Figure 3.13 Exploded views of the top-end joint B2.

The main body of the top-end joints is made of S355 steel and has a thickness of 30 mm. Welded to it, is a perpendicular 24 mm steel pin with right (or left) hand thread at its end.

(a) Photograph of the main body of the top-end joint A2.

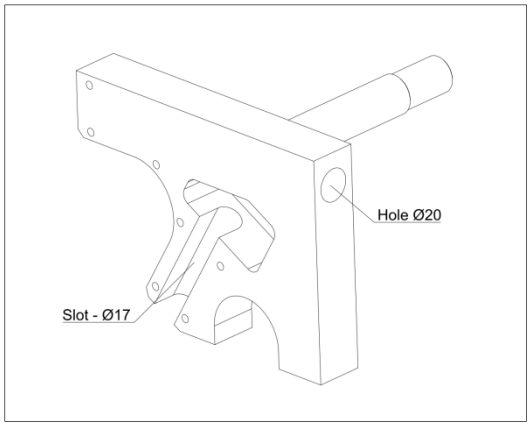

(b) Drawing of the main body of top-end joint A2.

Figure 3.14 Details of the main body of the top-end joint A2.

The main body has: an in-plane longitudinal circular hole (20 mm) for the 18 mm longitudinal steel bar; an in-plane slot for the 16mm diagonal steel bar; a contoured part for the corner of the triangular laminated glass panel, a hole big enough to insert the wrench for gripping and turning the hexagonal nut of the diagonal steel bar; 6 M6 threaded holes for fixing the inner and outer lateral plates to it.

The later plates are made of S355 steel and avoid the out-of-plane movement of the corner of the triangular laminated glass panel. Each lateral plate has a thickness of 5 mm, 6 countersunk holes for fixing it to the main body with hexagon socket countersunk head cap screws. A small perpendicular steel plate is welded to the inner lateral plate, which is connected the end of the bar of the torsional bracing system. The bottom U shaped steel element is a safe element.

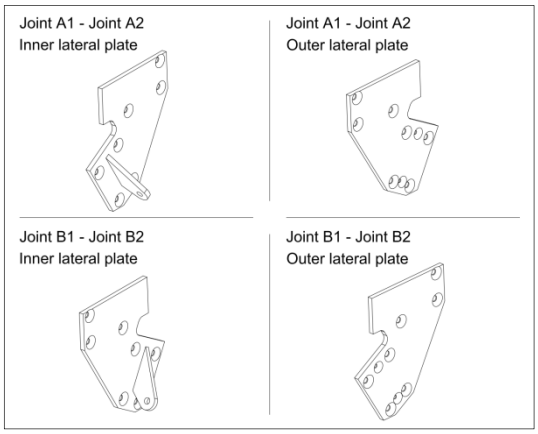

Figure 3.15 Lateral steel plates of the top-end joints.

An aluminium element and two polyethylene sheets are put between the glass corner and steel to avoid any local peak stress and dangerous stress concentration in the glass.

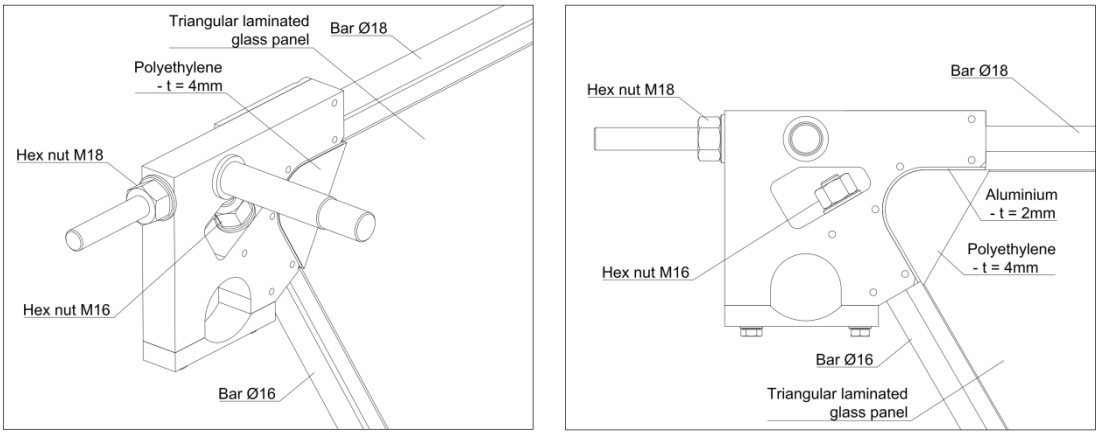

(a) Perspective view. (b) Front view.

Figure 3.16 Details of the top-end joint A2, the laminated glass panel and the steel bars.

The orthogonal 24 mm pin is welded to the main body and has a 35 mm long thread at its end. The pins of Joint A1 and Joint B1 have a left hand thread, whereas Joint A2 and Joint B2 have pins with right hand thread. The opposite threads are necessary to connect the opposite joints of the two vertical webs. The opposite joints are connected to each other with a circular hollow profile which has welded hexagonal nuts at its extremities. A clockwise rotation of the profile screws the nuts to the opposite joints, whereas a counterclockwise rotation unscrews the profile from the opposite steel joints.

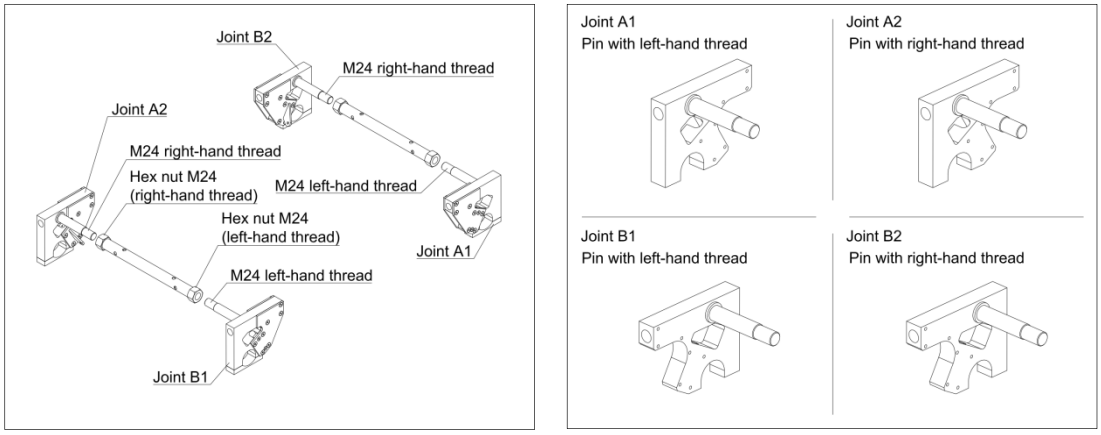

(a) Details of the connections. (b) Main bodies of the top-end joints.

Figure 3.17 The connection between the opposite top-end joints.

The four top-end joints transfer the loading to the four steel columns; each top-end joint only transfers vertical load and the rotation is free.

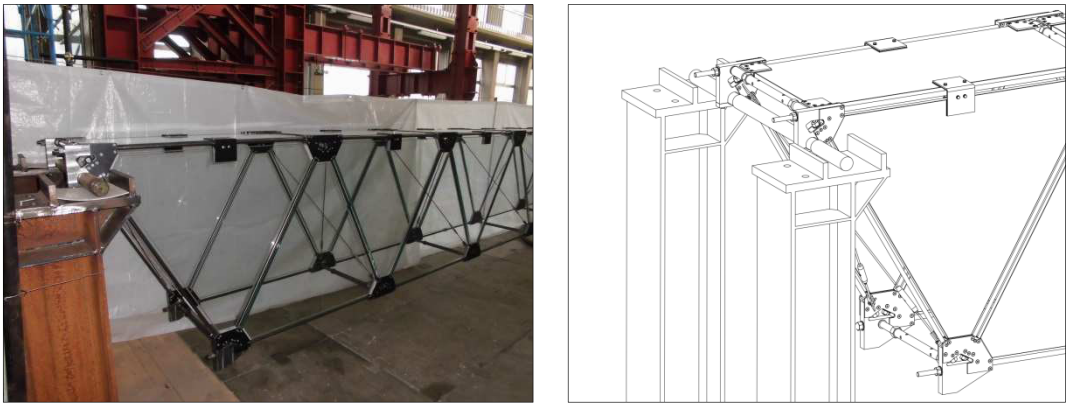

(a) Potograph. (b) View.

Figure 3.18 Detail of the beams on the columns.

Photographs and engineering drawings of the components are available in Appendix II and Appendix III.

Bottom-end joints

The four bottom-end joints have the same geometry and shape but some differences because of their position in the beam and the symmetry of the beam. The four bottom-end joints are named: Joint C1, Joint C2, Joint D1 and Joint D2.

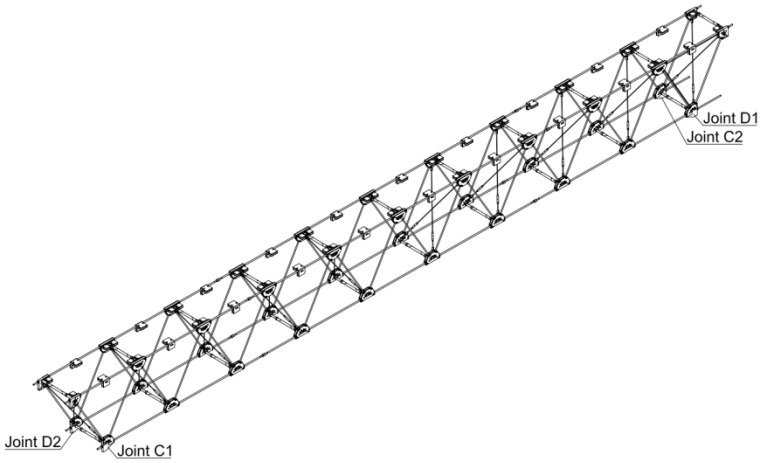

Figure 3.19 Position of the four bottom-end joints in the beam.

Each bottom-end joint consists of a main steel body, an inner lateral steel plate and an outer lateral steel plate.

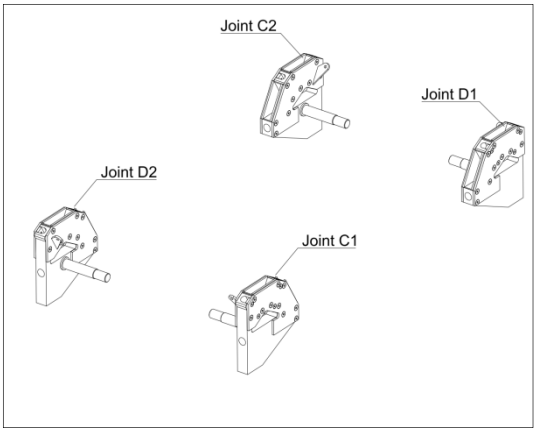

(a) Isometric view of the four bottom-end joints.

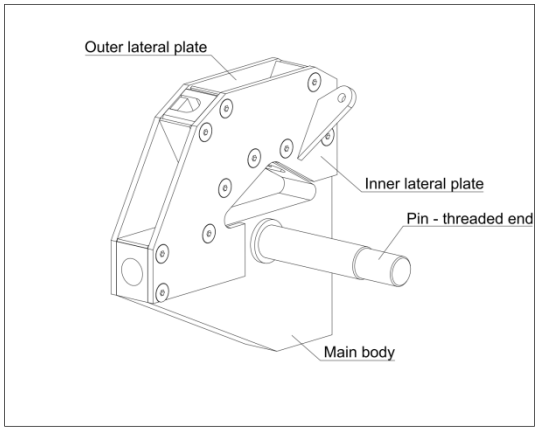

(b) Components of the bottom-end joint C2.

Figure 3.20 The four bottom-end joints and their components.

(a) Photograph of the bottom-end joint D2.

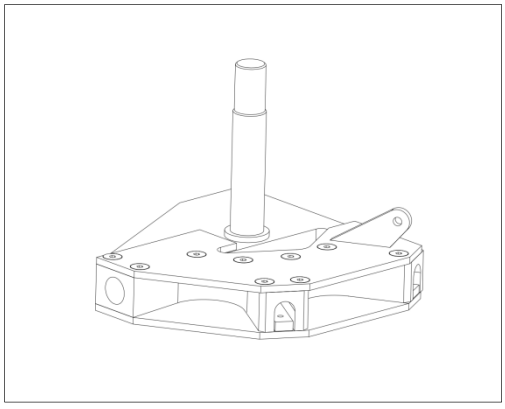

(b) Engineeering drawing of the bottom-end joint D2.

Figure 3.21 The bottom-end joint D1.

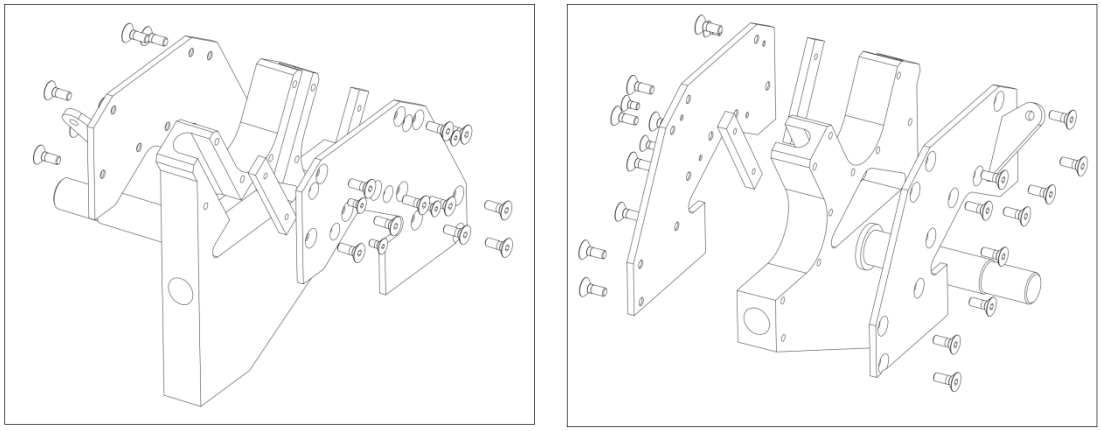

(a) First exploded view. (b) Second exploded view.

Figure 3.22 Exploded views of the bottom-end joint D2.

The main body of the bottom-end joints is made of S355 steel and has a thickness of 30 mm. Welded to it, is a perpendicular 24 mm steel pin with right (or left) hand thread at its end.

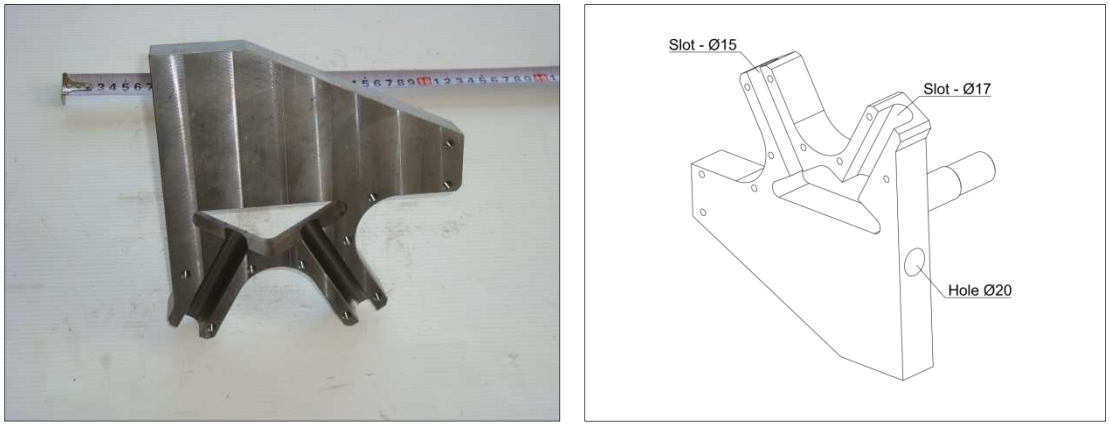

(a) Photograph of main body of the bottom-end joint D2. (b) Drawing of the main body of bottom-end joint D2.

Figure 3.23 Details of the main body of the bottom-end joint D2.

The main body has: an in-plane longitudinal circular hole (20 mm) for the 18 mm longitudinal steel bar; an in-plane slot for the 16mm diagonal steel bar; an in-plane slot for the 14mm diagonal steel bar; two contoured parts for the corners of two triangular laminated glass panels, a hole big enough to insert the wrench for gripping and turning the hexagonal nut of the diagonal steel bars; 7 M6 threaded holes for fixing the inner and outer lateral plates to it.

The later plates are made of S355 steel and avoid the out-of plane movement of the triangular laminated panels' corners. Each lateral plate has a thickness of 5 mm and 6 countersunk holes for fixing it to the main body with hexagon socket countersunk head cap screws. A small perpendicular steel plate is welded to the inner lateral plate, which is connected to the end of the bar of the torsional bracing system.

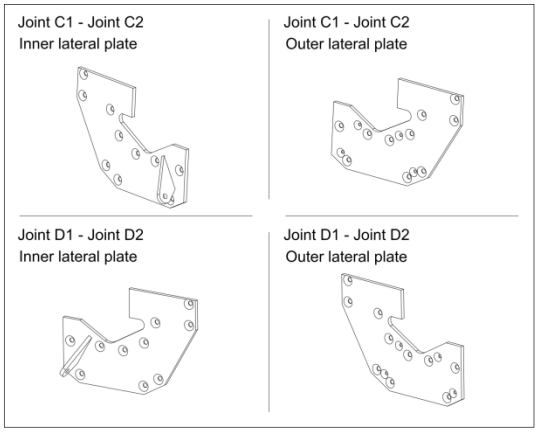

Figure 3.24 Lateral steel plates of the bottom-end joints.

An aluminium element and two polyethylene sheets are put between each glass corner and steel to avoid any local peak stress and dangerous stress concentration in the glass.

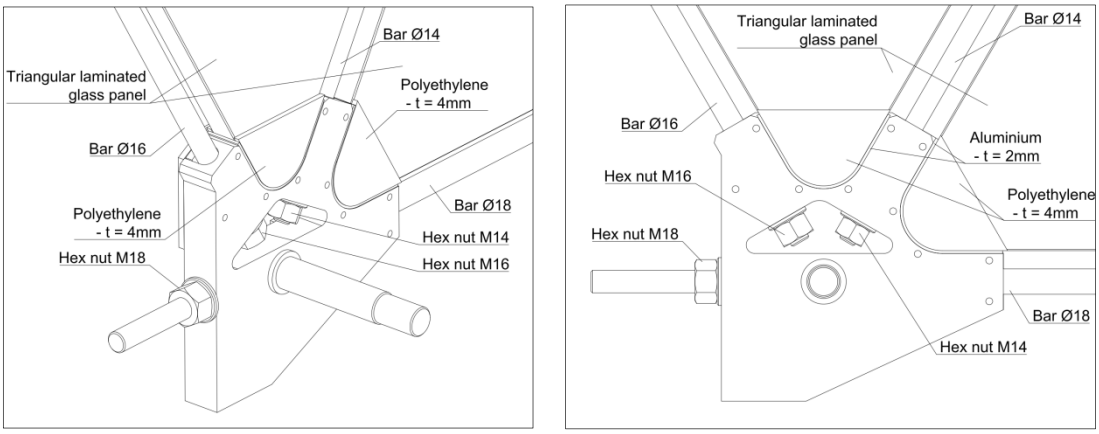

(a) Perspective view. (b) Front view.

Figure 3.25 Details of the bottom-end joint D2, the laminated glass panels and the steel bars.

The orthogonal 24 mm pin welded to the main body has a 35 mm long thread at its end. The pins of Joint C1 and Joint D1 have a left hand thread, whereas Joint C2 and Joint D2 have pins with right hand thread. The opposite threads are necessary to connect the opposite joints of the two vertical webs. The opposite joints are connected to each other with a circular hollow profile which has welded hexagonal nuts at its extremities. A clockwise rotation of the profile screws the nuts to the opposite joints, whereas a counterclockwise rotation unscrews the profile from the opposite steel joints.

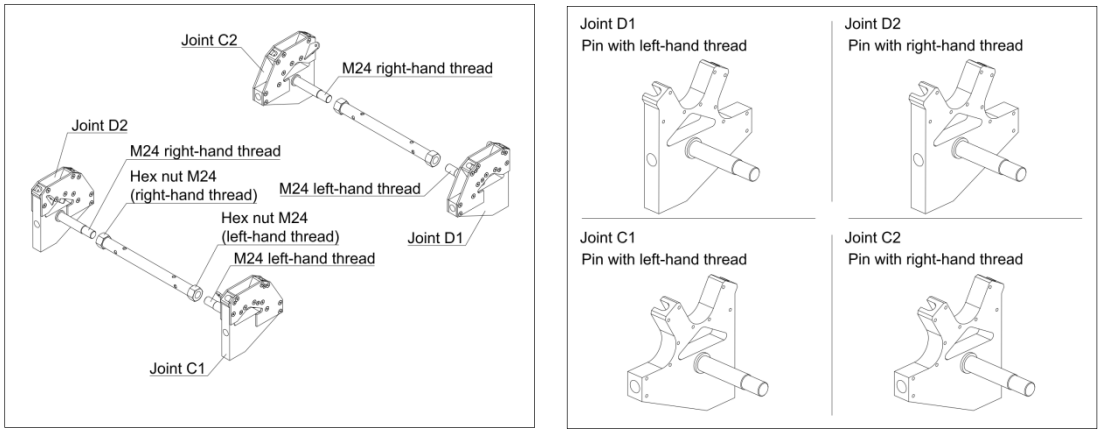

(a) Detail of the connections. (b) Main bodies of the bottom-end joints.

Figure 3.26 The connection between the opposite bottom-end joints.

Photographs and engineering drawings of the components are available in Appendix II and Appendix III.

Central joints

There are 34 central joints with the same geometry and shape; 17 of them have the perpendicular 24 mm steel pin with right hand thread, whereas the other 17 joints have the perpendicular 24 mm steel pin with left hand thread. Each central joint consists of a main steel body, an inner lateral steel plate and an outer lateral steel plate.

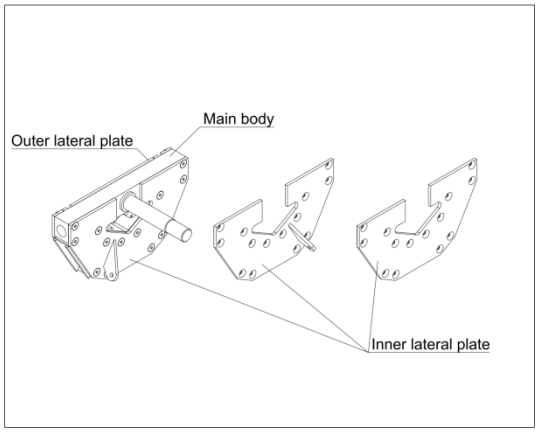

Figure 3.27 Components of the central joint.

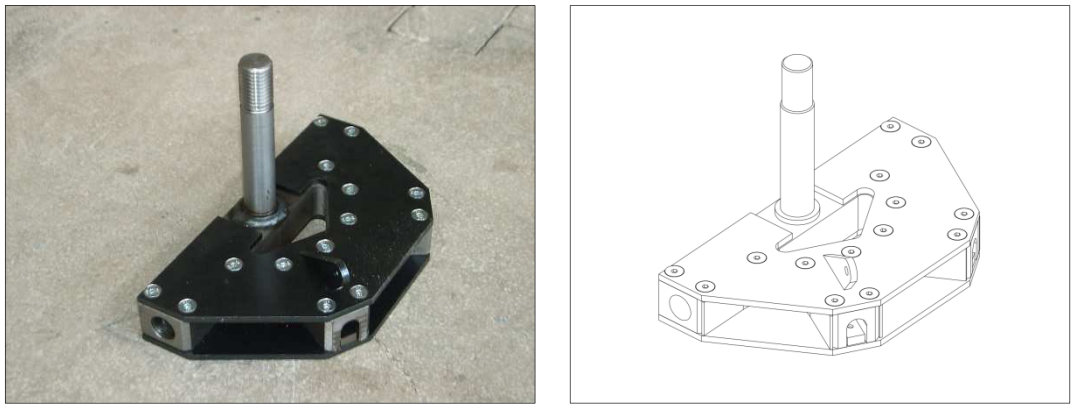

(a) Photograph of a central joint. (b) Engineering drawing of a central joint.

Figure 3.28 The central joint.

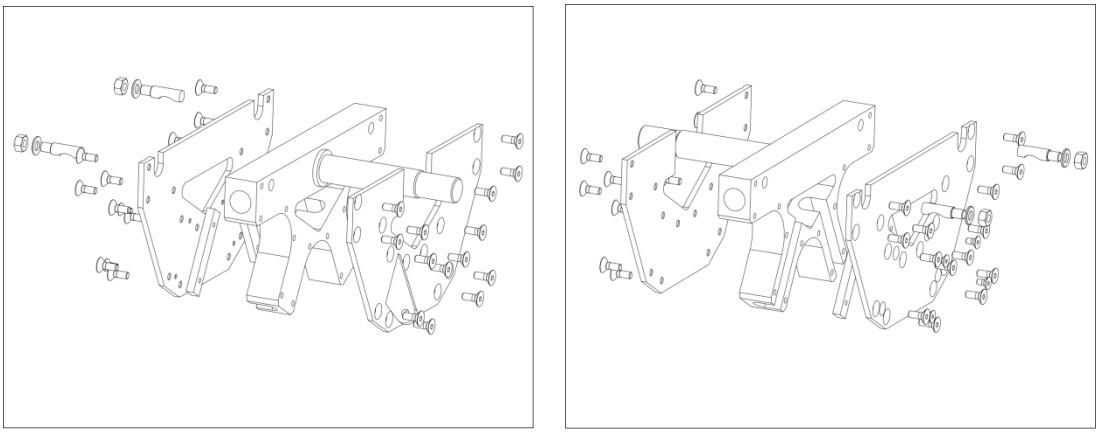

(a) First exploded view. (b) Second exploded view.

Figure 3.29 Exploded views of central joint.

The main body is made of S355 steel and has a thickness of 30 mm. Welded to it is a perpendicular 24 mm steel pin having right (or left) hand thread at its end.

The main body has: an in-plane longitudinal circular hole (20 mm) for the 18 mm longitudinal steel bar; two in-plane slot for the 14mm diagonal steel bars; three contoured parts for the corners of three triangular laminated glass panels, a hole big enough to insert the wrench for gripping and turning the hexagonal nut of the diagonal steel bars; 17 threaded holes for fixing the inner and outer lateral plates to the main body.

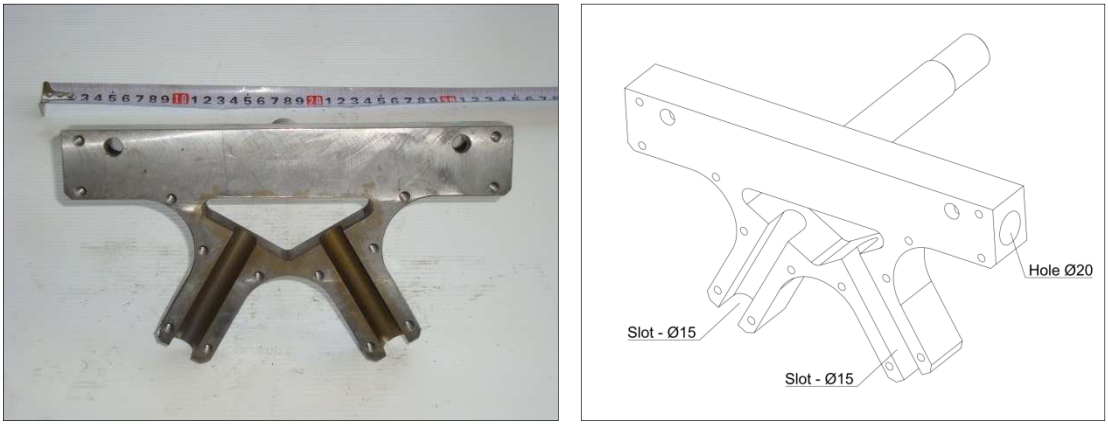

(a) Photograph of the main body. (b) Drawing of the main body.

Figure 3.30 Details of the main body of a central joint.

Two 10 mm circular holes are created perpendicularly to the main body in order to place two special shaped bolts. In this way, the longitudinal relative motion between the steel bar and the joint is partially restricted.

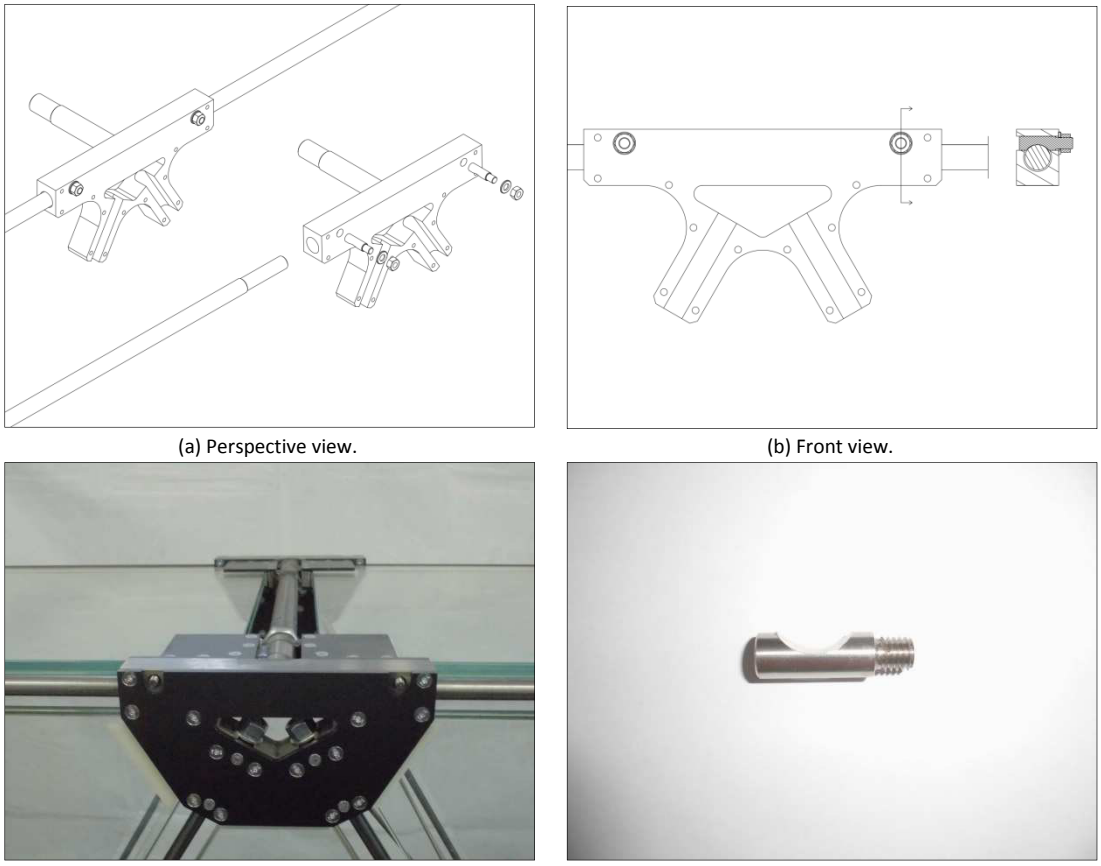

(a) Perspective view. (b) Front view.

(c) Photograph. (d) Photograph.

Figure 3.31 Details of the central joint and the special bolts.

The two later plates are made of S355 steel and avoid the out-of plane movement of the corners of the triangular laminated panels. Each lateral plate has a thickness of 5 mm and some countersunk holes to fix them to the main body with hexagon socket countersunk head cap screws. A small steel plate is welded to some inner lateral plates, which are connected the end of the bar of the torsional bracing system.

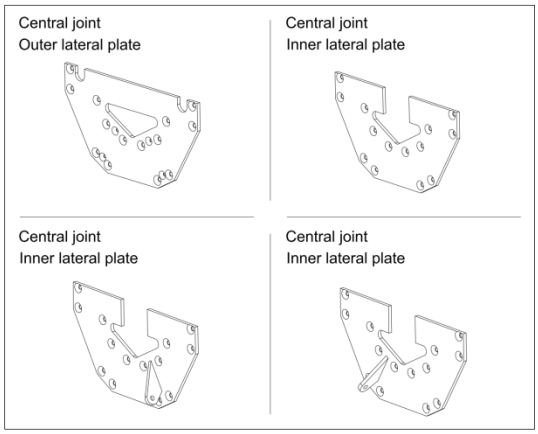

Figure 3.32 Lateral steel plates of the central joints.

An aluminium element and two polyethylene sheets are put between each glass corner and steel to avoid any local peak stress and dangerous stress concentration in the glass.

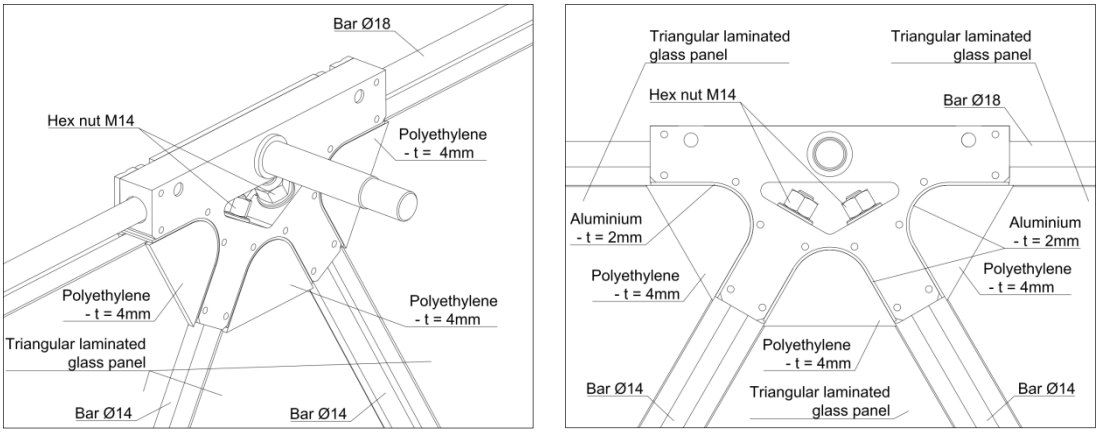

(a) Perspective view. (b) Front view.

Figure 3.33 Details of the central joint, the laminated glass panels and the steel bars.

The orthogonal 24 mm pin welded to the main body has a 35 mm long thread at its end. The pins of the joint belonging to the same web have left hand thread, whereas all the pins of the opposite web have right hand thread. The opposite threads are necessary to connect the opposite joints of the two vertical webs. The opposite joints are connected to each other by means of a circular hollow profile with welded hexagonal nuts at the extremities. A clockwise rotation of the profile screws the nuts to the opposite joints, whereas a counterclockwise rotation unscrews the profile from the opposite steel joints.

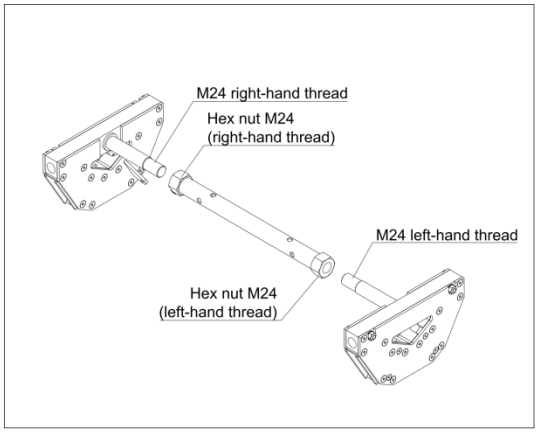

Figure 3.34 The connection between two opposite central joints.

Photographs and engineering drawings of the components are available in Appendix II and Appendix III.

3.3.5 Steel pinned conncections

The beam only has a top flange composed of 10 identical rectangular laminated glass panels. Each corner of these panels is joined to the top steel joints by means of a hinged connection that allows a relative free rotation. The connection only transfers compressive force in glass. No tensile stress is present because the glass corner is detached from the connection.

An aluminium element and two polyethylene sheets are put between the glass corners and steel to avoid any local peak stress and dangerous stress concentration in the glass.

The pin of the connection is the 24 mm pin, welded orthogonally to the main body of all steel joints, the connector consists of a steel circular hollow element (or two small circular hollow elements), an L-shaped steel element and two identical steel plates.

The connector is made of S355 steel, the steel circular hollow elements are obtained by circular hollow section profile 33.7x4, the L-shaped element is 24 mm thick with 5 M6 threaded holes for fixing the two plates to it; these are 5 mm thick and identical with 5 countersunk holes.

There are 4 pinned connections at the four top-end joints and 18 pinned connections at the central top joints.

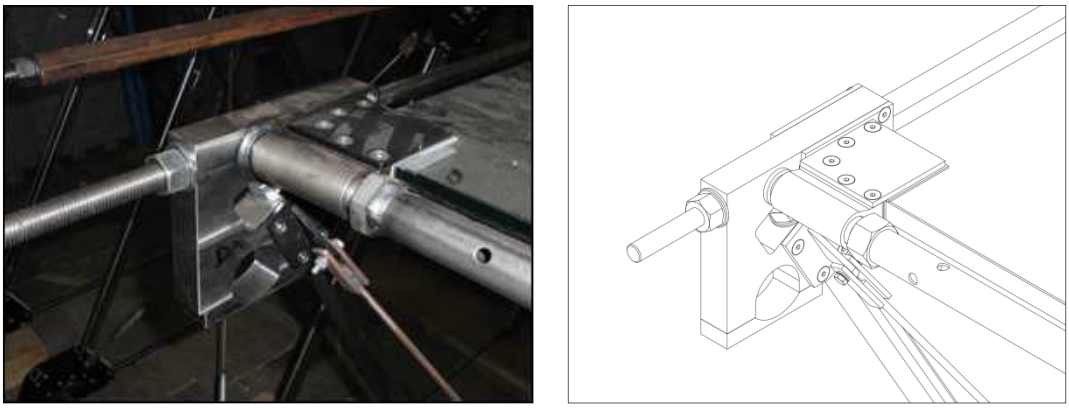

(a) Photograph. (b) Isometric view.

Figure 3.35 The pinned connection - top end joint.

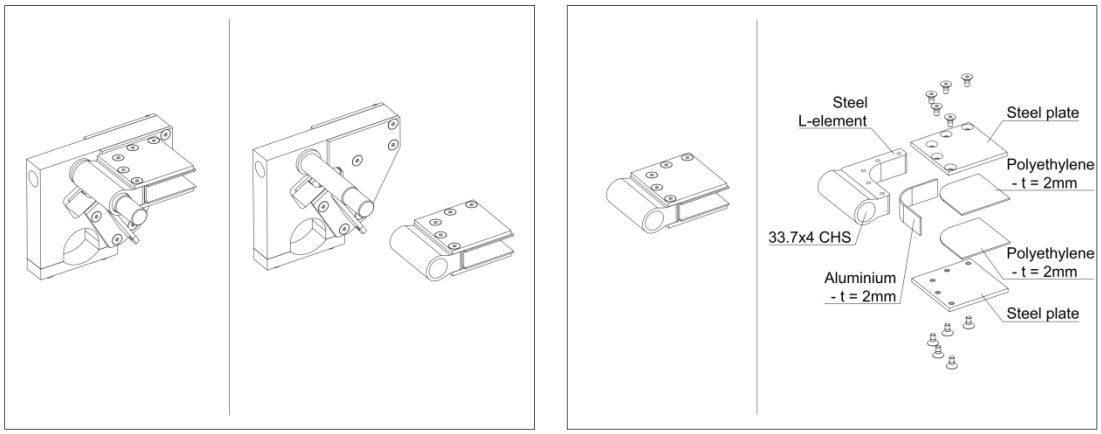

(a) Isometric view. (b) Exploded view.

Figure 3.36 Details of the pinned connection - top end joint.

(a) Photograph. (b) Photograph.

Figure 3.37 The pinned connection – central joint.

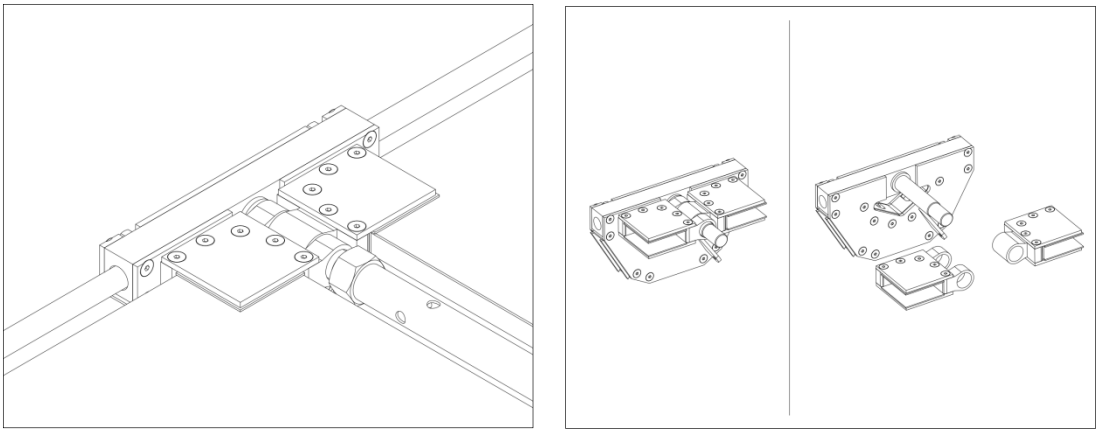

(a) Isometric view. (b) Exploded view.

Figure 3.38 Drawings of the pinned connection - central joint.

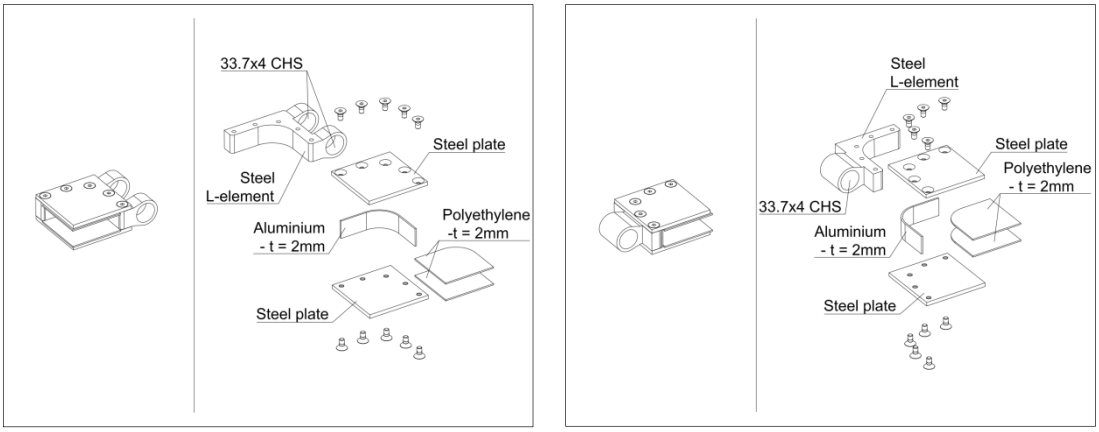

(a) Exploded view. (b) Exploded view.

Figure 3.39 Details of the pinned connection - central joint.

Photographs and engineering drawings of the components are available in Appendix II and Appendix III.

3.3.6 Steel joint-to-joint connections

The two segmented glass webs of the beam are joined together at the steel joints. The steel joints of one web are connected to the opposite steel joints of the other web.

The connector consist of a circular hollow section profile (30x2 - CHS) made of S355 steel having two M24 hexagonal nuts welded at its extremities. At one extremity an M24 hexagonal nut with right-hand thread is welded, whereas at the other extremity an M24 hexagonal nut with left-hand thread is welded.

(a) Photograph of a bottom connection.

(b) Photograph of the connector.

Figure 3.40 The steel joint-to-joint connection.

A clockwise rotation of the profile screws the nuts of the connector to the two opposite joints, whereas a counterclockwise rotation unscrews the connector.

There are 21 steel joint-to-joint connections, one for each couple of opposite steel joints.

Photographs and engineering drawings are available in Appendix II and Appendix III.

3.3.7 Steel friction – grip connections

A sort of clamped fitting has been developed in order to increase the buckling strength of the glass panels; the middle point of each upper edge of the vertical triangular panels has been connected to the middle point of the adjacent edge of the rectangular one by means of a friction-grip fixing. This connection reduces the effective buckling length and thus increases the buckling strength; it avoids the movement of the point perpendicularly connected to the glass panel.

The connection consists of three S355 steel elements joined with bolts. The direct contact between glass and steel is avoided by putting a rectangular polyethylene intermediate element between them. There are 20 steel friction – grip connections.

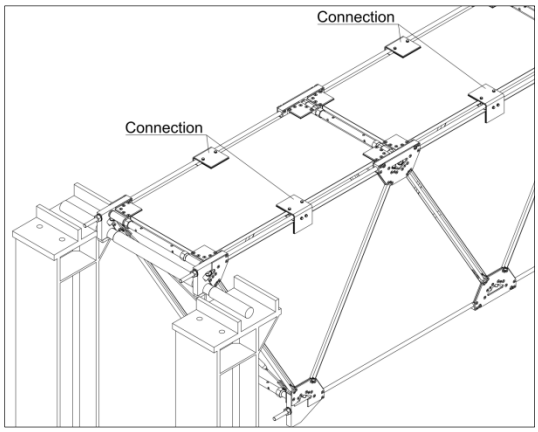

(a) Isometric view.

(b) Photograph of two connections.

Figure 3.41 The steel friction – grip connections.

(a) Photograph. (b) Photograph.

Figure 3.42 Photgraphs of a steel friction – grip connection.

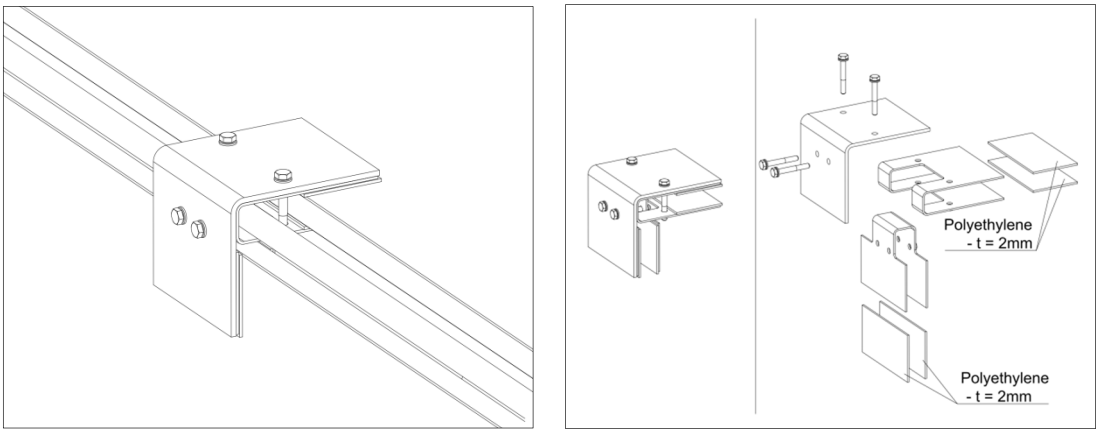

(a) Isometric view. (b) Exploded view.

Figure 3.43 Components of the steel friction – grip connection.

Photographs and engineering drawings of the components are available in Appendix II and Appendix III.

3.3.8 Steel bars

The post-tensioning system consists of diagonal and longitudinal steel round bars made of C40 steel and disposed in the glass webs following a Warren scheme. Both of the upper and lower longitudinal bars have a diameter of 18mm; the diagonal bars have a diameter of 14mm with the exception of those near the bearings which have a diameter of 16mm.

The relative motion of longitudinal steel bars inside the steel joints is partially reduced by screwing two special bolts located at each joint after the post-tensioning operations (see *paragraph 3.3.4.*).

Furthermore, a torsional bracing system composed of Ø6 S335 steel bars tensioned by screw tighteners, gives torsional stiffness and lateral torsional buckling stability to the beam.

Position	**Diameter [mm]**	**Number [n]**	**Length [mm]**
Top longitudinal bars	18	2 (3+3)	12300
Bottom longitudinal bars	18	2 (3+3)	11485
Diagonal bars	16	4	1135
Diagonal bars	14	36	1135
Bars of the torsional bracing system	6	20	1105

Table 3.1 Steel bars

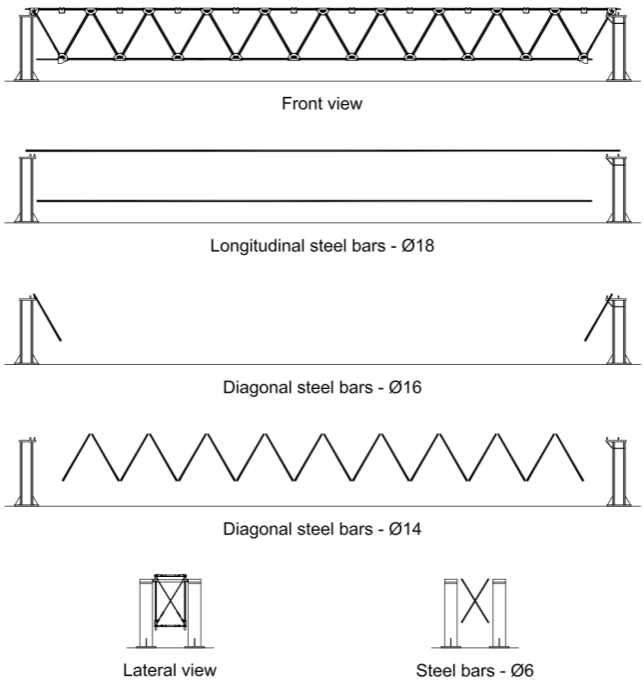

Figure 3.44 Position of the steel bars.

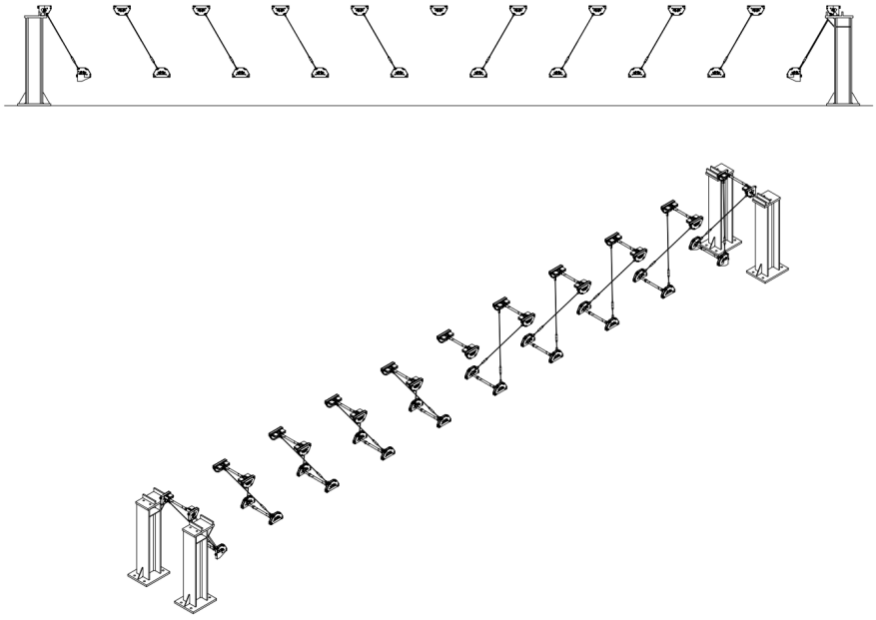

Figure 3.45 Schematic representation of the position of the torsional bracing system.

Photographs and engineering drawings are available in Appendix II and Appendix III.

3.3.9 Intermediate materials: aluminium and polyethylene

The brittleness of glass and its inability to redistribute local stress concentrations by yielding are critical in the design of glass element and connections. In order to prevent and to avoid stress concentrations, aluminium

elements (thickness of 2mm) are put between glass corners and steel to avoid any local dangerous contact tension peak in glass.

Polyethylene sheets (thickness of 2mm and 4mm) are put between the lateral glass surfaces of laminated glass panels and steel to avoid a direct glass-steel contact.

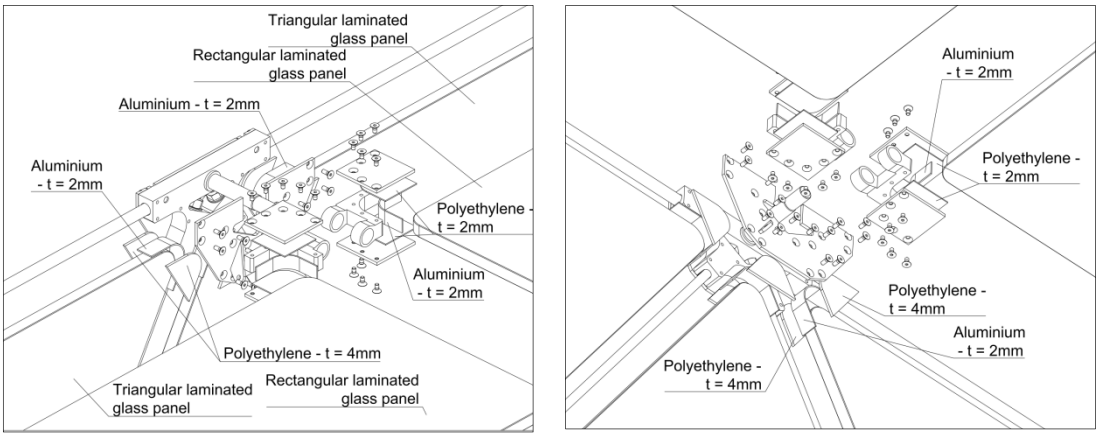

(a) Top exploded view. (b) Bottom exploded view.

Figure 3.46 Exploded views with location of the alluminim elements and the polyethylene sheets.

(a) Top central joint. (b) Bottom central joints.

Figure 3.47 Potographs of steel joints with location of the alluminim elements and the polyethylene sheets.

Moreover, in the connections between rectangular and triangular laminated glass panels, the direct contact between glass and steel is avoided by putting rectangular polyethylene sheets between them.

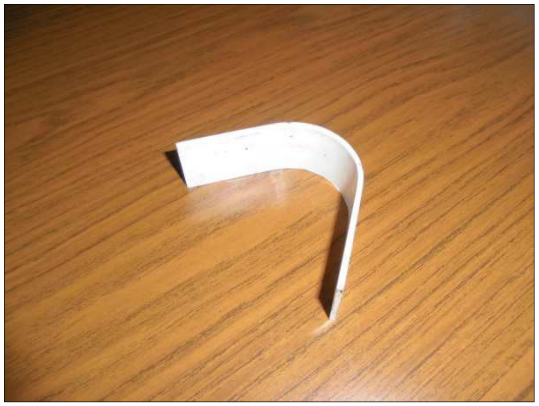

(a) Photograph of the aluminium element (2mm thick) – triangular panel.

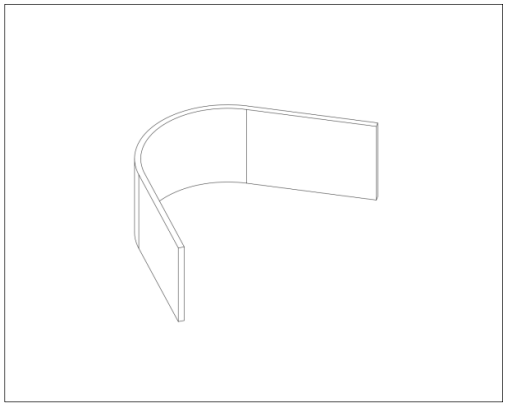

(b) View of the aluminium element (2mm thick) – triangular panel.

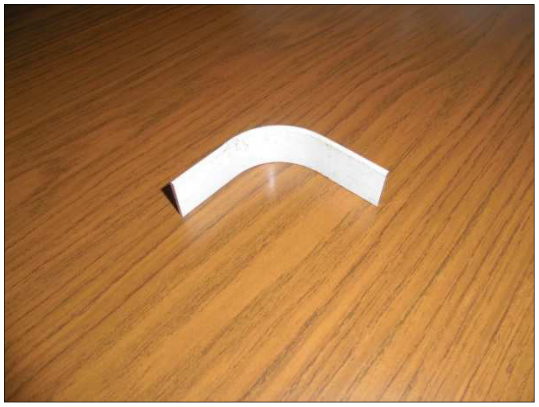

(c) Photograph of the aluminium element (2mm thick) – rectangular panel.

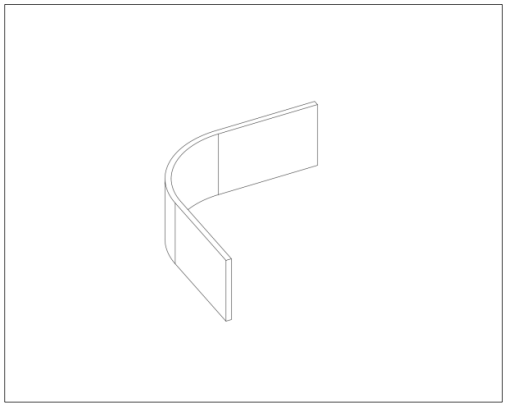

(d) View of the aluminium element (2mm thick) – rectangular panel.

Figure 3.48 Intermediate material: aluminium.

(a) Photograph of the polyethylene element (4mm thick) – triangular panel.

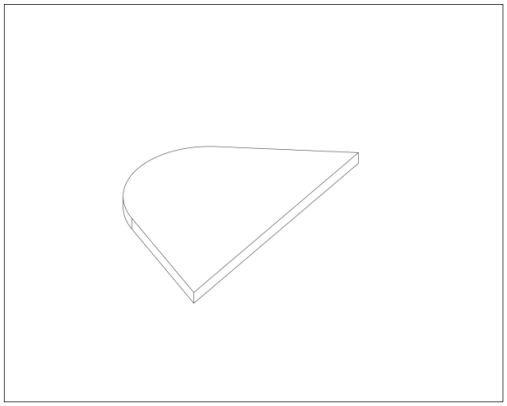

(b) View of the polyethylene element (4mm thick) – triangular panel.

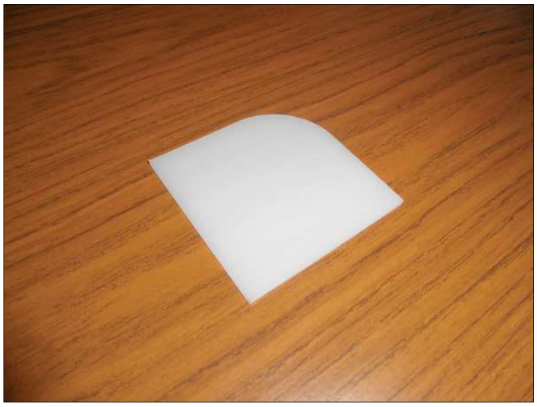

(c) Photograph of the polyethylene element (2mm thick) – rectangular panel.

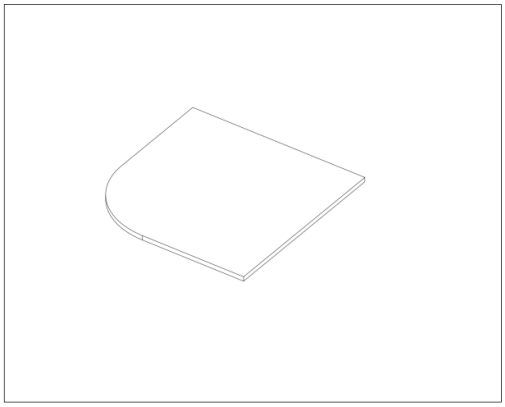

(d) View of the polyethylene element (2mm thick) – rectangular panel.

Figure 3.49 Intermediate material: polyethylene.

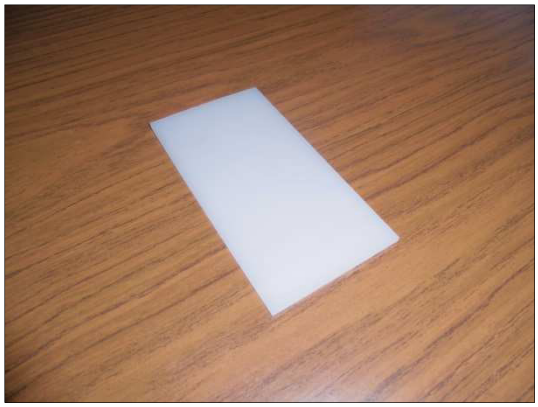

(a) Photograph.

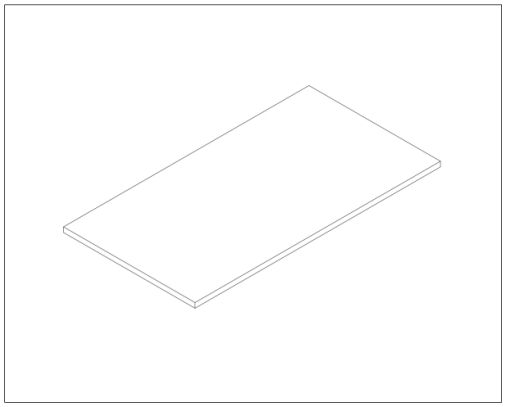

(b) View.

Figure 3.50 Intermediate elements of the connections between rectangular and triangular laminated panles - polyethylene 2mm thick.

Photographs and engineering drawings are available in Appendix II and Appendix III.

Chapter 4 Materials

This chapter provides an overview of the mechanical properties of the materials applied to construct the 12 m segmented post-tensioned hybrid steel-glass beam that has been experimentally investigated in this research. These materials are glass, steel, aluminium and polyethylene.

4.1 Introduction

The 12 m segmented post-tensioned hybrid steel-glass beam constructed and tested in this research consists of rectangular and triangular laminated glass panels, steel bars, steel joints and steel connections. Furthermore, aluminium and polyethylene inserts are put between glass and steel in order to avoid any local dangerous contact tension peak in glass.

All laminated glass panels consist of two 10 mm thick heat-strengthened glass sheets laminated with a 1.52 mm thick film of PVB interlayer.

The steel bars are made of C40 steel except for the bars of the torsional bracing system which are made of S335 steel. All the other steel elements are made of S355 steel.

The properties of the glass, the interlayer material, the steel and the intermediate materials used are discussed in the following sections.

4.2 Glass

Glass is a noncrystalline solid material showing glass transition. The glass used in construction is mostly soda-lime silicate glass (SLSG) except for some special applications like for fire protection glazing and heat resistant glazing where borosilicate glass (BSG) is used. The latter assures a high resistance to temperature changes and a high hydrolytic and acid resistance.

The following sub-paragraphs provide an overview of the glass production and treatment processes, the composition and chemical properties, and the mechanical properties of the glass used in this research.

4.2.1 Production processes

The most common production processes for flat glass are floating, casting and rolling. There are three production steps which are always very similar: melting at 1600-1800° C, forming at 800-1600°C and cooling at 100-800° C. Nowadays, the float production process is the most popular and beneficial process; 90% of worldwide flat glass production is from floating process. The float glass production process was introduced in 1959 by the Pilkington Brothers; it ows its success to low cost, reliability, the high optical quality and the large sizes of panes that can be produced. The float glass production provided a cheaper and higher quality glass compared with the flat glass produced at that time with the Fourcault, Pittsburgh and Libbey-Owens processes.

The float process is a continuous manufacturing process; float glass is produced in large manufacturing plants that operate continuously 24 hours a day, 365 days a year. In the production process, the raw materials are melted in a furnace at a temperature of 1550°C. The molten glass is poured continuously at a temperature of 1000°C into a pool of molten tin in an inert atmosphere consisting of hydrogen and nitrogen that prevents tin's oxidation. Thanks to the liquid physical state of tin at that temperature and to its higher specific weight, the

glass floats on the tin forming a flat surface whit a thickness of 6-7 mm. By adjusting the speed of the rollers, the glass thickness can be reduced or increased within a range of 2 to 25 mm, then the glass is gradually cooled down to a temperature of 600 °C. Subsequently, the glass enters into an oven called annealing lehr, where it is slowly cooled to prevent residual stress within the glass. Finally, automated machines inspect the float glass out of the annealing lehr and visual defects and imperfections are removed during cutting. The standard dimensions of standard float glass sheets are 3.21 m x 6.0 m, but larger glass sheets can be produced. The nominal thicknesses generally available are 2, 3, 4, 5, 6, 8, 10, 12, 15, 19 and 25 mm but production of 25 mm thick glass is limited due to the high costs.

The glass sheets' two surfaces are not identical; the contact of the tin side with the rollers marginally reduces the strength of the tin side. When exposed to ultraviolet radiation, the tin side shows a bluish fluorescence.

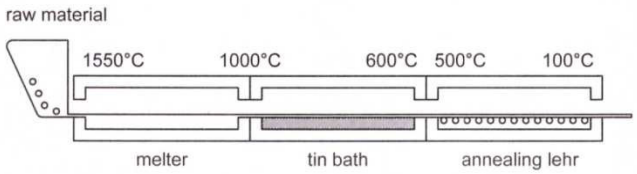

Figure 4.1 Schematic representation of the production process for float glass (Haldimann, et al., 2008).

4.2.2 Chemical composition

Glass is an amorphous solid without long range order and ordered atomic structure that shows the glass transition effect. Most glass is the product of fusion that is cooled to a rigid condition without crystallization. Glass consists of an irregular network of silicon and oxygen atoms with alkaline parts in between.

In this research, soda-lime silicate glass (SLSG) is used. *Table 4.1* gives the chemical composition of soda-lime silicate glass (SLSG) which is a mixture of silica sand, lime, magnesia and alumina. During the cooling process of the liquid glass, viscosity increases until solidification. The temperature at solidification is called glass transition temperature T_g and it is about 530° C for soda-lime silicate glass (SLSG). The transition between liquid and solid state takes places over a certain temperature range (Haldimann, et al., 2008).

Constituents		**Mass**
Silicon dioxide	SiO_2	69-74%
Calcium oxide	CaO	5-14%
Sodium oxide	Na_2O	10-16%
Magnesium oxide	MgO	0-6%
Aluminium oxide	Al_2O_3	0-3%
Others		0-5%

Table 4.1 Chemical composition of soda-lime silicate glass, indicatory values (mass %) according to [EN 572-1:2004].

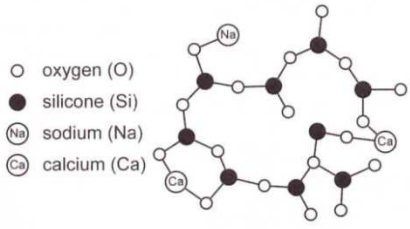

Figure 4.2 The irregular network of a soda-lime silicate glass (Haldimann, et al., 2008).

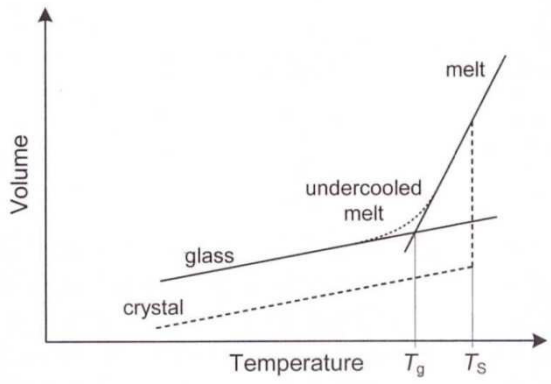

Figure 4.3 Schematic representation of the relationship between temperature and volume (Haldimann, et al., 2008).

4.2.3 Physical properties

The most important physical properties of soda-lime silicate glass are given in *Table 4.2*.

Characteristic	Symbol	Numerical value	Unit
Density (at 18°C)	ρ	2500	$\mathrm{kg/m^3}$
Hardness (Knoop)	$HK_{0.1/20}$	6	GPa
Young's modulus (modulus of elasticity)	E	70000	MPa
Poisson's ratio	μ	0.2	
Characteristic bending strength	$f_{g,k}$	45	MPa
Specific heat capacity	C	720	$\mathrm{J/(kg \cdot K)}$
Average coefficient of linear expansion between 20°C and 300°C	α	$9{\cdot}10^{-6}$	$\mathrm{K^{-1}}$
Resistance against temperature differential and sudden temperature change		40	K
Thermal conductivity	λ	1	$\mathrm{W/(m \cdot K)}$
Mean refractive index to visible radiation (380 nm to 780 nm)	N	1.5	
Emissivity (corrected)	ε	0.837	

Table 4.2 Physical properties of soda-lime silicate glass according to [EN 572-1:2004].

In research and applications, poisson's ratio values are typically between 0.22 and 0.24 (Haldimann, et al., 2008).

4.2.4 Mechanical properties

Glass is an isotropic, almost perfectly elastic material that exhibits brittle sudden fracture without any plastic deformation capacity. The brittle nature of glass is due to its irregular molecular structure which lack in slip planes that allow plastic deformation before fracture. Consequently, stress concentrations are not reduced through stress redistribution and plastic local deformation.

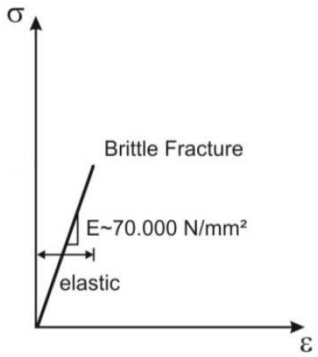

Figure 4.4 Schematic representation of the stress – strain relation of glass.

The theoretical tensile strength of glass is very high but its effective strength is much lower; it depends on mechanical flaws on the surface, where stress concentrations cannot be redistributed.

Most of the surface flaws are not visible to the naked eye and there are many more and more severe ones in glass panes than in small glass elements like glass fibers.

Glass fails when the stress intensity at the tip of the crack reaches its critical value. Depending on the size of the surface cracks, the tensile strength is controlled by the onset of a hypercritical crack growth without any plastic deformation. Hence, the effective tensile strength of glass is not a material constant; it depends on the size of the glass element, the condition of the surface, the water and humidity exposition, the intensity and the duration of load application and the residual stress.

Furthermore, the effective tensile strength in the case of permanent loads is lower than the strength in the case of loads with a short duration. The subcritical crack growth occurs due to stress-corrosion under environmental expositions together with long-term loading.

Theoretical strength of glass

The theoretical strength of glass depends on the molecular forces of the interatomic bonds; it is very high and may reach a value of 32 GPa. However, this value is not useful for engineering applications because the effective tensile strength of glass is greatly reduced by the inevitable presence of microscopic surface flaws (Haldimann, et al., 2008).

The theoretical strength of glass is calculated according to *Orowan* with the Equation (4.1) that gives the necessary stress to break an interatomic bond.

$$\sigma_M = \sqrt{\frac{E \cdot \gamma_s}{r_o}} \tag{4.1}$$

where

$E =$ Young's modulus

$\gamma_s =$ fracture surface energy

$r_o =$ equilibrium spacing of the atoms

According to (4.1), the theoretical strength of soda-lime silicate glass is:

$\sigma_M = 32\ GPa$

with

$E = 70\ GPa$

$\gamma_s = 3\ J/m^{-2}$

$r_o = 0.2\ nm$

Fracture toughness

The low value of the effective tensile strength was explained by *Griffith* who investigated and asserted that fracture starts from inevitable pre-existing flaws on the surface, named *Griffith flaws*. The high stress concentrations at the tip of flaws weaken glass and produce the flaw growth when loaded.

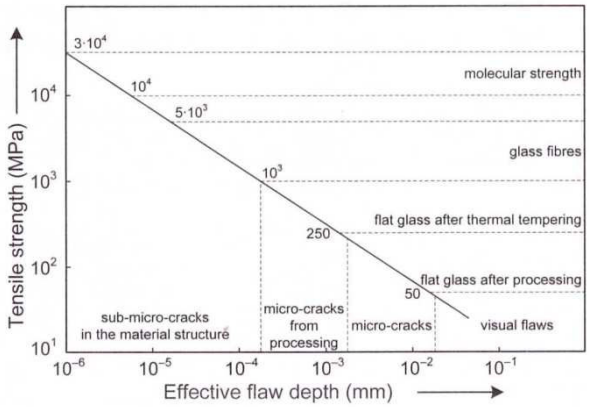

Figure 4.5 Relation between the tensile strength and the flaw depth (Haldimann, et al., 2008).

Starting from the *Griffith* study, *Irwin* introduced the concept of *stress intensity factor (SIF) K* to characterize the brittleness - fracture toughness - of a material. The stress intensity factor represents the elastic stress intensity near to the crack tip, for *mode I* loading corresponding to normal separation of the crack walls under the action of tensile stress it is K_I and is given by:

$$K_I = Y \cdot \sigma_N \cdot \sqrt{\pi \cdot a} \tag{4.2}$$

where

$\sigma_N =$ nominal tensile stress normal to the crack's plane

$Y =$ correction factor, also called geometry factor

$a =$ size of the crack, the crack dept or half of the crack length

The *geometry factor Y* depends on the crack's depth and geometry, on the specimen geometry and on the stress field. For a long, straight-fronted plane edge crack in a semi-infinite specimen *Y*=1.12; for half-penny shaped cracks in a semi-infinite specimen, the geometry factor is in the range of 0.637 to 0.713 (Haldimann, et al., 2008).

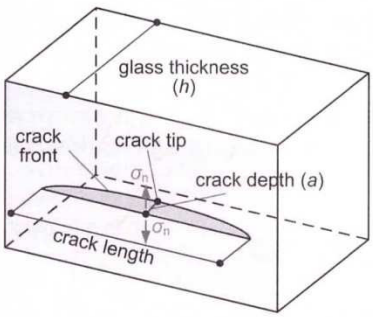

Figure 4.6 Schematic view of a surface flaw (Haldimann, et al., 2008).

When the stress intensity factor K_I due to tensile stress at the tip of the crack reaches the critical value K_{Ic}, the brittle failure of glass occurs suddenly. The critical stress intensity factor K_{Ic} is considered a material constant and represents the fracture toughness of the material. A value of K_{Ic} = 0.75 MPa·m$^{0.5}$ is suggested for soda-lime silicate glass (Haldimann, et al., 2008).

Stress corrosion

The strength of glass depends on humidity that in presence of a positive crack opening stress causes flaws to grow slowly. This means that the most critical flaw grows to its critical size and the glass element will fail suddenly even if the tensile stress is constant and lower than the momentary strength.

In other terms, static load causes a decreasing of the momentary strength with time; the growth of a surface flaw depends on the size of flaw, the stress history and the relationship between crack velocity and stress intensity. This phenomenon known as *sub-critical crack growth* is the consequence of a chemical process named *stress corrosion*. An almost linear correlation is observed between the logarithm of the crack velocity *v* and the logarithm of the humidity ratio *H*. Stress corrosion is due to the chemical reaction of a water molecule with silica at the crack tip (Haldimann, et al., 2008).

$$\text{Si} - \text{O} - \text{Si} \quad + \quad \text{H}_2\text{O} \qquad \rightarrow \qquad \text{Si} - \text{OH} \quad + \quad \text{OH} - \text{Si}$$

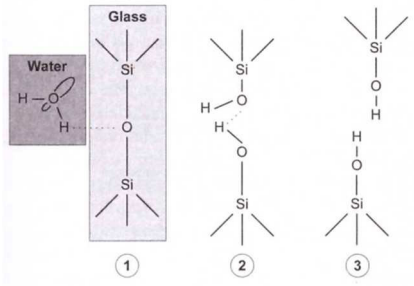

Figure 4.7 Chemical process of the stress corrosion: (1) adsorption of water to Si-O bond, (2) reaction, (3) formation of surface hydroxyl groups (Haldimann, et al., 2008).

Figure 4.8 shows the schematic relationship between the crack velocity *v* and the stress intensity factor K_I, three regions named *I*, *II* and *III* are indicated.

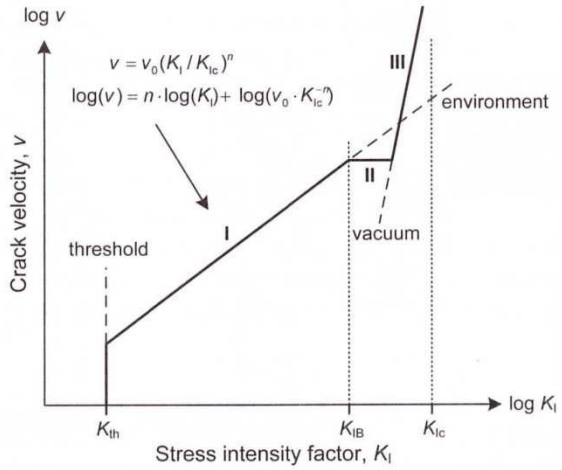

Figure 4.8 Simplified representation of v-K_I relationship (Haldimann, et al., 2008).

Figure 4.8 shows that for values of K_I close or greater than the critical stress intensity factor K_{Ic}, the crack velocity v is independent of the environmental conditions and the crack velocity reaches the characteristic crack propagation speed.

In region *III*, the region below K_{Ic}, the curve v-K_I is very steep. In inert environments this curve would extrapolate linearly to lower crack velocity. In normal environments, the behaviour strongly depends on the environmental conditions and the curve changes defining region *I* (Haldimann, et al., 2008).

In region *I* the relation between the crack velocity v and the stress intensity factor K_I is given by:

$$v = v_o \cdot (K_I / K_{Ic})^n \tag{4.3}$$

where

$v_o =$ crack velocity parameter (m/s)

$n =$ parameter dimensionless

On logarithmic scales v_o represents the position of the v-K_I curve and n the slope. Below the threshold stress intensity K_{th} no crack growth occurs in glass.

4.2.5 Tempered glass and laminated glass

The brittle nature of glass, its vulnerability to stress concentrations, the stress corrosion and the sensitivity to surface flaws require further treatments to assure a safe use of glass in structural applications. *Float*[1] *glass* can be processed to obtain *thermally toughened glass*, *heat strengthened glass*, *chemically strengthened glass* and *laminated glass*. The standard float glass without any tempering is called *annealed glass*.

The basic idea of the tempering process is to create a favourable residual stress field with tensile stresses in the core of the glass and compressive stresses on the surfaces. The absence of flaws in the glass core offers a good resistance to tensile stress. The compressive stress on and near the surfaces avoid the growth of flaws when exposed to tensile surface stresses smaller than the residual compressive stresses introduced by tempering. The bending strength of the tempered glass is much higher than the bending strength of float glass, see *Table 4.3*.

[1] The term float glass is for glass derived from floating process where the glass melt floats on a liquid bed of tin, as described in *paragraph 4.2.1*.

Characteristic	Annealed glass / Float glass	Heat strengthened glass (HSG)	Thermally toughened glass (TTG)
Characteristic bending strength f_k	45 MPa	70 MPa	120 MPa
Degree of surface prestress	~ 0 MPa	~ 30 – 50 MPa	> 90 MPa

Table 4.3 Characteristic bending strength for float, heat strengthened and thermally toughened glasses (Feldmann, et al., 2014).

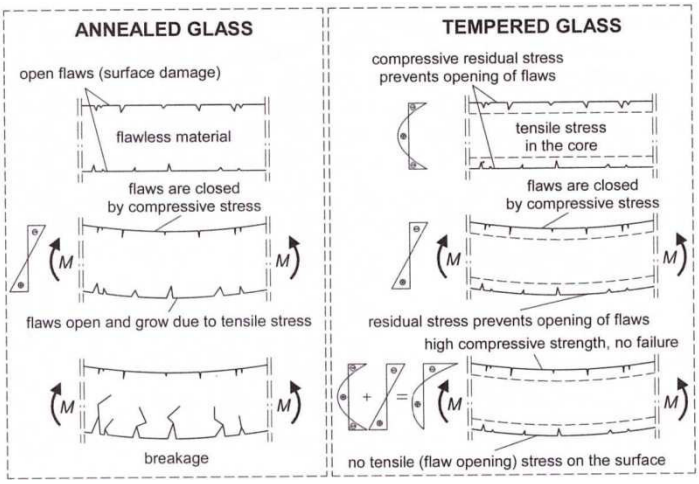

Figure 4.9 The glass tempering process (Haldimann, et al., 2008).

In case of breakage, the fracture pattern depends on the energy stored in the glass during the tempering process. *Figure 4.10* shows a comparison of fracture pattern of glass specimens loaded in a coaxial double ring test setup.

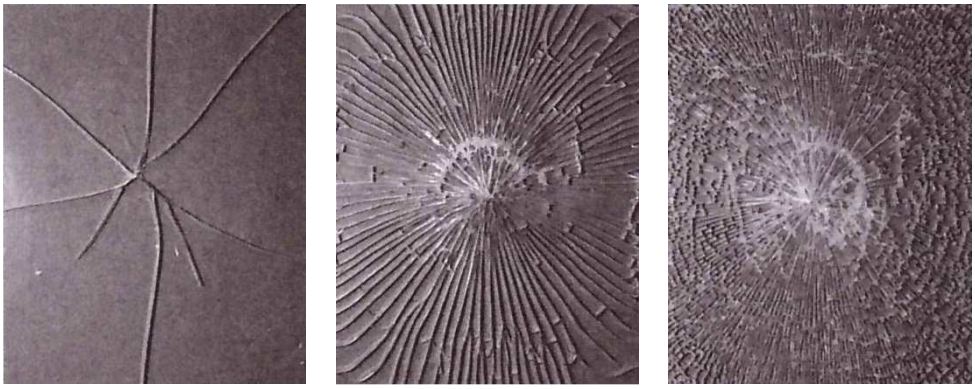

(a) Annealed glass. (b) Heat strengthened glass (c) Thermally toughened glass

Figure 4.10 Fracture pattern: annealed glass, heat strengthened glass, thermally toughened glass.

The high residual stress level in thermally toughened glass results in high fragmentations and breaks in small relatively harmless small pieces or dices. Thermally toughened glass has a high tensile strength but its post-failure capacity is very poor due to the small fragments. Heat strengthened glass fails in medium fragments and assures a good post-failure capacity. Annealed glass breaks into large fragments that can cause serious injury.

The thermal tempering process of float glass consists in heating the glass to 620 – 675°C and then quenching it down rapidly with jets of cold air. Quenching freezes and solidifies first the outer surfaces and subsequently the inner core of glass; this generates a residual parabolic stress field with the surfaces in compression and the core in tension.

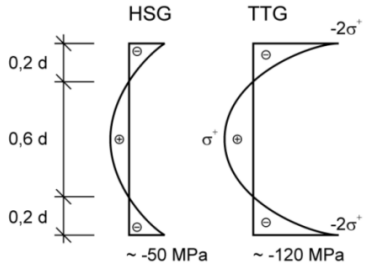

Figure 4.11 Stress field across the glass section generated by thermal tempering process: (HSG) heat strengthened glass, (TTG) thermally toughened glass.

Due to nickel sulfide inclusions (NiS), spontaneous failure of thermally toughened glass can occur. This is due to the expansion in volume by about 4% of NiS particles under the high temperature, combined with high tensile stresses in the glass core. With the heat-soak test, the risk of spontaneous failure due to NiS inclusions can be reduced but not totally eliminated; glass is heated and maintained at a certain temperature for several hours, causing the glass elements with nickel sulfide inclusions to fail.

Heat strengthened glass is produced with the same processing equipment as thermally toughened glass with the only difference that with heat-strengthened glass the cooling process is slower. This means that the residual tensile strength at the glass surface is lower.

Chemically strengthened glass is rarely used in structural applications; it is used mainly for special geometries, for optical applications, and in the aeronautical industry. The chemical tempering process is based on the exchange of sodium ions in the glass surface with 30% bigger potassium ions. The chemical tempering process only affects a thin depth at the glass surface. The influence of the chemical strengthened is limited to some micrometers into the material's depth. This means that if surface flaws are deeper than compression zone, their tips are in the tensile zone and subcritical crack occurs without external load. This phenomenon, named self-fatigue, can cause spontaneous failure (Haldimann, et al., 2008).

Laminated glass consists of two or more glass panes connected together with an interlayer, so that the cross section responds mechanically with a composite effect. The most common lamination process is autoclaving; the heat and the high pressure bonds the glass panes together removing the air inclusions between the glass and the interlayer. The interlayer improves the post-breakage behaviour of laminated glass. After breakage the glass fragments adhere to the interlayer. The result is a certain post-breakage structural capacity which depends on the size fragmentation of glass and on the adhesive properties of the interlayer material.

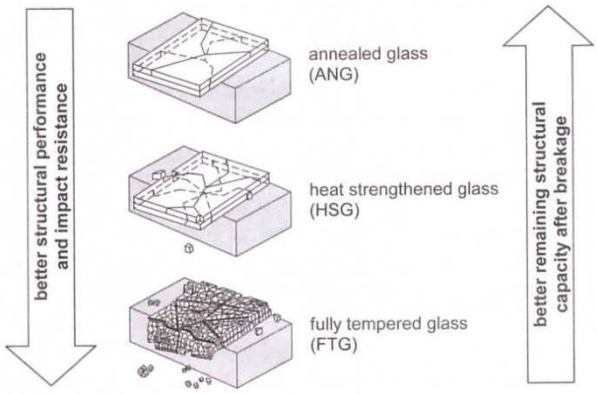

Figure 4.12 Schematic representation of the post-breakage behaviour of laminated glass (Haldimann, et al., 2008).

4.3 Interlayer

The most common interlayers in laminated glass panels are interlayer foils made of polyvinyl butyral (PVB), ethylene vinyl acetate (EVA) and SentryGlas® (SG®). Among all, the most common is PVB, the nominal thickness of a single PVB foil is 0.38 mm but normally two (0.76 mm) or four foils (1.52 mm) form one PVB interlayer.

In this research the interlayer material used is a 1.52 mm thick PVB interlayer. PVB is a viscoelastic material; its stiffness highly depends on the load duration and the temperature, and especially at temperatures higher than 25°C, the shear modulus drops drastically.

The determination of the shear stiffness of the interlayer is difficult because the product standard does not give either shear stiffness values of the interlayer or harmonised test procedures for its determination. Furthermore, European countries deal with the shear stiffness of interlayer materials in many different ways.

The creep and the relaxation behaviour of the interlayer in laminated glass panels may be experimentally investigated using different test setups, evaluation and interpretation techniques. The result is that the time dependent shear moduli obtained according to them vary significantly.

Several authors have tested the mechanical properties of the most common interlayer materials used to bond together glass sheets (PVB Butacite®, SG®, EVA) finding a strong dependence on the temperature and on the duration of the applied loads (Bennison, et al., 1999) (Van Duser & Jagota, 1999) (Bennison, et al., 2008) (D'Haene & Savineau, 2007). Consequently, in order to precisely describe the behavior of laminated glass elements, an accurate viscoelastic constitutive model for the interlayer should be used.

For this research, the shear moduli of PVB interlayer have been calculated according to the numerical and experimental investigations performed by Bennison, Jagota and Smith who tested glass–PVB Butacite® laminated panels providing a series of relaxation curves (Bennison, et al., 1999) (Van Duser & Jagota, 1999). *Table 4.4* lists the values of the PVB-Butacite® shear modulus calculated according to these studies.

	G_{int} (N/mm²)	Load-duration				ν_{int} (-)
		3 sec	1 day	1 month	1 year	
Temperature	**20°C**	8.060	0.840	0.372	0.266	0.498
	30°C	0.971	0.441	0.069	0.052	
	40°C	0.610	0.234	0.052	0.052	
	50°C	0.440	0.052	0.052	0.052	

Table 4.4 Mechanical properties of PVB-Butacite® according to (Bennison, et al., 1999).

In their computational modelling, Bennison, Jagota and Smith modelled the shear relaxation behaviour of the PVB interlayer by a generalized Maxwell series:

$$G(t) = G_\infty + \sum_{i=1}^{n} G_i \cdot e^{-t/\tau_i} \tag{4.4}$$

where:

$G_\infty =$ "long-time" plateau modulus (zero for viscoelastic liquids)

$G_i =$ shear moduli of individual terms in the generalized Maxwell series

$\tau_i =$ relaxation time associated with G_i

The instantaneous or glassy shear modulus G_∞ is given by:

$$G_o = G_\infty + \sum_{i=1}^{n} G_i \tag{4.5}$$

Table 4.5 provides individual terms in the generalized Maxwell series at a reference temperature of 20°C.

Term index $[i]$	G_i/G_o	$\tau_i(s)$
1	0.16060000	3.2557×10^{-11}
2	0.0787770	4.9491×10^{-9}
3	0.2912000	7.2427×10^{-8}
4	0.0711550	9.8635×10^{-6}
5	0.2688000	2.8059×10^{-3}
6	0.0895860	1.6441×10^{-1}
7	0.0301830	2.2648×10^{0}
8	0.0076056	3.5364×10^{1}
9	0.0009634	9.3675×10^{2}
10	0.0004059	6.4141×10^{5}
11	0.0006143	4.1347×10^{7}
Note: instantaneous shear modulus G_o=0.471 MPa WLF Parameters are C_1=20.7; C_2=91.1 at Reference Temperature of 20°C		

Table 4.5 Terms in generalized Maxwell series description (4.4) of shear relaxation modulus (Bennison, et al., 1999).

For temperature 10°C ≤ T ≤ 70°C the reduced time τ and the actual time t are related through the Williams-Landel-Ferry (WLF) equation:

$$\tau = \frac{t}{a_T} \tag{4.6}$$

where a_T is the shift function:

$$log_{10}(a_T) = -\frac{C_1 \cdot (T - T_0)}{C_2 + T - T_0} \tag{4.7}$$

where:

$\mathrm{C}_1;\ \mathrm{C}_2 =$ materials "constants", see *Table 4.5*

$\mathrm{T} =$ temperature

$\mathrm{T}_0 =$ reference temperature, see *Table 4.5*

For temperature 10°C ≤ T ≤ 70°C the *eq. (4.7)* gives the shift parameter a_T and the *eq. (4.6)* gives the reduced time τ. Hence, by substituting τ for t in the *eq. (4.4)* the shear modulus $G(T, t)$ for the temperature T at time t is calculated.

4.4 Steel

All steel elements are made of grade S355 structural steel according to [EN 1993-1-1:2005] and to [EN 10025-2:2004] except the steel bars of the post-tensioning system that are made of grade C40 steel - steel number 1.0511. The mechanical properties of grade S355 structural steel are given in *Table 4.6*.

Characteristic	**Symbol**	**Numerical value**	**Unit**
Young's modulus (modulus of elasticity)	E	210000	N/mm^2
Shear modulus	G	81000	N/mm^2
Poisson's ratio in elastic stage	ν	0.3	
Coefficient of linear thermal expansion	α	$12\text{x}10^{-6}$	$per\ °C$

Table 4.6 Mechanical and physical properties of S355 structural steel according to [EN 1993-1-1:2005].

The post-tensioning system consists of round C40 steel bars with diameters of 14, 16 and 18 mm. Their mechanical properties are given in [EN 10277-2:2008]. However, experimental tensile tests have been performed on 16mm and 18mm specimens and stress-strain curves have been obtained and used in the numerical and analytical modelling (see *paragraph 5.2*).

4.5 Intermediate materials: aluminium and polyethylene

Dangerous high local stress concentrations in glass and direct steel to glass contact have been avoided by employing adequate intermediate materials. The intermediate materials used for this research are aluminium and high density polyethylene. Their mechanical properties are given in *Table 4.7* and *Table 4.8*.

Characteristic	Symbol	Numerical value	Unit
Young's modulus (modulus of elasticity)	E	70000	N/mm^2
Shear modulus	G	27000	N/mm^2
Poisson's ratio in elastic stage	ν	0.3	
Coefficient of linear thermal expansion	α	$23x10^{-6}$	$per\ °C$
Unit mass	ρ	2700	kg/m^3

Table 4.7 Mechanical and physical properties of aluminium according to [EN 1999-1-1:2007].

Characteristic	Symbol	Numerical value	Unit
Young's modulus (modulus of elasticity), short time	E	1000	N/mm^2
Young's modulus (modulus of elasticity), long time	E_s	160	N/mm^2
Poisson's ratio in elastic stage	ν	0.4	
Coefficient of linear thermal expansion	α	$22x10^{-5}$	$per\ °C$
Unit mass	ρ	0.949	kg/m^3

Table 4.8 Mechanical and physical properties of high density polyethylene given by the producer.

Aluminium has a comparable stiffness to glass and the necessary strength to transfer the contact forces. Polyethylene is softer than glass but its function is to fill the gaps between the lateral surfaces of glass panels and steel.

Chapter 5 Experimental investigations

This chapter focuses on the dynamic and static experimental investigations performed on the 12 m post-tensioned hybrid steel-glass beam. An integrated discussion of the experimental results and a comparison with the analytical and numerical findings is provided in *Chapter 8*.

5.1 Introduction

This chapter investigates the structural response of the 12 m post-tensioned hybrid steel-glass beam by performing two series of tests. Firstly, a series of dynamic tests – to investigate the typical frequencies and mode shapes of the 12 m post-tensioned hybrid-steel glass beam simply supported - has been performed. Secondly, a four point bending test has been performed to investigate stiffness, strength, axial forces in steel bars, horizontal and vertical displacements and load-bearing capacity of the 12 beam. A detailed description of both experimental investigations and results is provided in the following sub-sections.

Furthermore, uniaxial tension tests on specimens of steel bars of the post-tensioning system and pull-out tests have been performed. The stress-strain curves of the steel bars have been exactly evaluated through uniaxial tension tests. These curves have been used to calculate the effective stresses and consequently the effective axial forces in the post-tensioning system during the four point bending test. Pull-out tests have been performed to investigate into the effects of the special shaped bolts used to reduce the longitudinal relative motion between the longitudinal steel bars and the central steel joints.

5.2 Uniaxial tension tests

The post-tensioning system consists of diagonal and longitudinal steel bars made of C40 steel. The top and the bottom longitudinal steel bars have a diameter of 18 mm, the diagonal steel bars have a diameter of 14 mm, except for those at the extremities which have a diameter of 16 mm, see *paragraph 3.3.8*.

Three uniaxial tension tests have been performed to evaluate:

- the engineering stress – strain curve of the 18 mm steel bars
- the engineering stress – strain curve of the 16 mm steel bars
- the breaking load of the threaded ends of the 18 mm steel bar - a coupling nut has been used to connect two pieces of 18 mm steel bars

5.2.1 Stress - strain curves

The mechanical properties of 18 mm and 16 mm steel bars have been experimentally determined through uniaxial tension tests; no tension test has been performed on the 14 mm steel bars.

Table 5.1 lists the uniaxial tension tests performed with a universal testing machine to determine the engineering stress – strain curves of 18 mm and 16 mm steel bars. The tests have been performed at room temperature RT (about + 20°C).

Diameter [mm]	Number of specimens [n]	Test temperature [°C]	Test speed [mm/min]
18	1	RT	1
16	1	RT	1

Table 5.1 Uniaxial tension tests performed to determine the engineering stress – strain curves.

Both specimens have been tested using two extensometers which automatically record the change in gauge length during the test. The data collected at a frequency of 2 Hz have been recorded using software. During the tension test, the force applied to the specimen and the elongation of the specimen was measured simultaneously. The applied force was measured by the test machine and the amount of elongation was measured with the two extensometers.

(a) During the test.

(b) After the test.

Figure 5.1 Uniaxial tension test – 18 mm steel bar.

Figure 5.2 Uniaxial tension test – 16 mm steel bar.

Figure 5.3 and *Figure 5.4* show the engineering stress – strain curves of the 18 mm and 16 mm steel bars; *Table 5.2* lists the engineering stress – strain values.

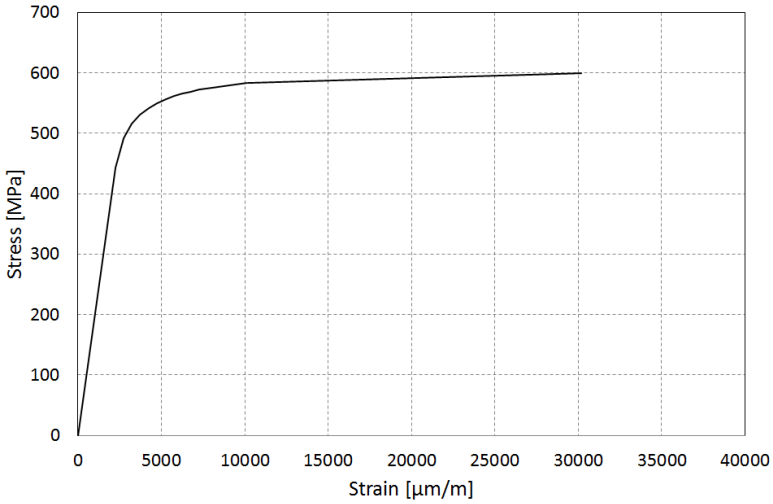

Figure 5.3 Engineering stress – strain curve (18 mm steel bar).

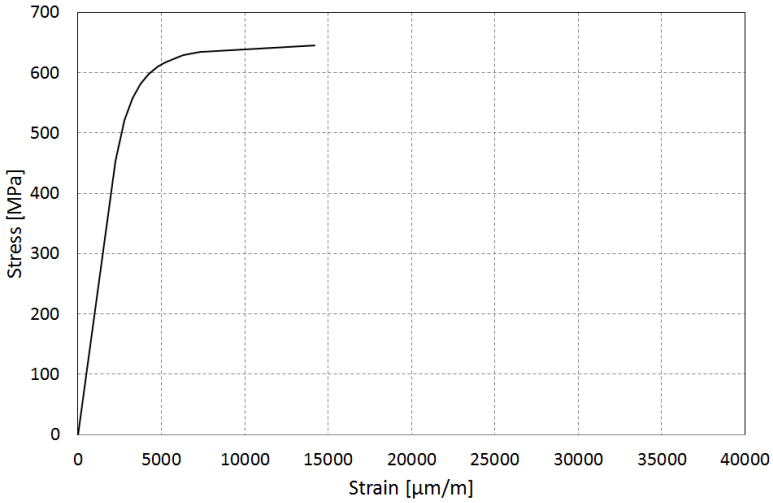

Figure 5.4 Engineering stress – strain curve (16 mm steel bar).

Engineering stress σ [MPa]	Engineering strain ε [µm/m]
0.00	0.00
443.81	2231.91
491.74	2730.67
516.12	3229.18
530.42	3727.44
541.77	4240.99
549.76	4738.75
556.48	5251.79
561.53	5733.53
565.73	6261.56
569.10	6742.82
572.46	7285.89
575.82	8014.7
582.63	10089.5
599.76	30150.3

(a) 18 mm steel bar.

Engineering stress σ [MPa]	Engineering strain ε [µm/m]
0.00	0.00
453.53	2263.04
521.26	2761.78
557.98	3244.73
582.45	3758.53
598.42	4256.53
609.59	4754.28
617.57	5236.27
623.96	5780.16
628.74	6277.16
631.94	6789.40
634.60	7332.45
644.71	14195.66

(b) 16 mm steel bar.

Table 5.2 Uniaxial tension tests: engineering stress – strain values.

5.2.2 Breaking load of the threaded connection of the 18 mm steel bars

Each longitudinal steel bar consists of three shorter pieces connected to each other with coupling nuts. To evaluate the breaking load of the threaded connection, a tension test has been performed on a specimen. The specimen consisted of two small pieces of 18 mm steel bars with threaded ends connected to each other with a M18 coupling nut.

Figure 5.5 Uniaxial tension test: the 18mm connection.

The tension test has been performed at room temperature RT (about + 20°C) at a test speed of 1 mm/min. The fracture of the threaded end occurred when the axial force has reached a value of 115 kN.

5.3 Pull-out test

The longitudinal steel bars go through the central steel joints; the diameter of the steel bars is 18 mm while the central steel joints' hole diamater is 20 mm. The free relative motion between the longitudinal steel bar and each central joint is partially restricted by two special shaped bolts which punch the steel bar against the inner surface of the 20 mm hole (see *paragraph 3.3.4*.)

To evaluate the grip/friction properties of this special shaped bolt, a series of pull-out tests have been performed. The pull-out test reproduces the bar-bolt-joint connection but there is a difference between the con-

nection tested and the real connection. The difference is that for the pull-out tests only one special shaped bolt was used, whereas each joint of the prototype has two special shaped bolts.

Three pull-out tests have been performed and the force – displacement relationships were measured and recorded automatically by software. *Table 5.3* gives the value of the tightening torque applied to the special bolt in each pull-out test, the value of the force which causes the start of the motion of the steel bar. The pull-out tests have been performed at room temperature RT (about + 20°C) at a test speed of 2 mm/min.

Test name	**Tightening torque [N·m]**	**Force at start of the motion of the bar [kN]**
Test 1 – tightening torque 10 N·m	10	8
Test 2 – tightening torque 15 N·m	15	4
Test 3 – tightening torque 20 N·m	20	2

Table 5.3 Results of the pull-out tests.

Figure 5.6 shows the force – displacement diagram.

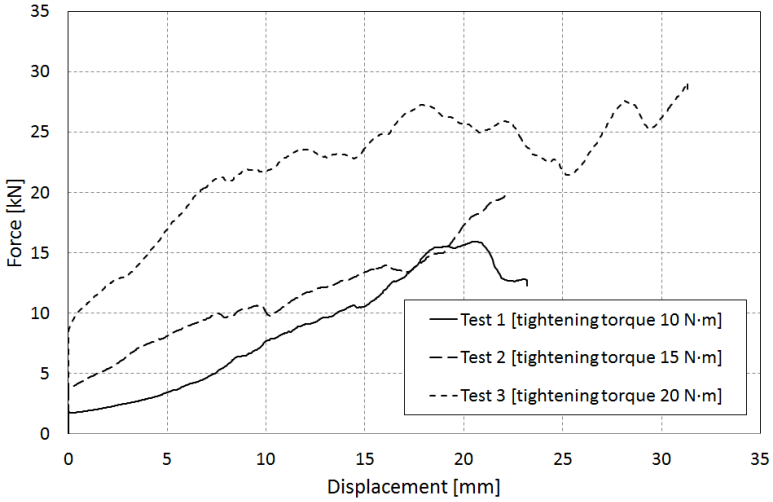

Figure 5.6 Pull-out tests: load – displacement diagram.

Figure 5.7 shows the test setup and the effects of the special shaped bolt on the longitudinal steel bar, showing damage to the longitudinal steel bar because it acts as a wedge.

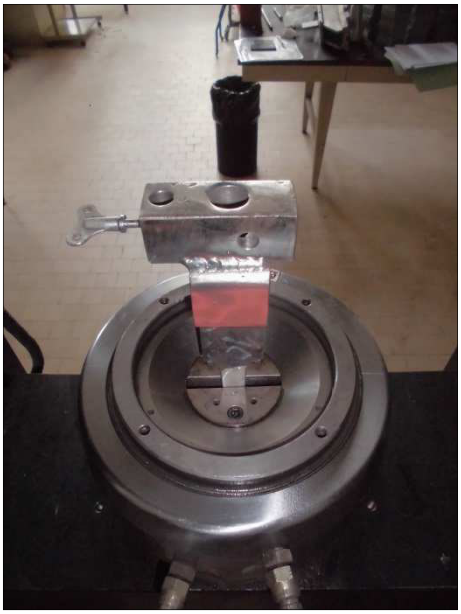

(a) Photograph of the test setup.

(b) Photograph of the test setup.

(c) Photograph of the bar during the test.

(d) Detail of the steel bars after the test.

Figure 5.7 Effects of the special bolt on the 18mm steel bar.

5.4 Four-point bending test

A four point bending test had been planned to experimentally evaluate the stiffness, the strength and the load bearing capacity of the 12 m prototype and the stresses in steel bars generated by an increasing test load. However, before reaching the yielding of the steel bar or the buckling of any glass panel, the threaded end of a M18 coupling connection of a bottom longitudinal steel bar broke.

After breakage, the beam was easily fixed by removing the two bottom longitudinal steel bars and by welding the three bar pieces to them which composed each lower longitudinal steel bar.

In the following subparagraphs, a description of both two four-point bending tests and their results is given.

5.4.1 The first four-point bending test

Strain gages are applied to some steel bar after the prototype construction and before putting it on the supports. The strain gages were glued before applying the post-tensioning forces to the steel bars; for this reason, the strain-gages were useful to apply exactly and to check the value of the post-tensioning forces.

Table 5.4 lists the position of strain gages applied to the steel bars.

Strain gage	Position	Diameter [mm]
Diag (16-f)	Diagonal steel bar (extremity) – front web	16
Diag (16-b)	Diagonal steel bar (extremity) – back web	16
Diag (14-f_1)	Diagonal steel bar (central) – front web	14
Diag (14-f_2)	Diagonal steel bar (central) – front web	14
Top (18-f)	Upper longitudinal steel bar – front web	18
Bottom (18-f_1)	Lower longitudinal steel bar – front web	18
Bottom (18-b_1)	Lower longitudinal steel bar – back web	18
Bottom (18-f_5)	Lower longitudinal steel bar – front web	18

Table 5.4 Positions of the strain gages.

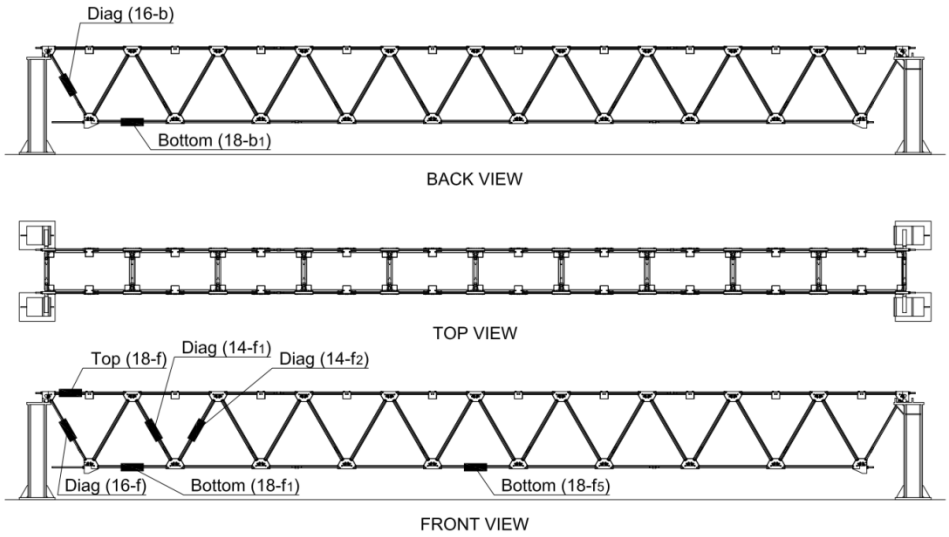

Figure 5.8 Positions of the strain gages.

Before putting the beam on its supports and after the application of the strain gages, the post-tensioning forces were applied to the beam. The values of tensile forces applied to the post-tensioning system are given in *Table 5.5*.

Position	Diameter [mm]	Post-tensioning force [kN]	Tool
Diagonal steel bars (extremity)	16	20	torque wrench
Diagonal steel bars (central)	14	10	torque wrench
Top longitudinal steel bars	18	15	torque wrench
Bottom longitudinal steel bars	18	33	hydraulic jack

Table 5.5 Tensile forces applied to the post-tensioning system.

The values of post-tensioning forces were applied to make the beam stiff enough and to avoid detachment of the glass panels' corners from the steel joints under its self-weight. Furthermore, the greater value of post-tensioning forces applied to the bottom longitudinal steel bars was to introduce a pre-camber and to increase

the stiffness of the beam. Previous numerical and analytical studies concerning the values of the post-tensioning forces were conducted by (Mamone, 2011).

Figure 5.9 shows the setup used to apply the post-tensioning force to the bottom longitudinal steel bars; both bars were tensioned together using a hydraulic jack controlled by a manual pump. After this activity, all the free special shaped bolts of the steel joints - designed to restrict the free relative motion between the longitudinal steel bar and each central joints - were tightened with a torque wrench. The value of the tightening torque was 15 N·m (see *paragraph 3.3.4* and *paragraph 5.3*).

(a) Photograph.

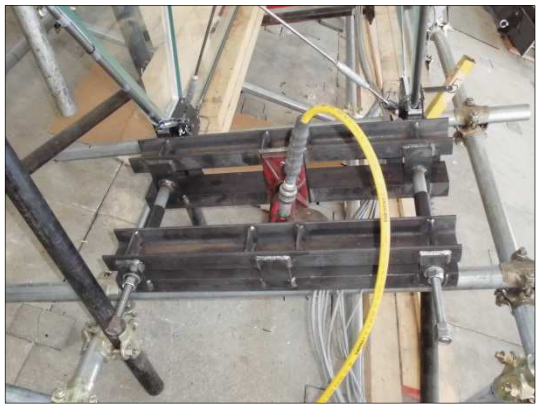

(b) Photograph.

Figure 5.9 Post-tensioning of the bottom longitudinal steel bars.

Subsequently, the beam was put on its supports by using an overhead crane. During this operation, the effective self-weight of the beam was measured - 18 kN. The prototype on its supports is a simply supported beam with a roller support and a pinned support. The roller support is free to rotate and translate along the horizontal surface of the support; the pinned support allows the prototype to rotate but not to translate in any direction (see *Figure 5.10*).

(a) Photograph of the pinned support.

(b) Photograph of the roller support.

Figure 5.10 Photographs of theprototypes' support.

The bending test setup consists of 4 steel beams, 4 steel bars, 2 hydraulic identical jacks, 1 manual pump, some steel plates and some hydraulic hoses. The test load was applied with two identical hydraulic jacks activated together with a manual pump. *Figure 5.11*, *Figure 5.12* and *Figure 5.13* show the test setup.

The weight of the two hydraulic jacks and the equipment (steel beams, steel bars, steel plates and hydraulic hoses) is 4.0 kN. This permanent load acts on the beam as concentrated load applied to the top four steel joints, 4800 mm away from the supports.

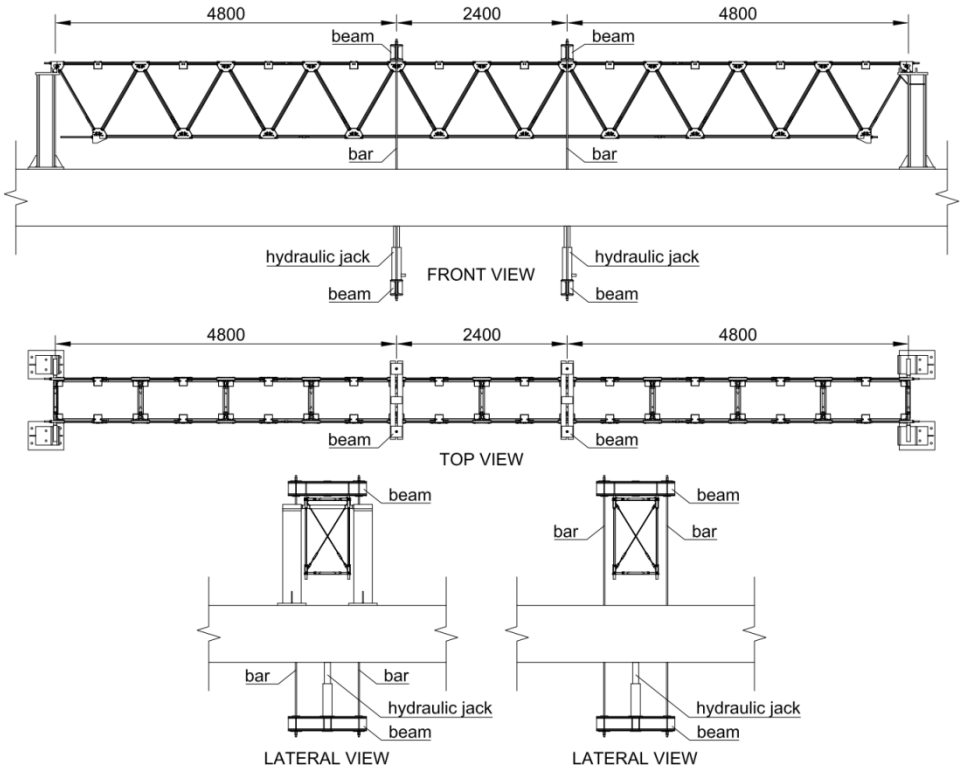

Figure 5.11 Engineering drawings of the test setup.

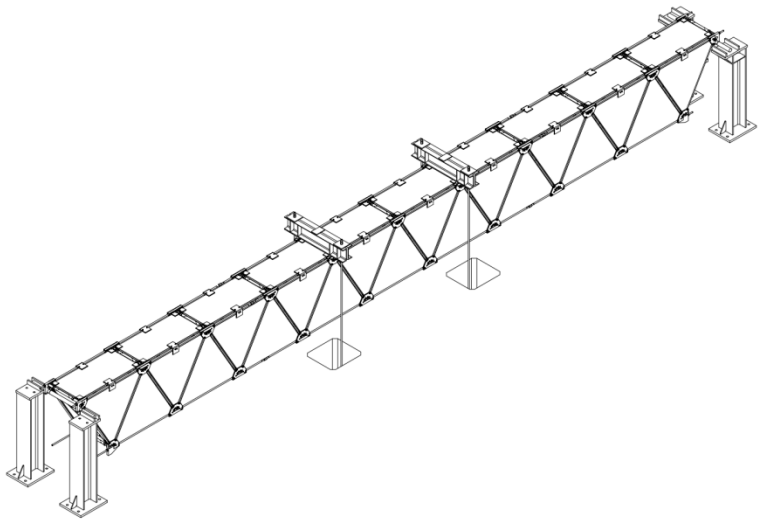

Figure 5.12 Isometric view of the test setup.

(a) Photograph of the prototype.

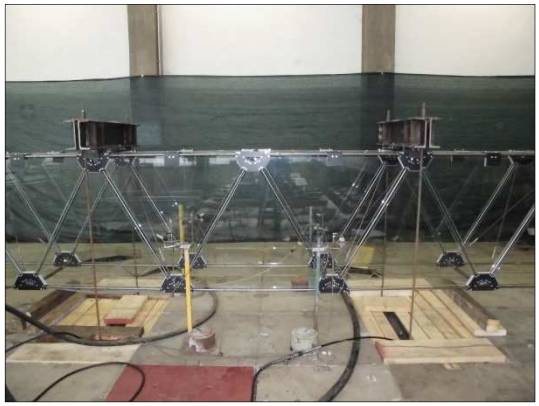

(b) Photograph of the protptype.

(c) Photograph of the hydraulic jack.

(d) Photograph of the hydraulic jack.

Figure 5.13 Photographs of the test setup.

Table 5.6 lists the loads acting upon the beam and their order of application.

Load	**Description**	**Value [kN]**	**Loading condition**
Post-tensioning forces	forces applied to generate compressive stress in glass	*Table 5.5*	---
Self-weight	dead load of the beam	18	Simply supported beam: 2 equal concentrated symmetric loads
Permanent load	weight of the hydraulic jacks and the equipment	4.0	Simply supported beam: 2 equal concentrated symmetric loads
Test load	increasing load	---	Simply supported beam: uniformly distributed load

Table 5.6 Experimental bending tests: order of load application and their values.

Before performing the bending test, 7 linear variable differential transformers – LVDTs - were arranged to measure the vertical displacements of 6 steel joints and the horizontal displacement of the roller support at the beam's end. *Table 5.7* lists the LVDTs used and *Figure 5.14* shows their position.

LVDT	Description
LVDT-f_1	vertical displacement – steel joint, front web
LVDT- f_2	vertical displacement – steel joint, front web
LVDT- f_3	vertical displacement – steel joint, front web
LVDT- b_1	vertical displacement – steel joint, back web
LVDT- b_2	vertical displacement – steel joint, back web
LVDT- b_3	vertical displacement – steel joint, back web
LVDT-h	horizontal displacement – end of the beam

Table 5.7 Positions of the LVDTs.

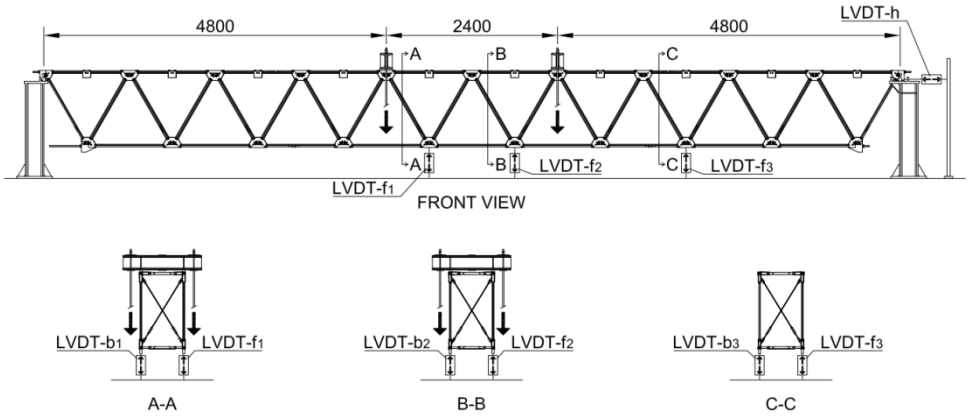

Figure 5.14 Positions of the LVDTs.

The four-point bending test was performed applying an increasing vertical test load to the top four steel joints 4800 mm away from their adjacent support points. The plan was to apply the laboratory test load in two stages (see *Table 5.8* and *Figure 5.15*):

1st stage: applying to the prototype increasing cyclic loads

2nd stage: increasing the test load monotonically up to the prototype's breakage

Stage [n.]	Cycle [n.]	Total test load [kN]
1st stage	1st cycle	30
		30
		30
	2nd cycle	60
		60
		60
	3rd cicle	90
		90
		90
2nd stage		up to prototype breakage

Table 5.8 Test load application plan.

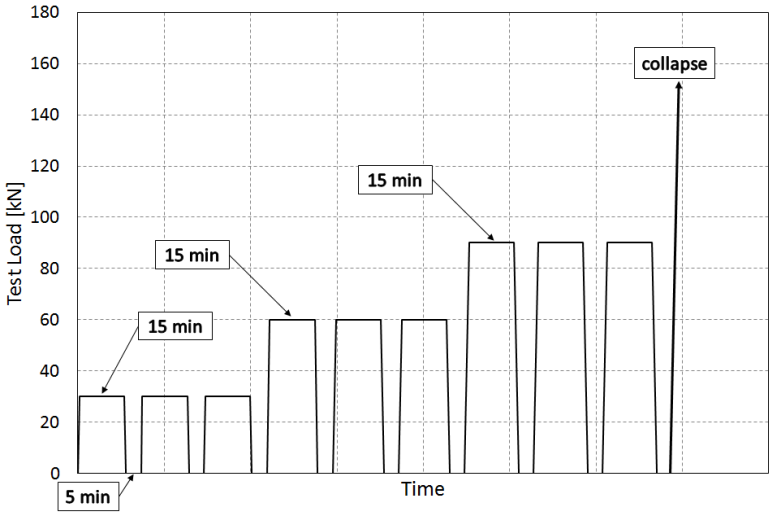

Figure 5.15 Test load – time diagram.

The test load was applied through a manual pump which activated the two identical hydraulic jacks. Thanks to a data acquisition board, the values of test load applied, the vertical and horizontal displacements of LVDTs and the elongation of all strain gages were simultaneously recorded at a frequency of 0.2Hz. The test was performed at room temperature RT - about + 20°C.

During the loading of the beam, when the test load reached a value of 89 kN, a brittle rupture of the thread end of one or the lower steel bars occurred, *Figure 5.16* and *Figure 5.17*. The rupture has caused only a large deflection of the beam and nothing else. Because of this, the test was stopped.

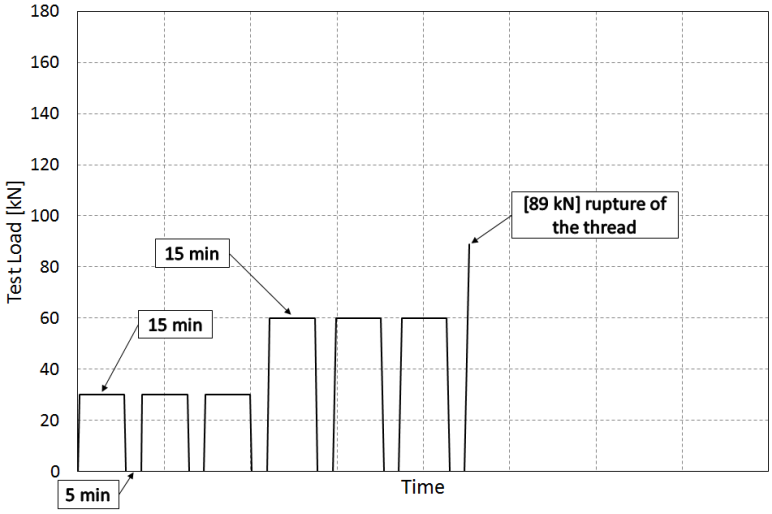

Figure 5.16 Effective test load – time diagram.

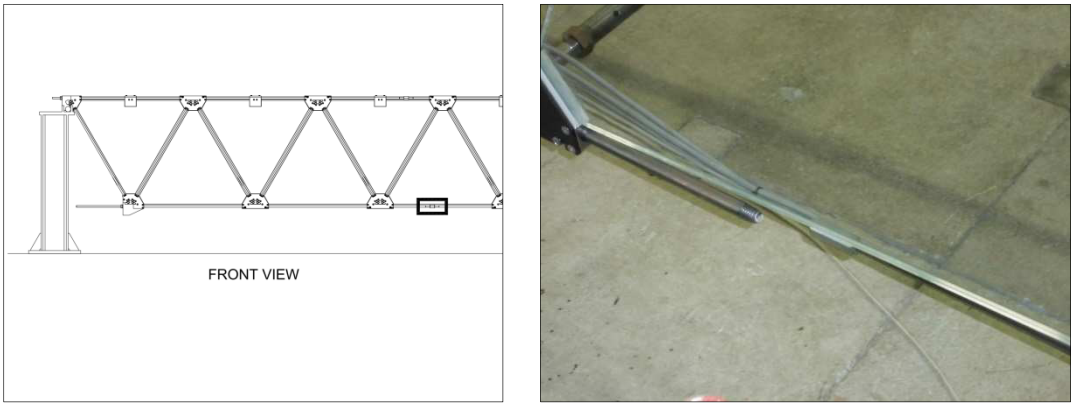

(a) Position. (b) Photograph of the thread after the rupture.

Figure 5.17 Thread after the rupture.

Test load – displacement diagrams

Figure 5.18 and *Figure 5.19* show the test load – vertical displacement diagrams of the bottom central steel joints measured by LVDT-f_1, LVDT-f_2, LVDT-b_1 and LVDT-b_2.

Figure 5.20 and *Figure 5.21* show the test load – vertical displacement diagrams of the bottom lateral steel joints measured by LVDT-f_3, LVDT-b_3.

Figure 5.22 shows the test load – horizontal displacement diagram of the roller support of the prototype measured by LVDT-h.

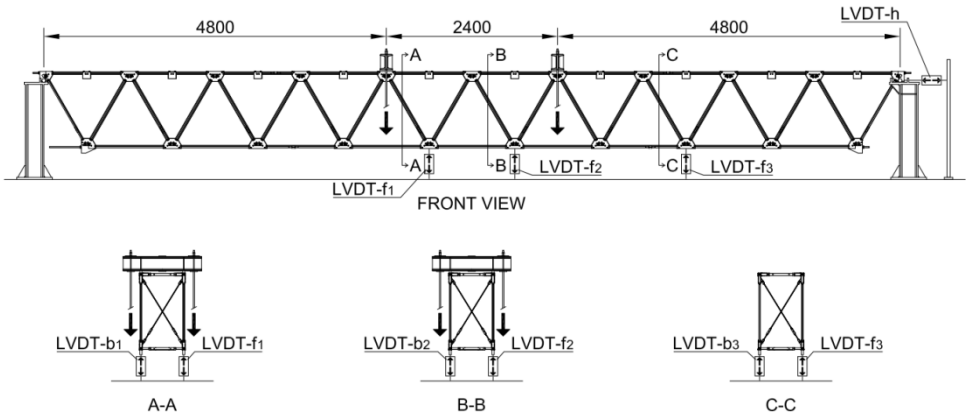

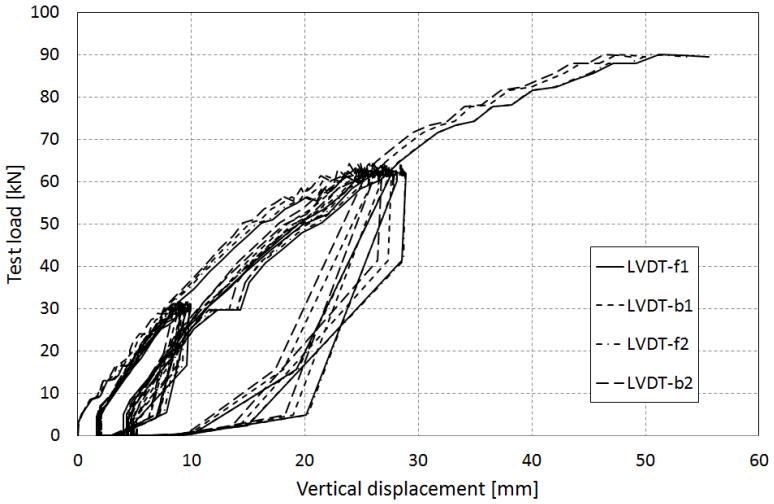

Figure 5.18 Bottom central steel joints: Test load – Vertical displacement diagram (1st test).

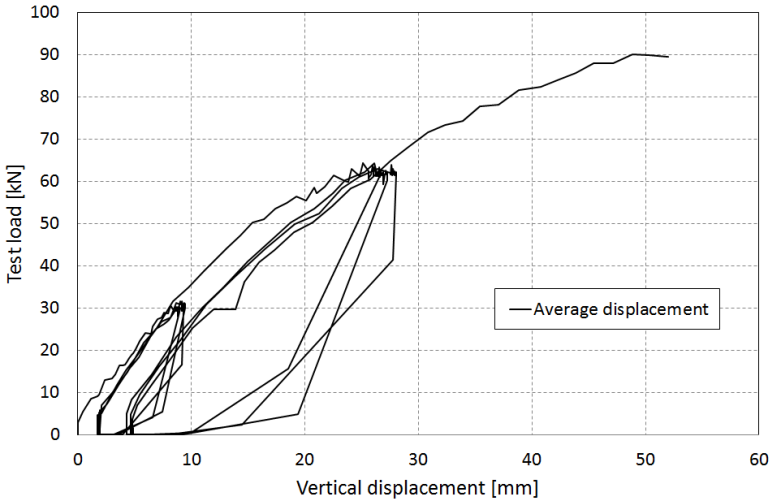

Figure 5.19 Bottom central steel joints: Test load – Average vertical displacement diagram (1st test).

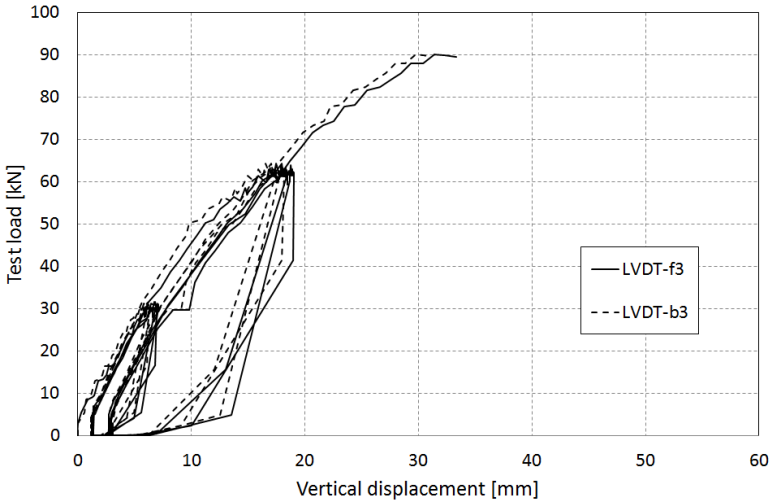

Figure 5.20 Bottom lateral steel joints: Test load – Vertical displacement diagram (1st test).

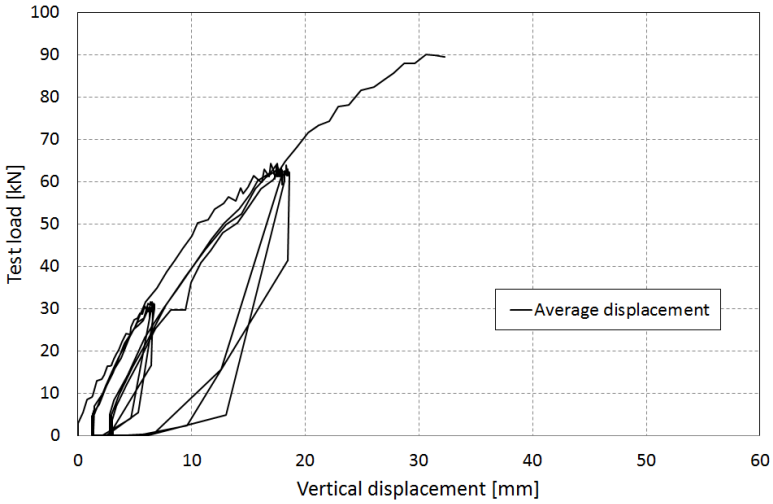

Figure 5.21 Bottom lateral steel joints: Test load – Average vertical displacement diagram (1st test).

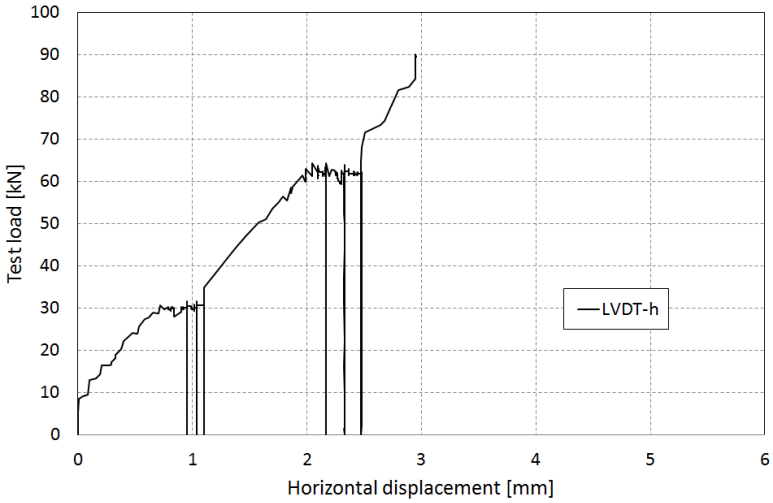

Figure 5.22 Roller support: Test load – Horizontal displacement diagram (1st test).

Test load – axial force diagrams

The following diagrams show the test load – axial force diagrams in steel bars. The experimental axial forces in steel bars were calculated by knowing the strain values measured by the strain gages during the test and by knowing the stress - strain curves obtained by tensile tests on specimens. No tensile test has been performed on 14 mm steel bars. For these, the stress - strain curve of 16 mm bar was used.

Tension test on specimen → Stress – strain curve + Bending test → Test load – strain diagram	→ Test load – axial force diagram

Table 5.9 Scheme: from elongation to axial force of the steel bars.

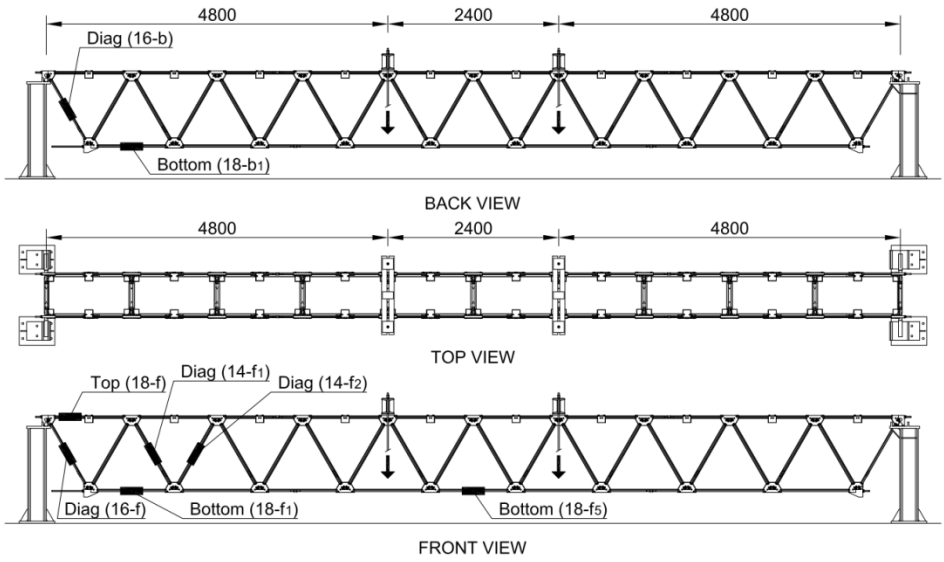

Figure 5.23 Positions of the strain gages (1st test).

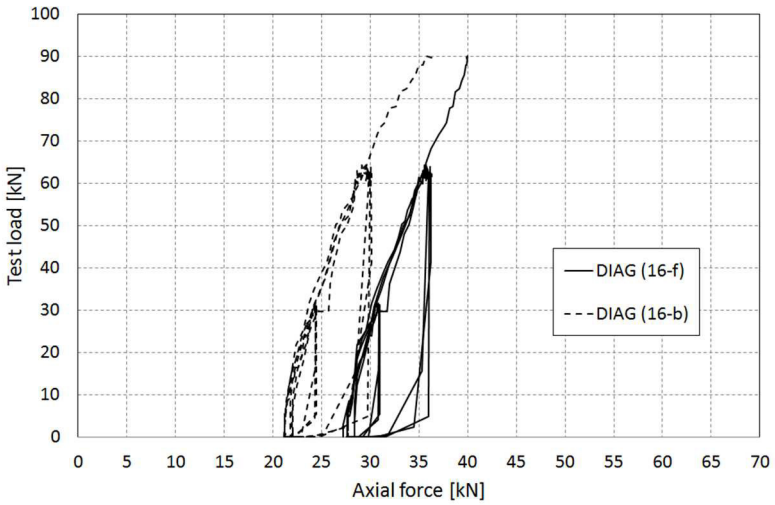

Figure 5.24 DIAG (16-f) and DIAG (16-b): Test load – Axial force diagram (1st test).

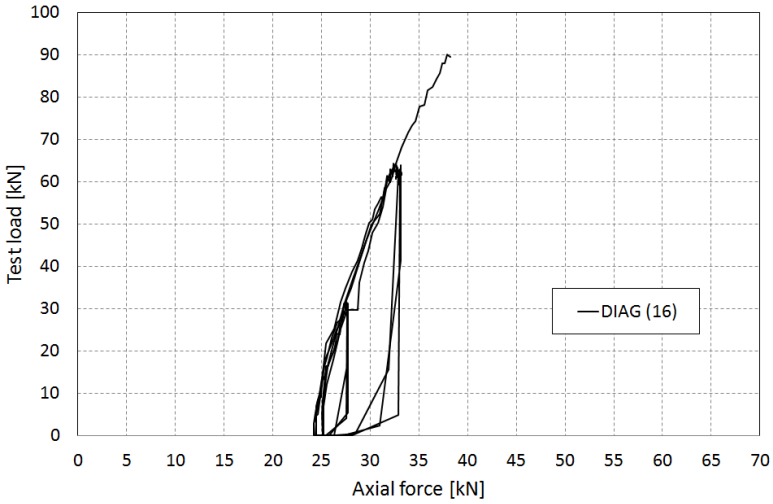

Figure 5.25 DIAG (16): Test load – Average axial force diagram (1st test).

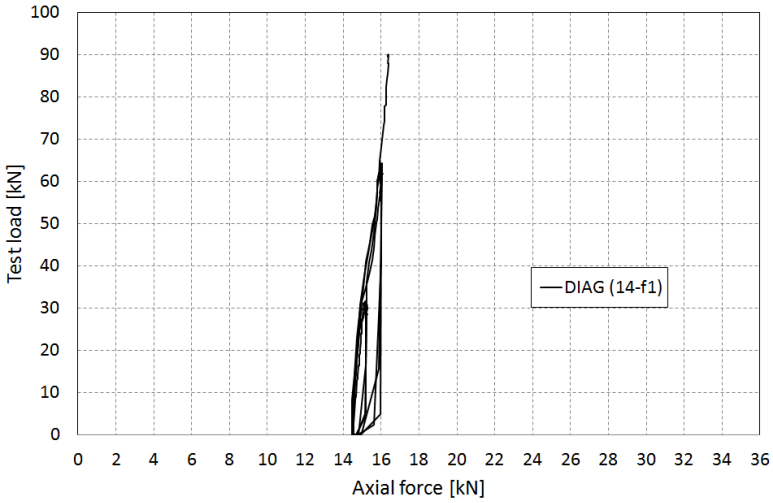

Figure 5.26 DIAG (14-f_1): Test load – Axial force diagram (1st test).

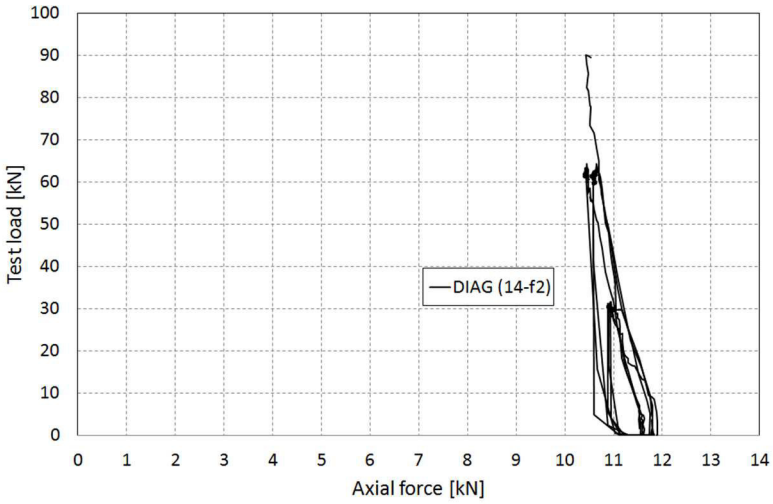

Figure 5.27 DIAG (14-f_2): Test load – Axial force diagram (1st test).

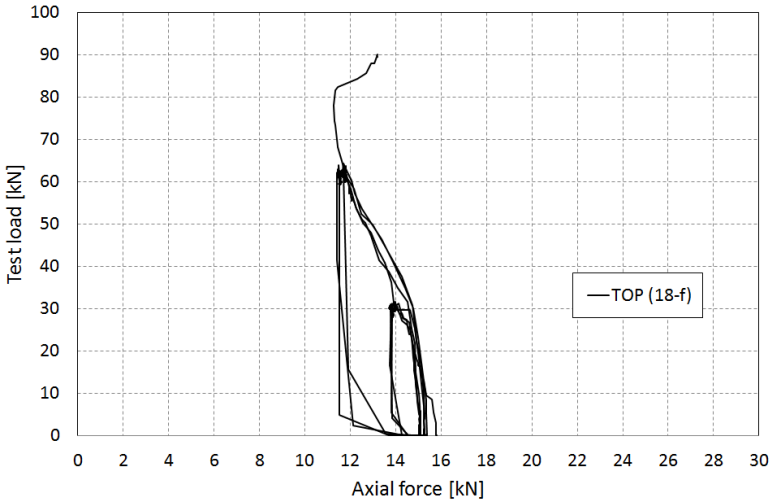

Figure 5.28 TOP (18-f): Test load – Axial force diagram (1st test).

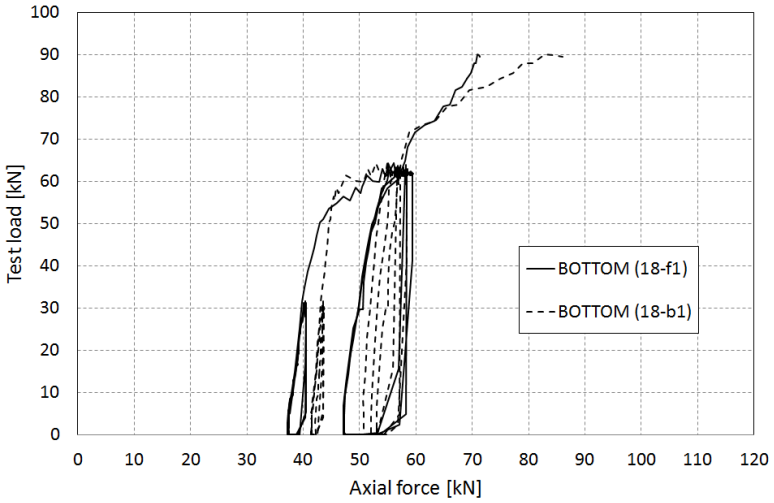

Figure 5.29 BOTTOM (18-f_1) and BOTTOM (18-b_1): Test load – Axial force diagram (1st test).

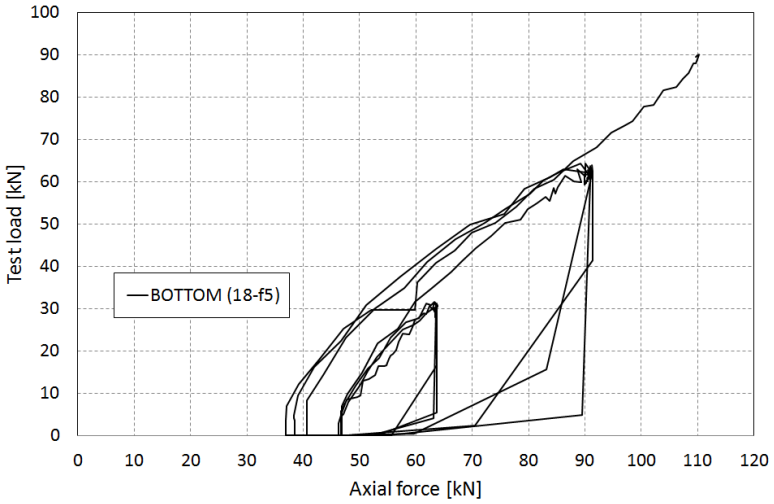

Figure 5.30 BOTTOM (18-f_5): Test load – Axial force diagram (1st test).

5.4.2 The second four-point bending test

After the thread of the bottom steel bar broke, the beam was fixed. The beam was propped up and all the bottom longitudinal steel bars were removed; the threads were cut and the shorter bar pieces were welded to each other.

(a) Photograph of two welded connections. (b) Details of the welded connection.

Figure 5.31 Bottom longitudinal steel bars after being repaired.

Three new strain gages were applied to the steel bars; they were glued before re-applying the post-tensioning forces to the steel bars, *Figure 5.32*.

Table 5.10 lists the position of all strain gages after the beam repair.

Strain gage	**Position**	**Diameter [mm]**
Diag (16-f)	Diagonal steel bar (extremity) – front web	16
Diag (16-b)	Diagonal steel bar (extremity) – back web	16
Diag (14-f_1)	Diagonal steel bar (central) – front web	14
Diag (14-f_2)	Diagonal steel bar (central) – front web	14
Top (18-f)	Upper longitudinal steel bar – front web	18
Bottom (18-f_1)	Lower longitudinal steel bar – front web	18
Bottom (18-b_1)	Lower longitudinal steel bar – back web	18
Bottom (18-f_2)	Lower longitudinal steel bar – back web	18
Bottom (18-f_3)	Lower longitudinal steel bar – back web	18
Bottom (18-f_4)	Lower longitudinal steel bar – back web	18
Bottom (18-f_5)	Lower longitudinal steel bar – front web	18

Table 5.10 Positions of the strain gages after being repaired.

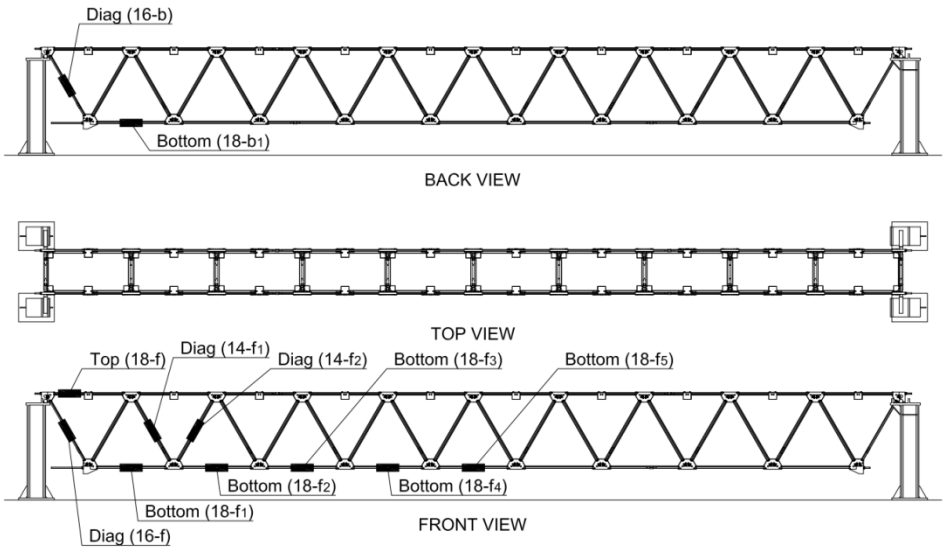

Figure 5.32 Positions of the strain gages after being repaired.

After repairs and the application of the new strain gages, the post-tensioning forces were applied to the beam again. The values of tensile forces applied to the post-tensioning system are given in *Table 5.11*.

Position	**Diameter [mm]**	**Post-tensioning force [kN]**	**Tool**
Diagonal steel bars (extremity)	16	26	torque wrench
Diagonal steel bars (central)	14	13	torque wrench
Top longitudinal steel bars	18	17	torque wrench
Bottom longitudinal steel bars	18	33	hydraulic jack

Table 5.11 Tensile forces applied to the post-tensioning system after the repairs.

Table 5.12 lists the loads acting upon the beam and their order of application after the repairs.

Load	**Description**	**Value [kN]**	**Loading condition**
Self-weight	dead load of the beam	18	Simply supported beam: 2 equal concentrated symmetric loads
Permanent load	weight of the hydraulic jacks and the equipment	4.0	Simply supported beam: 2 equal concentrated symmetric loads
Post-tensioning forces	forces applied to generate compressive stress in glass	*Table 5.11*	Simply supported beam
Test load	increasing load	---	Simply supported beam: uniform-ly distributed load

Table 5.12 Experimental bending test: order of load applications and their values after the repairs.

Before performing the bending test, the 7 linear variable differential transformers – LVDTs - were arranged to measure the vertical displacements of the steel joints and the horizontal displacement of the roller support at the beam's end. *Table 5.13* lists the LVDTs used and *Figure 5.33* shows their position.

LVDT	Description
LVDT-f_1	vertical displacement – steel joint, front web
LVDT- f_2	vertical displacement – steel joint, front web
LVDT- f_3	vertical displacement – steel joint, front web
LVDT- b_1	vertical displacement – steel joint, back web
LVDT- b_2	vertical displacement – steel joint, back web
LVDT- b_3	vertical displacement – steel joint, back web
LVDT-h	horizontal displacement – end of the beam

Table 5.13 Positions of the LVDTs after the repairs.

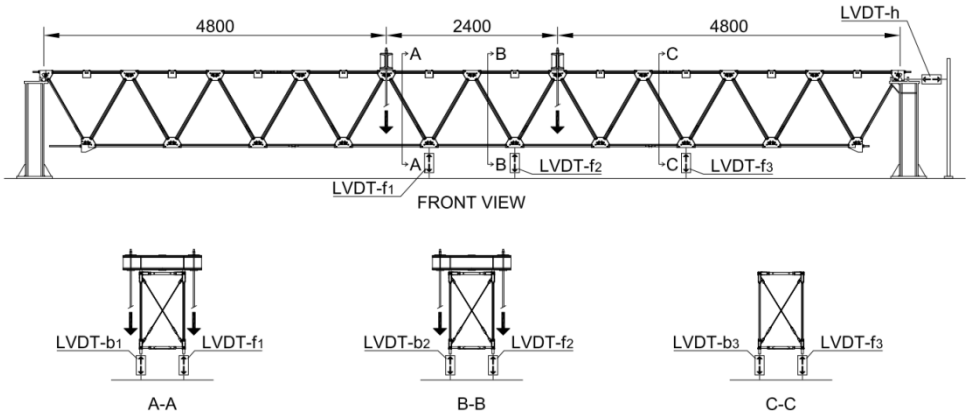

Figure 5.33 Positions of the LVDTs after the repairs.

The second four-point bending test was performed applying an increasing vertical test load to the top four steel joints, 4800mm away from their adjacent support points in two stages (see *Table 5.14* and *Figure 5.34*):

1st stage: applying increasing cyclic loads to the prototype

2nd stage: increasing the test load monotonically up to the prototype breakage

Stage [n.]	Cycle [n.]	Total test load [kN]
1st stage	1st cycle	30
		30
		30
	2nd cycle	60
		60
		60
	3rd cicle	90
		90
		90
2nd stage		136 (buckling of a triangular glass panel)

Table 5.14 Values of the test load applied (2nd test).

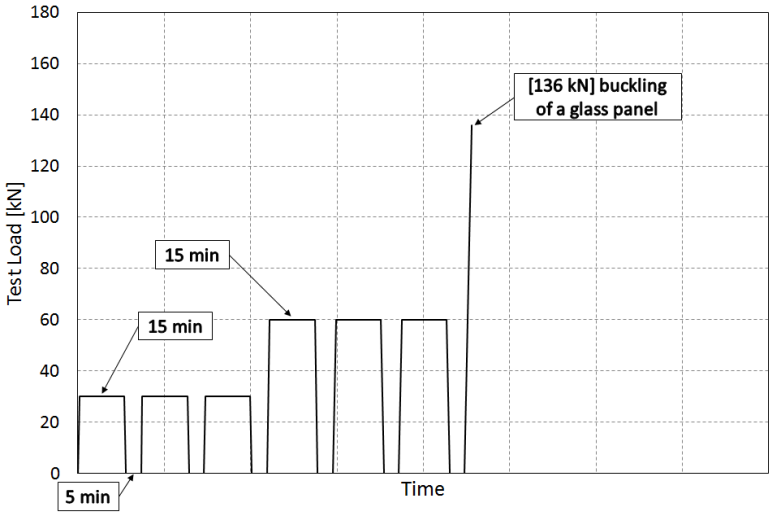

Figure 5.34 Effective test load – time diagram (2nd test).

The test load was applied with a manual pump which activated the two identical hydraulic jacks. Thanks to a data acquisition board, the values of the test load applied, the vertical and horizontal displacements of LVDTs and the elongation of all strain gages were recorded simultaneously at a frequency of 0.2Hz. The test was performed at room temperature RT - about + 20°C.

The collapse of the prototype occurred due to buckling of a triangular glass panel when the test load reached a value of 136 kN, *Figures 5.35 – 5.38*.

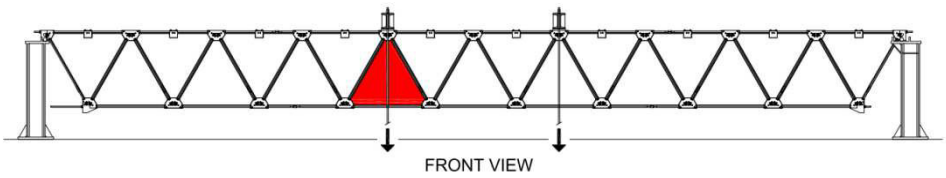

Figure 5.35 Position of the collapsed triangular glass panel (front view).

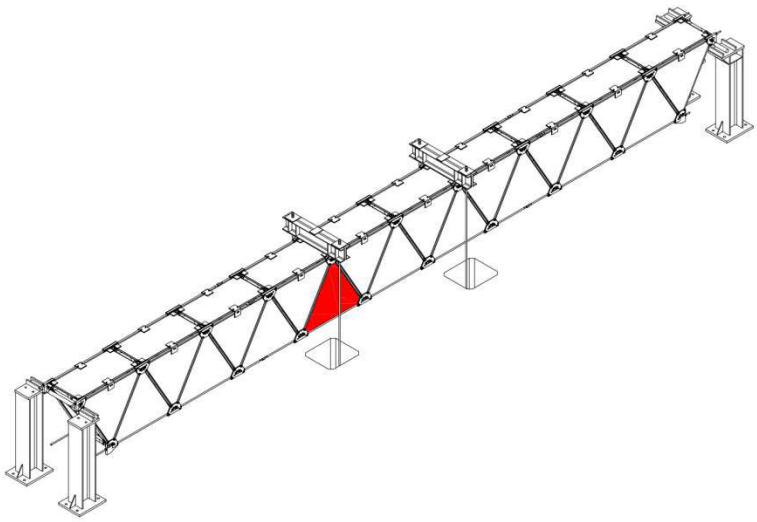

Figure 5.36 Position of the collapsed triangular glass panel (isometric view).

(a) Photograph of the prototype.

(b) Photograph of the protptype.

(c) Photograph of the protptype.

(d) Photograph of the protptype.

Figure 5.37 Photographs of the prototype after the collapse.

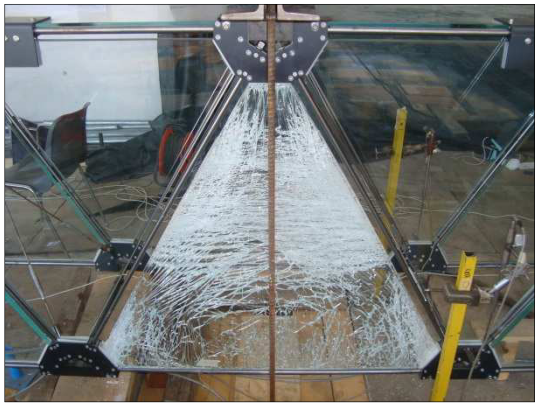

(a) Photograph of the glass panel.

(b) Photograph of the glass panel.

(c) Photograph of the glass panel.

(d) Photograph of the glass panel.

Figure 5.38 Photographs of the triangular glass panel after the collapse.

Test load – displacement diagrams

Figure 5.39 and *Figure 5.40* show the test load – vertical displacement diagrams of the bottom central steel joints measured by LVDT-f_1, LVDT-f_2, LVDT-b_1 and LVDT-b_2.

Figure 5.41 and *Figure 5.42* show the test load – vertical displacement diagrams of the bottom lateral steel joints measured by LVDT-f_3, LVDT-b_3.

Figure 5.43 shows the test load – horizontal displacement diagram of the roller support of the prototype measured by LVDT-h.

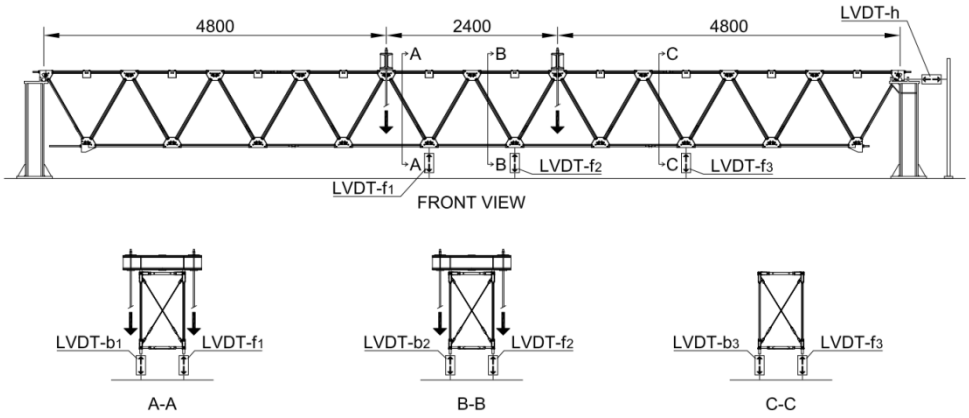

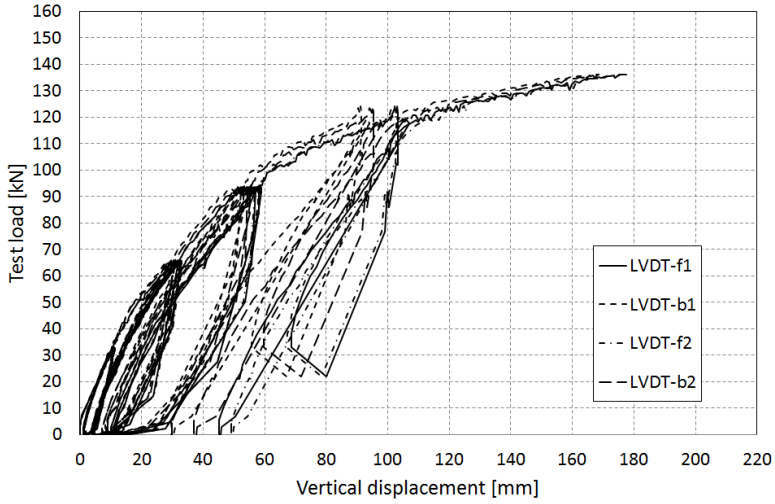

Figure 5.39 Bottom central steel joints: Test load – Vertical displacement diagram (2nd test).

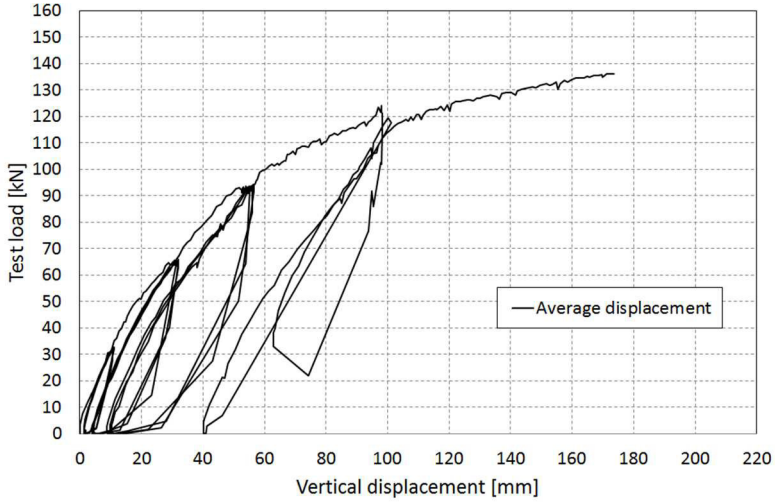

Figure 5.40 Bottom central steel joints: Test load – Average vertical displacement diagram (2nd test).

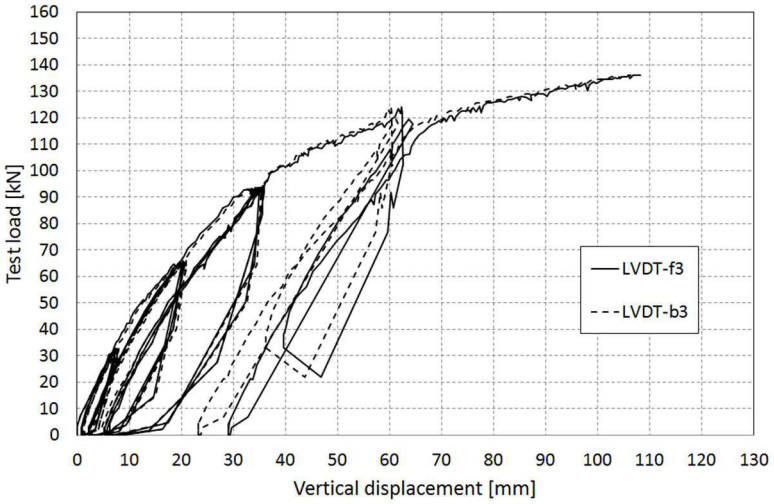

Figure 5.41 Bottom lateral steel joints: Test load – Vertical displacement diagram (2nd test).

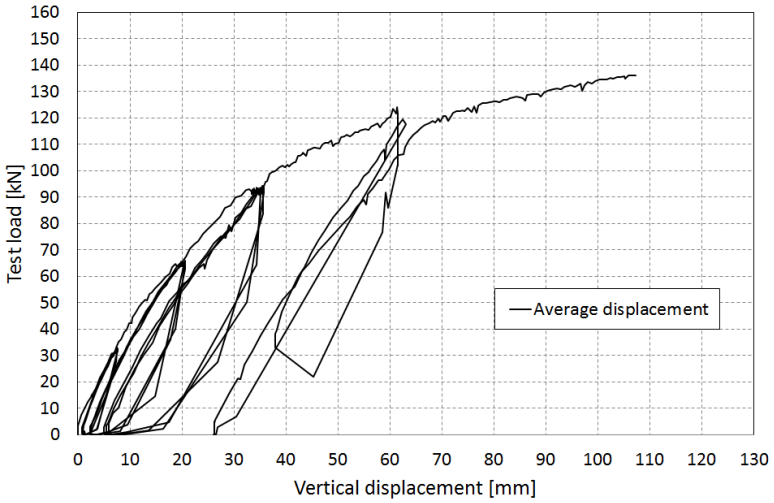

Figure 5.42 Bottom lateral steel joints: Test load – Average vertical displacement diagram (2nd test).

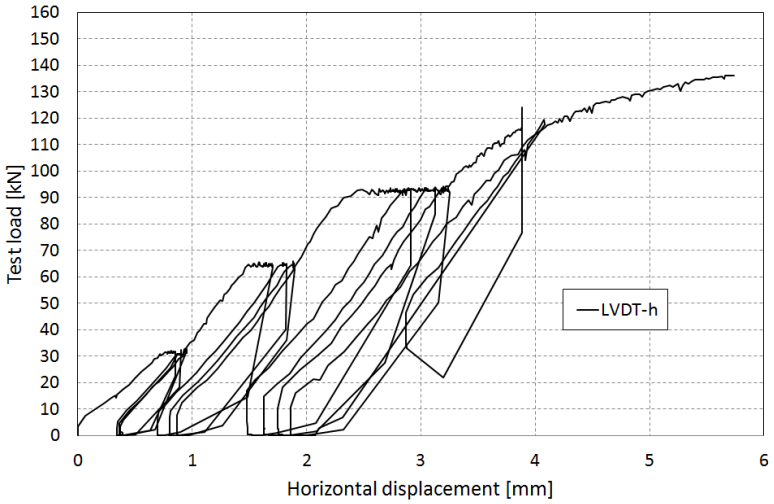

Figure 5.43 Roller support: Test load – Horizontal displacement diagram (2nd test).

Test load – axial force diagrams

The following diagrams show the test load – axial force diagrams in steel bars. Due to their great elongations, three strain gages collapsed at lower test load values than those that caused the buckling rupture of the glass panel, *Table 5.15*.

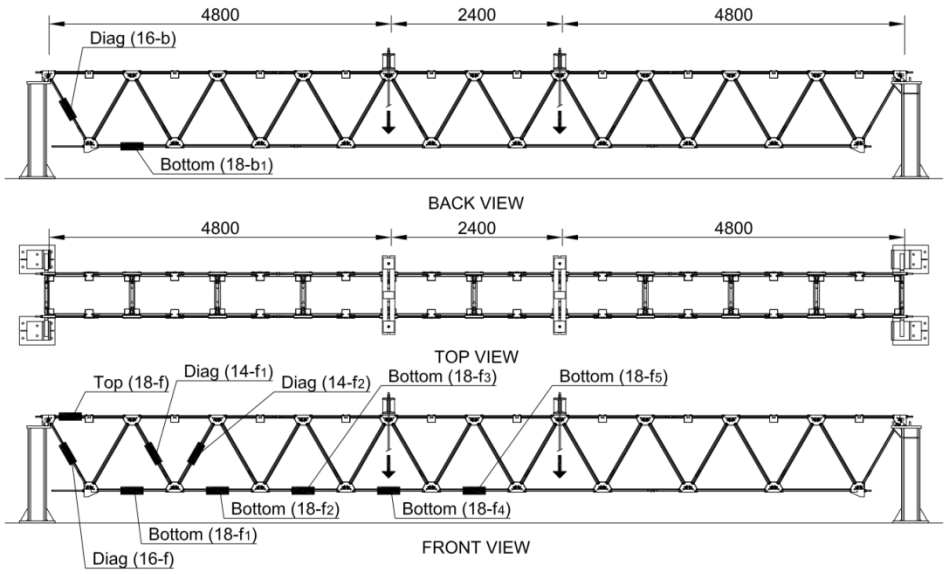

Figure 5.44 Positions of the strain gages (2nd test).

Strain gage	Value of test load causing the collapse of the strain gage [kN]
BOTTOM (18-f_2)	115
BOTTOM (18-f_3)	128
BOTTOM (18-f_4)	110

Table 5.15 Strain gages collapsed and corresponding test load values.

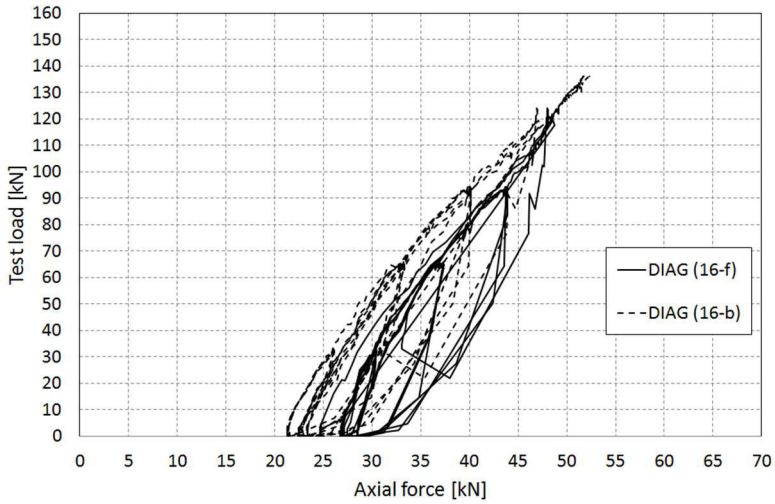

Figure 5.45 DIAG (16-f) and DIAG (16-b): Test load – Axial force diagram (2nd test).

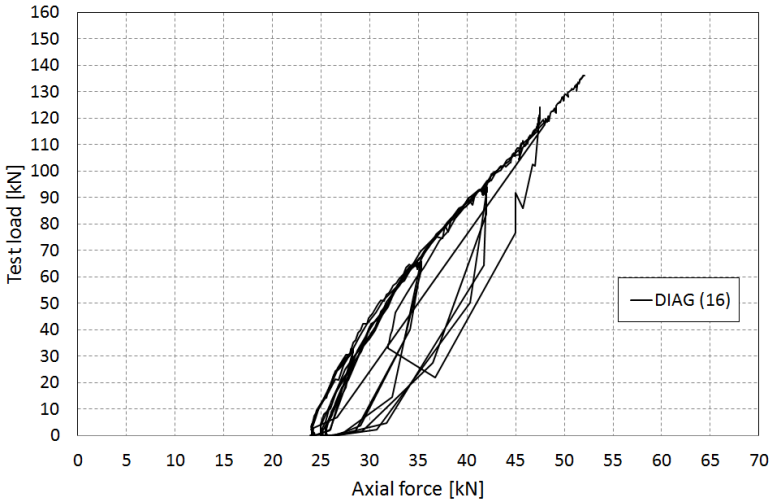

Figure 5.46 DIAG (16): Test load – Average axial force diagram (2nd test).

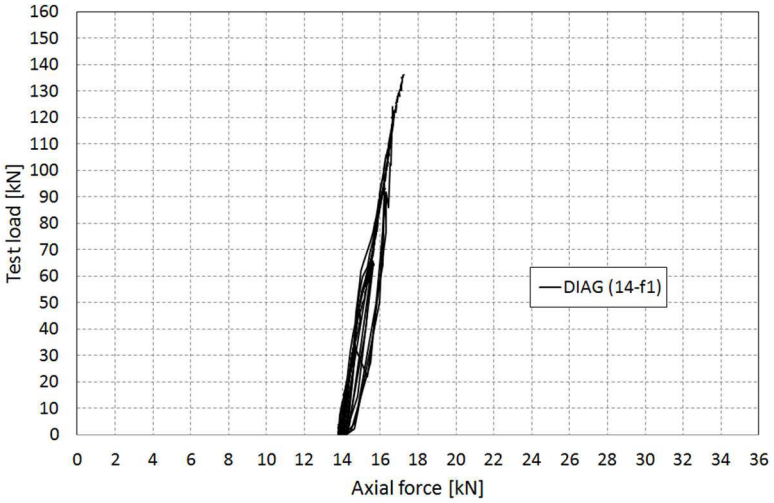

Figure 5.47 DIAG (14-f_1): Test load – Axial force diagram (2nd test).

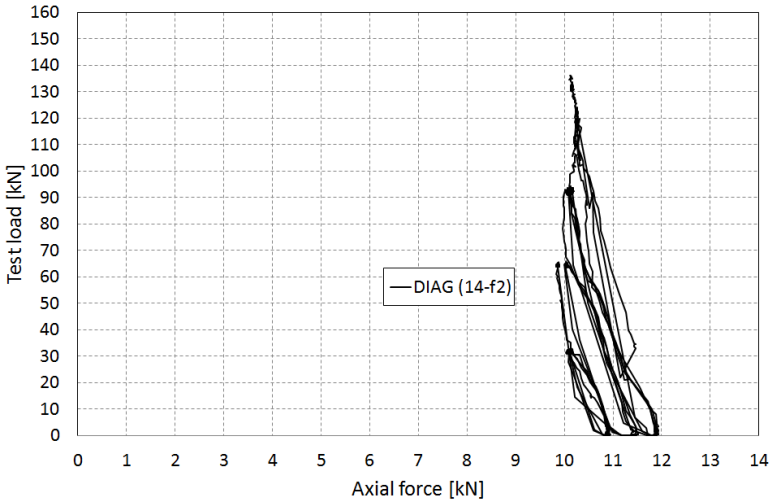

Figure 5.48 DIAG (14-f_2): Test load – Axial force diagram (2nd test).

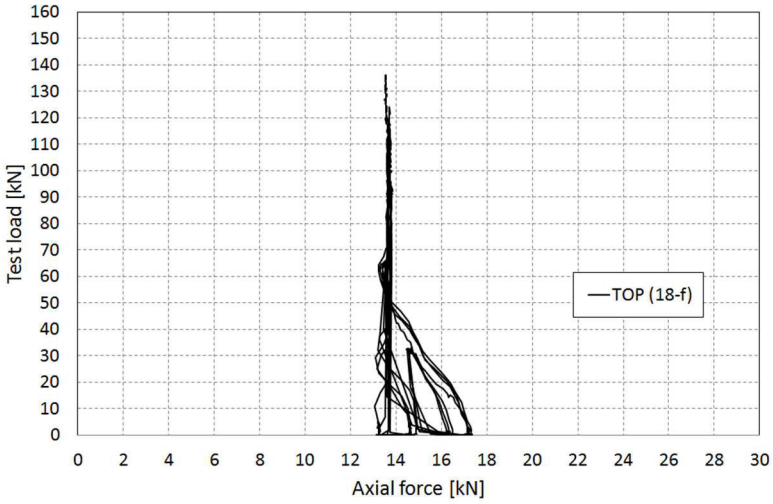

Figure 5.49 TOP (18-f): Test load – Axial force diagram (2nd test).

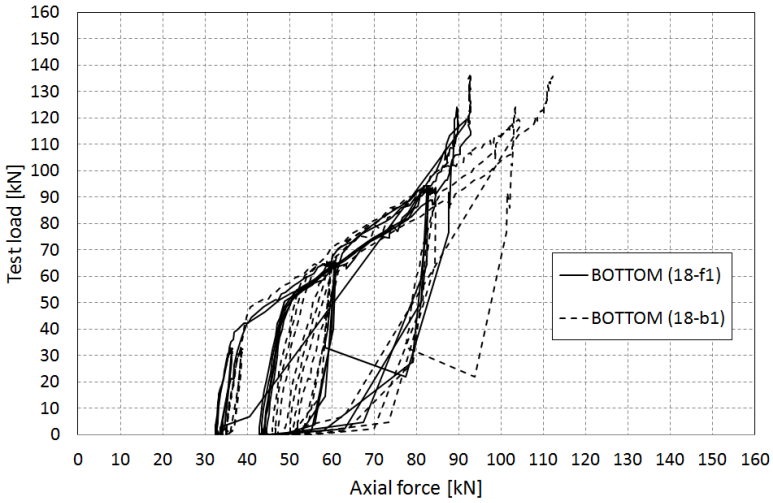

Figure 5.50 BOTTOM (18-f_1) and BOTTOM (18-b_1): Test load – Axial force diagram (2nd test).

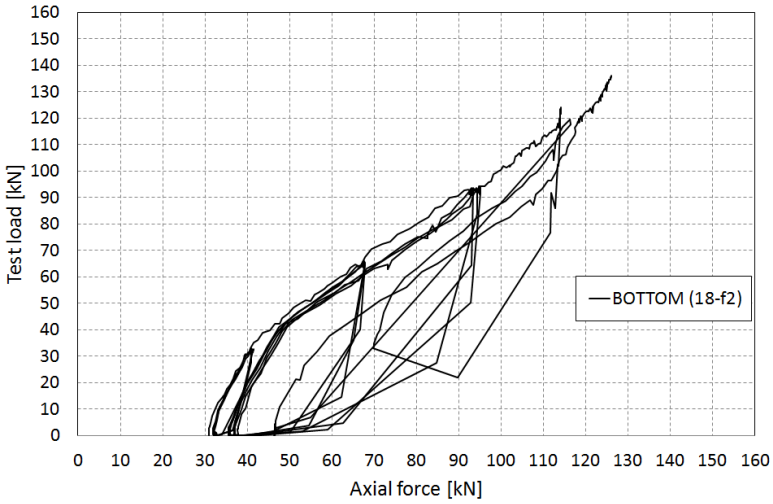

Figure 5.51 BOTTOM (18-f_2): Test load – Axial force diagram (2nd test).

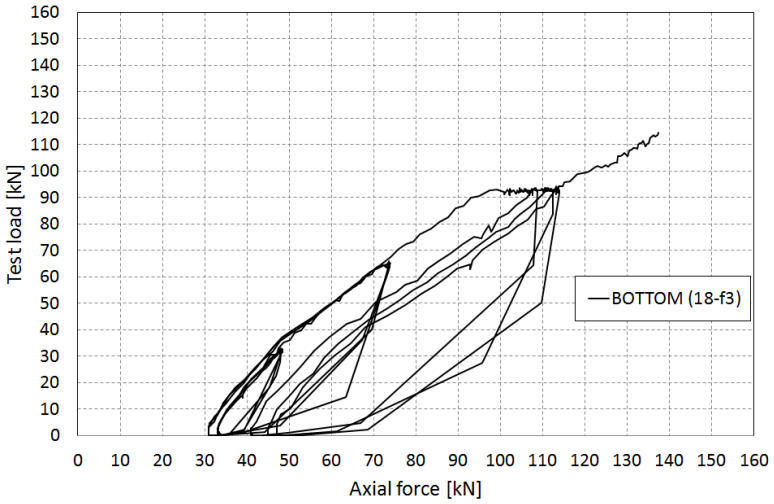

Figure 5.52 BOTTOM (18-f_3): Test load – Axial force diagram (2nd test).

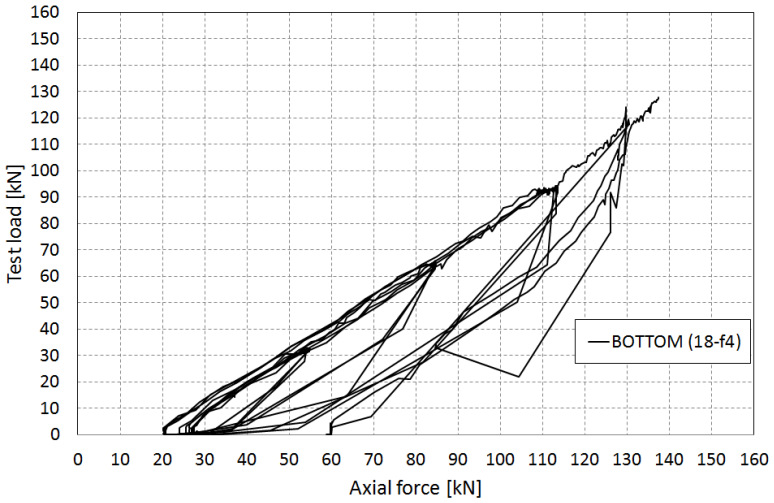

Figure 5.53 BOTTOM (18-f_4): Test load – Axial force diagram (2nd test).

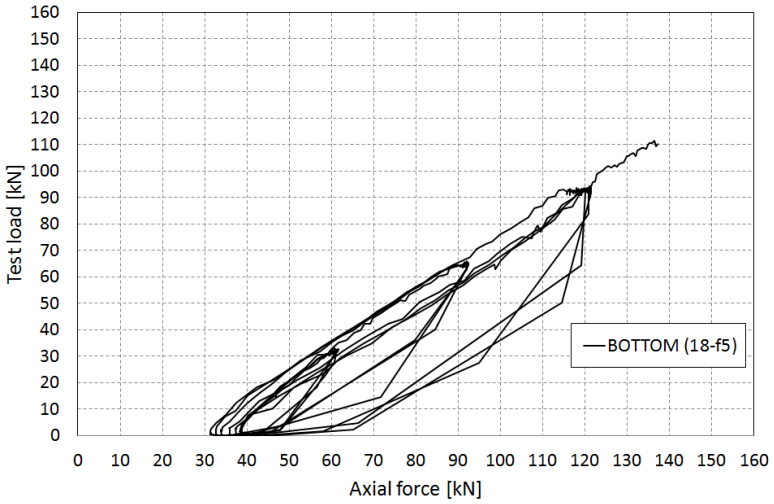

Figure 5.54 BOTTOM (18-f_5): Test load – Axial force diagram (2nd test).

5.5 Dynamic identification from free vibration test

The purpose of this identification was to accurately determine the natural frequencies and mode shapes under free vibration of the simply supported 12 m post-tensioned hybrid steel-glass beam.

The dynamic test was performed before the 1st four-point bending test and after putting the beam on the supports and applying the post-tensioning force to the post-tensioning system (see *paragraph 5.4.1*.).

The instruments used in measuring were 16 accelerometers which were put on the steel joints in three different configurations. For each configuration two measures were done, for a total of 6 measurements. The data was recorded by a centralized data acquisition board.

Due to the relatively low number of accelerometers (16) compared with the total number of steel joints (42), it was necessary to apply the accelerometers in the three positions in order to evaluate the beam's dynamic response. The mode shapes under free vibrations were obtained combining the results of each measurement. The steel joints were labelled with a letter and a number to illustrate the positioning of the accelerometers: the letter "f" has been used for the steel joints of the frontal web and the letter "b" for those of the back web, *Figure 5.55*.

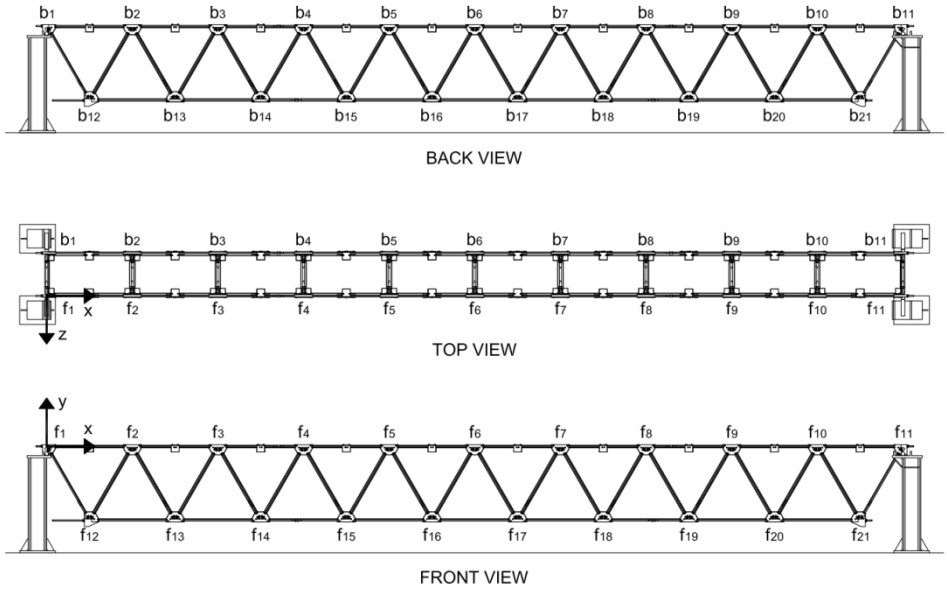

Figure 5.55 Dynamic investigations: names of steel joints.

Table 5.16 lists the coordinates of the steel joints with reference to a cartesian coordinate system whose origin is the top steel joint "f1".

Joint name	X [mm]	Y [mm]	Z [mm]
f_1	0	0	0
f_2	1200	0	0
f_3	2400	0	0
f_4	3600	0	0
f_5	4800	0	0
f_6	6000	0	0
f_7	7200	0	0
f_8	8400	0	0
f_9	9600	0	0
f_{10}	10800	0	0
f_{11}	12000	0	0
f_{12}	600	0	0
f_{13}	1800	-1039	0
f_{14}	3000	-1039	0
f_{15}	4200	-1039	0
f_{16}	5400	-1039	0
f_{17}	6600	-1039	0
f_{18}	7800	-1039	0
f_{19}	9000	-1039	0
f_{20}	10200	-1039	0
f_{21}	11400	-1039	0

Joint name	X [mm]	Y [mm]	Z [mm]
b_1	0	0	-600
b_2	1200	0	-600
b_3	2400	0	-600
b_4	3600	0	-600
b_5	4800	0	-600
b_6	6000	0	-600
b_7	7200	0	-600
b_8	8400	0	-600
b_9	9600	0	-600
b_{10}	10800	0	-600
b_{11}	12000	0	-600
b_{12}	600	0	-600
b_{13}	1800	-1039	-600
b_{14}	3000	-1039	-600
b_{15}	4200	-1039	-600
b_{16}	5400	-1039	-600
b_{17}	6600	-1039	-600
b_{18}	7800	-1039	-600
b_{19}	9000	-1039	-600
b_{20}	10200	-1039	-600
b_{21}	11400	-1039	-600

Table 5.16 Coordinates of the steel joints.

Table 5.17 lists the positions of the accelerometers for each configuration and the direction of measurement.

Configuration 1	Configuration 2	Configuration 3	Accelerometer	Direction
f_2	f_3	f_5	capacitive	Y
b_2	b_3	b_5	capacitive	Y
f_4	f_4	f_4	capacitive	Z
f_4	f_4	f_4	capacitive	Y
b_4	b_4	b_4	capacitive	Y
b_8	b_7	b_6	capacitive	Y
f_8	f_7	f_6	capacitive	Y
f_8	f_7	f_6	capacitive	Z
b_{10}	b_9	b_9	capacitive	Y
f_{10}	f_9	f_9	capacitive	Y
f_{12}	f_{13}	f_{15}	piezoelectric	Z
f_2	f_3	f_5	piezoelectric	Z
f_{14}	f_{14}	f_{14}	piezoelectric	Z
f_{19}	f_{18}	f_{17}	piezoelectric	Z
f_{21}	f_{20}	f_{16}	piezoelectric	Z
f_{10}	f_9	f_9	piezoelectric	Z

Table 5.17 Accelerometers: position, kind and direction.

(a) Photograph of the beam during the test.

(b) Photograph of the beam during the test.

(c) Photograph of the accelerometers.

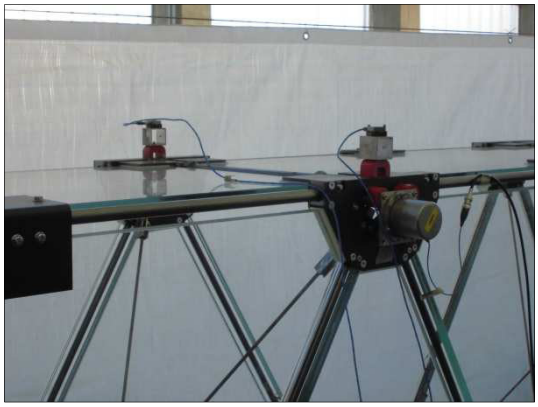

(d) Detail of the position of some accelerometers.

Figure 5.56 Positions of the accelerometers.

Table 5.18 gives the first four natural frequencies under free vibration of the 12 m post-tensioned hybrid-steel glass beam.

Mode [n]	Natural frequency [Hz]
1	3.86
2	10.92
3	11.53
4	15.64

Table 5.18 Natural frequencies.

Figure 5.57 shows the first four mode shapes of the beam under free vibration.

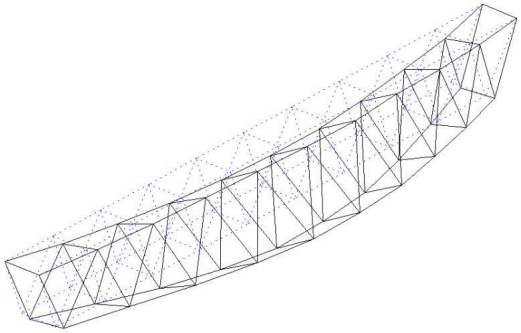

(a) The first mode shape (3.86 Hz).

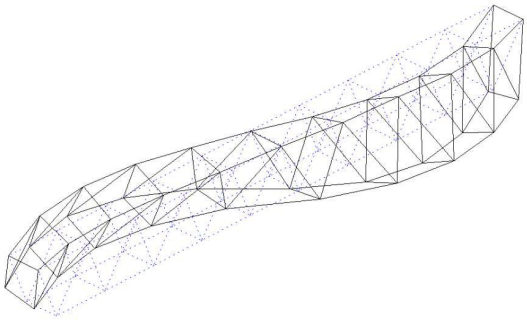

(b) The second mode shape (10.92 Hz).

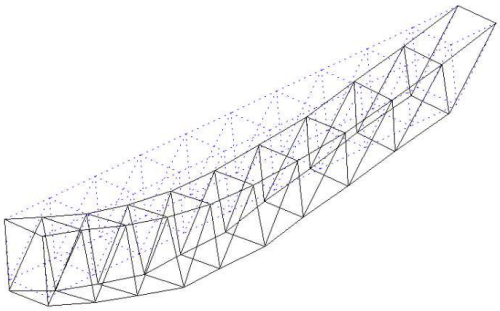

(c) The third mode shape (11.53 Hz).

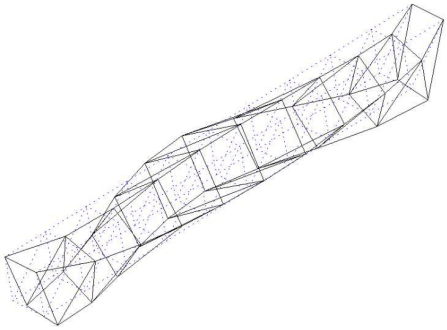

(d) The fourth mode shape (15.64 Hz).

Figure 5.57 The first four mode shapes.

The purpose of this identification was simply to evaluate the modal properties of the prototype. No further numerical and analytical analysis has been performed.

Chapter 6 Numerical modelling

This chapter focuses on the numerical modelling of the structural response of the 12 m post-tensioned hybrid steel-glass beam. The numerical model has been validated by using the experimental results illustrated in *Chapter 5*. An integrated discussion of the numerical results and a comparison with the experimental and numerical findings is provided in *Chapter 8*.

6.1 Introduction

This chapter gives a detailed explanation of the numerical model and numerical analyses made to describe the structural response of the 12 m beam under concentrated symmetric loads (four-point bending test). Numerical modelling and numerical analyses were developed with ABAQUS® Finite Element software[2].

The numerical analyses take account of the actual order of load application, of the geometric nonlinearities, of the material nonlinearity and of the contact nonlinearity. Furthermore, friction between longitudinal steel bars and central steel joints has been introduced to model the nonlinear effect of the special shaped bolts which partially restrict the free relative motion between the longitudinal steel bars and each central joint (see *paragraph 3.3.4* and *paragraph 5.3*).

The four-point bending test was modelled; the test load was increased monotonically up to the beam collapse - no load cycles. In addition, further analyses were carried out to investigate the effect of the restriction of relative movement between longitudinal steel bars and central steel joints, the effect of post-tensioning and the effect of environmental conditions - temperature and time of load application - by varying the PVB's mechanical properties. By investigating into the effects of these parameters, a more detailed understanding of the mechanical behavior of the beam is provided.

The comparison of the numerical results with the experimental results and analytical findings demonstrates that the numerical model well describes the structural response of the beam. The numerical model provides a promising method for describing the behaviour of the post-tensioned hybrid steel-glass beams because it takes account of all parameters.

6.2 Description of the numerical model

The numerical model was built using ABAQUS® Finite Element software (ABAQUS, 2010) (ABAQUS, 2012). Due to the symmetry of the 12 m post-tensioned hybrid steel-glass beam and the symmetry of test load – four point bending test - just a 3D model of a quarter of the beam was made. The following sub-sections describe the numerical model created.

6.2.1 Materials

Table 6.1 lists the materials used in the numerical model and their mechanical properties.

[2] The numerical analyses have been performed at ICOM, ENAC, EPFL, Lausanne, Switzerland.

Material	Mechanical properties	Laboratory test	Standard / paragraph
Glass	isotropic linear material E = 70000 MPa ν = 0.23 ρ = 2500 kg/m³	No	[EN 572-1:2004] [see *paragraph 4.2*]
PVB (20°C - 3sec)	isotropic linear material G = 8.060 MPa ν = 0.498 ρ = 1080 kg/m³	No	[see *paragraph 4.3*]
PVB (30°C - 3sec)	isotropic linear material G = 0.971 MPa ν = 0.498 ρ = 1080 kg/m³	No	[see *paragraph 4.3*]
Steel (plates and joints)	isotropic linear material E = 210000 MPa ν = 0.3 ρ = 7850 kg/m³	No	[EN 1993-1-1:2005] [see *paragraph 4.4*]
Steel (top and bottom longitudinal steel bars – 18 mm)	see *Figure 6.1 (a)* ρ = 7850 kg/m³	Uniaxial tension test	[see *paragraph 5.2*]
Steel (diagonal steel bars – 16 mm)	see *Figure 6.1 (b)* ρ = 7850 kg/m³	Uniaxial tension test	[see *paragraph 5.2*]
Steel* (diagonal steel bars – 14 mm)	*Figure 6.1 (b)* ρ = 7850 kg/m³	No*	[see *paragraph 5.2*]
* for the stress – strain curve of 14 mm diagonal steel bars the experimental stress – strain curve of 16 mm diagonal steel bar has been used.			
E = Young's modulus. G = Shear modulus. ν = poisson's ratio. ρ = density.			

Table 6.1 Mechanical properties of materials used in the numerical model.

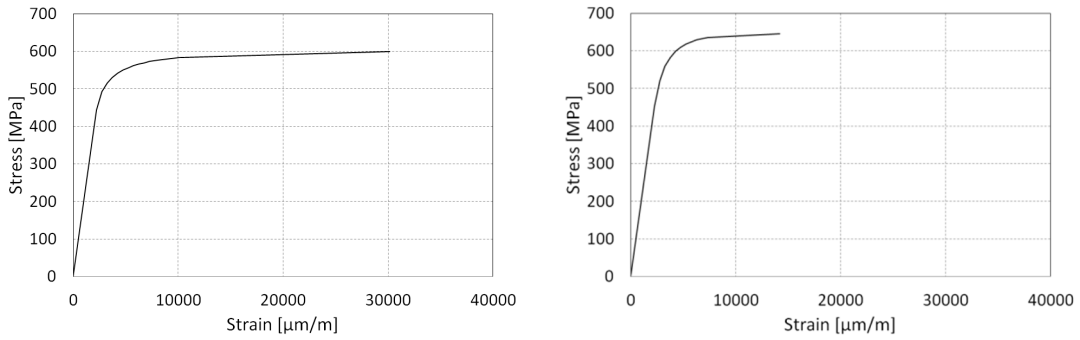

(a) Engineering stress – strain curve (18 mm steel bar). (b) Engineering stress – strain curve (16 mm steel bar).

Figure 6.1 Engineering stress – strain curves (18 mm and 16 mm steel bars).

The intermediate materials used to avoid dangerous high local stress concentrations in glass have been neglected. Aluminium and the polyethylene inserts have not been modelled because they do not affect the global behaviour of the beam.

The mechanical properties of the PVB interlayer are calculated according to (Bennison, et al., 1999) as illustrated in *paragraph 4.3*. To evaluate the effects of the PVB interlayer on the numerical structural response of the beam, two different conditions of temperature and load-duration have been investigated: PVB (20°C - 3sec) and PVB (30°C - 3sec), *Table 6.2*.

	G_{int} (N/mm²)	Load-duration	v_{int} (-)
		3 sec	
Temperature	**20°C**	8.060	0.498
	30°C	0.971	
	40°C	0.610	
	50°C	0.440	

Table 6.2 Mechanical properties of PVB-Butacite® according to (Bennison, et al., 1999).

6.2.2 Numerical model

The numerical model and numerical analyses have been performed using the ABAQUS® Finite Element software. Due to the geometrical complexity of each glass and steel component of the 12 beam, these elements have been modelled using a 3D CAD software and were subsequently imported in ABAQUS® (ABAQUS, 2010) (ABAQUS, 2012).

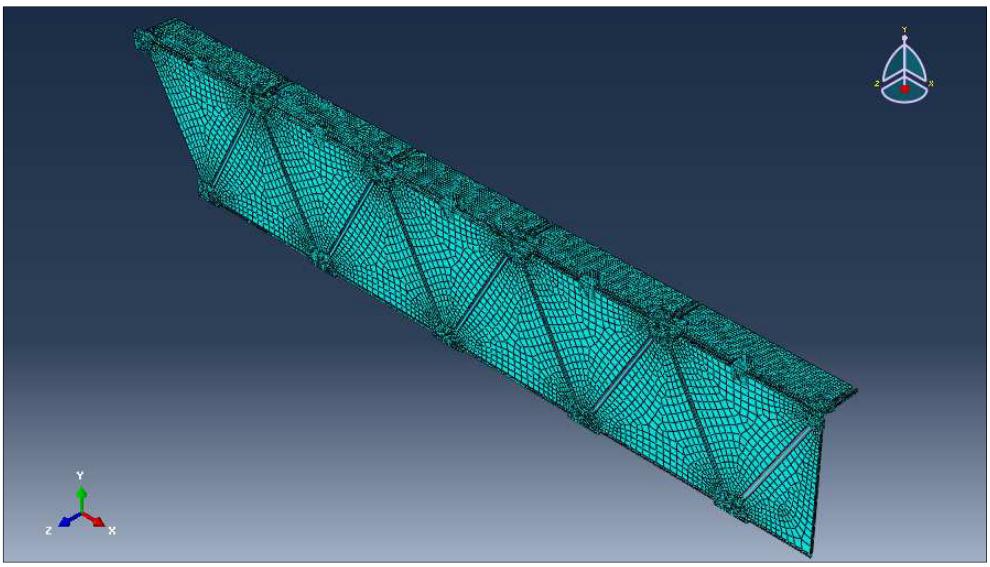

Figure 6.2 Isometric view of the numerical model.

All laminated glass panels have been modelled as layered - laminated glasses. This means that the exact thickness of each component and its own mechanical properties have also been modelled - two glass sheets (thicknesses - t_1=10mm and t_2= 10mm) and a middle PVB interlayer film (thickness - t=1.52mm).

Table 6.3 lists the element type used to model all components and a short description too.

Material	**Mechanical properties**	**Element type**	**Approximate mesh size**
Glass	isotropic linear material E = 70000 MPa ν = 0.23 ρ = 2500 kg/m³	C3D8I = 8-node linear brick, incompatible modes	~20x20x10mm
PVB (20°C - 3sec)	isotropic linear material G = 8.060 MPa ν = 0.498 ρ = 1080 kg/m³	C3D8H = 8-node linear brick, hybrid with constant pressure	~20x20x10mm
PVB (30°C - 3sec)	isotropic linear material G = 0.971 MPa ν = 0.498 ρ = 1080 kg/m³	C3D8H = *8-node linear brick, hybrid with constant pressure*	~20x20x10mm
Steel (plates and joints)	isotropic linear material E = 210000 MPa ν = 0.3 ρ = 7850 kg/m³	C3D8R = 8-node linear brick, reduced integration with hourglass control - - - - C3D4 = 4-node linear tetrahedron	~8x8x8mm
Steel (top and bottom longitudinal steel bars – 18 mm)	see *Figure 6.1 (a)* ρ = 7850 kg/m³	C3D8R = 8-node linear brick, reduced integration with hourglass control	~20x10x10mm
Steel (diagonal steel bars – 16 mm)	see *Figure 6.1 (b)* ρ = 7850 kg/m³	T3D2 = 2-node linear 3-D truss	~1000mm
Steel* (diagonal steel bars – 14 mm)	*Figure 6.1 (b)* ρ = 7850 kg/m³	T3D2 = 2-node linear 3-D truss	~1000mm
* for the stress – strain curve of 14 mm diagonal steel bars the experimental stress – strain curve of 16 mm diagonal steel bar has been used.			
E = Young's modulus. G = Shear modulus. ν = poisson's ratio. ρ = density.			

Table 6.3 Numerical model: element type.

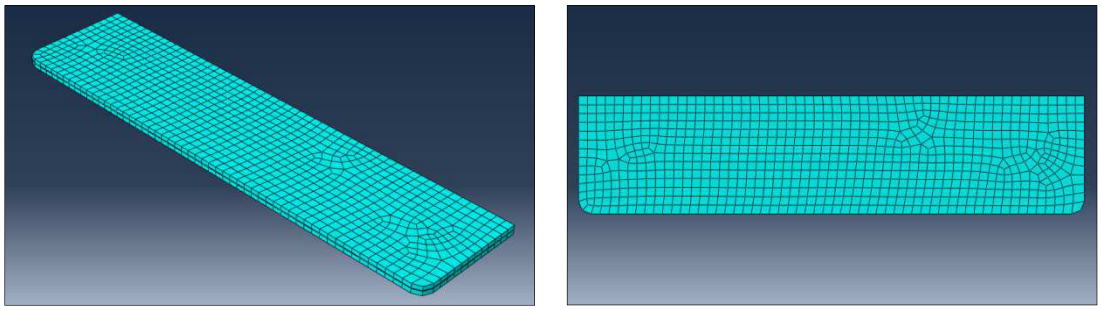

(a) Isometric view. (b) Front view.

Figure 6.3 Details of the numerical model of the rectangular glass panel.

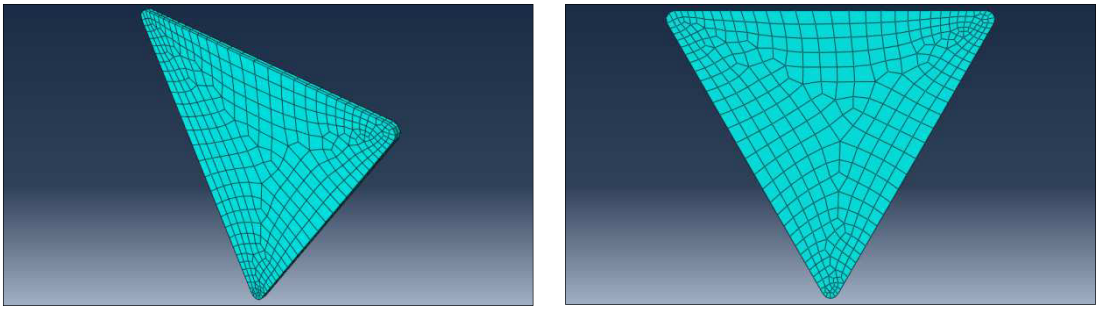

(a) Isometric view. (b) Front view.

Figure 6.4 Details of the numerical model of the triangular glass panel.

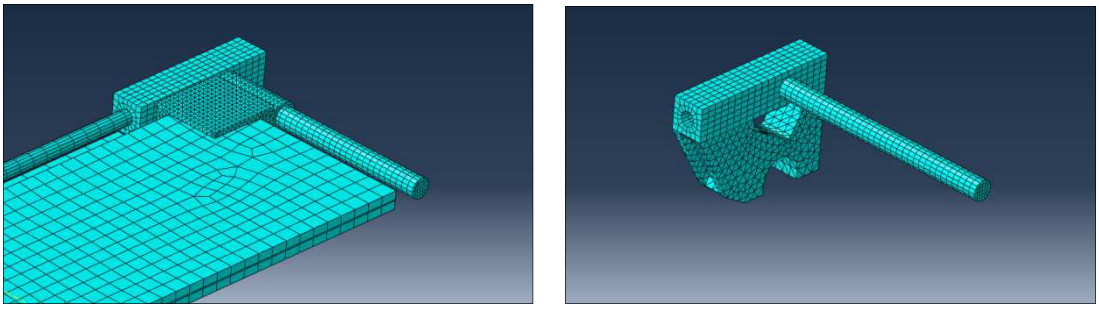

(a) Top end joint. (b) Top end joint.

Figure 6.5 Details of the numerical model of the top end joint.

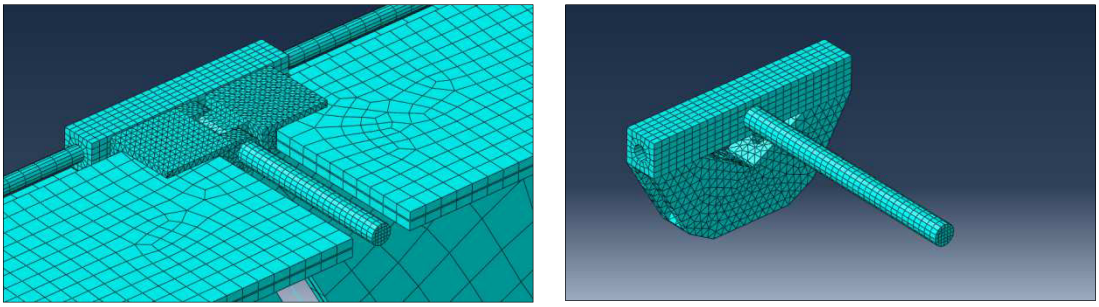

(a) Top central joint. (b) Top central joint.

Figure 6.6 Details of the numerical model of the top central joint.

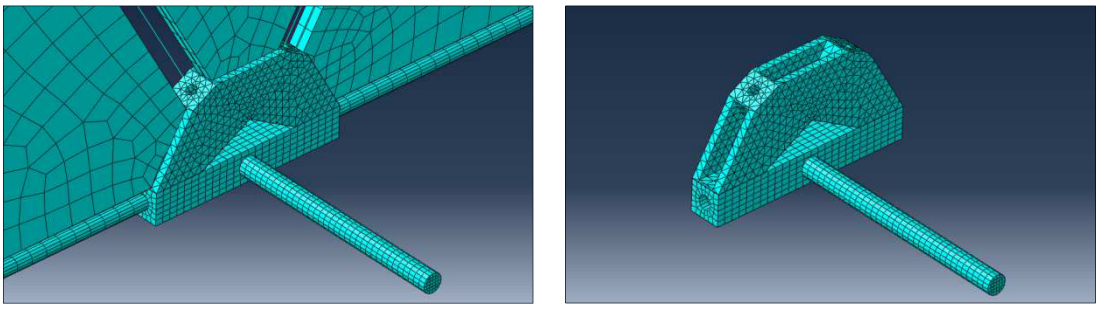

(a) Bottom central joint. (b) Bottom central joint.

Figure 6.7 Details of the numerical model of the bottom central joint.

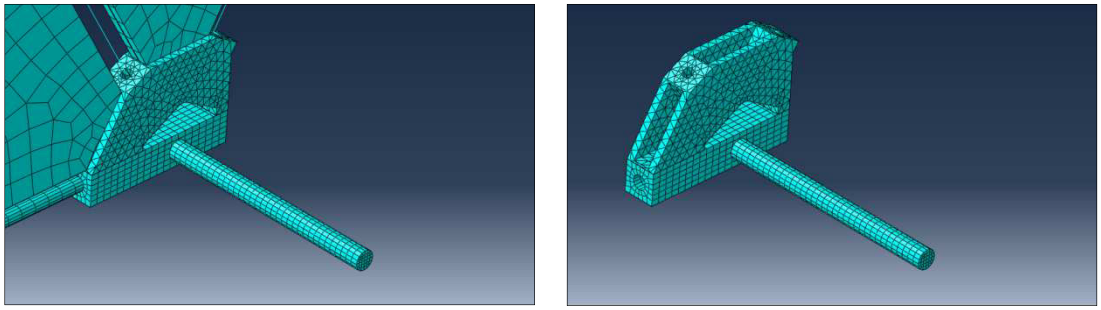

(a) Bottom end joint. (b) Bottom end joint.

Figure 6.8 Details of the numerical model of the bottom end joint.

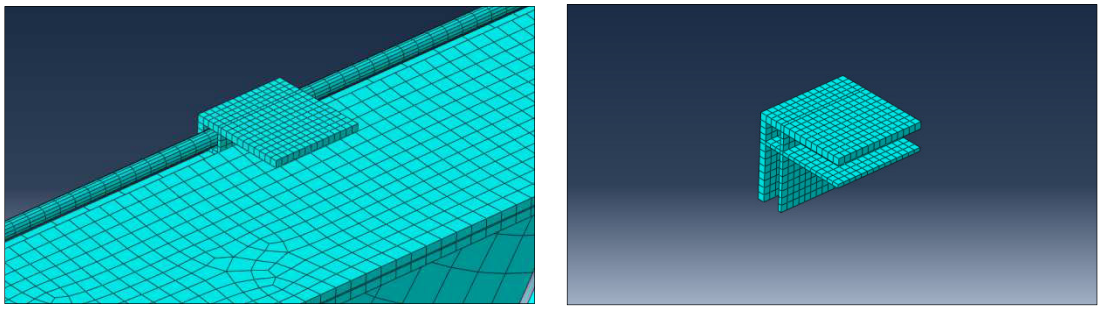

(a) Connection. (b) Connection.

Figure 6.9 Details of the connection between the triangular glass panel and the rectangular glass panel.

As described in *paragraph 3.3.4* and in *paragraph 5.3*, the relative motion between longitudinal steel bars and central steel joints is partially restricted thanks to some special shaped steel bolts. Experimental investigations to evaluate the effects of one bolt on this kind of joint-bar-bolt connection have been performed during this research and the findings have been adopted in the numerical model. Friction between longitudinal steel bars and central steel joints was introduced to take account of the effect of the special shaped bolts. In the numerical model, the special shaped bolts have not been modelled; their effects on longitudinal steel bars have been introduced as friction between the lateral surface of the longitudinal steel bars and the surfaces of the holes of the central steel joints.

Figure 6.10 (a) shows the experimental force - displacement diagram obtained from the experimental investigations that have been performed on a connection with just one special shaped bolt (see *paragraph 5.3*). Each central steel joint have two special shaped bolts and the tightening torque applied to them was 15 N·m. *Figure 6.10 (b)* shows the simplified numerical force – displacement diagram used in the numerical model together with the experimental force – displacement diagram for two bolts obtained multiplying by 2 the value of the force of the *Test 2 [tightening torque 15N·m]* shown in *Figure 6.10 (a)*.

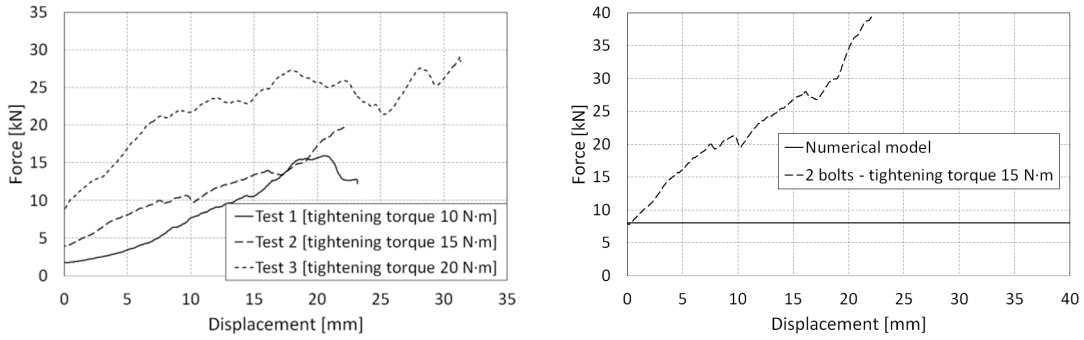

(a) Pull-out tests performed on one bolt: load – displacement diagram. (b) Effective load – displacement diagram for two bolts and the diagram used in the numerical model.

Figure 6.10 Load – displacement diagram used to model friction.

This means that when the axial force is lower than 8 kN, there is no relative motion between steel bar and steel joint and the bar transmits by contact the axial force (≤ 8 kN) to the steel joint. When the axial force exceeds 8 kN there is a relative motion between steel bar and steel joint, and the bar transmits a force of 8 kN to the steel joint by contact.

6.2.3 Actions

The values and the order of application of loads in the model have been introduced to simulate the 2nd four point bending test (see *paragraph 5.4.2*). *Table 6.4* lists the order of application of loads.

N.	Action	Description
1	Self-weight	dead load of the beam
2	Permanent load	weight of the hydraulic jacks and the equipment
3	Post-tensioning load	forces applied to produce compressive stress in glass
4	Test load	monotonically increasing test load

Table 6.4 Numerical model: order of application of loads.

The self-weight of the beam depends on the density of all components, their shape and dimensions and it is automatically taken into account by the software.

The total value of permanent load is 4.0 kN then a value of 1.0 kN was applied to the top central steel joint, 4800 mm away from the support, *Figure 6.11*:

$$F_{pl} = 4.0\ kN$$

the concentrated force acting on the steel joint is:

$$\frac{F_{pl}}{4} = 1.0\ kN$$

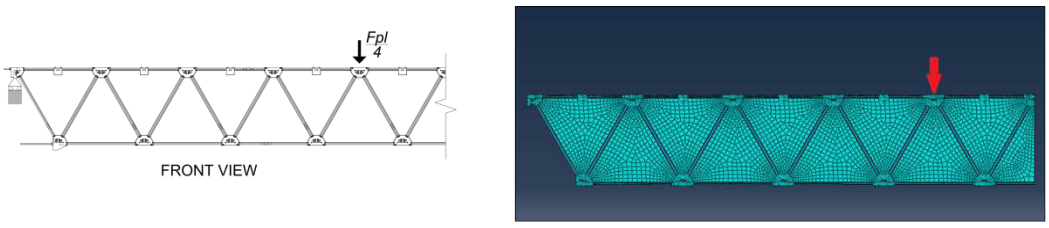

(a) Permanent load - engineering drawing. (b) Permanent load - numerical model.

Figure 6.11 Schematic representation of the point of application of the permanent load.

The tensile forces applied to the post-tensioning system are listed in *Table 6.5*.

Element / position	Diameter [mm]	Post-tensioning load [kN]
Diagonal steel bar (extremity)	16	26
Diagonal steel bar (central)	14	13
Top longitudinal steel bar	18	17
Bottom longitudinal steel bar	18	33

Table 6.5 Numerical model: tensile forces applied to the post-tensioning system.

The total value of test load was applied to the top steel joint 4800 mm away from the support (*Figure 6.12)*. In the numerical model, the test load was increased monotonically until the analysis did not converge; no load cycle was applied.

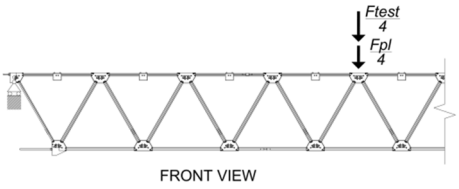

(a) Test load and permanent load – engineering drawing.

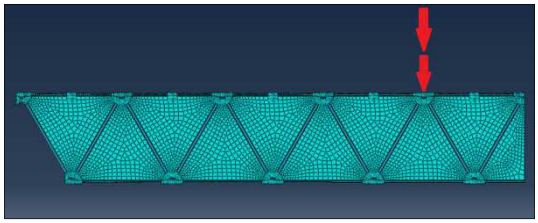

(b) Test load and permanent load – numerical model.

Figure 6.12 Schematic representation of the point of application of the test load and permanent load.

6.2.4 Numerical analyses

Ten numerical non-linear analyses have been performed; two of them simulate exactly the 2nd four-point bending test with two different values of shear modulus of PVB interlayer in order to evaluate the influence of temperature and load-duration on the numerical response of the beam. The other 8 numerical analyses have been performed to investigate the effects of the post-tensioning forces and the friction between longitudinal steel bars and central steel joints on the numerical behaviour of the beam. The purpose is to evaluate the influence of these parameters on the structural response of the beam. *Table 6.6* lists all the numerical analyses performed.

	N.	Analysis	PVB	Self-weight	Permament load	Post-tensioning load	Test load
Basic analyses	1	PVBa-Fr-PT	G = 8.060 MPa	yes	yes	yes	yes
				no friction			friction [8 kN]
	2	PVBb-Fr-PT	G = 0.971 MPa	yes	yes	yes	yes
				no friction			friction [8 kN]
Further analyses	3	PVBa-PT	G = 8.060 MPa	yes	yes	yes	yes
				no friction			no friction
	4	PVBb-PT	G = 0.971 MPa	yes	yes	yes	yes
				no friction			no friction
	5	PVBa	G = 8.060 MPa	yes	yes	no	yes
				no friction			no friction
	6	PVBb	G = 0.971 MPa	yes	yes	no	yes
				no friction			no friction
	7	PVBa-Fr	G = 8.060 MPa	yes	yes	no	yes
				no friction			friction [8 kN]
	8	PVBb-Fr	G = 0.971 MPa	yes	yes	no	yes
				no friction			friction [8 kN]
	9	PVBa-Fix	G = 8.060 MPa	yes	yes	no	yes
				fix*			fix*
	10	PVBb-Fix	G = 0.971 MPa	yes	yes	no	yes
				fix*			fix*
* no relative motion is possible between longitudinal steel bars and central steel joints because they are rigidly connected.							

Table 6.6 Numerical analyses.

The nonlinear analyses n. 1 and n. 2 model exactly the 2nd four-point bending laboratory test with two different values of shear modulus for PVB interlayer. The friction between longitudinal steel bars and central steel joints is activated immediately before applying the test load because the special shaped bolts in the prototype are tightened only before the application of the test load, then the self-weight of the beam, the permanent load and the post-tensioning loads act without any friction.

The nonlinear analyses n.3, 4, 5, 6 simulate the four-point bending test without any friction between longitudinal steel bars and central steel joints. These analyses have been performed to evaluate the numerical behaviour of the beam in case of free relative motion between longitudinal steel bars and central steel joints.

The nonlinear analyses n.9 and n.10 simulate the four-point bending test assuming that the longitudinal steel bars are rigidly connected to central steel joints. The purpose of these analyses is to investigate the numerical behaviour of the beam in case of rigid connections between longitudinal steel bars and central steel joints.

6.2.5 Numerical results

The current paragraph and the following subparagraphs provide the results of the numerical investigations. These findings are compared with the numerical and experimental results in *Chapter 8,* where an integrated discussion is provided.

As described in *paragraph 5.4.2*, the collapse of the prototype occurred because of buckling of a triangular laminated glass panel when the test load reached a value of 136 kN. Instead, all numerical analyses ceased to run when the maximum strain – stress value in the bottom longitudinal steel bar was reached and not because of buckling of glass panels in compression. Moreover, there is no difference between the numerical findings obtained from the numerical analyses performed with PVB [G = 8.060 MPa] and the numerical analyses performed with PVB [G = 0.971 MPa]. For this reason, the following diagrams show the numerical results obtained from the analyses performed with PVB [G = 8.060 MPa], *Table 6.7*.

Analysis	PVB	Self-weight	Permament load	Post-tensioning load	Test load
PVBa-Fr-PT	G = 8.060 MPa	yes	yes	yes	yes
		no friction			friction [8 kN]
PVBa-PT	G = 8.060 MPa	yes	yes	yes	yes
		no friction			no friction
PVBa	G = 8.060 MPa	yes	yes	no	yes
		no friction			no friction
PVBa-Fr	G = 8.060 MPa	yes	yes	no	yes
		no friction			friction [8 kN]
PVBa-Fix	G = 8.060 MPa	yes	yes	no	yes
		fix*			fix*
* no relative motion is possible between longitudinal steel bars and central steel joints because they are rigidly connected					

Table 6.7 Main numerical analyses.

Test load – displacement diagrams

Figure 6.13 shows the points where the vertical and the horizontal displacements were measured.

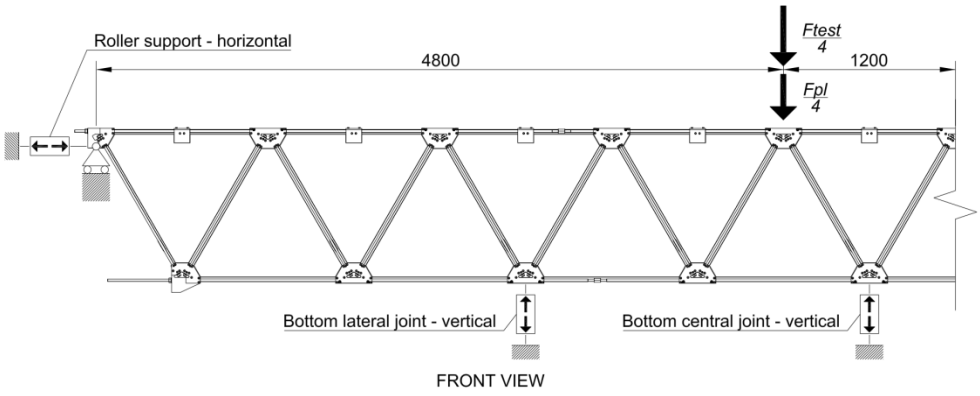

Figure 6.13 Positions and names of the points where the displacements are measured.

Figure 6.14 shows the test load – vertical displacement diagrams of the bottom central steel joint, *Figure 6.15* shows the test load – vertical displacement diagrams of the bottom lateral steel joint. *Figure 6.16* shows the test load – horizontal displacement diagram of the roller support.

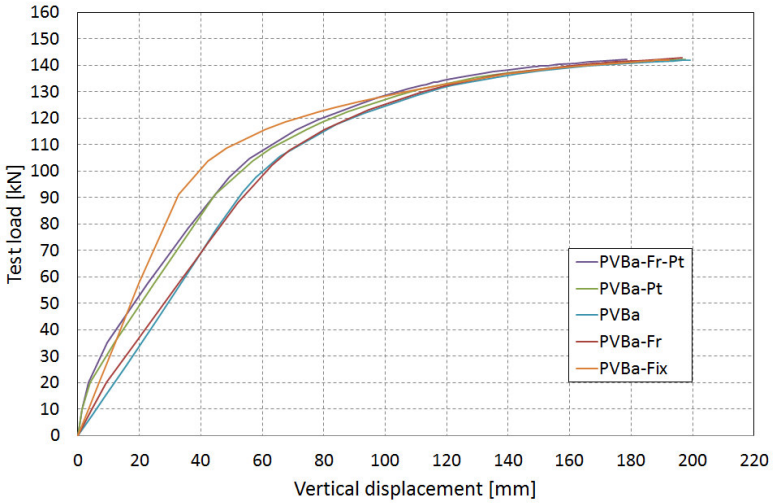

Figure 6.14 Bottom central steel joint: Test load – Vertical displacement diagram (numerical model).

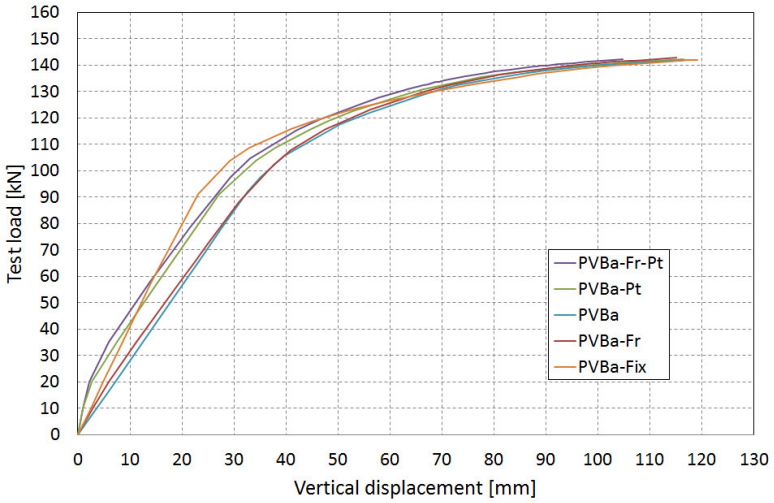

Figure 6.15 Bottom lateral steel joint: Test load – Vertical displacement diagram (numerical model).

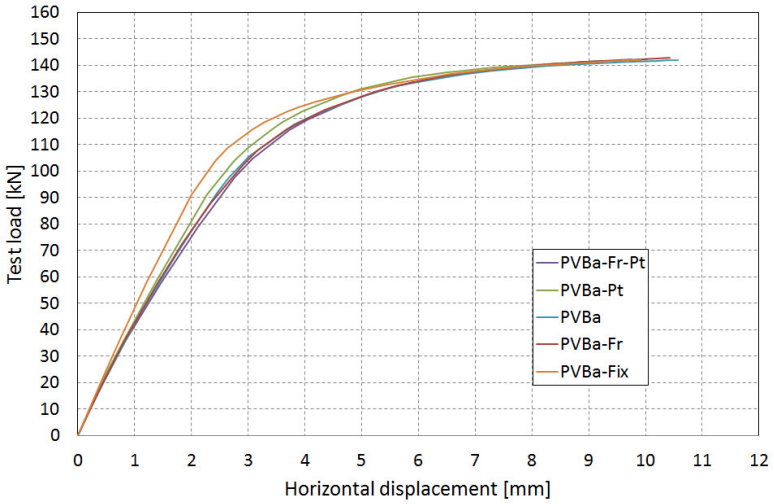

Figure 6.16 Roller support: Test load – Horizontal displacement diagram (numerical model).

Test load – axial force diagrams

Figure 6.17 shows the points and the cross-sections where the axial forces in longitudinal steel bars have been measured.

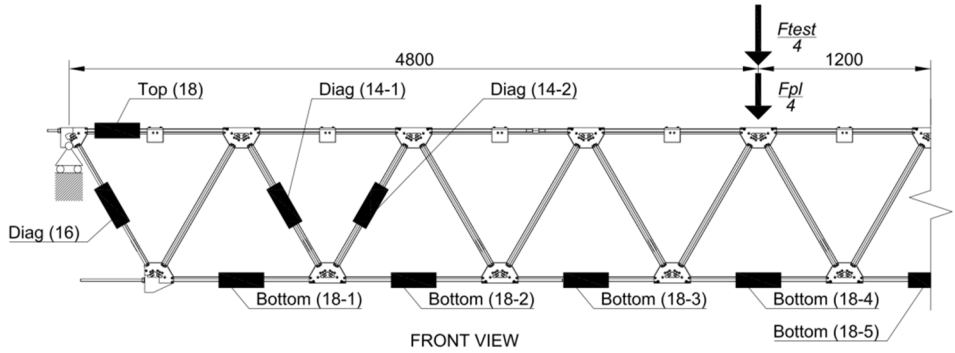

Figure 6.17 Positions and names of the steel bars.

The following diagrams show the test load – axial force diagrams in steel bars.

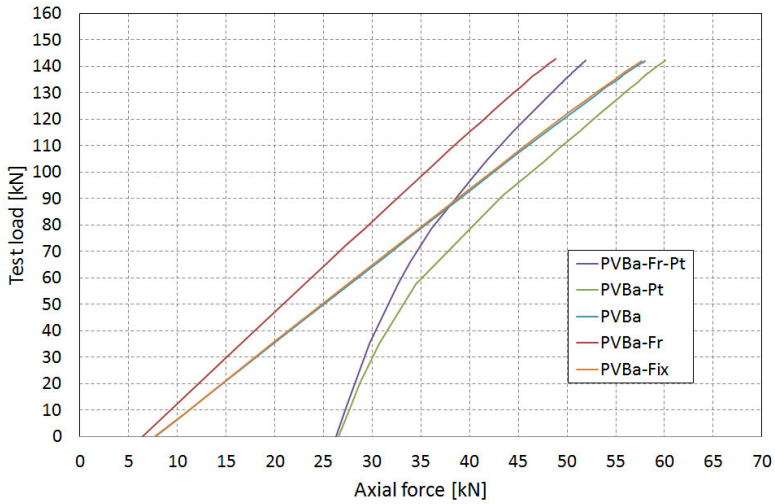

Figure 6.18 DIAG (16): Test load – Axial force diagram (numerical model).

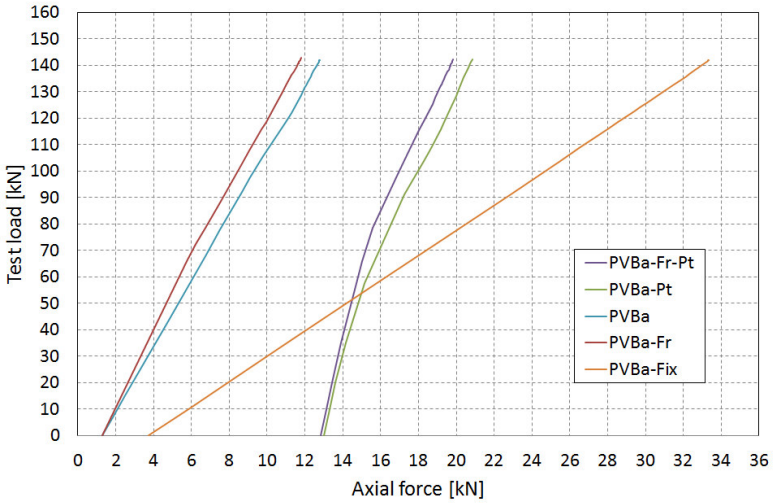

Figure 6.19 DIAG (14-1): Test load – Axial force diagram (numerical model).

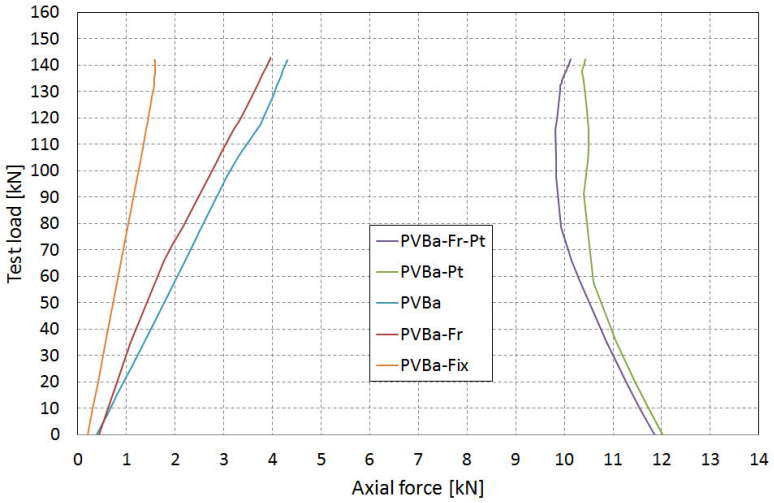

Figure 6.20 DIAG (14-2): Test load – Axial force diagram (numerical model).

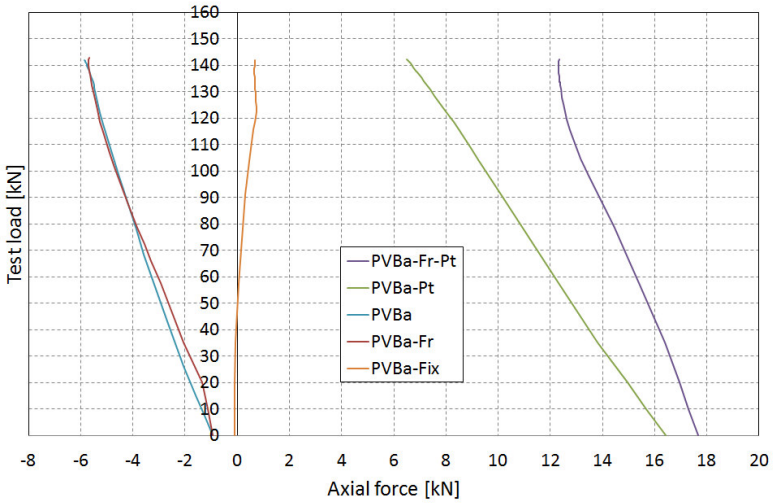

Figure 6.21 TOP (18): Test load – Axial force diagram (numerical model).

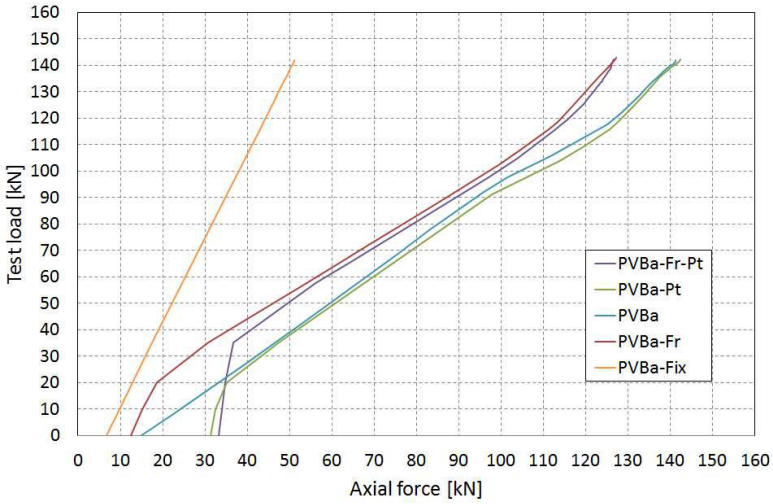

Figure 6.22 BOTTOM (18-1): Test load – Axial force diagram (numerical model).

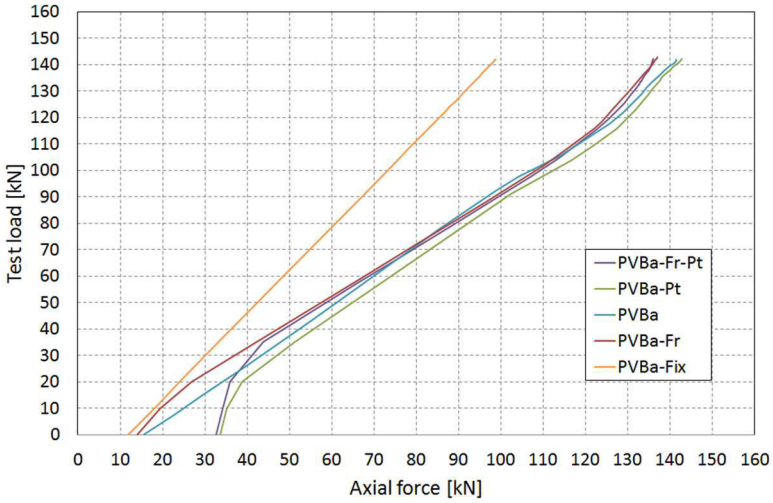

Figure 6.23 BOTTOM (18-2): Test load – Axial force diagram (numerical model).

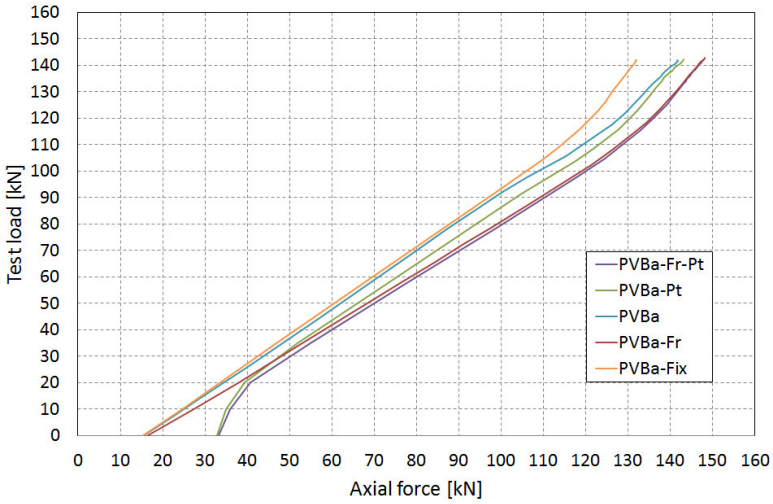

Figure 6.24 BOTTOM (18-3): Test load – Axial force diagram (numerical model).

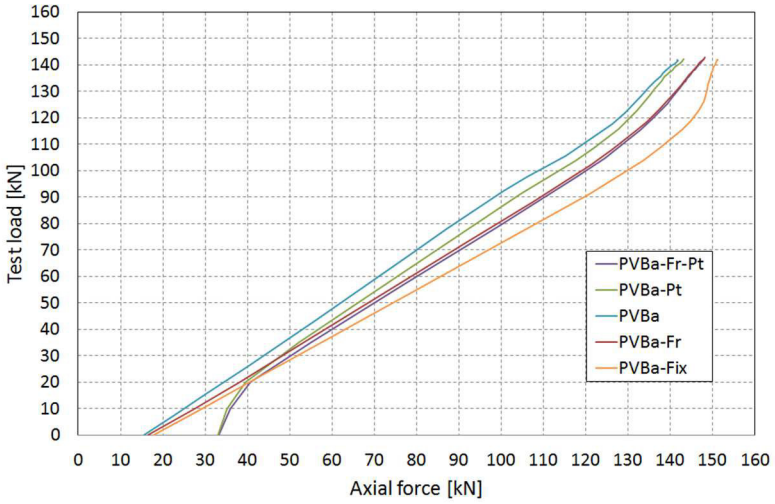

Figure 6.25 BOTTOM (18-4): Test load – Axial force diagram (numerical model).

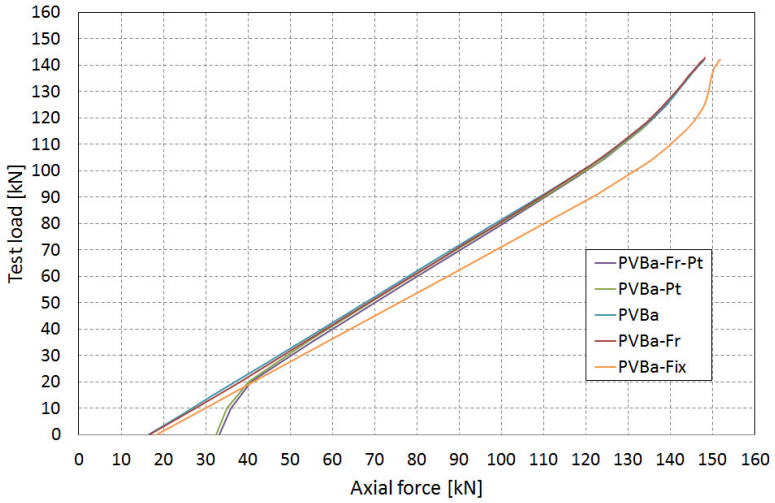

Figure 6.26 BOTTOM (18-5): Test load – Axial force diagram (numerical model).

6.3 Conclusions

From the results of the numerical analyses it is concluded that the numerical modelling is a useful method for describing the behaviour of the post-tensioned hybrid steel-glass beams because it takes account of several parameters such as friction, geometric nonlinearity, material nonlinearities, post-tensioning forces and mechanical properties of the interlayer.

In particular, the numerical findings show that the post-tensioning forces applied to steel bars affect just slightly the stiffness of the beam and that the breakage of the beam is ductile due to the plastic deformation of tensile steel bars.

Chapter 7 Analytical modelling

This chapter focuses on the analytical modelling of the structural response of segmented post-tensioned hybrid steel-glass beams. The experimental results of *Chapter 5* and the numerical findings of *Chapter 6* are used as reference to validate the analytical model. The findings from analytical and numerical models are compared with the experimental results and an integrated discussion of the structural response of segmented post-tensioned hybrid steel-glass prototype is given in *Chapter 8*.

7.1 Introduction

This part of the current research focuses on the analytical determination of the internal forces in steel bars and in glass generated by the moment. The internal forces enable the beam to carry load; these forces are tensile forces in the bottom longitudinal steel bars and in the diagonal steel bars, and compressive forces in the glass panels. The compressive forces in glass panels are contact forces generated because the glass panels come in contact with the steel joints.

The following subparagraphs illustrate the analytical modelling and its application for calculating the internal forces in the bottom longitudinal steel bars of the prototype. The analytical model neglects the post-tensioning of steel bars because it does not affect the global structural response of the beam but it reduces the amount of parameters into the investigations.

7.2 Derivation of the equations of the analytical model

The current section explains the analytical model. For this purpose, the analytical response of a single glass web loaded by pure bending is investigated (*Figure 7.1)*. It helps to understand the mechanical behaviour of the glass web and the connected internal motion between the triangular segments and the steel joints. The following basic assumptions are fixed:

- one glass web
- no glass flanges
- no intermediate materials between glass panels and steel joints
- no top longitudinal steel bars
- equilateral triangular glass panels = rigid bodies
- steel joints = rigid bodies
- diagonal steel bars = all bars have the same diameter and are modelled as truss elements
- no post-tensioning forces
- bottom longitudinal steel bars = truss elements hinged to steel joints
- pure bending (constant bending moment)

The pure bending generates a deformation of the glass web as shown in *Figure 7.1*. The dashed lines in figure indicate the axes of symmetry.

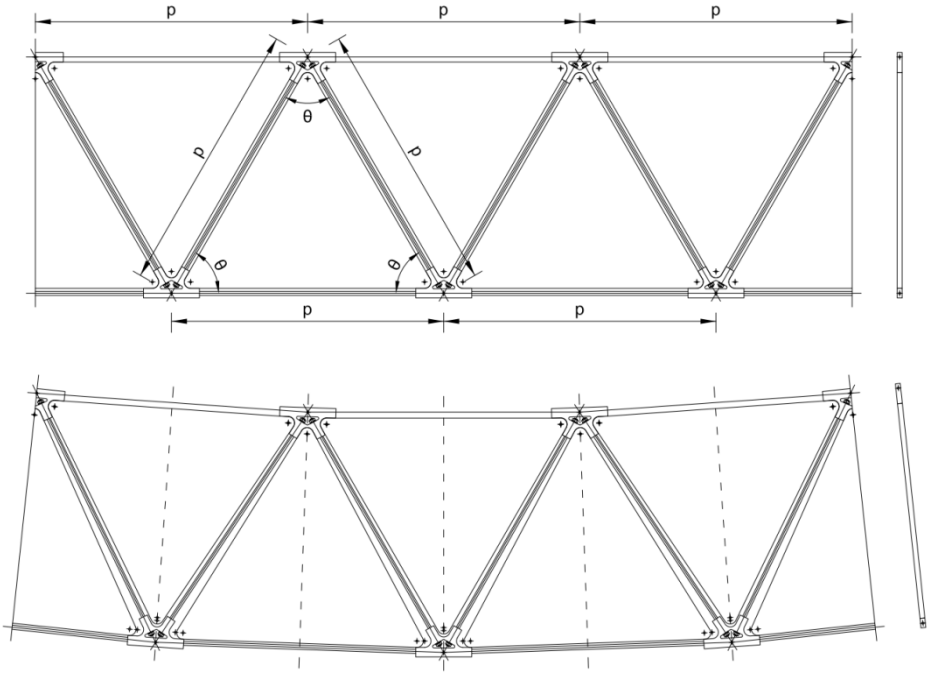

Figure 7.1 Glass web and pure bending deformation.

The pure bending generates:

1. the detachment of the bottom corners of the triangular panels named ***TR.A*** from the bottom joints (*Figure 7.2 (c)*)

2. a punctual contact between the bottom corners of the triangular panels named ***TR.B*** and the bottom joints (*Figure 7.2 (c)*)

3. no movement between the triangular panels named ***TR.B*** and the top joints (*Figure 7.2 (b)*)

4. punctual contacts between the top corners of the triangular panels named ***TR.A*** and the top joints (*Figure 7.2 (b)*)

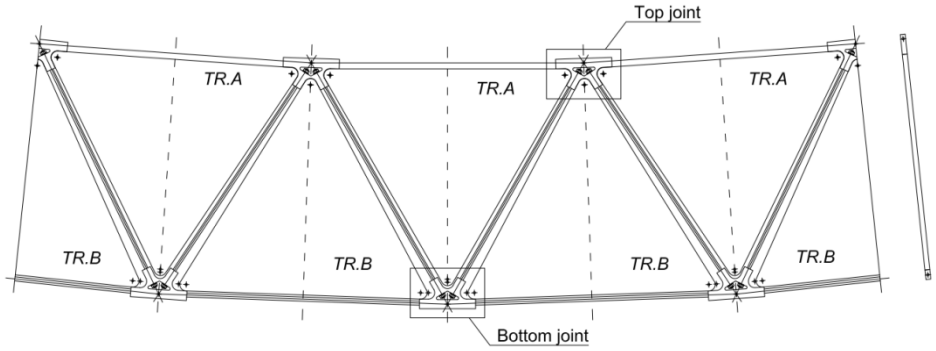

(a) Deformation of the glass web generated by pure bending.

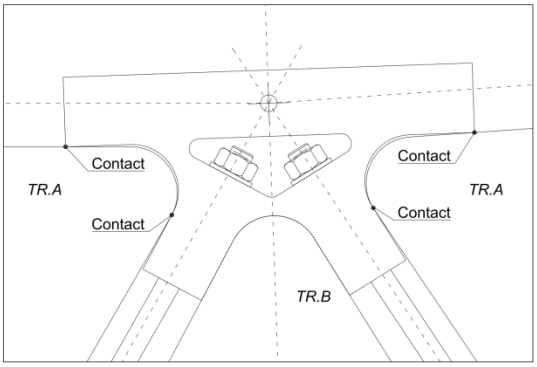

(b) Effects of pure bending on the top joint.

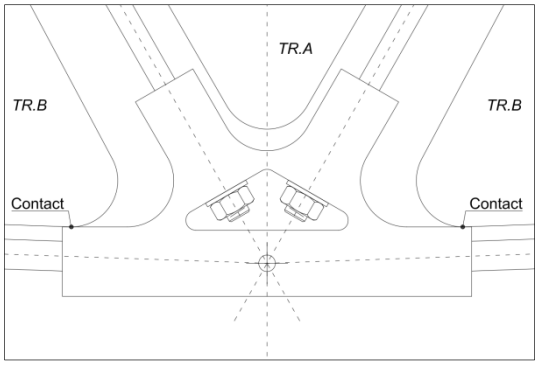

(c) Effects of pure bending on the bottom joint.

Figure 7.2 Effects of pure bending on the top and the bottom joints.

Due to symmetry, the pure bending generates the same effects on all triangular panels, on all diagonal steel bars and on all longitudinal steel bars. For this reason, it is preferable to investigate the effects of the pure bending on a vertical strip of the glass web comprised between two axes of symmetry (*Figure 7.3)*.

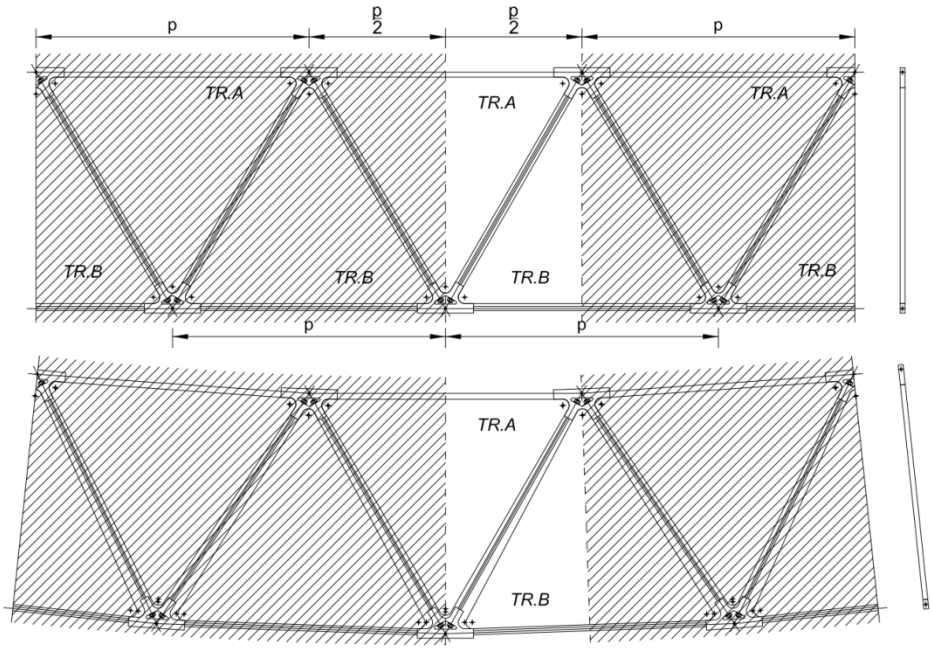

Figure 7.3 Detail of the part of glass web between two axes of symmetry.

A rectangular coordinate system is introduced; the x-axis corresponds with the longitudinal edge of the triangular panel ***TR.A*** and the y-axis with the axis of symmetry of the triangular panel ***TR.A***, *Figure 7.4*.

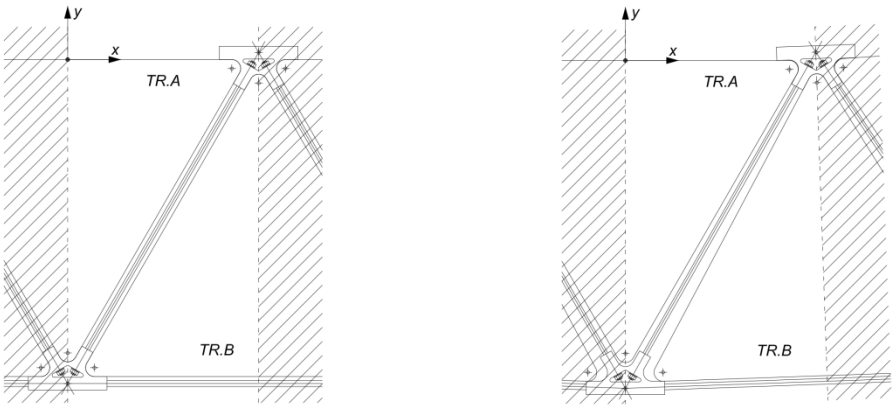

Figure 7.4 Cartesian coordinate system.

Figure 7.5 shows the actual geometry and the shape of the joint and a simplified sketch of the joint. The simplified joint helps to better identify the mechanical response of the web generated by pure bending.

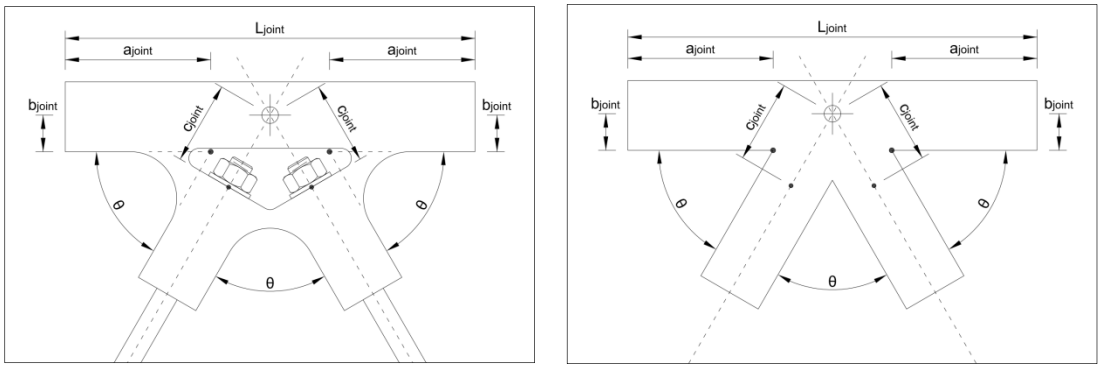

(a) Actual geometry and shape of the joint. (b) Simplified geometry and shape of the joint.

Figure 7.5 Actual and simplified shape of the joint.

The following symbols and descriptions identify the shape of the joint:

L_{joint}	longitudinal length of the joint
a_{joint}	length of the longitudinal edge of the lateral slot
b_{joint}	distance of the longitudinal edge of the lateral slot from the centre point ot the joint
c_{joint}	distance of the hex nuts of the diagonal steel bars from the centre point of the joint
$\theta = 60°$	internal angle formed by the edges of the slots

Figure 7.6 shows the shape of the triangular panel.

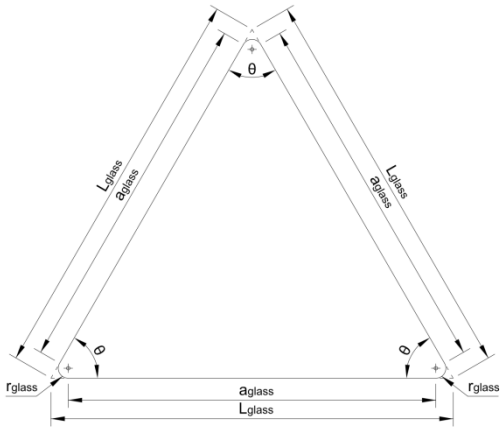

Figure 7.6 Shape of the triangular panel.

The following symbols and descriptions identify the shape of the triangular panel:

L_{glass}	length of the edges of the triangular panels before processing the corners
r_{glass}	radius of the round corners
$\theta = 60°$	internal angle formed by the panel edges
$a_{glass} = L_{glass} - 2 \cdot \frac{r_{glass}}{tan\left(\frac{\vartheta}{2}\right)}$	distance between the centres of the circles defining the round corners

The moment causes the motion of the top joint and the equilateral triangular panel ***TR.B***, *Figure 7.7*. In order to describe the mechanical response and motion of the joint and the triangular panel ***TR.B***, a secondary cartesian coordinate system ***O'***$(x_{0'}; y_{0'})$ is necessary. The secondary rectangular coordinate system has the origin ***O'***$(x_{0'}; y_{0'})$ at the extremity of the longitudinal edge of the lateral slot of the joint, the x'-axis corresponds with the horizontal edge of the triangular panel ***TR.A***, and the y'-axis is parallel to the y-axis, *Figure 7.8*.

Figure 7.7 Motion of the top joint generated by pure bending.

Figure 7.8 Secondary cartesian coordinate system ***O'***$(x_{0'}; y_{0'})$.

The motion of the top joint and the equilateral triangular panel ***TR.B*** generates motion of the bottom round corner of the triangular panel ***TR.B***. The round corner of the panel ***TR.B*** is in contact with one point of the bottom joint, and generates a translation of the bottom joint along to the y-axis, *Figure 7.9* and *Figure 7.10*.

The movements generated by the pure bending are described by investigating its effects separately:

1. rotation α of the top joint and the triangular panel ***TR.B***
2. translation $\delta_x(\alpha)$ of the top joint and the triangular panel ***TR.B*** along the x-axis

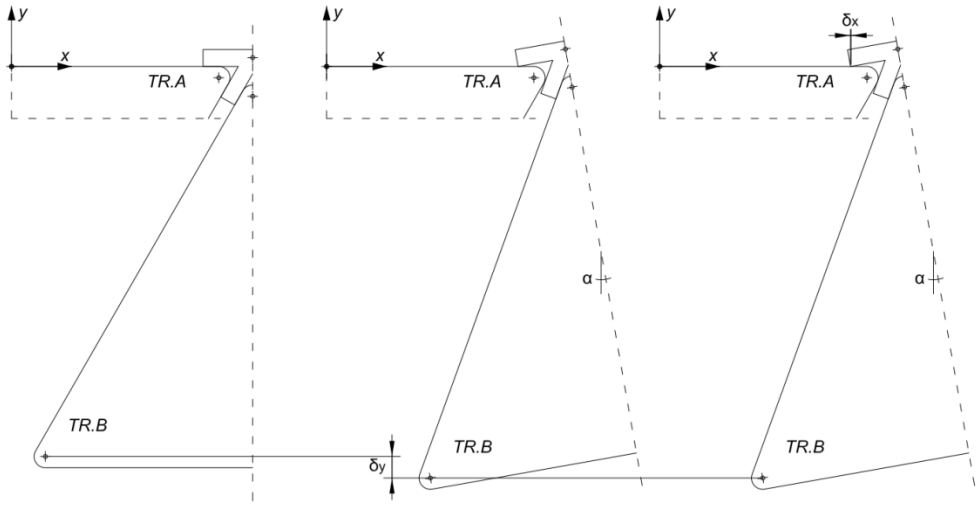

Figure 7.9 View of the motion of the bottom corner of the triangular panel ***TR.B***.

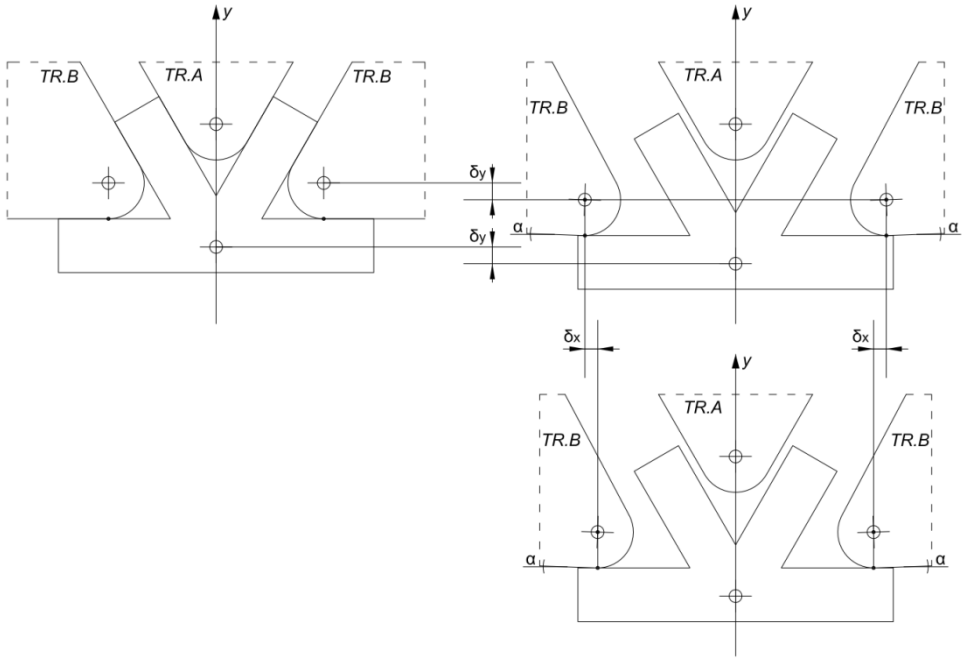

Figure 7.10 Detail of the motion of the bottom joint ***TR.B***.

First of all, the position of the origin of the secondary cartesian system ***O'***$(x_{0'}; y_{0'})$ is specified, *Figure 7.8*. *Table 7.1* gives the coordinates of the origin of the secondary cartesian system ***O'***$(x_{0'}; y_{0'})$.

Point	x	y
O'	$x_{0'} = \frac{p}{2} - \frac{L_{joint}}{2}$	$y_{0'} = 0$

Table 7.1 Coordinates of the origin of the secondary cartesian system ***O'***$(x_{0'}; y_{0'})$.

The position of point ***A*** and the equation of the straight line ***r*** passing through the point ***A*** and parallel to the inclined edge of lateral slot are defined with reference to the secondary Cartesian system ***O'(x₀'; y₀')***, *Figure 7.11*. Point ***A*** is the point of intersection of the edges of the lateral slot of the top joint. *Tables 7.2* gives the coordinates of the of the point ***A*** and the equation of the straight line ***r*** with reference to the secondary cartesian system ***O'(x₀'; y₀')***.

Point	x'	y'
A	$x'_A = a_{joint}$	$y'_A = 0$

Straight line	$y' = f(x')$
r	$y'_r(x') = x' \cdot tan(\theta) + [y'_A - x'_A \cdot tan(\theta)]$

Table 7.2 Point ***A*** coordinates and equation of the straight line ***r*** in the secondary cartesian system ***O'(x₀'; y₀')***.

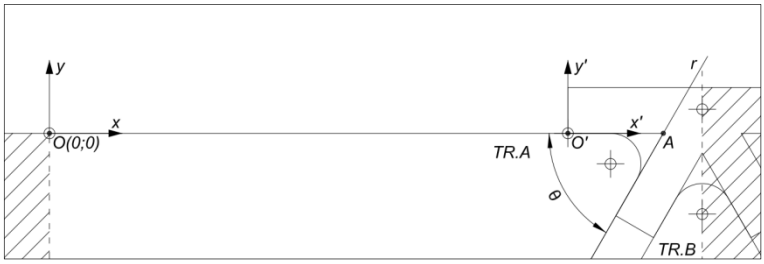

Figure 7.11 Position of point ***A*** and the straight line ***r*** passing through point ***A***.

The following symbols are defined:

$$\rho'_A = \sqrt{{x'_A}^2 + {y'_A}^2} = a_{joint} \tag{7.1}$$

$$\beta'_A = tan^{-1}\left(\frac{y'_A}{x'_A}\right) = 0° \tag{7.2}$$

The moment generates a rotation $\boldsymbol{\alpha}$ of the top joint about the point ***O'(x₀'; y₀')***. This rotation causes a motion of point ***A*** to a new position named ***A₁*** and a motion of the inclined edge of the lateral slot from ***r*** to ***r₁***, *Figure 7.12*. *Table 7.3* gives the coordinates of point ***A₁*** and the equation of the straight line ***r₁*** with reference to the secondary cartesian system ***O'(x₀'; y₀')***.

Point	x'	y'
A₁	$x'_{A_1}(\alpha) = \rho'_A \cdot cos(\beta'_A + \alpha)$	$y'_{A_1}(\alpha) = \rho'_A \cdot sin(\beta'_A + \alpha)$

Straight line	$y' = f(x', \alpha)$
r₁	$y'_{r_1}(x', \alpha) = x' \cdot tan(\theta + \alpha) + \left[y'_{A_1}(\alpha) - x'_{A_1}(\alpha) \cdot tan(\theta + \alpha)\right]$

Table 7.3 Coordinates of point ***A₁*** and equation of the straight line ***r₁*** in the secondary cartesian system ***O'(x₀'; y₀')***.

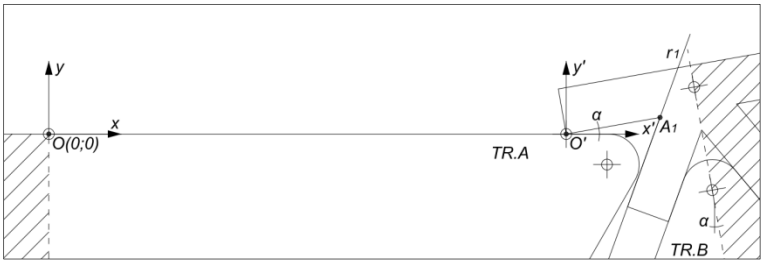

Figure 7.12 Position of the point A_1 and of the straight line r_1 passing through the point A_1.

In order to describe the effects of pure bending on the bottom joint, it is necessary to define the position of point **Q**, which is the centre of the circle defining the bottom round corner of the triangular panel ***TR.B***, *Figure 7.13*. Point **Q** coordinates in the secondary cartesian system ***O'***$(x_{0'}; y_{0'})$ are given in *Table 7.4*.

Point	x'	y'
Q	$x'_Q = \frac{L_{joint}}{2} - \frac{a_{glass}}{2}$	$y'_Q = 2 \cdot b_{joint} + r_{glass} - p \cdot sin(\theta)$

Table 7.4 Point **Q** coordinates in the secondary cartesian system ***O'***$(x_{0'}; y_{0'})$.

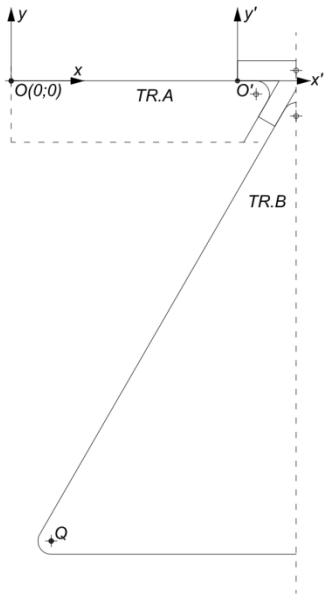

Figure 7.13 Position of point **Q**.

The following symbols are defined:

$$\rho'_Q = \sqrt{{x'_Q}^2 + {y'_Q}^2} = \sqrt{\left(\frac{L_{joint}}{2} - \frac{a_{glass}}{2}\right)^2 + \left(2 \cdot b_{joint} + r_{glass} - p \cdot sin(\theta)\right)^2} \tag{7.3}$$

$$\beta'_Q = tan^{-1}\left(\frac{y'_Q}{x'_Q}\right) = tan^{-1}\left(\frac{4 \cdot b_{joint} + 2 \cdot r_{glass} - 2 \cdot p \cdot sin(\theta)}{L_{joint} - a_{glass}}\right) \tag{7.4}$$

These enable us to write the coordinates of point **Q** in the secondary cartesian system ***O'***$(x_{0'}; y_{0'})$, as given in *Table 7.5*.

Point	x'	y'
Q	$x'_Q = -\rho'_Q \cdot cos(\beta'_Q)$	$y'_Q = -\rho'_Q \cdot sin(\beta'_Q)$

Table 7.5 Coordinates of point **Q** in the secondary cartesian system **O'**($x_{0'}$; $y_{0'}$).

The rotation α of the top joint and the triangular panel ***TR.B*** about the point ***O'***($x_{0'}$; $y_{0'}$) moves point **Q** to the position $\boldsymbol{Q_1}$, *Figure 7.14*. The coordinates of point $\boldsymbol{Q_1}$ in the secondary cartesian system ***O'***($x_{0'}$; $y_{0'}$) are given in *Table 7.6*.

Point	x'	y'
$\boldsymbol{Q_1}$	$x'_{Q_1}(\alpha) = -\rho'_Q \cdot cos(\beta'_Q + \alpha)$	$y'_{Q_1}(\alpha) = -\rho'_Q \cdot sin(\beta'_Q + \alpha)$

Table 7.6 Coordinates of point $\boldsymbol{Q_1}$ in the secondary cartesian system ***O'***($x_{0'}$; $y_{0'}$).

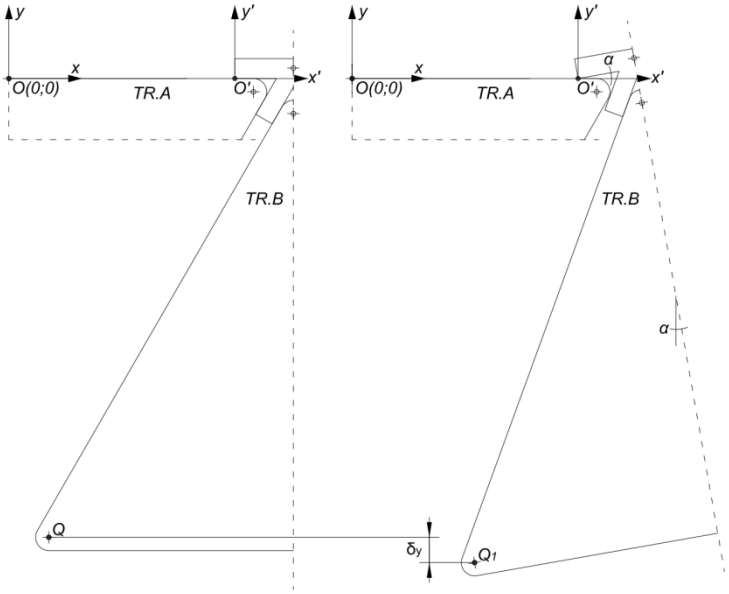

Figure 7.14 Motion of the top joint and the triangular panel ***TR.B*** generated by the rotation α and position of point $\boldsymbol{Q_1}$.

The rotation α causes a motion of point **Q** to position $\boldsymbol{Q_1}$. The y-component of this motion is:

$$\delta_y(\alpha) = y'_{Q_1}(\alpha) - y'_Q = \rho'_Q \cdot \left[sin(\beta'_Q) - sin(\beta'_Q + \alpha)\right] \tag{7.5}$$

$$\delta_y(\alpha) = \left[\sqrt{\left(\frac{L_{joint}}{2} - \frac{a_{glass}}{2}\right)^2 + \left(2 \cdot b_{joint} + r_{glass} - p \cdot sin(\theta)\right)^2}\right] \cdot \left[sin(\beta'_Q) - sin(\beta'_Q + \alpha)\right] \tag{7.6}$$

The rotation α generates the detachment of the inclined edge of the top joint from the inclined edge of the triangular segment ***TR.A***. The joint is in contact with the triangular segment at point ***0'***, *Figure 7.12*.

At this point it would be necessary to introduce the following points and the following line, *Figure 7.15*:

- point ***C***, centre of the circle defining the top corner of the triangular panel ***TR.A***
- point ***D***, endpoint of the lateral straight edge of the triangular panel ***TR.A***
- tangent line ***t*** to point ***D***

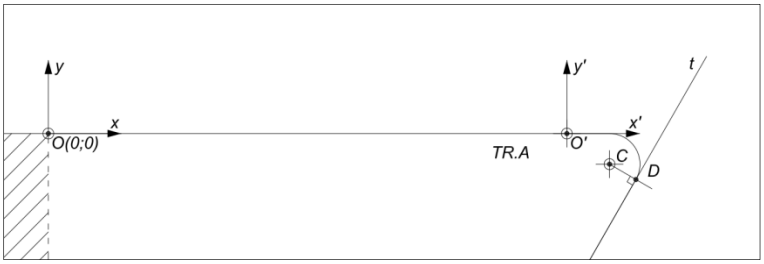

Figure 7.15 Position of point ***C***, point ***D*** and tangent line ***t***.

Table 7.7 gives the coordinates of point ***C***, point ***D*** and the equation of the tangent line ***t*** with reference to the cartesian system ***O****(0; 0).*

Point	x	y
C	$x_C = \frac{a_{glass}}{2}$	$y_C = -r_{glass}$
D	$x_D = x_C + r_{glass} \cdot cos\left(\frac{\theta}{2}\right)$	$y_D = y_C - r_{glass} \cdot sin\left(\frac{\theta}{2}\right)$

Straight line	$y = f(x)$
t	$y_t(x) = x \cdot tan(\theta) + [y_D - x_D \cdot tan(\theta)]$

Table 7.7 Coordinates of point ***C***, point ***D*** and equation of the straight line ***t*** in the cartesian system ***O****(0; 0)*.

The rotation α of point ***D*** about point ***C*** causes a motion of point ***D*** to a new position ***D₁***, and the tangent line moves from ***t*** to ***t₁***, *Figure 7.16*. *Table 7.8* gives the coordinates of point ***D₁*** and the equation of the tangent ***t₁*** in the cartesian system ***O****(0; 0).*

Point	x	y
D₁	$x_{D_1}(\alpha) = x_C + r_{glass} \cdot cos\left(\frac{\theta}{2} - \alpha\right)$	$y_{D_1}(\alpha) = y_C - r_{glass} \cdot sin\left(\frac{\theta}{2} - \alpha\right)$

Straight line	$y = f(x, \alpha)$
t₁	$y_{t_1}(x, \alpha) = x \cdot tan(\theta + \alpha) + \left[y_{D_1}(\alpha) - x_{D_1}(\alpha) \cdot tan(\theta + \alpha)\right]$

Table 7.8 Coordinates of point ***D₁*** and equation of the straight line ***t₁*** in the cartesian system ***O****(0; 0)*.

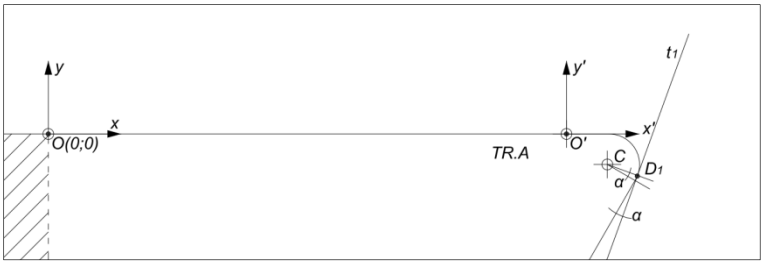

Figure 7.16 Position of point ***D₁*** and tangent line ***t₁***.

Figure 7.17 shows that the line ***t₁*** and the line ***r₁*** are parallel but not coincident. A translation of the top joint and the triangular panel ***TR.B*** along the x-axis moves the line ***t₁*** to coincide with the line ***r₁***. The motion along the x-axis is:

$$\delta_x(\alpha) = x_{D_1}(\alpha) - \left[x_{0'} + x'_{A_1}(\alpha)\right] + \frac{\left[y_{0'} + y'_{A_1}(\alpha)\right] - y_{D_1}(\alpha)}{tan(\theta + \alpha)} \tag{7.7}$$

$$\delta_x(\alpha) = \frac{a_{glass}}{2} - \frac{p}{2} + \frac{L_{joint}}{2} + r_{glass} \cdot cos\left(\frac{\theta}{2} - \alpha\right) - a_{joint} \cdot cos(\alpha) + \frac{a_{joint} \cdot sin(\alpha) + r_{glass} \cdot \left[1 + sin\left(\frac{\theta}{2} - \alpha\right)\right]}{tan(\theta + \alpha)} \tag{7.8}$$

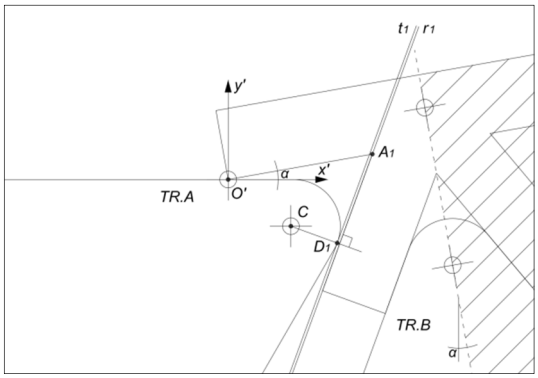

Figure 7.17 Motion of the top joint, position of the point D_1 and the tangent line t_1.

The secondary cartesian system $O'(x_{0'}; y_{0'})$ moves to a new position $O''(x_{0''}; y_{0''})$. Its coordinates referring to the cartesian system $O(0; 0)$ are given in *Table 7.9*.

Point	x	y
$0''$	$x_{0''}(\alpha) = x_{0'} + \delta_x(\alpha) = \frac{p}{2} - \frac{L_{joint}}{2} + \delta_x(\alpha)$	$y_{0''}(\alpha) = y_{0'} = 0$

Table 7.9 Coordinates of the origin of the secondary cartesian system $O''(x_{0''}; y_{0''})$ after the translation.

The top joint is in contact with the triangular panel ***TR.A***; there are two contact points, point ***O''*** and point D_1, *Figure 7.18*.

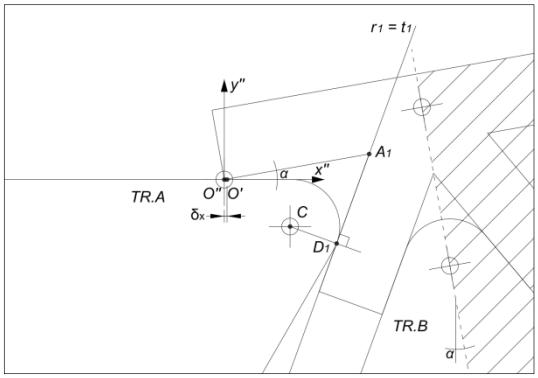

Figure 7.18 Contact points between the top joint and the triangular panel ***TR.A***.

Starting from the values of the displacements $\delta_x(\alpha)$ and $\delta_y(\alpha)$, it is possible to calculate the position of all points of the top joint, of the bottom joint and of the triangular panel ***TR.B*** generated by pure bending. It is necessary to introduce the following points, *Figure 7.19*:

- point ***M***, centre point of the top joint
- point ***N***, centre point of the bottom joint
- point ***R***, connection point of the diagonal steel bar to the top joint

- point ***S***, connection point of the diagonal steel bar to the bottom joint
- point ***P***, point of the edge of the triangular panel ***TR.B*** having same y-coordinate as point ***Q*** (contact point between the bottom corner of the panel ***TR.B*** and the longitudinal edge of the lateral slot of the bottom joint)

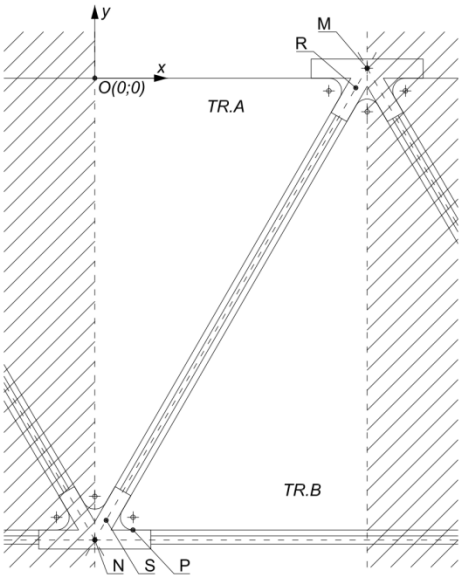

Figure 7.19 Position of points ***M***, ***N***, ***R***, ***S*** and ***P***.

Table 7.10 lists the coordinates of points ***M***, ***R*** and ***P*** referring to the secondary cartesian system ***O'(x$_{0'}$; y$_{0'}$)***.

Point	x'	y'
M	$x'_M = \frac{L_{joint}}{2}$	$y'_M = b_{joint}$
P	$x'_P = x'_Q$	$y'_P = y'_Q - r_{glass}$
R	$x'_R = \frac{L_{joint}}{2} - c_{joint} \cdot cos(\theta)$	$y'_R = b_{joint} - c_{joint} \cdot sin(\theta)$

Table 7.10 Coordinates of point ***M***, ***P*** and ***R*** in the secondary cartesian system ***O'(x$_{0'}$; y$_{0'}$)***.

The following symbols are defined:

$$\rho'_M = \sqrt{{x'_M}^2 + {y'_M}^2} = \sqrt{\left(\frac{L_{joint}}{2}\right)^2 + \left(b_{joint}\right)^2} \tag{7.9}$$

$$\beta'_M = tan^{-1}\left(\frac{y'_M}{x'_M}\right) = tan^{-1}\left(\frac{2 \cdot b_{joint}}{L_{joint}}\right) \tag{7.10}$$

$$\rho'_R = \sqrt{{x'_R}^2 + {y'_R}^2} = \sqrt{\left[\frac{L_{joint}}{2} - c_{joint} \cdot cos(\theta)\right]^2 + \left[b_{joint} - c_{joint} \cdot sin(\theta)\right]^2} \tag{7.11}$$

$$\beta'_R = tan^{-1}\left(\frac{y'_R}{x'_R}\right) = tan^{-1}\left(\frac{b_{joint} - c_{joint} \cdot sin(\theta)}{\frac{L_{joint}}{2} - c_{joint} \cdot cos(\theta)}\right) \tag{7.12}$$

Table 7.11 gives the coordinates of points ***M***, ***N***, ***P***, ***R***, ***S*** referring to cartesian system ***O****(0; 0)*.

Point	x	y
M	$x_M = x_{0'} + \rho'_M \cdot cos(\beta'_M)$	$y_M = y_{0'} + \rho'_M \cdot sin(\beta'_M)$
N	$x_N = 0$	$y_N = b_{joint} - p \cdot sin(\theta)$
P	$x_P = x_{0'} + x'_Q$	$y_P = y_{0'} + y'_Q - r_{glass}$
R	$x_R = x_{0'} + \rho'_R \cdot cos(\beta'_R)$	$y_R = y_{0'} + \rho'_R \cdot sin(\beta'_R)$
S	$x_S = c_{joint} \cdot cos(\theta)$	$y_S = b_{joint} + (c_{joint} - p) \cdot sin(\theta)$

Table 7.11 Coordinates of the point ***M***, ***N***, ***P, R*** and ***S*** in the cartesian system ***O****(0; 0)*.

The pure bending generates a motion of points ***M***, ***N***, ***P***, ***R***, **S** to the positions ***M(α)***, ***N(α)***, ***P(α)***, **R(α)**, and ***S(α)***, *Figure 7.20*. The coordinates of these points are given in *Table 7.12*.

Point	x	y
M(α)	$x_M(\alpha) = x_{0''}(\alpha) + \rho'_M \cdot cos(\beta'_M + \alpha)$	$y_M(\alpha) = y_{0''}(\alpha) + \rho'_M \cdot sin(\beta'_M + \alpha)$
N(α)	$x_N(\alpha) = x_N$	$y_N(\alpha) = y_N + \delta_y(\alpha)$
P(α)	$x_P(\alpha) = x_{0''}(\alpha) + x'_{Q_1}(\alpha)$	$y_P(\alpha) = y_{0''}(\alpha) + y'_{Q_1}(\alpha) - r_{glass}$
R(α)	$x_R(\alpha) = x_{0''}(\alpha) + \rho'_R \cdot cos(\beta'_R + \alpha)$	$y_R(\alpha) = y_{0''}(\alpha) + \rho'_R \cdot sin(\beta'_R + \alpha)$
S(α)	$x_S(\alpha) = x_S$	$y_S(\alpha) = y_S + \delta_y(\alpha)$

Table 7.12 Coordinates of point ***M(α)***, ***N(α)***, ***P(α)***, ***R(α)***, and ***S(α)*** in the cartesian system ***O****(0; 0)*.

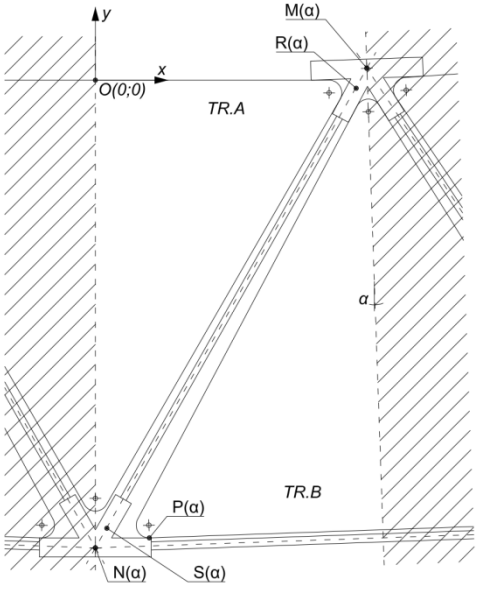

Figure 7.20 Position of points ***M(α)***, ***N(α)***, ***R(α)***, ***S(α)*** and ***P(α)***.

Once the coordinates of the points are known, it is possibile to calculate the elongations of the diagonal and longitudinal steel bars generated by pure bending.

The distance between the centre point of the top joint and the centre point of the bottom joint is, *Figure 7.21*:

$$L_{MN}(\alpha) = \sqrt{[x_M(\alpha) - x_N(\alpha)]^2 + [y_M(\alpha) - y_N(\alpha)]^2} \tag{7.13}$$

The angle formed by line $L_{MN}(\alpha)$ and the y-axis is, *Figure 7.21*:

$$\theta_{MN}(\alpha) = tan^{-1}\left(\frac{x_M(\alpha) - x_N(\alpha)}{y_M(\alpha) - y_N(\alpha)}\right) \tag{7.14}$$

The length of the diagonal steel bar is, *Figure 7.22*:

$$L_{diag}(\alpha) = \sqrt{[x_R(\alpha) - x_S(\alpha)]^2 + [y_R(\alpha) - y_S(\alpha)]^2} \tag{7.15}$$

The angle formed by the axis of the diagonal steel bar $L_{diag}(\alpha)$ and the y-axis is, *Figure 7.22*:

$$\theta_{diag}(\alpha) = tan^{-1}\left(\frac{x_R(\alpha) - x_S(\alpha)}{y_R(\alpha) - y_S(\alpha)}\right) \tag{7.16}$$

The angle formed by the axis of the diagonal steel bar $L_{diag}(\alpha)$ and the x-axis is, *Figure 7.22*:

$$\beta_{diag}(\alpha) = \frac{\pi}{2} - \theta_{diag}(\alpha) \tag{7.17}$$

The angle formed by the axis of the diagonal steel bars $L_{diag}(\alpha)$ connected to the same top joint is, *Figure 7.22*:

$$\gamma_{diag}(\alpha) = 2 \cdot \left[\theta_{diag}(\alpha) + \alpha\right] \tag{7.18}$$

The distance between the centre points of two adjacent bottom joints - length of the longitudinal steel bar is, *Figure 7.22*:

$$L_{long}(\alpha) = 2 \cdot [L_{MN}(\alpha) \cdot sin(\theta_{MN}(\alpha) + \alpha)] \tag{7.19}$$

The angle formed by the axis of the longitudinal steel bar $L_{long}(\alpha)$ and the x-axis is, *Figure 7.22*:

$$\beta_{long}(\alpha) = \alpha \tag{7.20}$$

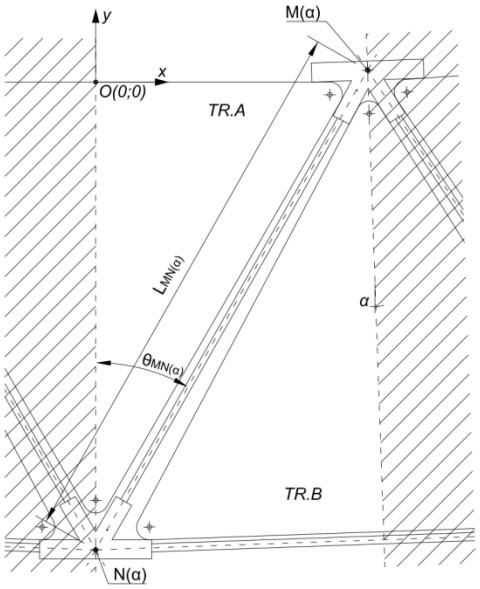

Figure 7.21 Effects of pure bending.

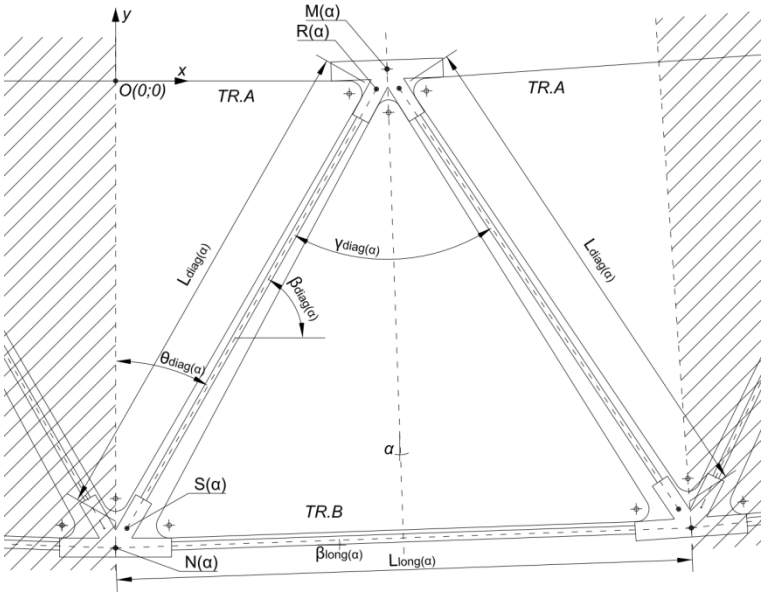

Figure 7.22 Effects of pure bending.

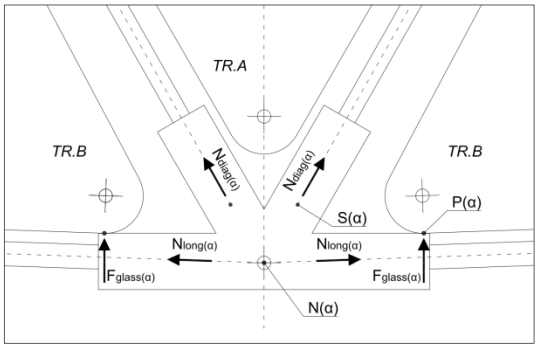

Figure 7.23 Axial forces in diagonal steel bars and in the longitudinal steel bars, and compressive forces in the triangular panel.

The strain $\varepsilon_{diag}(\alpha)$ of the diagonal steel bar generated by bending is calculated with the length $L_{diag}(\alpha)$ of the diagonal steel bar:

$$\varepsilon_{diag}(\alpha) = f\left(L_{diag}(\alpha)\right) = \int \frac{\Delta L_{diag}(\alpha)}{L_{diag}(\alpha)} \tag{7.21}$$

Starting from the strain $\varepsilon_{diag}(\alpha)$ of the diagonal steel bar and by means of the stress – strain curve of the material, the tensile stress is calculated:

$$\sigma(\varepsilon) \rightarrow \sigma\left(\varepsilon_{diag}(\alpha)\right) \rightarrow \sigma_{diag}(\alpha) \tag{7.22}$$

With cross section A_{diag} of the diagonal steel bar, the axial tensile force is calculated, *Figure 7.23*:

$$N_{diag}(\alpha) = A_{diag} \cdot \sigma_{diag}(\alpha) \tag{7.23}$$

The strain $\varepsilon_{long}(\alpha)$ of the longitudinal steel bar generated by bending is calculated with the length $L_{long}(\alpha)$ of the longitudinal steel bar:

$$\varepsilon_{long}(\alpha) = f\left(L_{long}(\alpha)\right) = \int \frac{\Delta L_{long}(\alpha)}{L_{long}(\alpha)} \tag{7.24}$$

Starting from the strain $\varepsilon_{long}(\alpha)$ of the longitudinal steel bar and with the stress – strain curve of the material, the tensile stress is calculated:

$$\sigma(\varepsilon) \rightarrow \sigma\left(\varepsilon_{long}(\alpha)\right) \rightarrow \sigma_{long}(\alpha) \tag{7.25}$$

The axial tensile force is calculated from cross section A_{long} of the longitudinal steel bar, *Figure 7.23*:

$$N_{long}(\alpha) = A_{long} \cdot \sigma_{long}(\alpha) \tag{7.26}$$

The compressive force transferred by contact from the bottom joint to the triangular panel ***TR.B*** is, *Figure 7.23*:

$$F_{glass}(\alpha) = -\left[N_{long}(\alpha) \cdot sin\left(\beta_{long}(\alpha)\right) + N_{diag}(\alpha) \cdot sin\left(\beta_{diag}(\alpha)\right)\right] \tag{7.27}$$

Due to the symmetry, the compressive force $\mathrm{F_{glass}}(\alpha)$ acts parallel to y-axis, *Figure 7.23*.

The compressive force transferred by the top joint to the triangular panel ***TR.B*** is, *Figure 7.24*:

$$F_{glass.top}(\alpha) = 2 \cdot F_{glass}(\alpha) \cdot \cos(\alpha) \tag{7.28}$$

The compressive force $N_{glass}(\alpha)$ at the top edge of the triangular panel ***TR.A*** is parallel to the x-axis, *Figure 7.24*. The compressive force $N_{glass}(\alpha)$ is the resultant of the contact forces transferred from the top joint to the triangular panel ***TR.A***. The contact points are point ***0''*** and point ***D_1***. The action lines of the contact forces are perpendicular to the edges of the triangular panel ***TR.A*** at point ***O''*** and point ***D_1***.

$$N_{glass}(\alpha) = -\left[N_{long}(\alpha) \cdot cos\left(\beta_{long}(\alpha)\right) + N_{diag}(\alpha) \cdot cos\left(\beta_{diag}(\alpha)\right)\right] \tag{7.29}$$

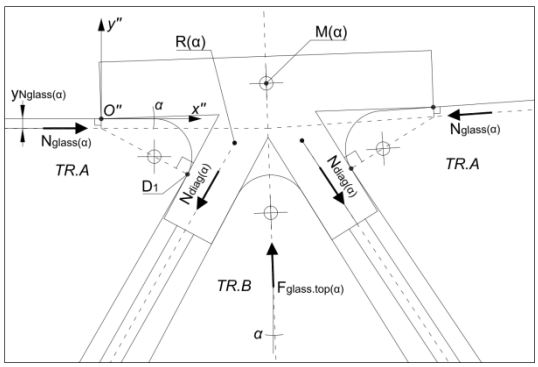

Figure 7.24 Forces transferred by the top joint.

The compressive force $N_{glass}(\alpha)$ is calculated by summing the two contact forces; the action line of the compressive force $N_{glass}(\alpha)$ is parallel to the x-axis and passes through the intersection of the action lines of the contact forces.

The equation of the action line of the contact force through point ***O''*** - the y-coordinate of the secondary cartesian system ***O''****($x_{0''}$; $y_{0''}$)* - in the cartesian system ***0****(x; y)* is, *Figure 7.24*:

$$x = x_{0''}(\alpha) = x_{0'} + \delta_x(\alpha) = \frac{p}{2} - \frac{L_{joint}}{2} + \delta_x(\alpha) \tag{7.30}$$

The equation of the action line of the contact force through point ***D_1*** in the cartesian system ***O****(0; 0)* is, *Figure 7.24*:

$$y_{s_1}(x, \alpha) = x \cdot tan\left(\frac{\pi}{2} + \theta + \alpha\right) + \left[y_{D_1}(\alpha) - x_{D_1}(\alpha) \cdot tan\left(\frac{\pi}{2} + \theta + \alpha\right)\right] \tag{7.31}$$

The equation of the action line of the compressive force $N_{glass}(\alpha)$ in the cartesian system ***O****(0; 0)* is, *Figure 7.24*:

$$y_{N_{glass}}(\alpha) = x_{0''}(\alpha) \cdot tan\left(\frac{\pi}{2} + \theta + \alpha\right) + \left[y_{D_1}(\alpha) - x_{D_1}(\alpha) \cdot tan\left(\frac{\pi}{2} + \theta + \alpha\right)\right] \tag{7.32}$$

The internal bending moment $M(\alpha)$ generated by pure bending - the rotation α of the section - is:

$$M(\alpha) = -N_{long}(\alpha) \cdot cos\left(\beta_{long}(\alpha)\right) \cdot \left(y_N(\alpha) - y_{N_{glass}}(\alpha)\right) + F_{glass}(\alpha) \cdot x_P(\alpha) + N_{diag}(\alpha) \cdot \\ \cdot \left[-\left(y_R(\alpha) - y_{N_{glass}}(\alpha)\right) \cdot cos\left(\beta_{diag}(\alpha)\right) + x_R(\alpha) \cdot sin\left(\beta_{diag}(\alpha)\right)\right] \tag{7.33}$$

The curvature $\chi(\alpha)$ is:

$$\chi(\alpha) = \frac{1}{\sqrt{\left(\frac{p}{2}\right)^2 \left\{\cdot \left[tan\left(\frac{\pi}{2} + \alpha\right)\right]^2 + 1\right\}}} \tag{7.34}$$

Furthermore, the relationship moment – curvature $[M(\alpha) - \chi(\alpha)]$ is calculated:

$$M(\alpha) - \chi(\alpha) \tag{7.35}$$

Thanks to these equations, the axial tensile forces in the longitudinal steel bars, the axial tensile forces in the diagonal steel bars, the compressive forces in the triangular segments and the bending moment generated by the pure bending can be calculated easily.

Furthermore, with the relationship moment – curvature $[M(\alpha) - \chi(\alpha)]$ it is possible to calculate the vertical displacement of every section of the beam. After determining the bending moment generated by the applied loads $M(Loads, x)$ it is easy to calculate the corresponding curvature $\chi(Loads, x)$ and then the vertical displacement of the sections of the beam generated by the loads. The vertical displacement is calculated with the "*principle of virtual work*".

In the following paragraphs, the analytical model is implemented in order to calculate the internal forces in the prototype generated by the self-weight of the beam, the permanent load and the test load. Furthermore, the vertical displacements of the two bottom central steel joints are calculated.

There are two important differences between the prototype and the theoretical model. The first is that in the prototype there is a top glass flange and two top longitudinal steel bars, whereas in the theoretical model they have been neglected; this means that the position of the compressive force $N_{glass}(\alpha)$ in the top edge of the beam generated by the bending in the prototype is different to the one obtained by the theoretical model. The second difference is that, in the theoretical model, the bottom longitudinal steel bars are rigidly fixed to the steel joints but in the prototype there is a raw friction connection between the bars and the joints (see *paragraph 3.3.4* and *paragraph 5.3*).

The exact position of the action line of the compressive force $N_{glass}(\alpha)$ in the top edge of the beam depends on the stiffness of the rectangular glass panel, the stiffness of the top edge of the triangular glass panel and the axial stiffness of the longitudinal steel bar. The presence of the rectangular glass panel and the presence of the top longitudinal steel bar moves up the action line of the compressive force $N_{glass}(\alpha)$ that acts between the eq. *(7.32)* and the midplane of the rectangular glass panel. Because $y_N(\alpha) - y_{N_{glass}}(\alpha) \cong y_N(\alpha)$ and $y_R(\alpha) - y_{N_{glass}}(\alpha) \cong y_N(\alpha)$ the bending moment calculated with eq. *(7.33)* is not really influenced by the exact position $y_N(\alpha)$ of the compressive force $N_{glass}(\alpha)$. For this reason, in the following paragraphs the fomula *(7.32)* will be used to calculate the position of the compressive force $N_{glass}(\alpha)$ in the top edge of the beam.

7.3 Analytical modelling of the structural response of the prototype

The analytical model has been implemented in order to calculate the axial forces in the bottom longitudinal steel bars of the 12 m prototype and the vertical displacements of two bottom central steel joints, *Figure 7.25* and *Figure 7.26*.

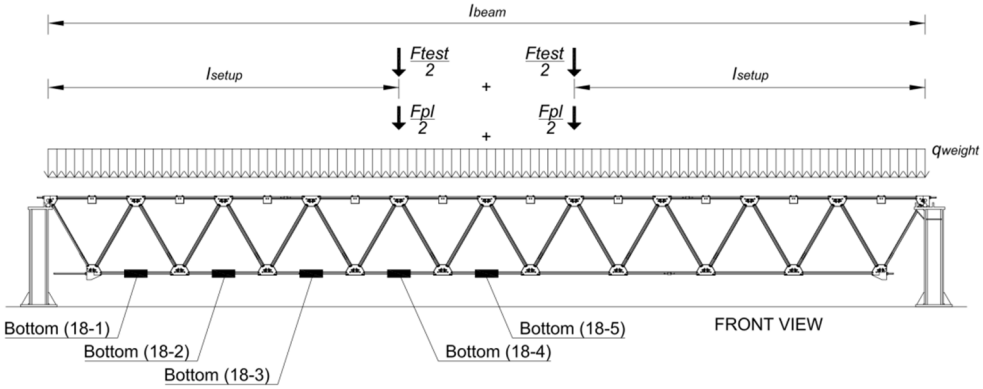

Figure 7.25 Analytical model: actions and names of the steel bars.

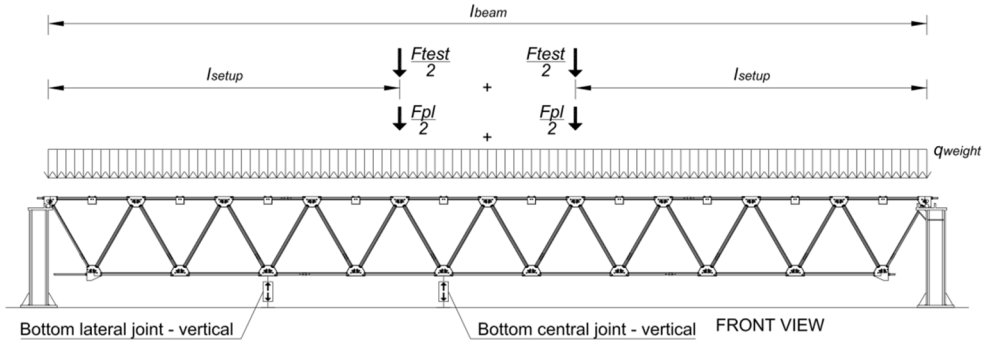

Figure 7.26 Analytical model: actions and names of the bottom steel joints.

The values and the order of load applications have been introduced to simulate the 2nd four point bending test (see *paragraph 5.4.2*). *Table 7.13* lists the values and the order of load applications.

N.	Action	Description		Value [kN]
1	Self-weight	dead load of the beam	uniformly distributed load	$F_{weight} = 18.0kN$
2	Permanent load	weight of the hydraulic jacks and the equipment	concentrated loads / beam under four point bending	$F_{pl} = 4.0kN$
3	Test load	monotonically increasing test load	concentrated loads / beam under four point bending	F_{test}

Table 7.13 Analytical model: values and load application order.

The self-weight of the prototype is 18.0 kN and acts as a uniformly distributed load, *Figure 7.27*.

$$q_{weight} = \frac{F_{weight}}{l_{beam}} = \frac{18.0kN}{12m} = 1.50\frac{kN}{m} \tag{7.36}$$

The bending moment is, *Figure 7.27*:

$$M_{weight}(x) = \frac{1}{2} \cdot q_{weight} \cdot x \cdot (l_{beam} - x) \tag{7.37}$$

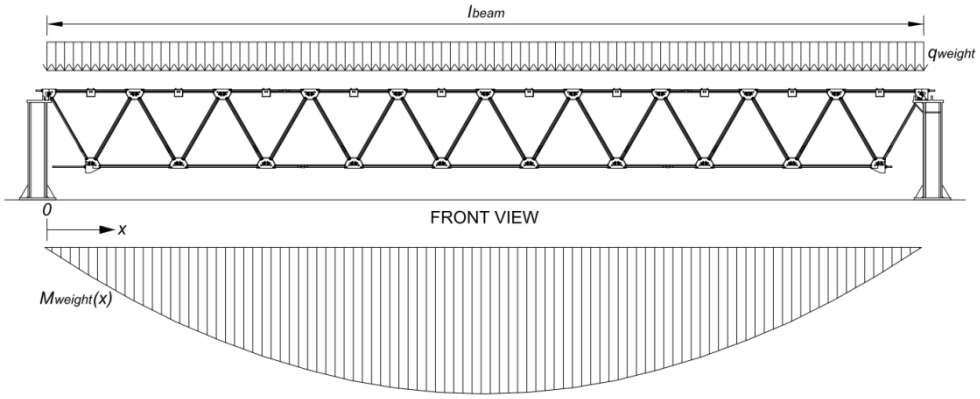

Figure 7.27 Analytical model: bending moment generated by the self weight of the beam.

The weight of test equipment – the permanent load – $F_{pl} = 4.0kN$ acts symmetrically on two couples of top steel joints, which are 4800 mm away (l_{setup}) from the beam supports, *Figure 7.28*. The bending moment is:

$$M_{pl}(x) = \begin{cases} \frac{F_{pl}}{2} \cdot x & x \le l_{setup} \\ \frac{F_{pl}}{2} \cdot l_{setup} & l_{setup} < x \le (l_{beam} - l_{setup}) \\ \frac{F_{pl}}{2} \cdot (l_{beam} - x) & (l_{beam} - l_{setup}) < x \le l_{beam} \end{cases} \tag{7.38}$$

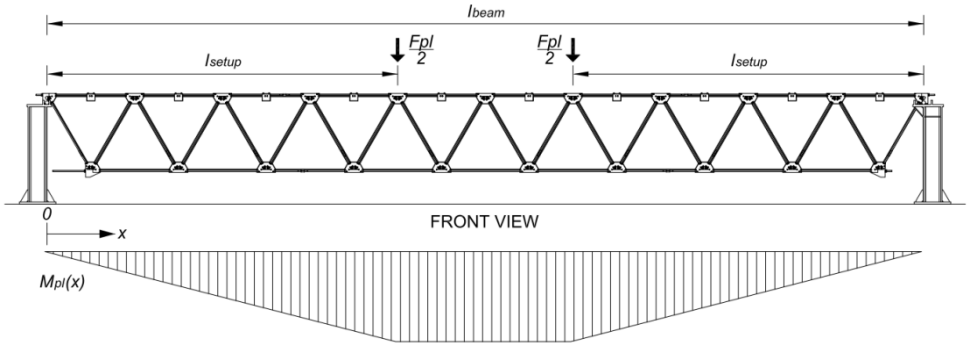

Figure 7.28 Analytical model: bending moment generated by the permanent load – weight of the equipment.

The test load is applied symmetrically to the two couples of the top steel joints at a distance l_{setup} from the beam supports, *Figure 7.29*. The bending moment is:

$$M_{test}(F_{test}, x) = \begin{cases} \frac{F_{test}}{2} \cdot x & x \le l_{setup} \\ \frac{F_{test}}{2} \cdot l_{setup} & l_{setup} < x \le (l_{beam} - l_{setup}) \\ \frac{F_{test}}{2} \cdot (l_{beam} - x) & (l_{beam} - l_{setup}) < x \le l_{beam} \end{cases} \tag{7.39}$$

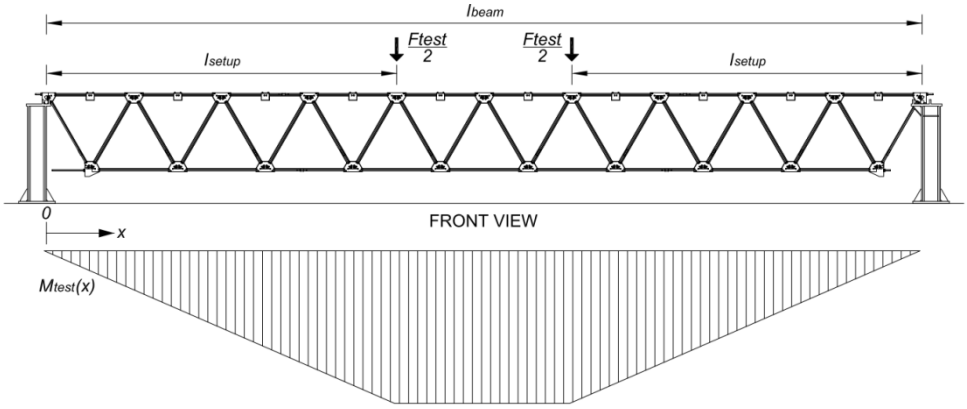

Figure 7.29 Analytical model: bending moment generated by the test load.

The bending moment in the prototype is the sum of the bending moment generated by the self-weight of the prototype, the weight of the equipment and, finally, by the test load, *Figure 7.30*:

$$M(F_{test}, x) = M_{weight}(x) + M_{pl}(x) + M_{test}(F_{test}, x) \tag{7.40}$$

$$M(F_{test}, x) = \begin{cases} \frac{1}{2} \cdot q_{weight} \cdot x \cdot (l_{beam} - x) + \left(\frac{F_{pl}}{2} + \frac{F_{test}}{2}\right) \cdot x & x \le l_{setup} \\ \frac{1}{2} \cdot q_{weight} \cdot x \cdot (l_{beam} - x) + \left(\frac{F_{pl}}{2} + \frac{F_{test}}{2}\right) \cdot l_{setup} & l_{setup} < x \le \left(l_{beam} - l_{setup}\right) \\ \frac{1}{2} \cdot q_{weight} \cdot x \cdot (l_{beam} - x) + \left(\frac{F_{pl}}{2} + \frac{F_{test}}{2}\right) \cdot (l_{beam} - x) & \left(l_{beam} - l_{setup}\right) < x \le l_{beam} \end{cases} \tag{7.41}$$

with

$l_{beam} = 12000\ mm$

$l_{setup} = 4800\ mm$

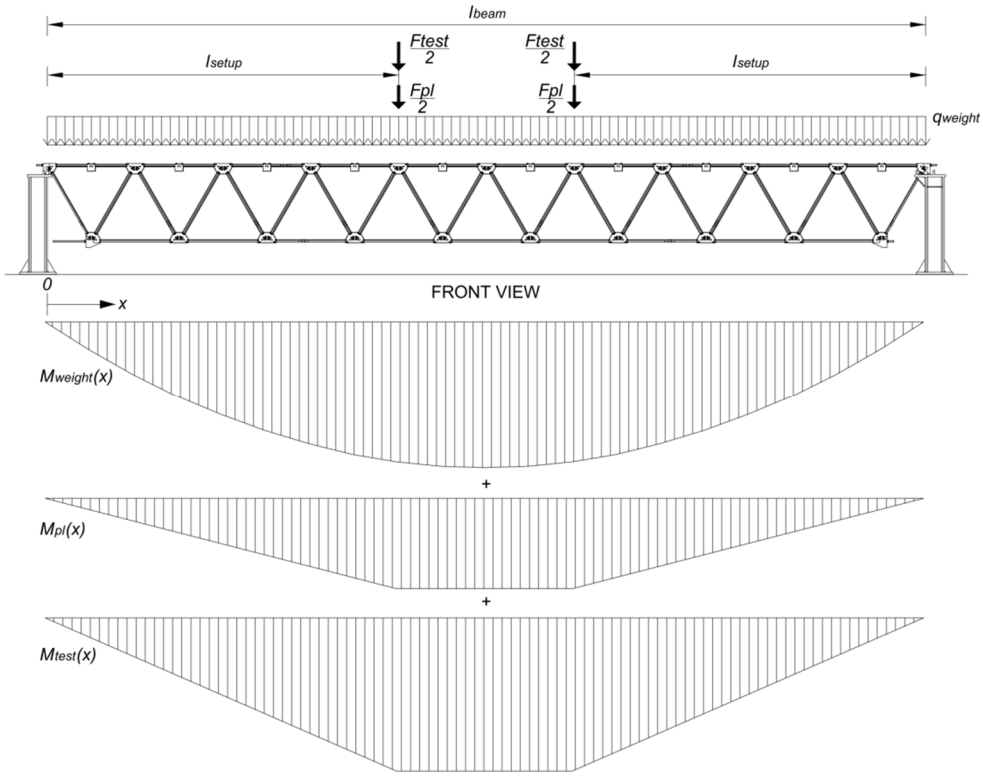

Figure 7.30 Analytical model: bending moment.

In order to calculate the internal forces in the bottom longitudinal steel bars and the vertical displacements of the two bottom steel joints generated by the loads acting upon the beam with the formulas illustrated in *paragraph 7.2* it is necessary to define the effective dimensions of the central steel joints, the steel bars, the triangular glass panels and the stress – strain curves of the steel bars (*Figure 7.31*).

$L_{joint} = 247.00\ mm$ longitudinal length of the joint

$a_{joint} = 87.70\ mm$ length of the longitudinal edge of the lateral slot of the joint

$b_{joint} = 22.00\ mm$ distance of the longitudinal edge of the lateral slot from the centre point ot the joint

$c_{joint} = 50.01\ mm$ distance of the hex nuts of the diagonal steel bars from the centre point of the joint

$\theta = 60°$ internal angle formed by the edges of the slots of the joint – internal angle formed by the edges of the panels

$L_{glass} = 1128.41\ mm$ length of the edges of the triangular panels before processing the corners

$r_{glass} = 28.00\ mm$ radius of the round corners of the triangular panels

$A_{long} = 254.469\ mm^2$ cross section of the longitudinal steel bars (diameter of 18 mm)

$A_{diag} = 153.938\ mm^2$ cross section of the diagonal steel bars (diameter of 14 mm)

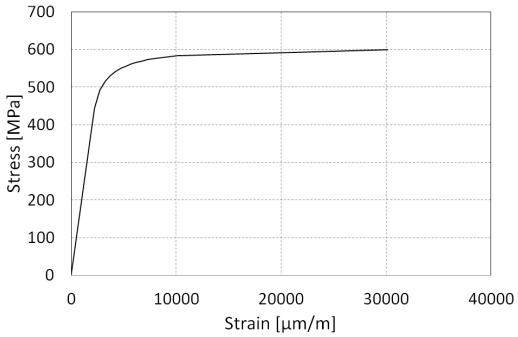

(a) Engineering stress – strain curve (18 mm steel bar) – longitudinal steel bars.

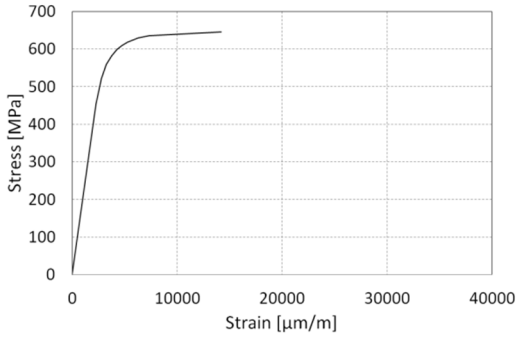

(b) Engineering stress – strain curve (16 mm steel bar) – diagonal steel bars.

Figure 7.31 Engineering stress – strain curves (18 mm and 16 mm steel bars).

The axial forces in the bottom longitudinal steel bars generated by the loads have been calculated for two cases, *Table 7.14*.

Analysis	Name	Description
1	AN - Fix	the longitudinal steel bars are rigidly connected to the central steel joints
2	AN - Fr	the friction between the longitudinal steel bars and the central steel joints has been modelled

Table 7.14 Analytical model: analyses.

The analysis **AN-Fix** allows a validation of the analytical model by comparing it with the numerical analysis **PVBa-Fix**.

The analysis **AN-Fr** allows a validation of the analytical model by comparing it with the other numerical analyses and with the experimental results.

7.3.1 The first analysis

In the analysis named **AN-Fix**, the longitudinal steel bars are considered to be rigidly connected to the central steel joints.

Table 7.15 gives the x-coordinate of the cross-section of the beam, where the bending moment is calculated, as well as the names of the corresponding bottom longitudinal steel bars. *Figure 7.32* shows the position of the cross-sections and the names of the bottom longitudinal steel bars.

Cross-section	X-coordinate [mm]	Name	Bending moment [kN·m]
1-1	$x_1 = 1200$	Bottom (18-1)	$M_1(F_{test}) = M(F_{test}, x_1) = 12.20kN \cdot m + (F_{test} \cdot 0.6m)$
2-2	$x_2 = 2400$	Bottom (18-2)	$M_2(F_{test}) = M(F_{test}, x_2) = 22.08kN \cdot m + (F_{test} \cdot 1.2m)$
3-3	$x_3 = 3600$	Bottom (18-3)	$M_3(F_{test}) = M(F_{test}, x_3) = 29.88kN \cdot m + (F_{test} \cdot 1.8m)$
4-4	$x_4 = 4800$	Bottom (18-4)	$M_4(F_{test}) = M(F_{test}, x_4) = 35.52kN \cdot m + (F_{test} \cdot 2.4m)$
5-5	$x_5 = 6000$	Bottom (18-5)	$M_5(F_{test}) = M(F_{test}, x_5) = 36.60kN \cdot m + (F_{test} \cdot 2.4m)$

Table 7.15 Analytical model: coordinates of the cross-sections.

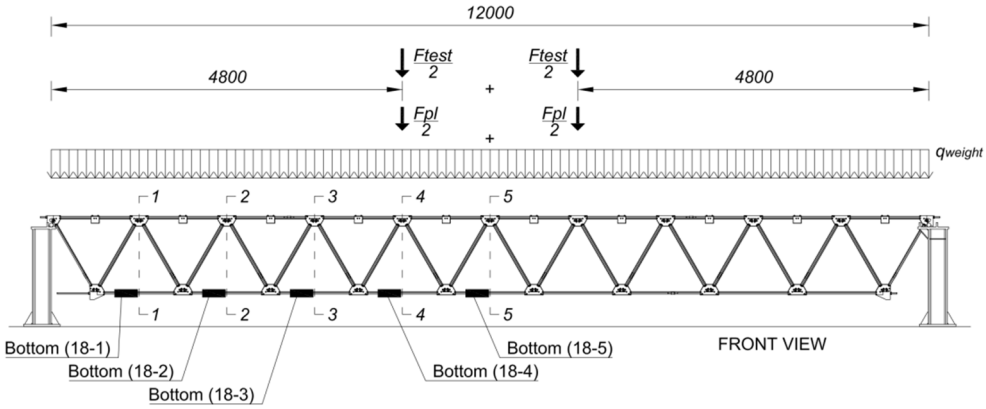

Figure 7.32 Analytical model: positions of the cross-sections.

The bending moment $M(F_{test}, x)$ depends on one parameter, the value of the test load F_{test}. By making $M(F_{test}, x)$ equal to the bending moment $M(\alpha)$ calculated in *paragraph 7.2*, the correlation between the test load F_{test} and the rotation α is found. Once the correlation between the test load F_{test} and the rotation α is known, the axial forces in the bottom longitudinal steel bars are then calculated. The following list describes the steps:

Step 1 With the equations illustrated in *paragraph 7.2* the relationship $M(\alpha)$ is calculated

Step 2 By making $M(F_{test}, x)$ equal to $M(\alpha)$ the relation between the test load F_{test} and the rotation α is calculated in each section 1-1, 2-2, 3-3, 4-4 and 5-5. The rotation α can be written as a function of the test load F_{test} in each section 1-1, 2-2, 3-3, 4-4 and 5-5: $\alpha = f(F_{test})$

Step 3 Now that we know the relationship $\alpha = f(F_{test})$, the axial forces in each bottom longitudinal steel bar are calculated as a function of the test load $N_{Long}(F_{test})$

In section 1-1, the axial force in the steel bar ***Bottom (18-1)*** is $\mathrm{N}_{\mathrm{B}\,(18-1)}(F_{test})$.

In section 2-2, the axial force in the steel bar ***Bottom (18-2)*** is $\mathrm{N}_{\mathrm{B}\,(18-2)}(F_{test})$.

In section 3-3, the axial force in the steel bar ***Bottom (18-3)*** is $\mathrm{N}_{\mathrm{B}\,(18-3)}(F_{test})$.

In section 4-4, the axial force in the steel bar ***Bottom (18-4)*** is $\mathrm{N}_{\mathrm{B}\,(18-4)}(F_{test})$.

In section 5-5, the axial force in the steel bar ***Bottom (18-5)*** is $\mathrm{N}_{\mathrm{B}\,(18-5)}(F_{test})$

The maximum value of the test load $F_{test.ult}$ is reached when the ultimate tensile strength is reached in the steel bar ***Bottom (18-5)***, $\mathrm{N}_{\mathrm{B}\,(18-5)}(F_{test.ult}) = A_{long} \cdot \sigma_r = 254.469\ mm^2 \cdot 599.76\ MPa = 152.62\ kN$.

$\sigma_r = 599.76\ MPa$ is the ultimate tensile stress of the engineering stress-strain curve of the 18 mm steel bar, see *paragraph 5.2.1*.

Figure 7.33 shows the positions and the names of the bottom central steel joints where the vertical displacements are calculated.

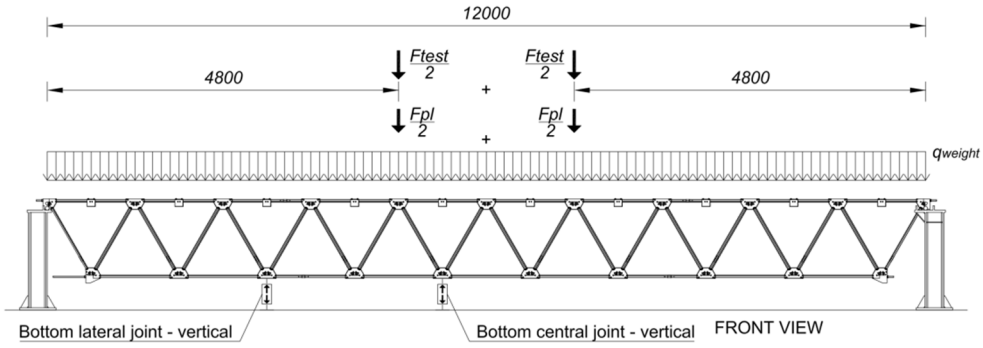

Figure 7.33 Analytical model: names of the two bottom central steel joints.

The vertical displacements of the two joints are calculated applying the "*principle of virtual work*":

$$External\ work = Internal\ work$$

Figure 7.34 and *Figure 7.35* show the point where the virtual vertical force ($F_V = 1\ kN$) is applied and the moment caused by virtual vertical force ($M_V(x)$).

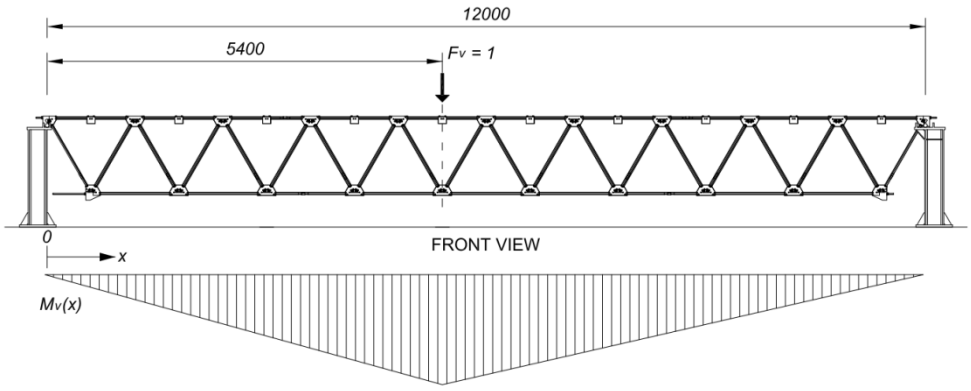

Figure 7.34 Analytical model: point of application of virtual force – central steel joint (principle of virtual work).

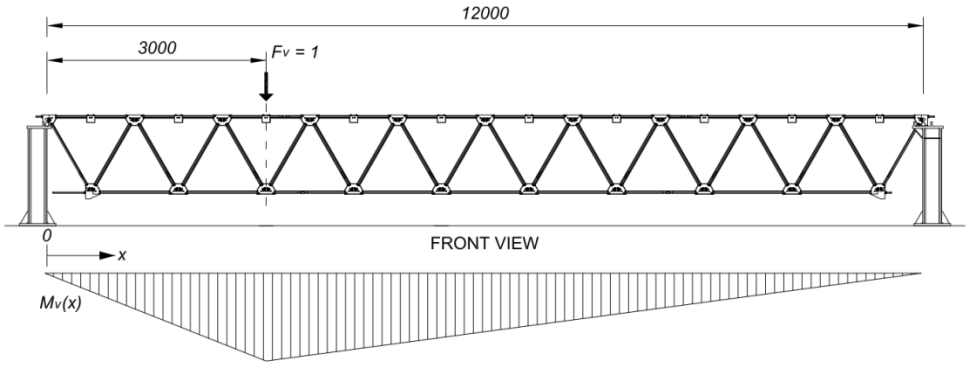

Figure 7.35 Analytical model: point of application of virtual force – lateral steel joint (principle of virtual work).

The displacement of the point of application of the virtual force is given by:

$$F_V \cdot \delta_{vert}(F_{test}) = \int_{l_{beam}}^{0mm} M_V(x) \cdot \chi(F_{test}, x) dx \tag{7.42}$$

$$\delta_{vert}(F_{test}) = \frac{1}{F_V} \cdot \int_{l_{beam}}^{0mm} M_V(x) \cdot \chi(F_{test}, x) dx \tag{7.43}$$

where $\chi(F_{test}, x)$ is the curvature in every section of the beam generated by the self-weight of the prototype, by the weight of the equipment and finally by the test load. The curvature $\chi(F_{test}, x)$ depends on the moment - eq. *(7.41)* - and the relationship moment – curvature $[M - \chi]$, eq. *(7.35)*. *Figure 7.36* shows the diagram moment – curvature $[M(F_{test}) - \chi(F_{test})]$.

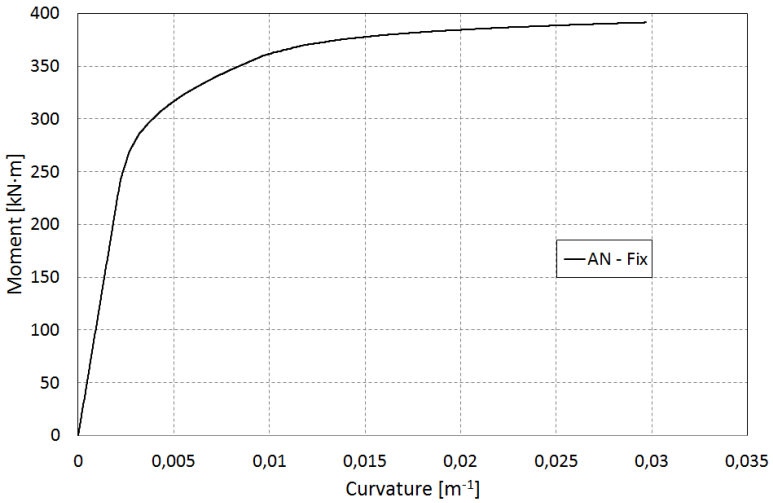

Figure 7.36 Analytical model: diagram moment – curvature $[M - \chi]$ (analytical model – analysis AN-Fix).

7.3.2 The second analysis

In the analysis named **AN-Fr**, the friction between the longitudinal steel bars and the central steel joints has been modelled.

In the analytical model, the value of friction between the bottom longitudinal steel bars and the steel joints has been chosen according to the experimental results illustrated in *paragraph 5.3*. Before applying the test load, the bottom longitudinal steel bars are in tension with the same value of the axial force. In fact, when the test load is:

$$F_{test} = 0.0kN$$

the maximum bending moment in the cross section 5-5 of the beam is:

$$M_5(0.0kN) = M(F_{test} = 0.0kN, x = 6000mm) = 36.60kN \cdot m$$

and the axial force in the bottom longitudinal steel bars has the same value:

$$\mathrm{N}_{\mathrm{B.fr\,(18-5)}}(0.0kN) = \mathrm{N}_{\mathrm{B.fr\,(18-4)}}(0.0kN) = \mathrm{N}_{\mathrm{B.fr\,(18-3)}}(0.0kN) = \mathrm{N}_{\mathrm{B.fr\,(18-2)}}(0.0kN) = \mathrm{N}_{\mathrm{B.fr\,(18-1)}}(0.0kN) = \mathrm{N}_{\mathrm{B\,(18-5)}}(0.0kN)$$

Starting from the value of the axial force $\mathrm{N}_{\mathrm{B\,(18-5)}}(F_{test})$, calculated in *paragraph 7.3.1*, in order to calculate the axial forces in the adjacent parts of bottom longitudinal steel bars, the following approximations are used:

$$\mathrm{N}_{\mathrm{B.fr\,(18-5)}}(F_{test}) = \mathrm{N}_{\mathrm{B\,(18-5)}}(F_{test})$$

$$\mathrm{N}_{\mathrm{B.fr\,(18-4)}}(F_{test}) = \begin{cases} \mathrm{N}_{\mathrm{B.fr\,(18-4)}}(0\ kN) & if\ \ \mathrm{N}_{\mathrm{B\,(18-4)}}(F_{test}) \le \mathrm{N}_{\mathrm{B.fr\,(18-4)}}(0\ kN) \\ \mathrm{N}_{\mathrm{B\,(18-4)}}(F_{test}) & if\ \ \mathrm{N}_{\mathrm{B.fr\,(18-5)}}(F_{test}) - \Delta N_{fr} \le \mathrm{N}_{\mathrm{B\,(18-4)}}(F_{test}) > \mathrm{N}_{\mathrm{B.fr\,(18-4)}}(0\ kN) \\ \mathrm{N}_{\mathrm{B.fr\,(18-5)}}(F_{test}) - \Delta N_{fr} & if\ \ \mathrm{N}_{\mathrm{B\,(18-4)}}(F_{test}) < \mathrm{N}_{\mathrm{B.fr\,(18-5)}}(F_{test}) - \Delta N_{fr} \end{cases}$$

$$\mathrm{N}_{\mathrm{B.fr\,(18-3)}}(F_{test}) = \begin{cases} \mathrm{N}_{\mathrm{B.fr\,(18-3)}}(0\ kN) & if\ \ \mathrm{N}_{\mathrm{B\,(18-3)}}(F_{test}) \le \mathrm{N}_{\mathrm{B.fr\,(18-3)}}(0\ kN) \\ \mathrm{N}_{\mathrm{B\,(18-3)}}(F_{test}) & if\ \ \mathrm{N}_{\mathrm{B.fr\,(18-4)}}(F_{test}) - \Delta N_{fr} \le \mathrm{N}_{\mathrm{B\,(18-3)}}(F_{test}) > \mathrm{N}_{\mathrm{B.fr\,(18-3)}}(0\ kN) \\ \mathrm{N}_{\mathrm{B.fr\,(18-4)}}(F_{test}) - \Delta N_{fr} & if\ \ \mathrm{N}_{\mathrm{B\,(18-3)}}(F_{test}) < \mathrm{N}_{\mathrm{B.fr\,(18-4)}}(F_{test}) - \Delta N_{fr} \end{cases}$$

$$\mathrm{N}_{\mathrm{B.fr\,(18-2)}}(F_{test}) = \begin{cases} \mathrm{N}_{\mathrm{B.fr\,(18-2)}}(0\ kN) & if\ \ \mathrm{N}_{\mathrm{B\,(18-2)}}(F_{test}) \le \mathrm{N}_{\mathrm{B.fr\,(18-2)}}(0\ kN) \\ \mathrm{N}_{\mathrm{B\,(18-2)}}(F_{test}) & if\ \ \mathrm{N}_{\mathrm{B.fr\,(18-3)}}(F_{test}) - \Delta N_{fr} \le \mathrm{N}_{\mathrm{B\,(18-2)}}(F_{test}) > \mathrm{N}_{\mathrm{B.fr\,(18-2)}}(0\ kN) \\ \mathrm{N}_{\mathrm{B.fr\,(18-3)}}(F_{test}) - \Delta N_{fr} & if\ \ \mathrm{N}_{\mathrm{B\,(18-2)}}(F_{test}) < \mathrm{N}_{\mathrm{B.fr\,(18-3)}}(F_{test}) - \Delta N_{fr} \end{cases}$$

$$\mathrm{N}_{\mathrm{B.fr\,(18-1)}}(F_{test}) = \begin{cases} \mathrm{N}_{\mathrm{B.fr\,(18-1)}}(0\ kN) & if\ \ \mathrm{N}_{\mathrm{B\,(18-1)}}(F_{test}) \le \mathrm{N}_{\mathrm{B.fr\,(18-1)}}(0\ kN) \\ \mathrm{N}_{\mathrm{B\,(18-1)}}(F_{test}) & if\ \ \mathrm{N}_{\mathrm{B.fr\,(18-2)}}(F_{test}) - \Delta N_{fr} \le \mathrm{N}_{\mathrm{B\,(18-1)}}(F_{test}) > \mathrm{N}_{\mathrm{B.fr\,(18-1)}}(0\ kN) \\ \mathrm{N}_{\mathrm{B.fr\,(18-2)}}(F_{test}) - \Delta N_{fr} & if\ \ \mathrm{N}_{\mathrm{B\,(18-1)}}(F_{test}) < \mathrm{N}_{\mathrm{B.fr\,(18-2)}}(F_{test}) - \Delta N_{fr} \end{cases}$$

with

$\Delta N_{fr} = 8.00\ kN$

7.3.3 Analytical results

Test load – displacement diagrams

Figure 7.37 and *Figure 7.38* show the test load – vertical displacement of the bottom central and lateral steel joints.

Analysis	Description
AN - Fix	the longitudinal steel bars are rigidly connected to the central steel joints

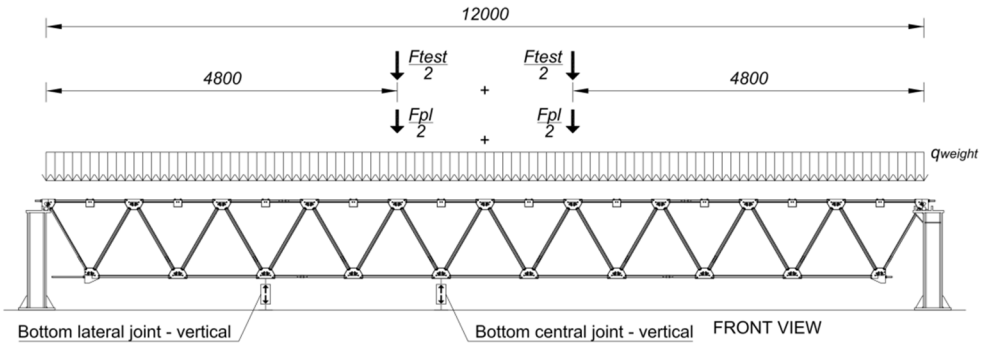

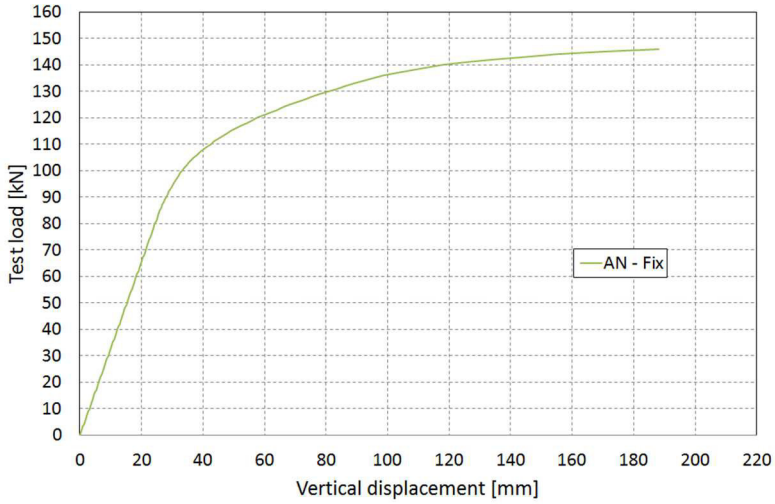

Figure 7.37 Bottom central steel joint: Test load – Vertical displacement diagram (analytical model).

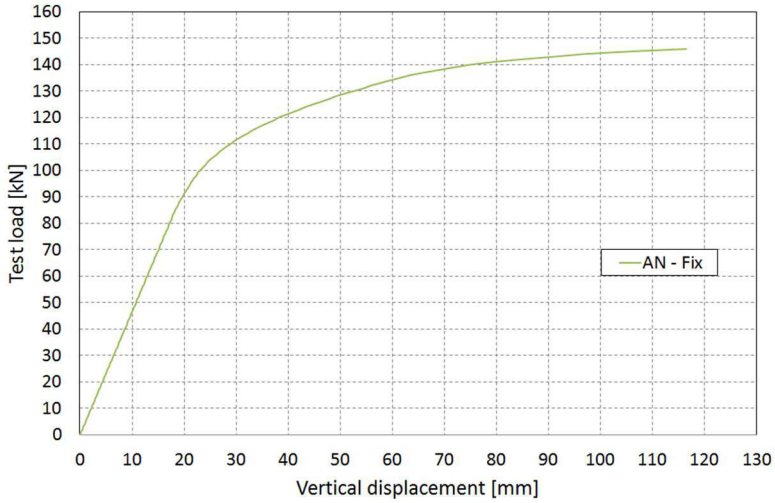

Figure 7.38 Bottom lateral steel joint: Test load – Vertical displacement diagram (analytical model).

Test load – axial force diagrams

The following diagrams show the test load – axial force diagrams in the bottom longitudinal steel bars.

Analysis	Description
AN - Fix	the longitudinal steel bars are rigidly connected to the central steel joints
AN - Fr	the friction between the longitudinal steel bars and the central steel joints has been modelled

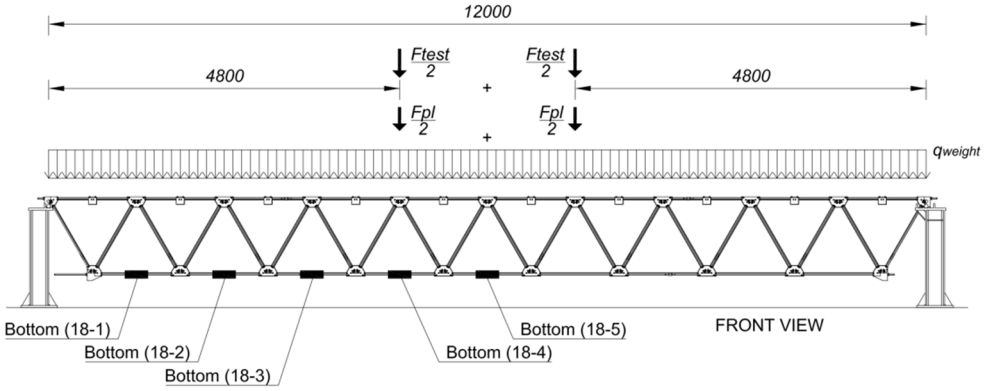

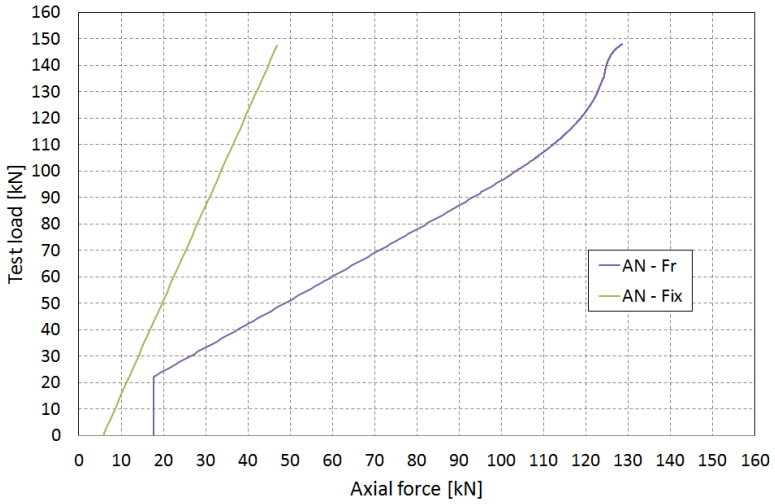

Figure 7.39 BOTTOM (18-1): Test load – Axial force diagram (analytical model).

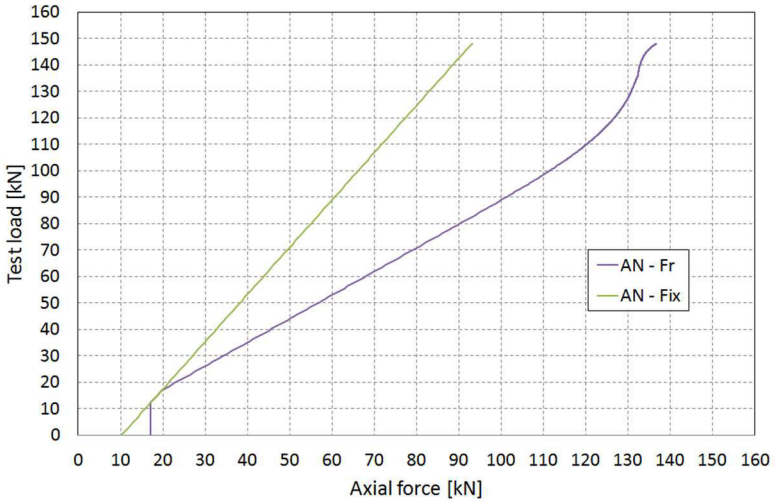

Figure 7.40 BOTTOM (18-2): Test load – Axial force diagram (analytical model).

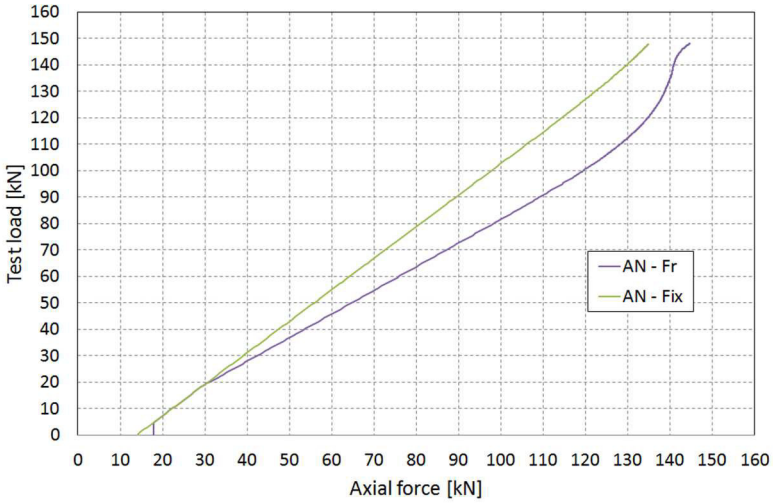

Figure 7.41 BOTTOM (18-3): Test load – Axial force diagram (analytical model).

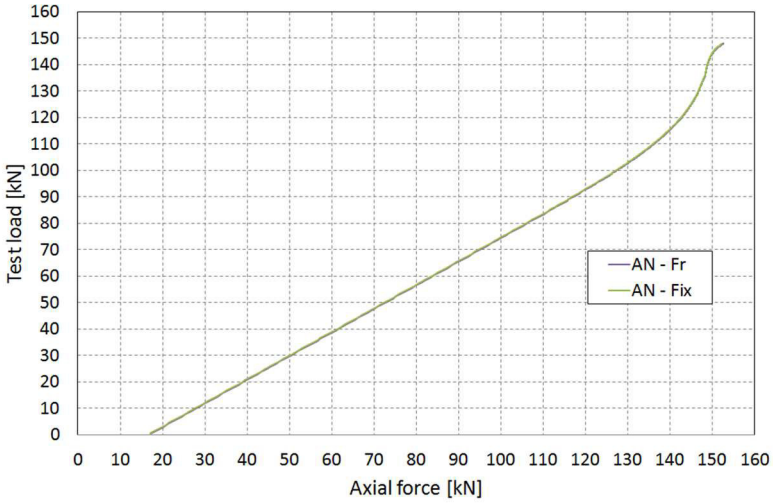

Figure 7.42 BOTTOM (18-4): Test load – Axial force diagram (analytical model); the curves overlap perfectly.

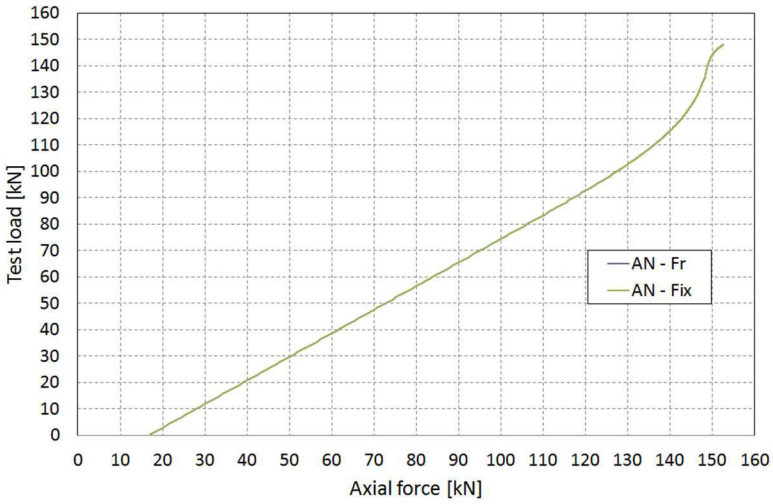

Figure 7.43 BOTTOM (18-5): Test load – Axial force diagram (analytical model); the curves overlap perfectly.

7.4 Conclusions

From the analytical results it is concluded that the analytical modelling is a useful method for calculating the axial forces in steel bars, the compressive forces in the triangular glass panels and the deformations of the beam. Even though rather coarse assumptions are made, the analytical modelling is validated in *Chapter 8* by comparing the analytical findings with the experimental and numerical results.

It is expected that the analytical model could be enhanced by taking account of the post-tensioning of steel bars and the presence of the rectangular laminated glass panels.

Chapter 8 Comparing experimental results with numerical and analytical findings

This chapter provides an integrated discussion of the structural response of the segmented post-tensioned hybrid steel-glass prototype. It focuses on a comparison of the experimental results with the numerical and analytical findings, illustrated in *Chapter 5*, *Chapter 6* and *Chapter 7*.

8.1 Introduction

Based on the experimental, analytical and numerical investigations, an integrated discussion on the structural response of the 12 m prototype is provided in this chapter. The comparison of the results validates the numerical and the analytical modelling of the beam and improves the understanding of the basic safety concept of the segmented post-tensioned hybrid steel-glass beam.

8.2 Result comparison

The numerical and the analytical modelling simulate the 2nd four-point bending test performed on the prototype illustrated in *paragraph 5.4.2*.

Figures 8.1 shows the positions of the strain gages applied in order to determine the axial forces in steel bars generated by the loads during the 2nd four-point bending test.

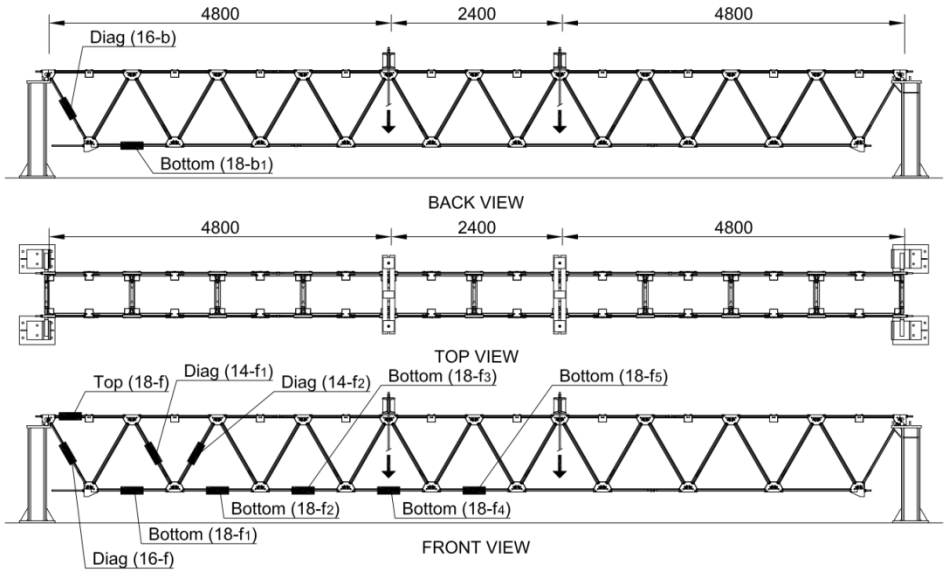

Figure 8.1 Position of the strain gages (2nd four-point bending test).

Figures 8.2 shows the positions of the LVDTs applied in order to determine the vertical displacements of 6 bottom steel joints and to determine the horizontal displacement generated by the loads during the 2nd four-point bending test.

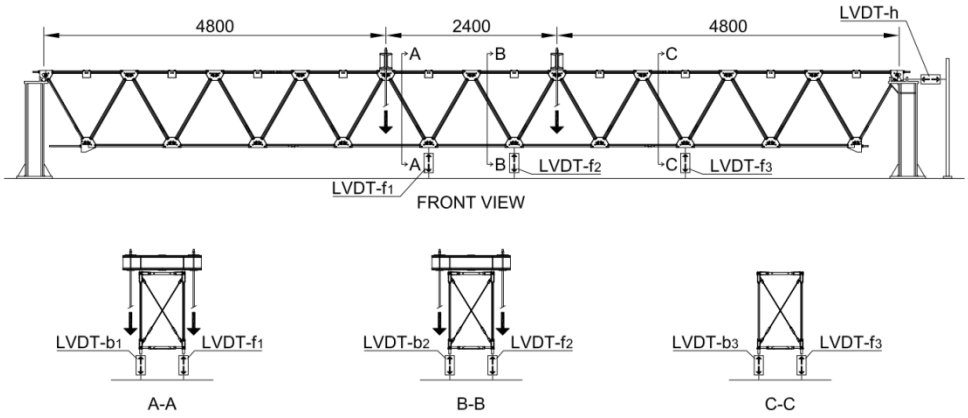

Figure 8.2 Positions of the LVDTs (2nd four-point bending test).

The 3D numerical model was built in ABAQUS® Finite Element software. Geometric nonlinearities, friction and material nonlinearities have been implemented in the model, and various analyses have been performed to investigate the effects of friction, the effects of the post-tensioning forces and the effects of mechanical properties of the interlayer, see *paragraph 6.2.4* and *paragraph 6.2.5*.

Table 8.1 lists the numerical analysis performed in ABAQUS® Finite Element software.

Analysis	PVB	Self-weight	Permament load	Post-tensioning load	Test load
PVBa-Fr-PT	G = 8.060 MPa	yes	yes	yes	yes
		no friction			friction [8 kN]
PVBa-PT	G = 8.060 MPa	yes	yes	yes	yes
		no friction			no friction
PVBa	G = 8.060 MPa	yes	yes	no	yes
		no friction			no friction
PVBa-Fr	G = 8.060 MPa	yes	yes	no	yes
		no friction			friction [8 kN]
PVBa-Fix	G = 8.060 MPa	yes	yes	no	yes
		fix*			fix*
* no relative motion is possible between longitudinal steel bars and central steel joints because they are rigidly connected					

Table 8.1 Main numerical analyses.

Figures 8.3 shows the steel bars of the numerical model where the axial forces have been measured.

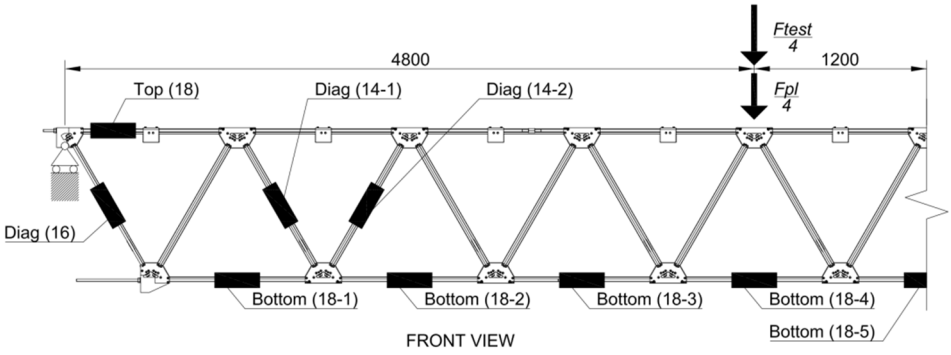

Figure 8.3 Positions and names of the steel bars (numerical model).

Figure 8.4 shows the points of the numerical model where the vertical and the horizontal displacements have been measured.

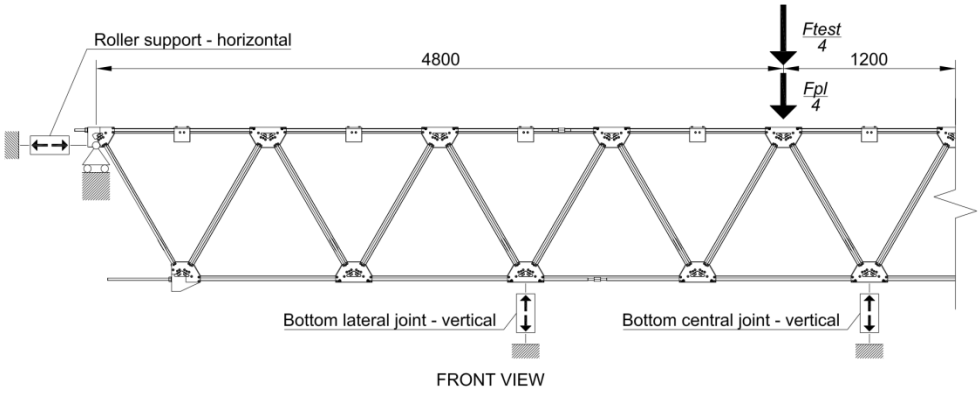

Figure 8.4 Positions and names of the points where the displacements are measured (numerical model).

The analytical model has been developed to calculate the deformations and the axial forces in steel bars and to determine the deformation of the beam. Even though rather coarse assumptions are made in the analytical modelling, it is validated by comparing the analytical results with the experimental and numerical results. See *paragraph 5.4.2*, *paragraph 6.2.5* and *paragraph 7.3.3*. *Table 8.2* lists the analyses performed.

Analysis	Name	Description
1	AN - Fix	the longitudinal steel bars are rigidly connected to the central steel joints
2	AN - Fr	the friction between the longitudinal steel bars and the central steel joints has been modelled

Table 8.2 Analytical model: analyses.

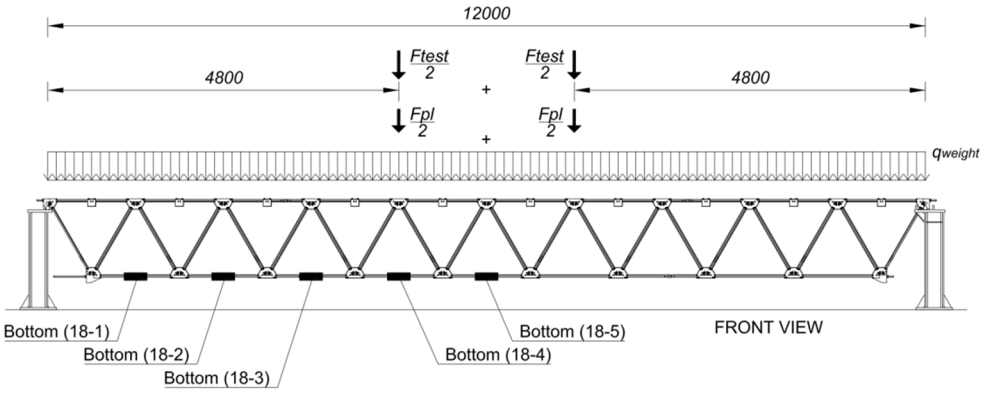

Figure 8.5 Positions and names of the steel bars (analytical model).

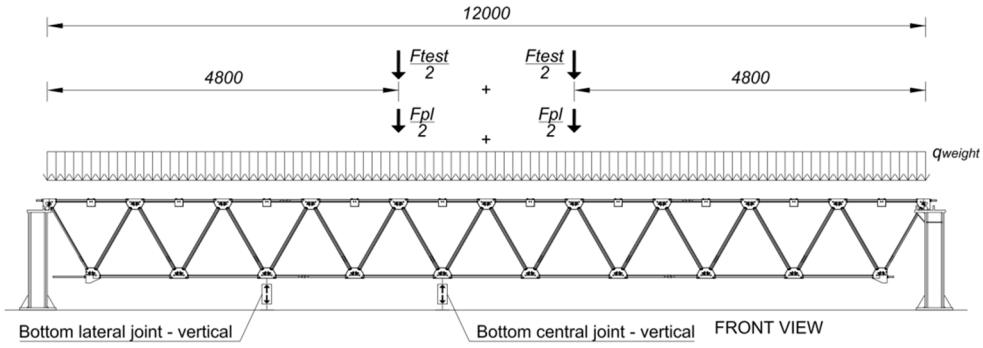

Figure 8.6 Positions and names of the points where the displacements are measured (analytical model)

8.2.1 Test load – displacement diagrams

The following figures compare the vertical displacements of the steel joints and the horizontal displacement of the roller support of the beam shown in *Figure 8.2*, *Figure 8.4* and *Figure 8.6*. Additional diagrams are available in Appendix I.

Central steel joints: test load – vertical displacement diagrams

Figure 8.7 compares the experimental average vertical displacement of the 4 bottom central steel joints with the vertical displacements obtained by the numerical analysis **PVBa-Fr-PT** and by the analitycal analysis **AN-Fix**. The numerical analysis **PVBa-Fr-PT** models the post-tensioning of the diagonal and longitudinal steel bars and takes account of the friction between the longitudinal steel bars and the central steel joints. In the analytical analysis **AN-Fix** the post-tensioning of the diagonal and longitudinal steel bars is neglected and the longitudinal steel bars are rigidly connected to the central steel joints.

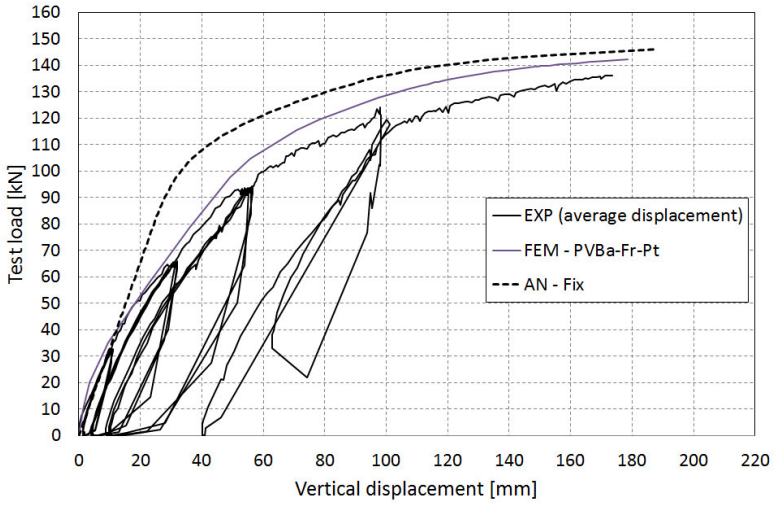

Figure 8.7 Bottom central steel joint: Test load – Vertical displacement diagram (2nd experimental test, numerical model, and analytical model).

Lateral steel joints: test load – vertical displacement diagrams

Figure 8.8 compares the experimental average vertical displacement of the 2 bottom lateral steel joints with the vertical displacements obtained by the numerical analysis **PVBa-Fr-PT** and by the analitycal analysis **AN-Fix**.

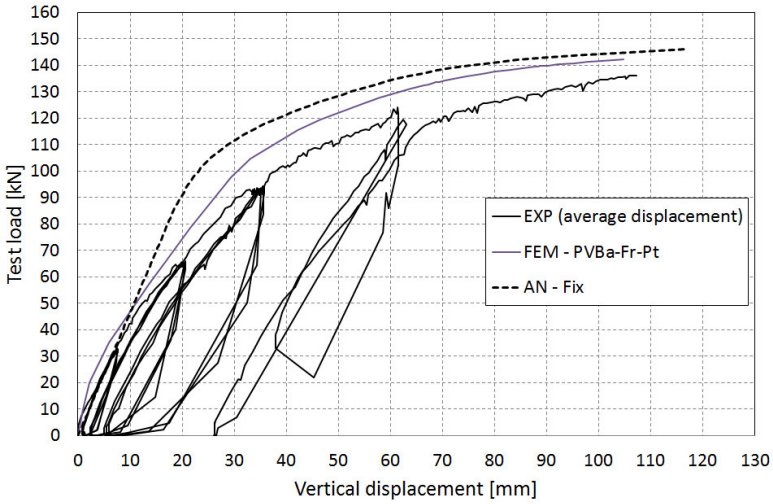

Figure 8.8 Bottom lateral steel joint: Test load – Vertical displacement diagram (2nd experimental test, numerical model and analytical model).

Roller support: test load – horizontal displacement diagrams

Figure 8.9 compares the horizontal displacement of the roller support of the prototype with the displacement of the same support obtained by the numerical analysis **PVBa-Fr-PT**.

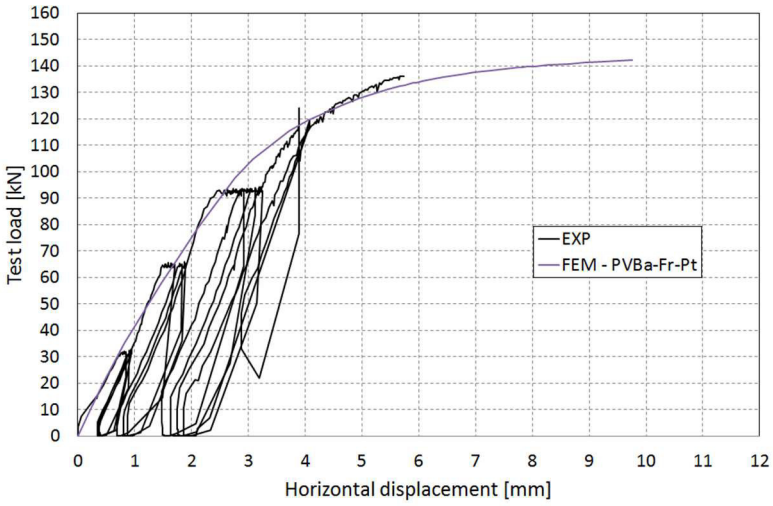

Figure 8.9 Roller support: Test load – Horizontal displacement diagram (2nd experimental test and numerical analysis **PVBa-FR-Pt**).

8.2.2 Test load – axial force diagrams

The following figures compare the most significant test load – axial force diagrams in steel bars shown in *Figure 8.1*, *Figure 8.3* and *Figure 8.5*. Additional diagrams are available in Appendix I.

Diagonal steel bars: test load – axial force diagrams

Figure 8.10, *Figure 8.11* and *Figure 8.12* compare the experimental axial forces in the diagonal steel bars DIAG (16-f), DIAG (16-b), DIAG (14-1) and DIAG (14-2) of the prototype with the axial forces obtained by the numerical analysis **PVBa-Fr-PT**.

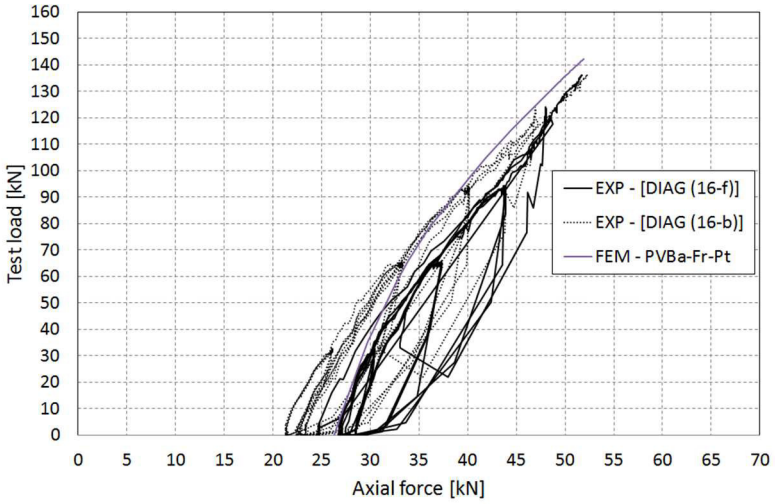

Figure 8.10 DIAG (16-f) and DIAG (16-b): Test load – Axial force diagram (2nd experimental test and numerical analysis **PVBa-FR-Pt**).

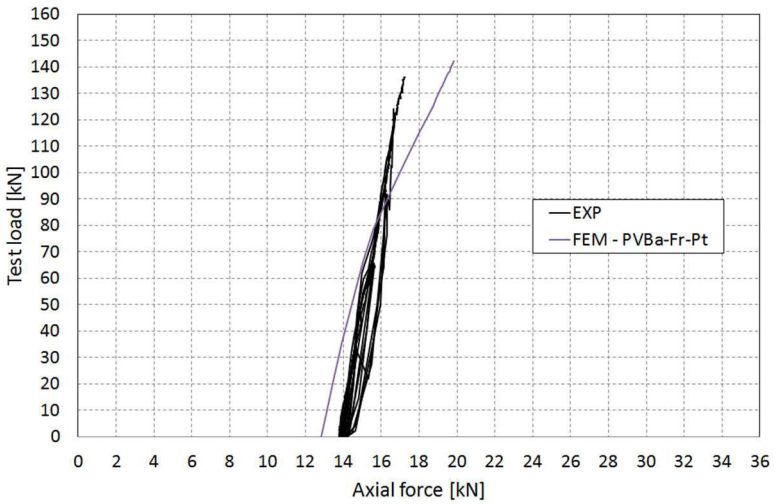

Figure 8.11 DIAG (14-f_1): Test load – Axial force diagram (2nd experimental test and numerical analysis **PVBa-Fr-Pt**).

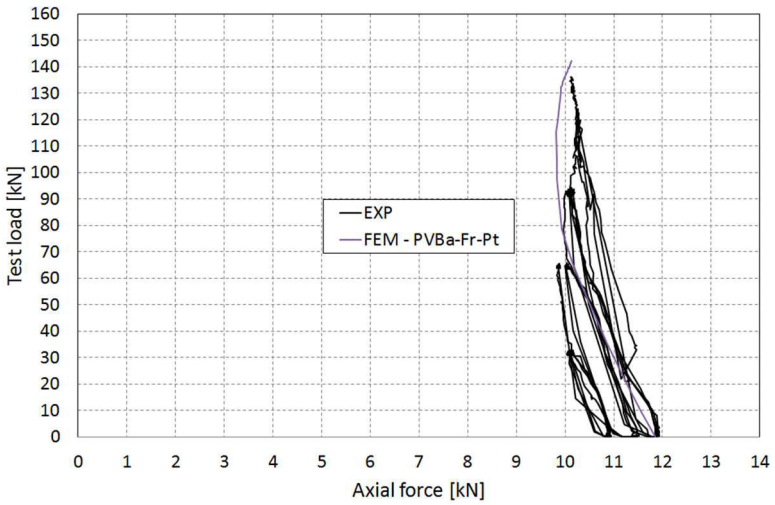

Figure 8.12 DIAG (14-f_2): Test load – Axial force diagram (2nd experimental test and numerical analysis **PVBa-Fr-Pt**).

Bottom longitudinal steel bars: test load – axial force diagrams

The following figures compare the axial forces in the bottom longitudinal steel bars of the prototype with the axial force in the same steel bars obtained by the numerical analysis **PVBa-Fr-PT** and by the analytical analysis **AN-Fr**. The numerical analysis **PVBa-Fr-PT** models the post-tensioning of the diagonal and longitudinal steel bars and takes account of the friction between the longitudinal steel bars and the central steel joints; the analytical analysis **AN-Fr** neglects the post-tensioning of the diagonal and longitudinal steel bars but takes account of the friction between the longitudinal steel bars and the central steel joints

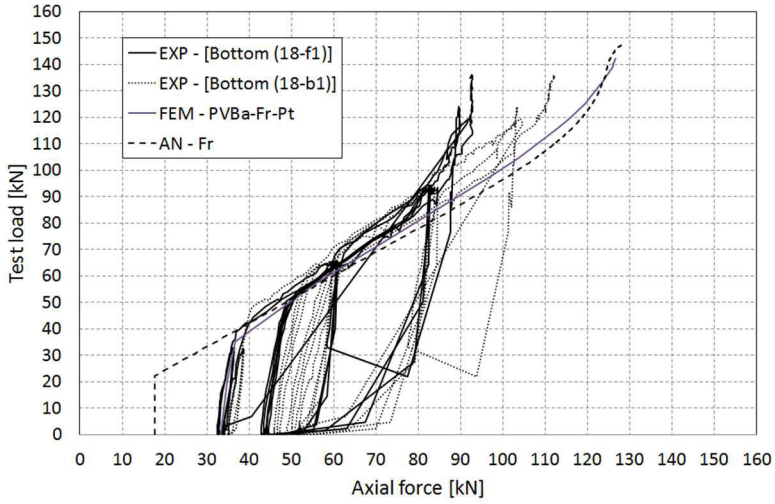

Figure 8.13 BOTTOM (18-f_1) and BOTTOM (18-b_1): Test load – Axial force diagram (2nd experimental test, numerical analysis **PVBa-Fr-Pt** and analytical analysis **AN-Fr**).

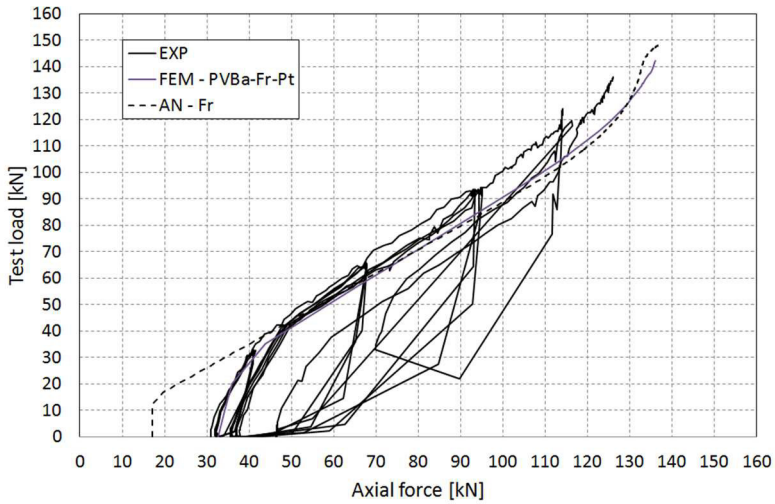

Figure 8.14 BOTTOM (18-f_2): Test load – Axial force diagram (2nd experimental test, numerical analysis **PVBa-Fr-Pt** and analytical analysis **AN-Fr**).

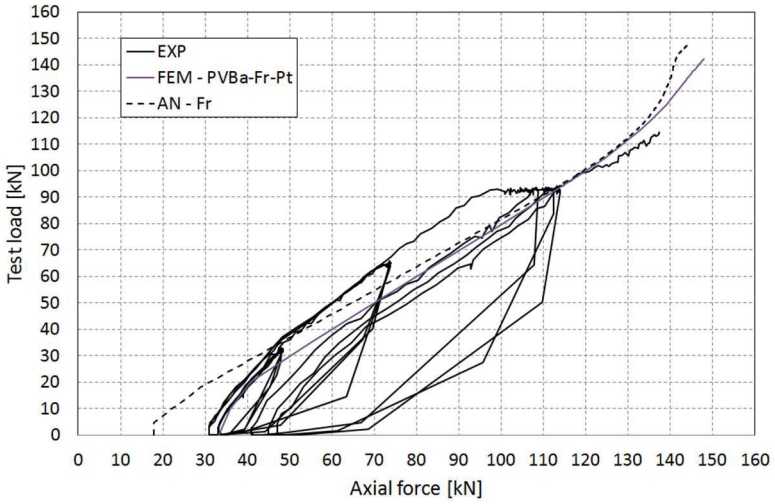

Figure 8.15 BOTTOM (18-f_3): Test load – Axial force diagram (2nd experimental test, numerical analysis **PVBa-Fr-Pt** and analytical analysis **AN-Fr**).

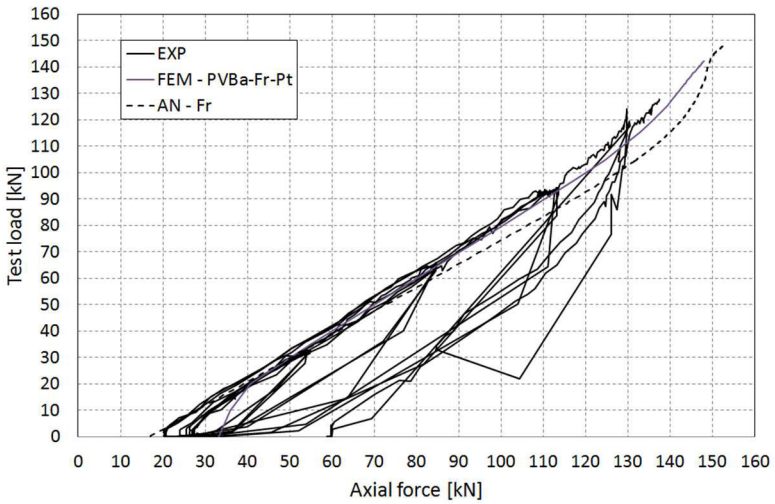

Figure 8.16 BOTTOM (18-f_4): Test load – Axial force diagram (2nd experimental test, numerical analysis **PVBa-Fr-Pt** and analytical analysis **AN-Fr**).

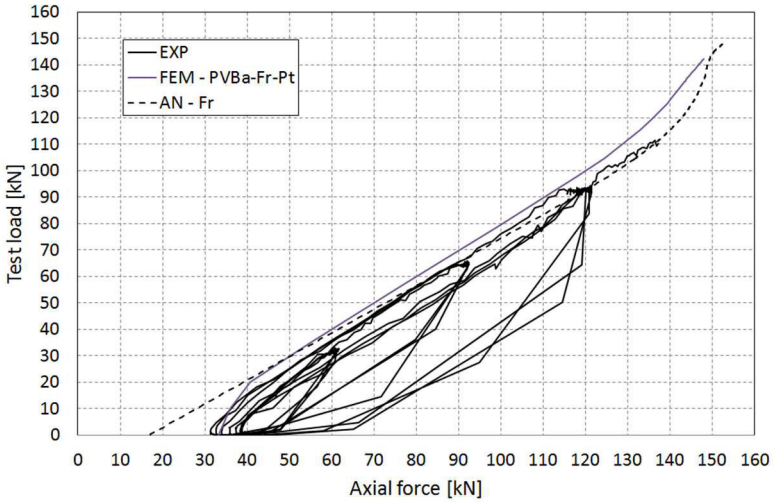

Figure 8.17 BOTTOM (18-f_5): Test load – Axial force diagram (2nd experimental test, numerical analysis **PVBa-Fr-Pt** and analytical analysis **AN-Fr**).

8.3 Conclusions and further considerations

Paragraph 8.2 briefly illustrates and compares the experimental results of the 2nd four-point bending test and the findings of the numerical and analytical modelling. The diagrams in *paragraph 8.2* demonstrate how the numerical and analytical findings are in rather good agreement with the experimental results.

By comparing the test load – displacement diagrams in *paragraph 8.2.1* it is observed that the numerical analysis **PVBa-Fr-PT** and the analytical analysis **AN-Fix** overestimate the stiffness of the beam. The difference between the numerical analysis and the experimental investigations is less than 10% for values of test load lower than 100 kN but reaches 20% at collapse. The difference between the results of the analytical modelling and the experimental investigations is greater because of coarse assumptions made in the analytical modelling.

By comparing the test load – axial force diagrams in *paragraph 8.2.2* it is observed that the numerical analysis **PVBa-Fr-PT** and the analytical analysis **AN-Fr** give almost the same results. The difference between the numerical and analytical results is less than 6%, and the difference between the numerical and experimental results is less than 8% with the exception of the axial forces in the bottom longitudinal steel bars BOTTOM (18-f_1) and BOTTOM (18-b_1). In these bars the difference reaches a value of 31% and 10% at collapse, it is probably due to the real frictional behaviour steel joint – steel bars that the model neglects.

Furthermore, by comparing the numerical findings of the analysis **PVBa-Fix** and the results of the analytical analysis **AN-Fix**, it is observed that the analytical modelling well describes the numerical structural response of the beam. This comparison validates the numerical modelling. In order to further demonstrate how the numerical modelling and the analytical modelling are in good agreement, *Figure 8.19* compares the axial force in the central diagonal steel bars generated by the test load, *Figure 8.18*.

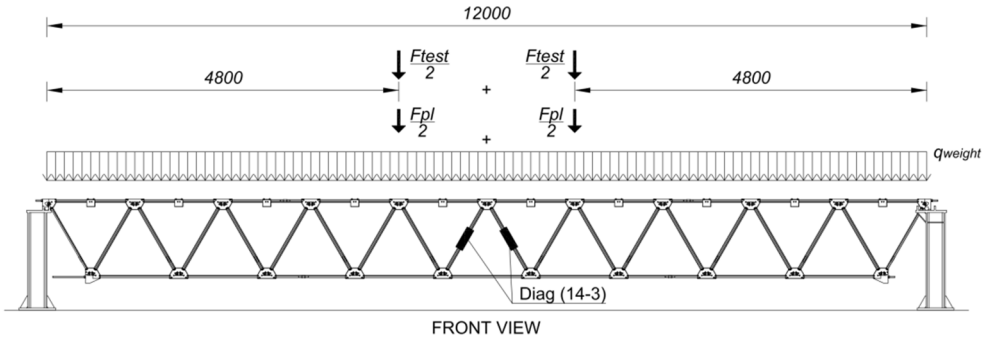

Figure 8.18 Position of the central diagonal steel bars DIAG (14-3).

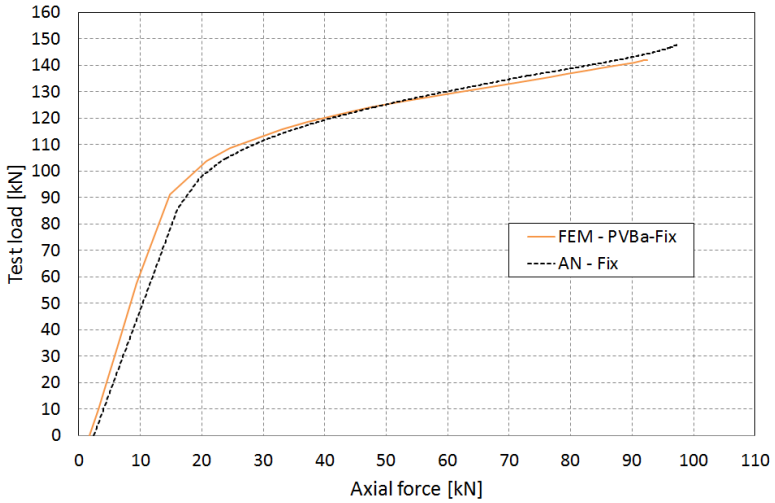

Figure 8.19 DIAG (14-3): Test load – Axial force diagram (numerical analysis **PVBa-Fix** and analytical analysis **AN-Fix**).

Thanks to the validation of the analytical model and eq. *(7.28)*, the compressive force $F_{glass.top}(F_{test})$ transferred to the central triangular glass panel is easily calculated. *Figure 8.20* shows the position of the central triangular glass panel and *Figure 8.21* shows the test load – compressive force $F_{glass.top}$ diagram in the central triangular glass panel.

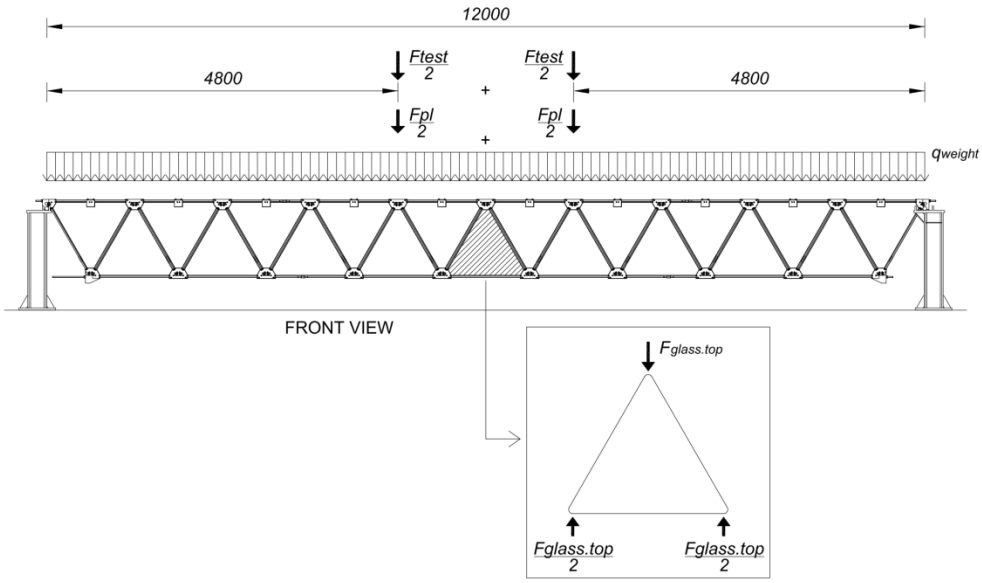

Figure 8.20 Position of the central triangular glass panel and detail of the compressive force $F_{glass.top}$ (analytical model).

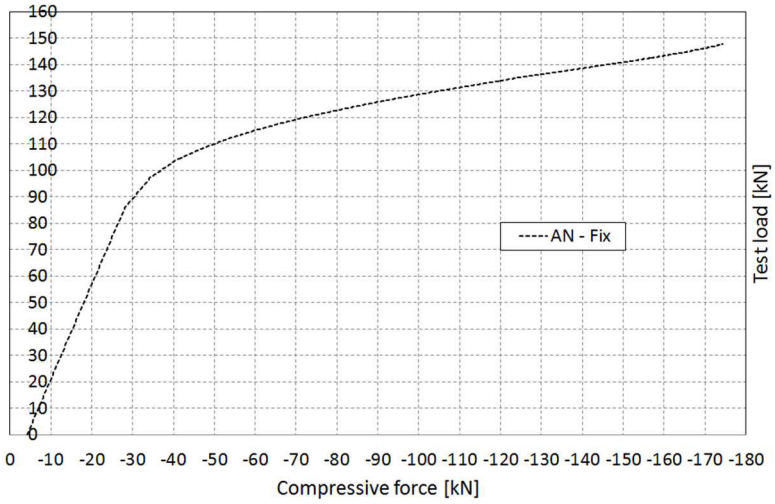

Figure 8.21 Central triangular glass panel: Test load – Compressive force $F_{glass.top}$ diagram (analytical analysis AN-Fix).

Chapter 9 Conclusions and recommendations

This dissertation illustrates and summarizes the research activity conducted during the PhD research. The main objective was to contribute to a better understanding of the structural response of the segmented post-tensioned hybrid steel-glass beam TVTɣ. The experimental investigations performed on the 12 m prototype, together with the numerical and analytical models shed light on the structural behaviour of this kind of glass beams. Nonetheless, this research should be considered the first step for further studies and investigations.

9.1 Conclusions

As described in more detail in *Chapter 8*, the static structural response of a 12 m prototype of segmented post-tensioned hybrid steel-glass beam is investigated. The experimental four-point bending tests and the numerical and analytical modelling give almost matching results.

9.1.1 Experimental investigations

From the experimental investigations, it can be said that the post-tensioning forces applied to steel bars slightly affect the stiffness of the beam, and the breakage of the beam is ductile due to the plastic deformation of tensile steel bars, while the final collapse is due to buckling of glass in compression. The experimental tests show that it would be desirable to develop a better connection between the longitudinal steel bars and the central steel joints.

9.1.2 Numerical investigations

The 3D numerical model and the numerical analyses allowed inclusion of several parameters such as friction, geometric nonlinearity, material nonlinearities, and mechanical properties of the interlayer. The numerical model has been validated by comparing numerical results with the results of static experimental investigations. The numerical findings are accurate and in good agreement with experimental results. The numerical model is therefore useful for design process of further prototypes to test.

9.1.3 Analytical investigations

The analytical model represents the most important result of this research because it allows us to calculate the axial forces in steel bars, the compressive forces in the triangular glass panels and the deformations of the beams. Even though rather coarse assumptions are made in the analytical modelling, they are validated by comparing the analytical results with the experimental and numerical results. In particular, the analytical modelling gives a clear explanation of the internal mechanical behaviour of the beam.

Nonetheless, in the analytical modelling, some parameters have been neglected. They should be investigated in more detail in order to evaluate exactly their influences on the structural response of this kind of beam.

9.2 Recommendations

Starting from the results of the investigations performed, it is recommended to carry out additional studies into the effects of various parameters on the structural response of segmented post-tensioned hybrid steel-glass beam, especially into the effects of the parameter interlayer type and the parameter glass type on the final buckling collapse of the laminated glass panels in compression.

It is recommended to investigate the effects of the size parameter of the beam on the structural response and on its breakage and post-breakage response. It would be interesting to investigate the exact effects of the bar size on the response of beams in terms of stiffness and strength, and especially the relation between the diameter of bars and the dimensions, sizes and thickness of laminated glass panels.

It would also be interesting to further develop the analytical model taking account of the exact effects of shear force and its relation with the bending moment on the glass elements and the steel bars.

Finally, it is recommended to further investigate into the possibilities of embedded reinforcement in glass panels, which could offer a structural benefit in terms of ultimate strength.

Appendix I Experimental, numerical and analytical results

This appendix provides the diagrams in which the experimental results are compared with the numerical and analytical findings.

I.1 Description

The numerical and the analytical modelling simulate the 2nd four-point bending test performed on the prototype illustrated in *paragraph 5.4.2*.

Figures I.1 shows the positions of the strain gages applied in order to determine the axial forces in steel bars generated by the loads during the 2nd four-point bending test.

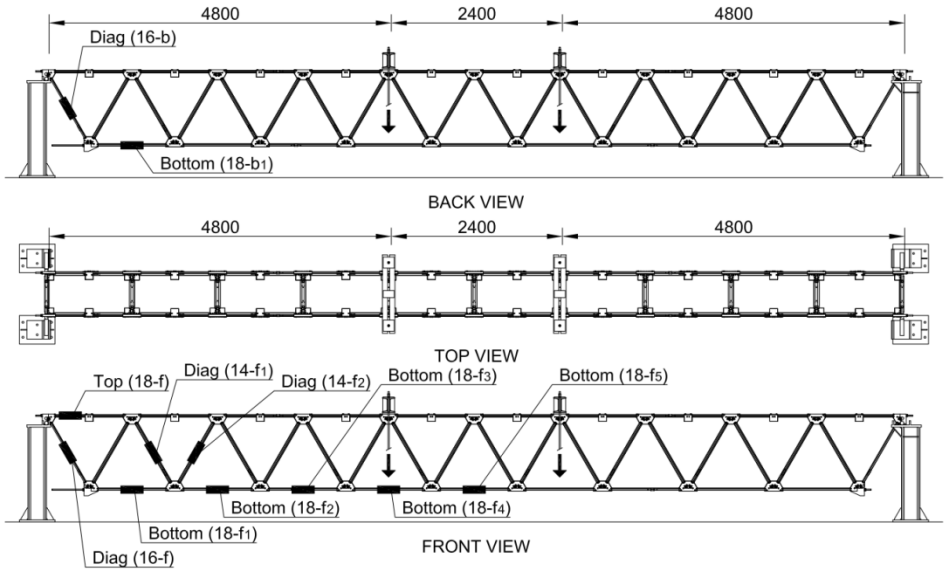

Figure I.1 Position of the strain gages (2nd four-point bending test).

Figures I.2 shows the positions of the LVDTs applied in order to determine the vertical displacements of 6 bottom steel joints and to determine the horizontal displacement generated by the loads during the 2nd four-point bending test.

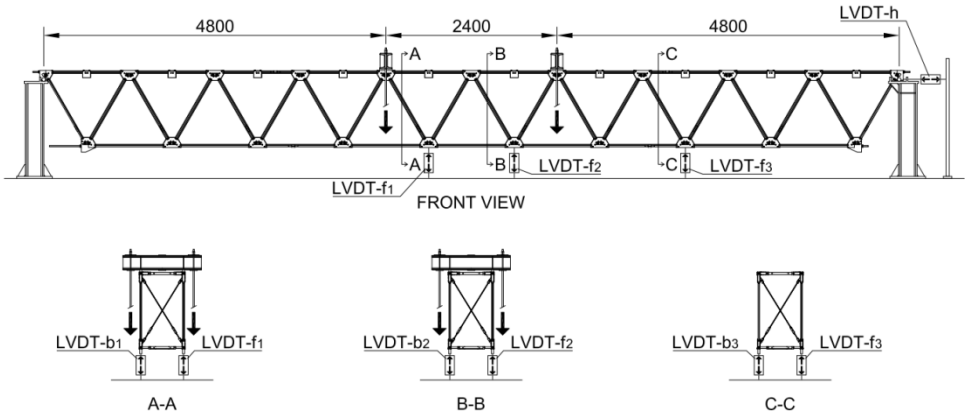

Figure I.2 Positions of the LVDTs (2nd four-point bending test).

The 3D numerical model was built in ABAQUS® Finite Element software. Geometric nonlinearities, friction and material nonlinearities have been implemented in the model, and various analyses have been performed to investigate the effects of friction, the effects of the post-tensioning forces and the effects of mechanical properties of the interlayer, see *paragraph 6.2.4* and *paragraph 6.2.5*.

Table I.1 lists the numerical analysis performed in ABAQUS® Finite Element software.

Analysis	PVB	Self-weight	Permament load	Post-tensioning load	Test load
PVBa-Fr-PT	G = 8.060 MPa	yes	yes	yes	yes
		no friction			friction [8 kN]
PVBa-PT	G = 8.060 MPa	yes	yes	yes	yes
		no friction			no friction
PVBa	G = 8.060 MPa	yes	yes	no	yes
		no friction			no friction
PVBa-Fr	G = 8.060 MPa	yes	yes	no	yes
		no friction			friction [8 kN]
PVBa-Fix	G = 8.060 MPa	yes	yes	no	yes
		fix*			fix*
* no relative motion is possible between longitudinal steel bars and central steel joints because they are rigidly connected					

Table I.1 Main numerical analyses.

Figures I.3 shows the steel bars of the numerical model where the axial forces have been measured.

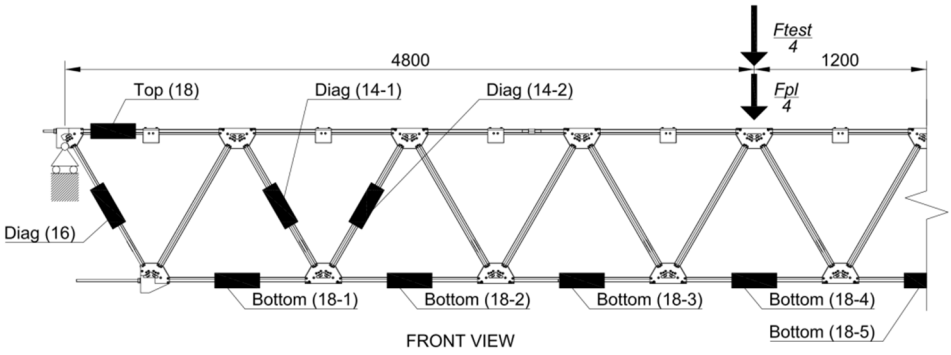

Figure I.3 Positions and names of the steel bars (numerical model).

Figure I.4 shows the points of the numerical model where the vertical and the horizontal displacements have been measured.

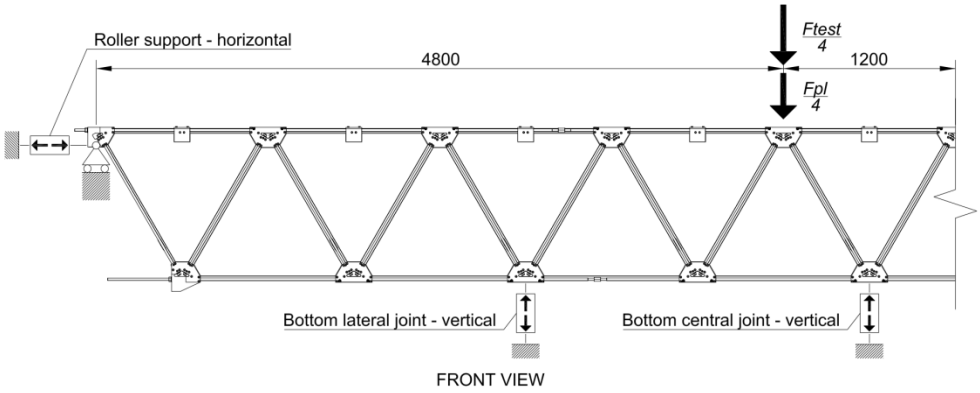

Figure I.4 Positions and names of the points where the displacements are measured (numerical model).

The analytical model has been developed to calculate the deformations and the axial forces in steel bars and to determine the deformation of the beam. Even though rather coarse assumptions are made in the analytical modelling, it is validated by comparing the analytical results with the experimental and numerical results. See *paragraph 5.4.2*, *paragraph 6.2.5* and *paragraph 7.3.3*. *Table I.2* lists the analyses performed.

Analysis	Name	Description
1	AN - Fix	the longitudinal steel bars are rigidly connected to the central steel joints
2	AN - Fr	the friction between the longitudinal steel bars and the central steel joints has been modelled

Table I.2 Analytical model: analyses.

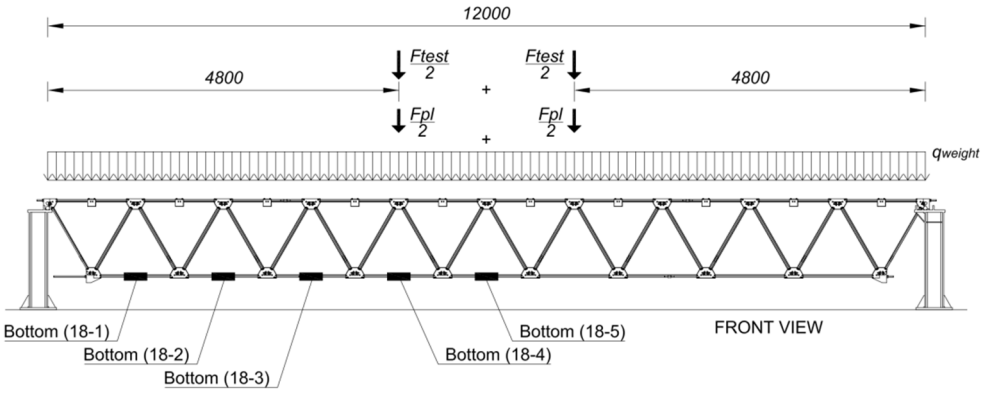

Figure I.5 Positions and names of the steel bars (analytical model).

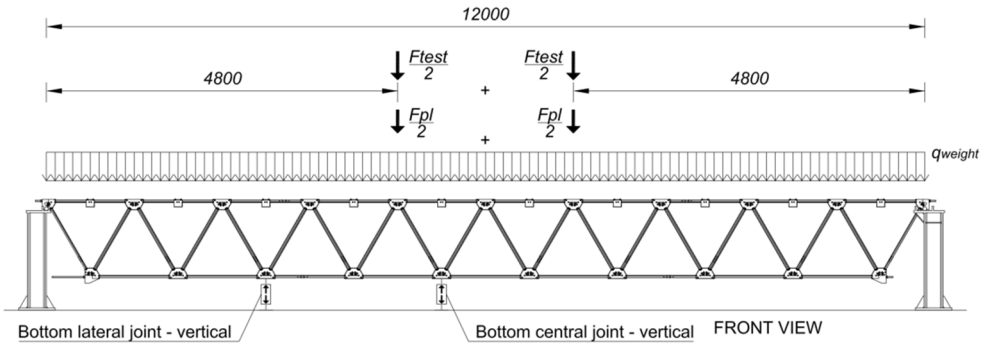

Figure I.6 Positions and names of the points where the displacements are measured (analytical model)

I.2 Test load – displacement diagrams

Central steel joints: test load – vertical displacement diagrams

The following figures compare the test load – vertical displacement diagrams of the bottom central steel joints shown in *Figure I.2*, *Figure I.4* and *Figure I.6*. The average vertical displacement of the LVDT-f_1, LVDT-f_2, LVDT-b_1 and LVDT-b_2 is given.

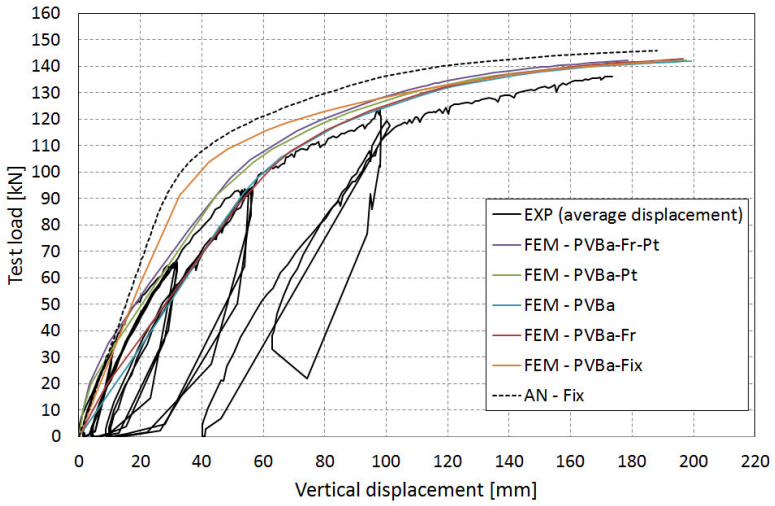

Figure I.7 Bottom central steel joint: Test load – Vertical displacement diagram (2nd experimental test, numerical model, and analytical model).

Figure I.8 compares the experimental average vertical displacement of the 4 bottom central steel joints with the vertical displacement of the numerical analysis **PVBa-Fr-PT** that models the post-tensioning of the diagonal and longitudinal steel bars and takes account of the friction between the longitudinal steel bars and the central steel joints.

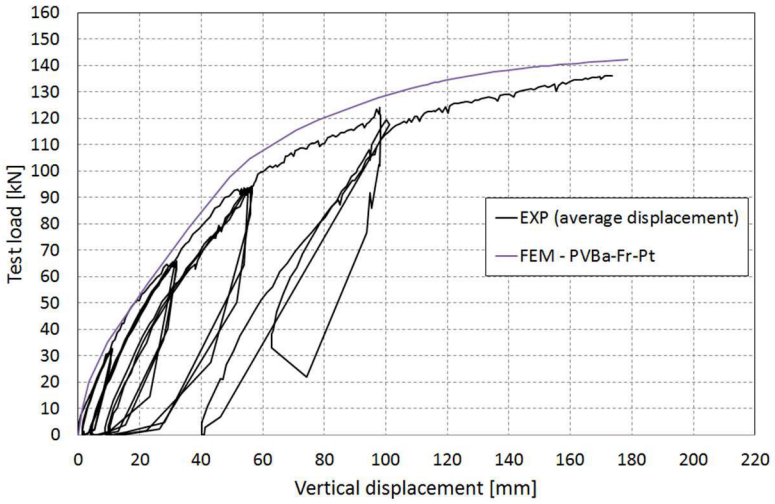

Figure I.8 Bottom central steel joint: Test load – Vertical displacement diagram (2nd experimental test and numerical analysis **PVBa-FR-Pt**).

Figure I.9 compares the vertical displacement of the numerical analysis **PVBa-Fix** and the vertical displacement of the analysis **AN-Fix** in which the post-tensioning of the diagonal and longitudinal steel bars is neglected, while the longitudinal steel bars are rigidly connected to the central steel joints.

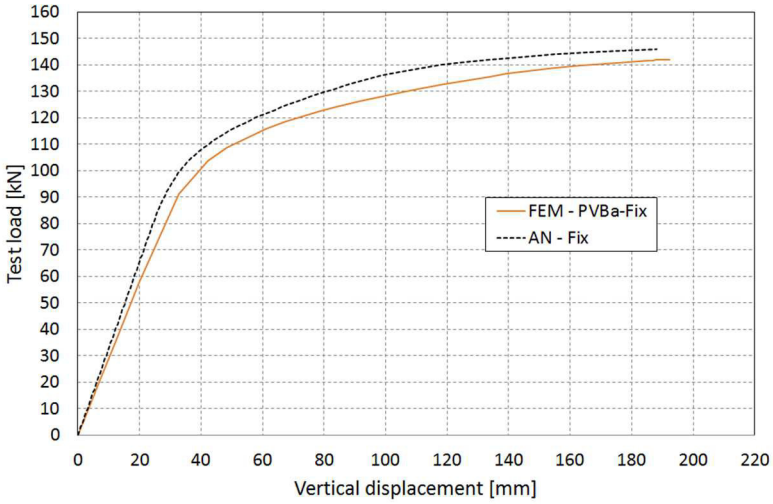

Figure I.9 Bottom central steel joint: Test load – Vertical displacement diagram (numerical analysis **PVBa-Fix**, analytical analysis **AN-Fix**).

Lateral steel joints: test load – vertical displacement diagrams

The following figures compare the test load – vertical displacement diagrams of the bottom central steel joints shown in *Figure I.2*, *Figure I.4* and *Figure I.6*. The average vertical displacement of the LVDT-f_3, and LVDT-b_3 is given.

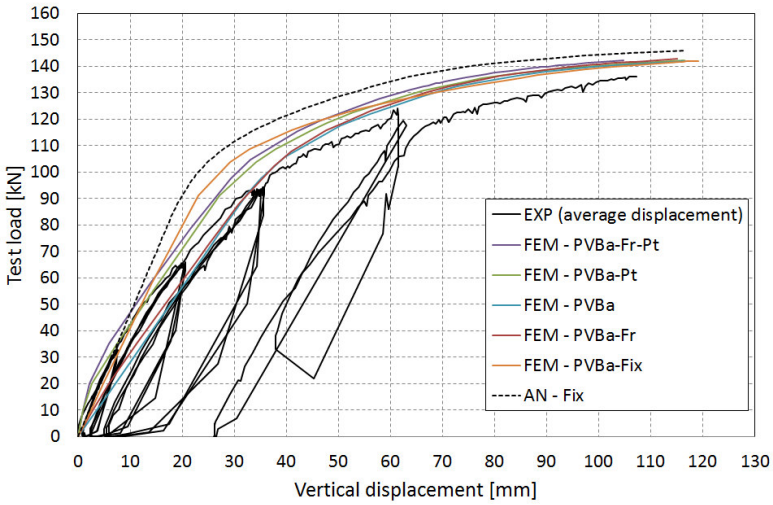

Figure I.10 Bottom lateral steel joint: Test load – Vertical displacement diagram (2nd experimental test, numerical model and analytical model).

Figure I.11 compares the experimental average vertical displacement of the 2 bottom lateral steel joints with the vertical displacement of the numerical analysis **PVBa-Fr-PT** that models the post-tensioning of the diagonal and longitudinal steel bars and takes account of the friction between the longitudinal steel bars and the central steel joints.

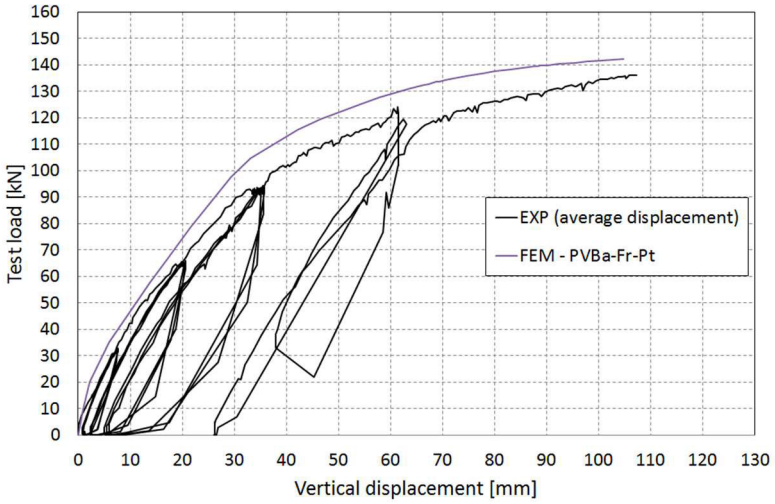

Figure I.11 Bottom lateral steel joint: Test load – Vertical displacement diagram (2nd experimental test and numerical analysis **PVBa-FR-Pt**).

Figure I.12 compares the vertical displacement of the numerical analysis **PVBa-Fix** and the vertical displacement of the analytical analysis **AN-Fix** in which the post-tensioning of the diagonal and longitudinal steel bars is neglected, while the longitudinal steel bars are rigidly connected to the central steel joints.

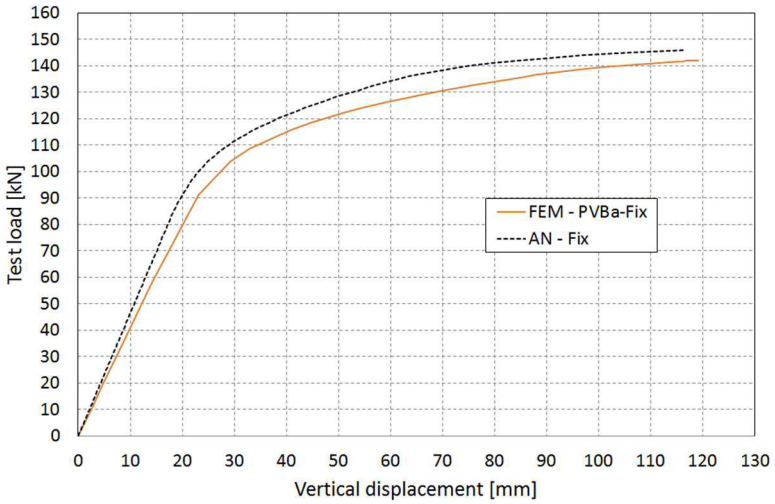

Figure I.12 Bottom lateral steel joint: Test load – Vertical displacement diagram (numerical analysis **PVBa-Fix**, analytical analysis **AN-Fix**).

Roller support: test load – horizontal displacement diagrams

The following figures compare the test load – horizontal displacement diagrams of the roller support of the beam shown in *Figure I.2*, *Figure I.4* and *Figure I.6*.

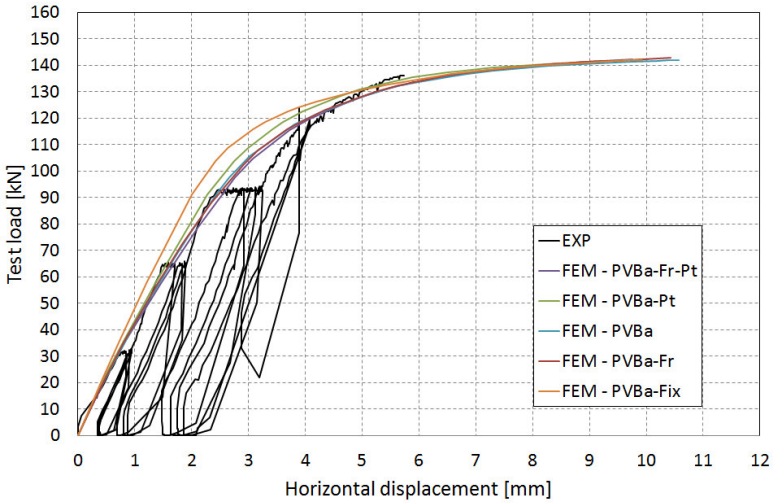

Figure I.13 Roller support: Test load – Horizontal displacement diagram (2nd experimental test and numerical model).

Figure I.14 compares the horizontal displacement of the roller support of the prototype with the displacement of the same support obtained by the numerical analysis **PVBa-Fr-PT**.

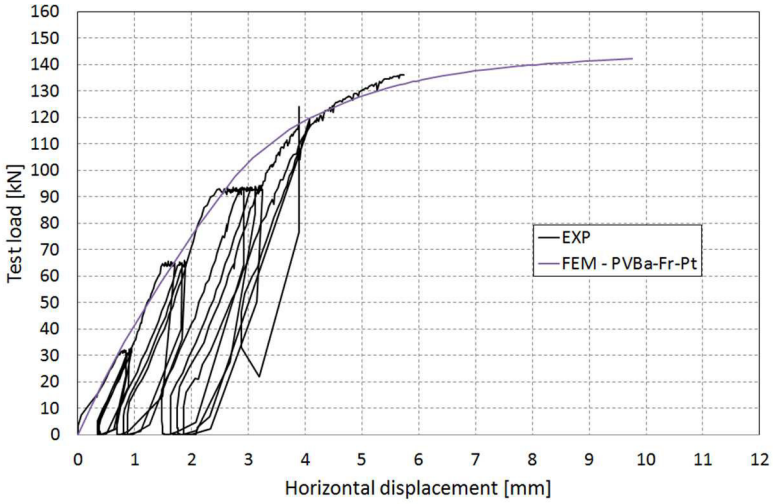

Figure I.14 Roller support: Test load – Horizontal displacement diagram (2nd experimental test and numerical analysis **PVBa-FR-Pt**).

I.3 Test load – axial force diagrams

The following figures compare the test load – axial force diagrams in the steel bars shown in *Figure I.1*, *Figure I.3* and *Figure I.5*.

Diagonal steel bars: test load – axial force diagrams

Figure I.15 compares the experimental axial forces in the diagonal steel bars DIAG (16-f) and DIAG (16-b) of the prototype with the axial force obtained by the numerical analyses in the same diagonal steel bar DIAG (16) of the numerical model.

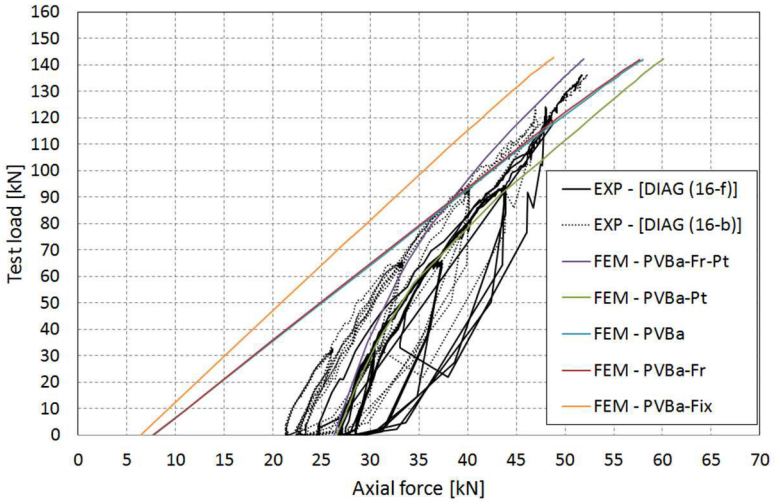

Figure I.15 DIAG (16-f) and DIAG (16-b): Test load – Axial force diagram (2nd experimental test and numerical model).

Figure I.16 compares the experimental axial forces in the diagonal steel bars DIAG (16-f) and DIAG (16-b) of the prototype with the axial force in the diagonal steel bar DIAG (16) obtained by the numerical analysis **PVBa-Fr-PT**.

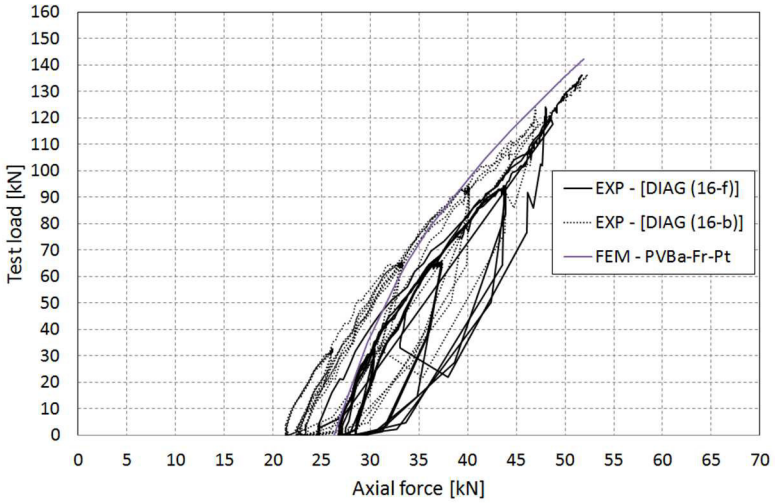

Figure I.16 DIAG (16-f) and DIAG (16-b): Test load – Axial force diagram (2nd experimental test and numerical analysis **PVBa-FR-Pt**).

Figure I.17 compares the experimental axial force in the diagonal steel bar DIAG (14-f_1) of the prototype with the axial force obtained by the numerical analyses in the same diagonal steel bar DIAG (14-1) of the numerical model.

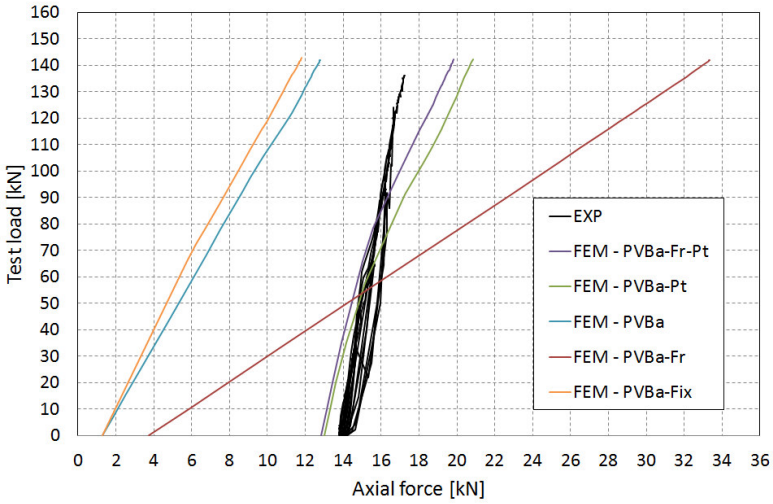

Figure I.17 DIAG (14-f_1): Test load – Axial force diagram (2nd experimental test and numerical model).

Figure I.18 compares the axial force in the diagonal steel bars DIAG (14-f_1) of the prototype with the axial force in the diagonal steel bar DIAG (14-1) obtained by the numerical analysis **PVBa-Fr-PT**.

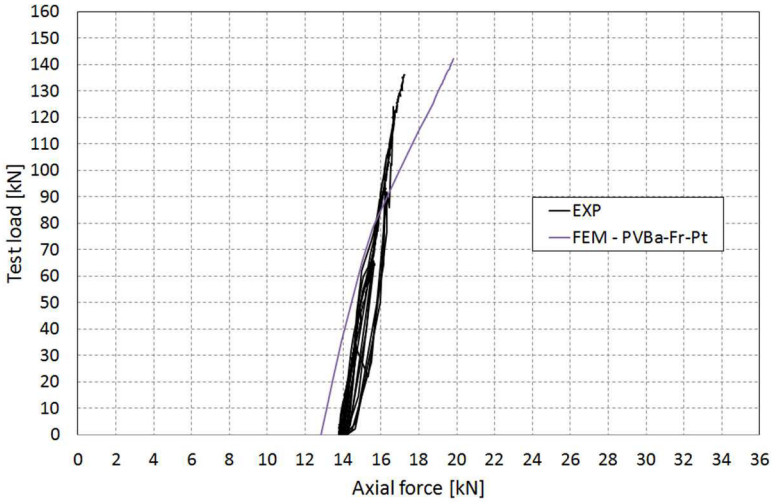

Figure I.18 DIAG (14-f_1): Test load – Axial force diagram (2nd experimental test and numerical analysis **PVBa-Fr-Pt**).

Figure I.19 compares the experimental axial force in the diagonal steel bar DIAG (14-f_2) of the prototype with the axial force obtained by the numerical analyses in the same diagonal steel bar DIAG (14-2) of the numerical model.

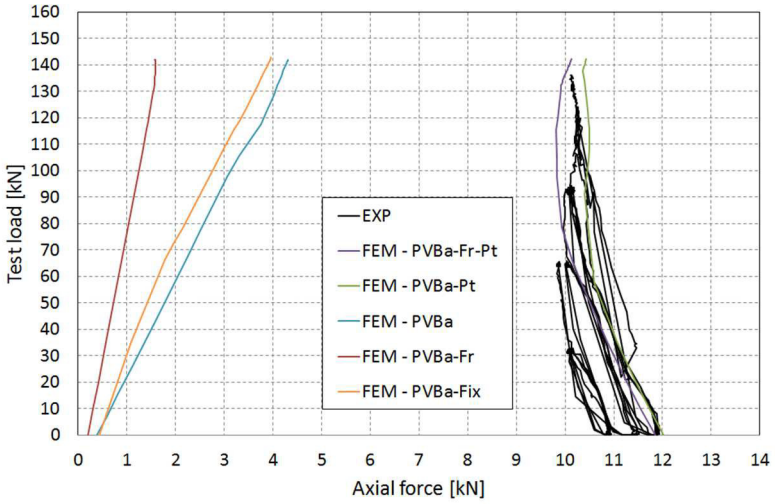

Figure I.19 DIAG (14-f_2): Test load – Axial force diagram (2nd experimental test and numerical model).

Figure I.20 compares the axial force in the diagonal steel bars DIAG (14-f_2) of the prototype with the axial force in the diagonal steel bar DIAG (14-2) obtained by the numerical analysis **PVBa-Fr-PT**.

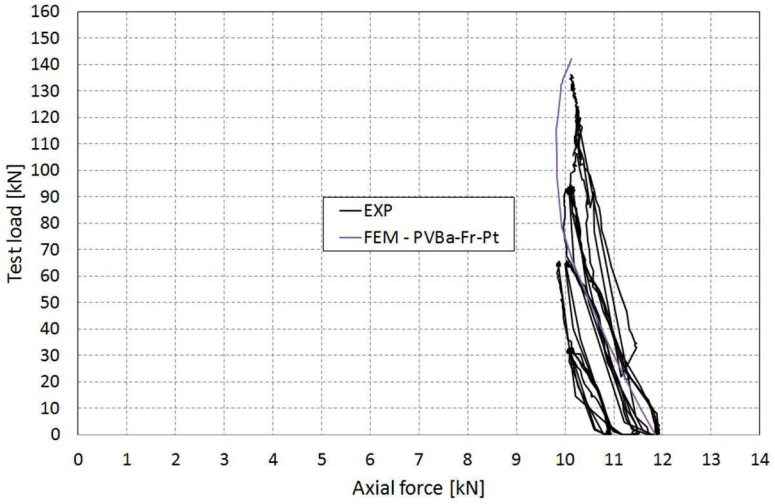

Figure I.20 DIAG (14-f_2): Test load – Axial force diagram (2nd experimental test and numerical analysis **PVBa-Fr-Pt**).

Top longitudinal steel bar: test load – axial force diagrams

Figure I.21 compares the experimental axial force in the top longitudinal steel bar TOP (18-f) of the prototype with the axial force obtained by the numerical analyses in the same steel bar TOP (18) of the numerical model.

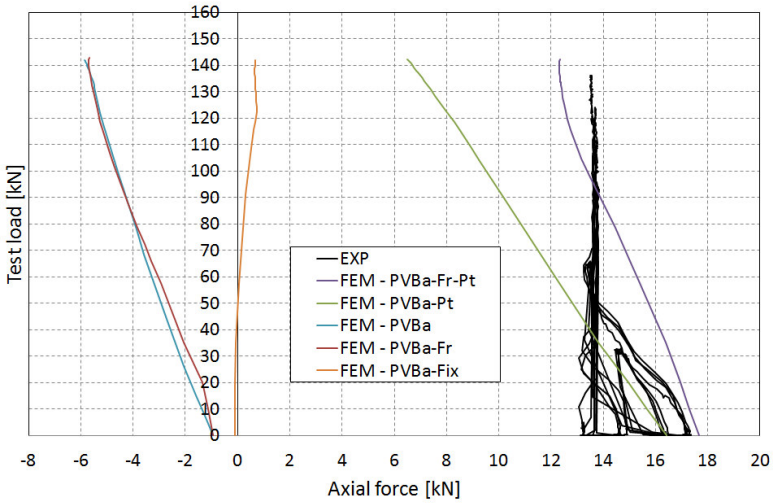

Figure I.21 TOP (18-f): Test load – Axial force diagram (2nd experimental test and numerical model).

Figure I.22 compares the axial force in the top longitudinal steel bar TOP (18-f) of the prototype with the axial force in the top longitudinal steel bar TOP (18) of the numerical analysis **PVBa-Fr-PT**.

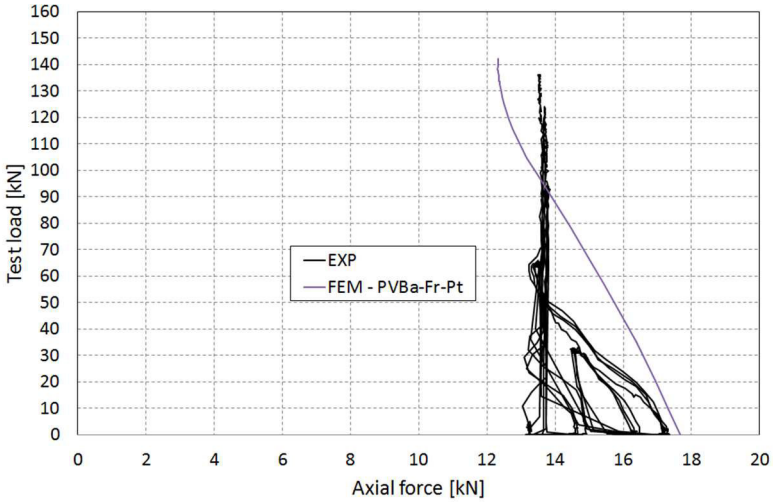

Figure I.22 TOP (18-f): Test load – Axial force diagram (2nd experimental test and numerical analysis **PVBa-Fr-Pt**).

Bottom longitudinal steel bars: test load – axial force diagrams

Figure I.23 compares the experimental axial forces in the bottom longitudinal steel bars BOTTOM (18-f_1) and BOTTOM (18-b_1) of the prototype with the axial force in the same steel bar BOTTOM (18-1) obtained by the numerical analyses and by the analytical analyses.

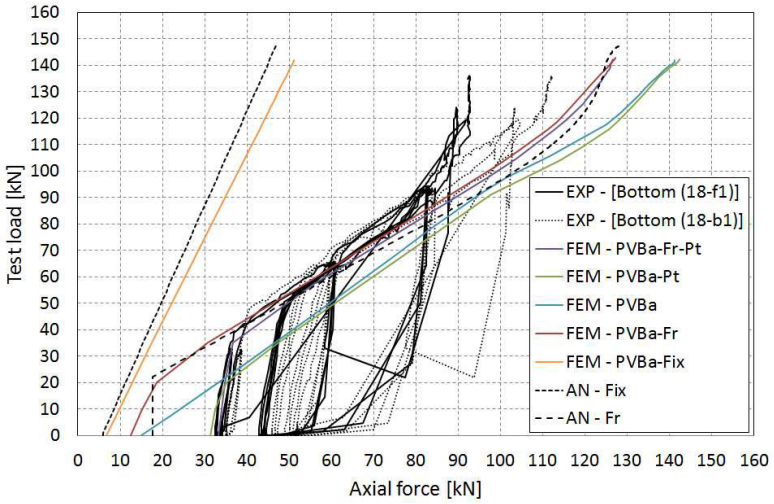

Figure I.23 BOTTOM (18-f_1) and BOTTOM (18-b_1): Test load – Axial force diagram (2nd experimental test, numerical model and analytical model).

Figure I.24 compares the axial forces in the bottom longitudinal steel bars BOTTOM (18-f_1) and BOTTOM (18-b_1) of the prototype with the axial force in the steel bar BOTTOM (18-1) obtained by the numerical analysis **PVBa-Fr-PT** that models the post-tensioning of the diagonal and longitudinal steel bars and takes account of the friction between the longitudinal steel bars and the central steel joints. Furthermore, *Figure I.24* shows the axial force – test load diagrams in the same steel bar BOTTOM (18-1) obtained by the analytical analysis **AN-Fr** that neglects the post-tensioning of the diagonal and longitudinal steel bars but takes account of the friction between the longitudinal steel bars and the central steel joints.

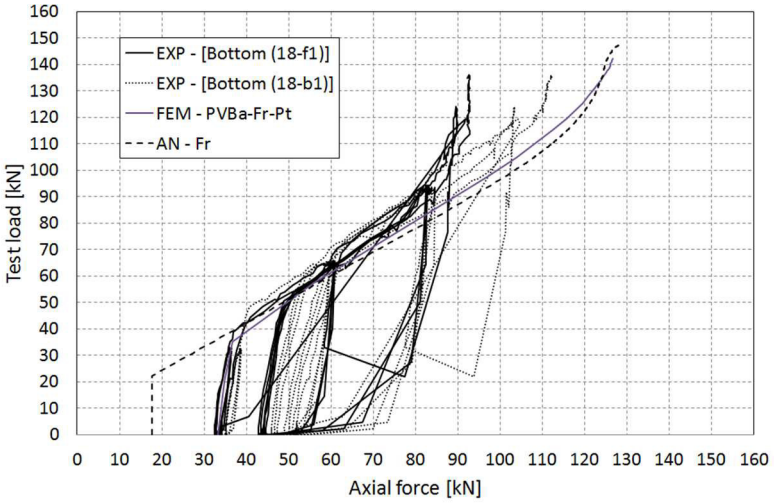

Figure I.24 BOTTOM (18-f_1) and BOTTOM (18-b_1): Test load – Axial force diagram (2nd experimental test, numerical analysis **PVBa-Fr-Pt** and analytical analysis **AN-Fr**).

Figure I.25 compares the axial force in the steel bar BOTTOM (18-1) of the numerical model with the analytical model. It shows the results of the numerical analysis **PVBa-Fix** and the results of the analytical analysis **AN-Fix**. In both analyses, the post-tensioning of the diagonal and longitudinal steel bars is neglected and the longitudinal steel bars are rigidly connected to the central steel joints.

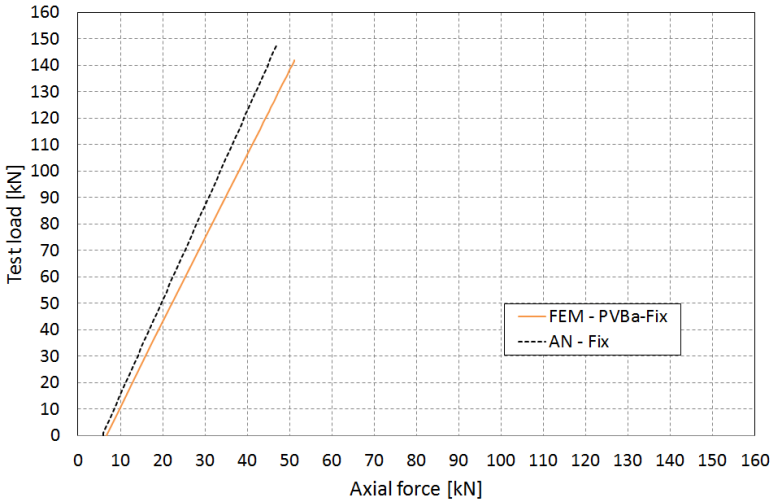

Figure I.25 BOTTOM (18-1): Test load – Axial force diagram (numerical analysis **PVBa-Fix** and analytical analysis **AN-Fix**).

Figure I.26, *Figure I.27* and *Figure I.28* compare the experimental axial force in the bottom longitudinal steel bar BOTTOM (18-f_2) of the prototype with the axial force in the same steel bar BOTTOM (18-2) obtained by the numerical analyses and by the analytical analyses.

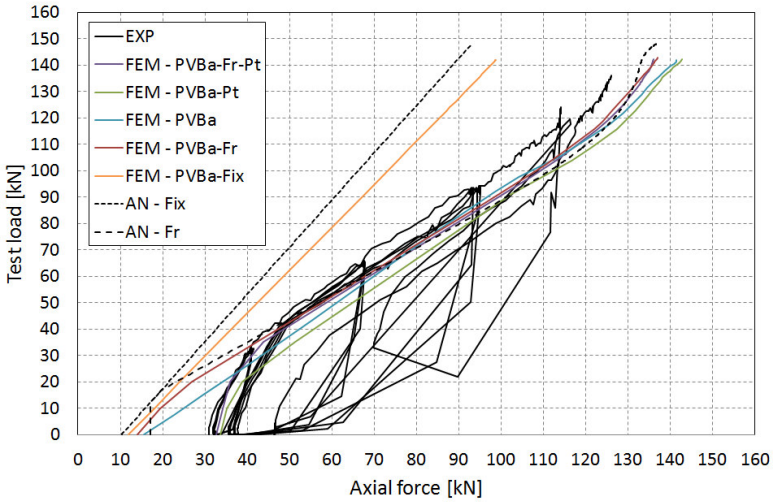

Figure I.26 BOTTOM (18-f_2): Test load – Axial force diagram (2nd experimental test, numerical model and analytical model).

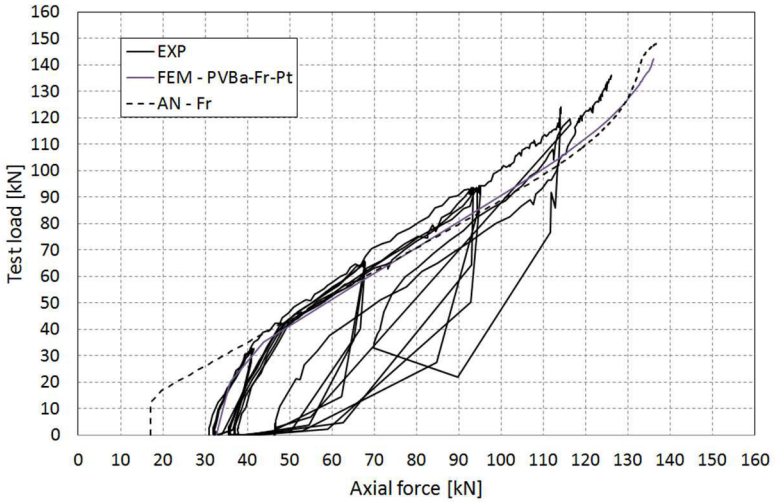

Figure I.27 BOTTOM (18-f_2): Test load – Axial force diagram (2nd experimental test, numerical analysis **PVBa-Fr-Pt** and analytical analysis **AN-Fr**).

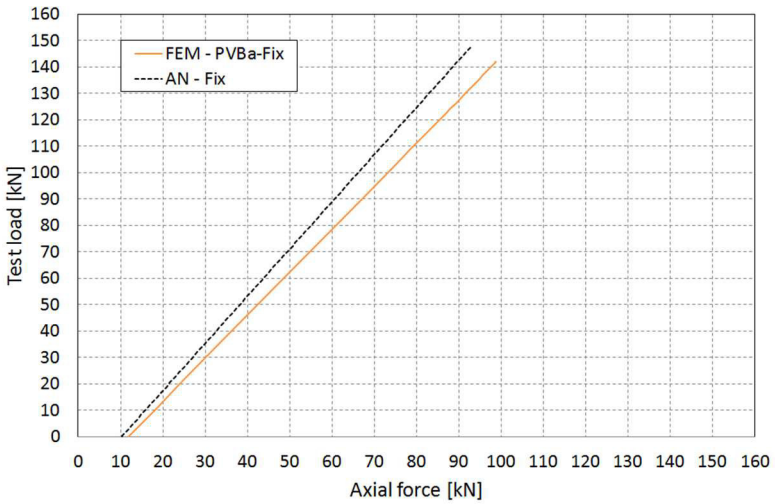

Figure I.28 BOTTOM (18-2): Test load – Axial force diagram (numerical analysis **PVBa-Fix** and analytical analysis **AN-Fix**).

Figure I.29, *Figure I.30* and *Figure I.31* compare the experimental axial force in the bottom longitudinal steel bar BOTTOM (18-f_3) of the prototype with the axial force in the same steel bar BOTTOM (18-3) obtained by the numerical analyses and by the analytical analyses.

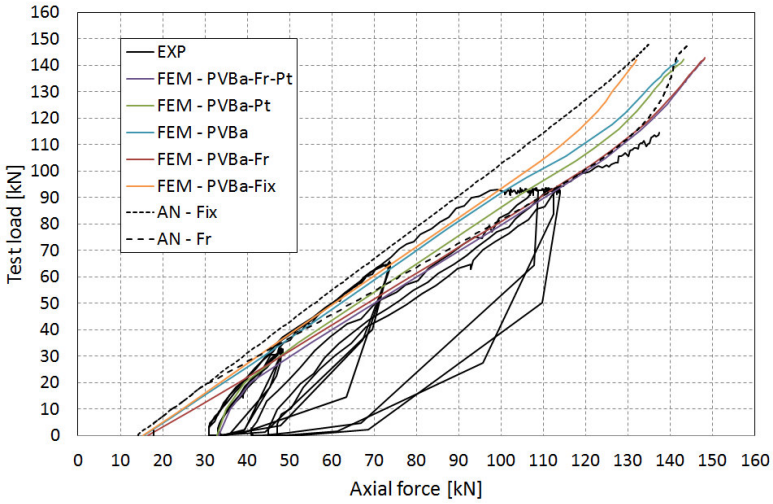

Figure I.29 BOTTOM (18-f_3): Test load – Axial force diagram (2nd experimental test, numerical model and analytical model).

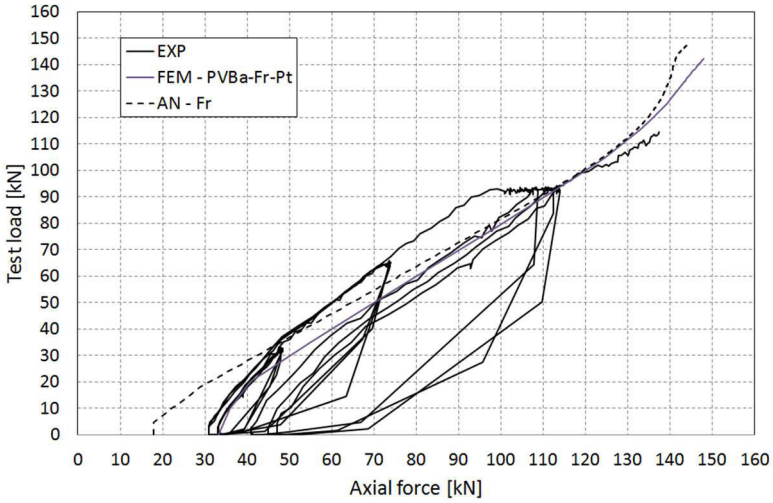

Figure I.30 BOTTOM (18-f_3): Test load – Axial force diagram (2nd experimental test, numerical analysis **PVBa-Fr-Pt** and analytical analysis **AN-Fr**).

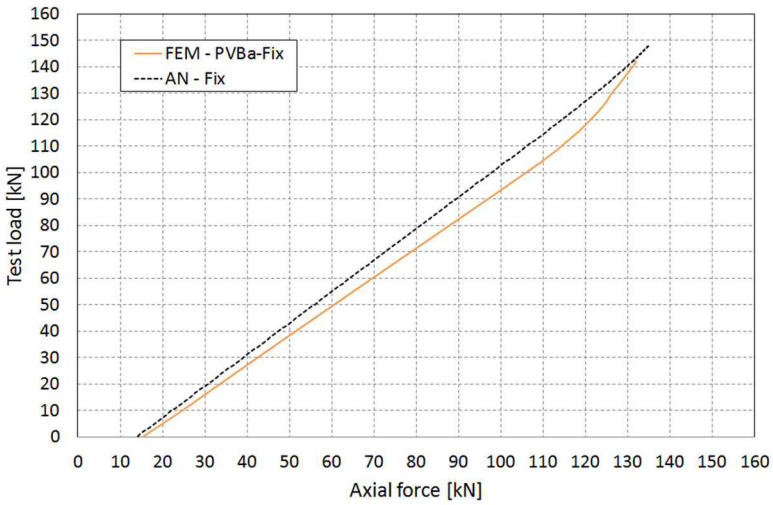

Figure I.31 BOTTOM (18-3): Test load – Axial force diagram (numerical analysis **PVBa-Fix** and analytical analysis **AN-Fix**).

Figure I.32, *Figure I.33* and *Figure I.34* compare the experimental axial force in the bottom longitudinal steel bar BOTTOM (18-f_4) of the prototype with the axial force in the same steel bar BOTTOM (18-4) obtained by the numerical analyses and by the analytical analyses.

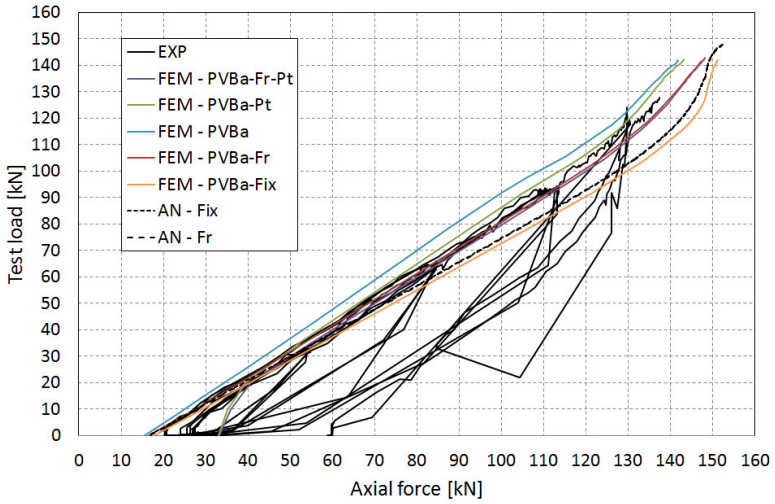

Figure I.32 BOTTOM (18-f_4): Test load – Axial force diagram (2nd experimental test, numerical model and analytical model).

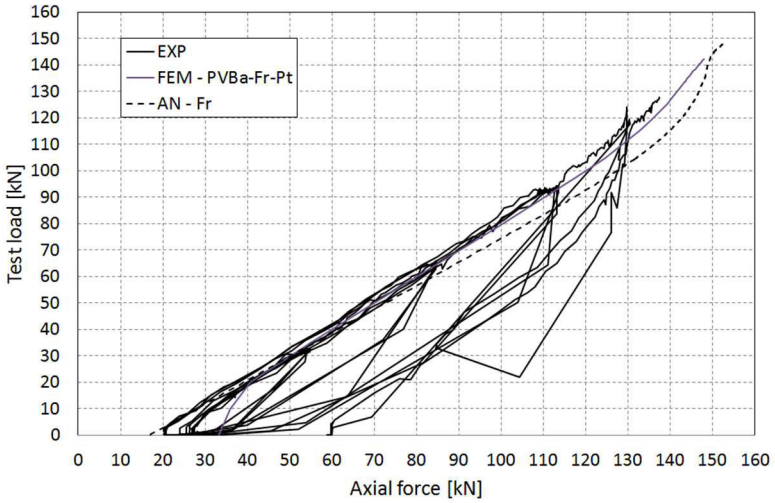

Figure I.33 BOTTOM (18-f_4): Test load – Axial force diagram (2nd experimental test, numerical analysis **PVBa-Fr-Pt** and analytical analysis **AN-Fr**).

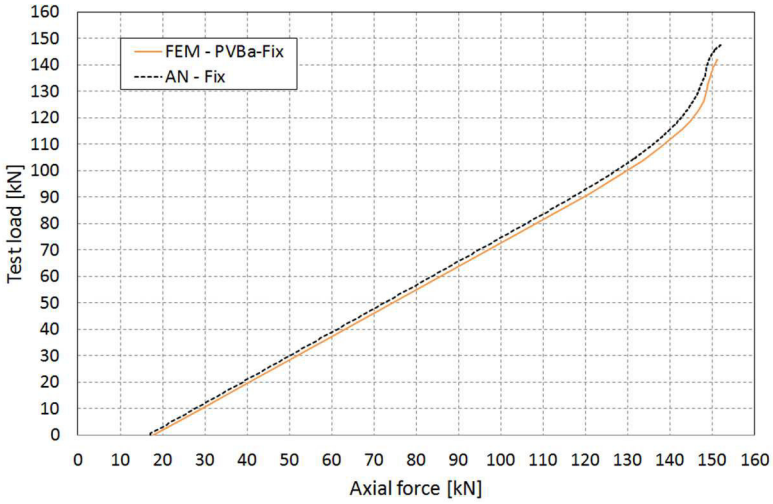

Figure I.34 BOTTOM (18-4): Test load – Axial force diagram (numerical analysis **PVBa-Fix** and analytical analysis **AN-Fix**).

Figure I.35, *Figure I.36* and *Figure I.37* compare the experimental axial force in the bottom longitudinal steel bar BOTTOM (18-f_4) of the prototype with the axial force in the same steel bar BOTTOM (18-4) obtained by the numerical analyses and by the analytical analyses.

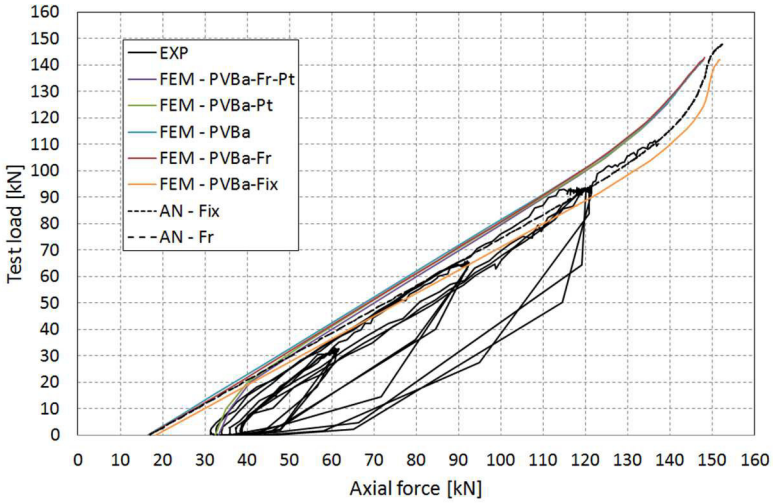

Figure I.35 BOTTOM (18-f_5): Test load – Axial force diagram (2nd experimental test, numerical model and analytical model).

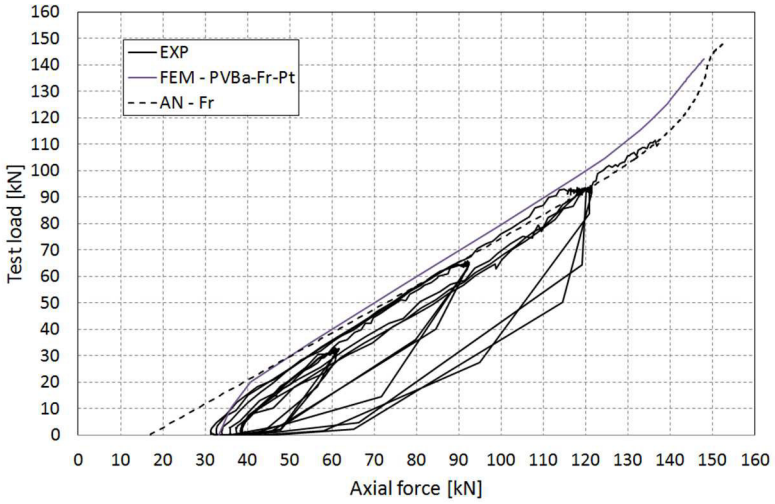

Figure I.36 BOTTOM (18-f_5): Test load – Axial force diagram (2nd experimental test, numerical analysis **PVBa-Fr-Pt** and analytical analysis **AN-Fr**).

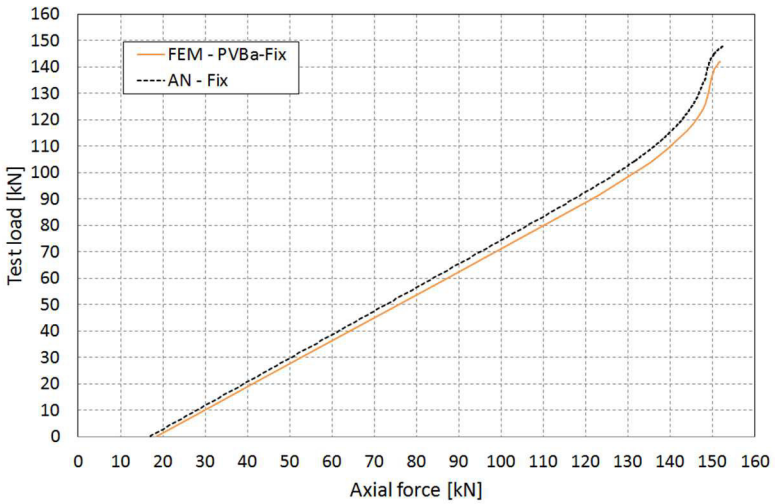

Figure I.37 BOTTOM (18-5): Test load – Axial force diagram (numerical analysis **PVBa-Fix** and analytical analysis **AN-Fix**).

Appendix II Photographs

Photographs of the beam









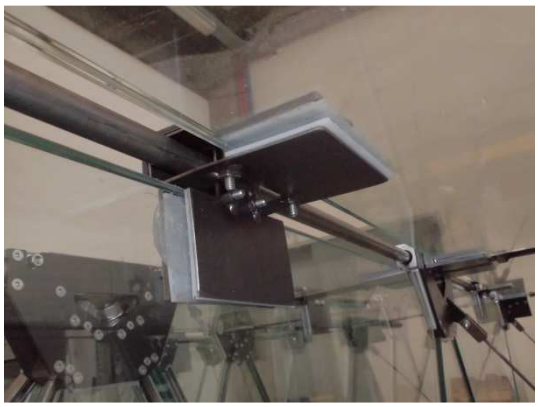
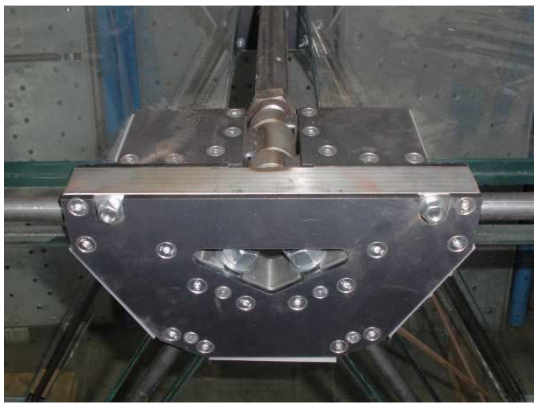
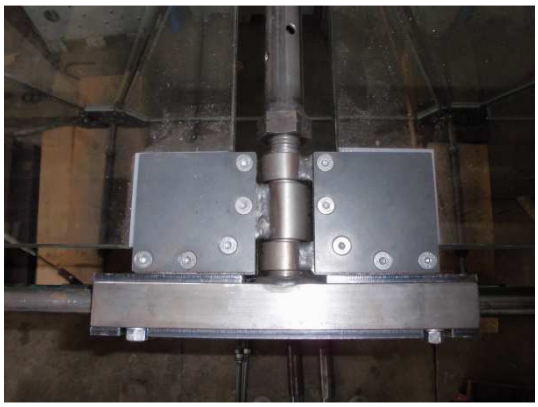
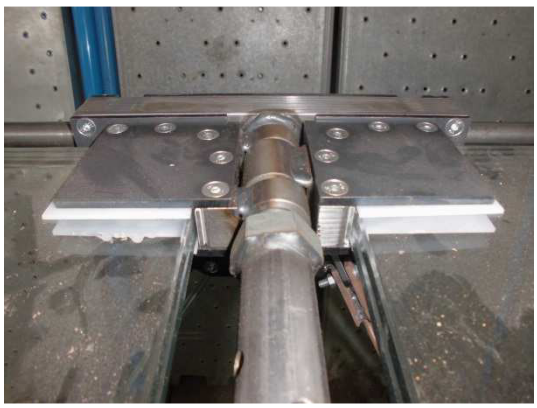
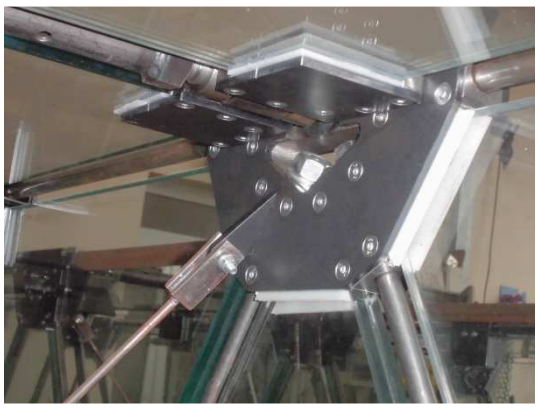

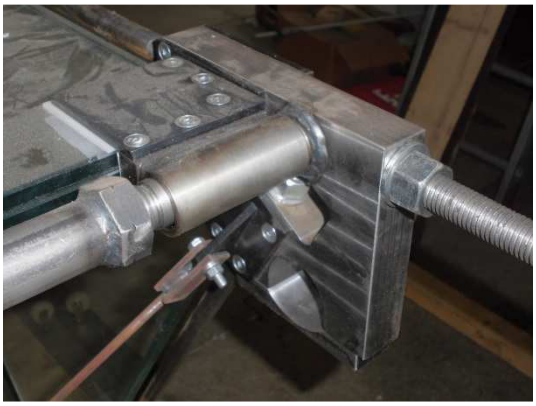

Photographs of the beam during the four-point bending test

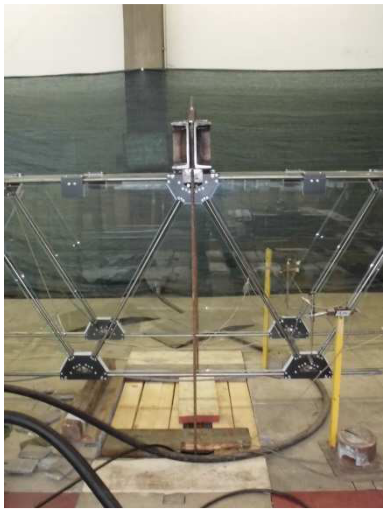

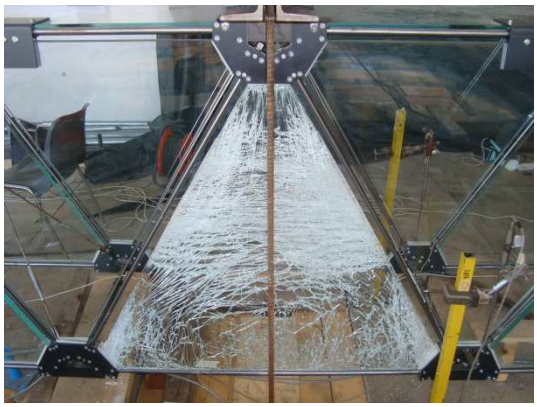

Photographs of the beam during the construction


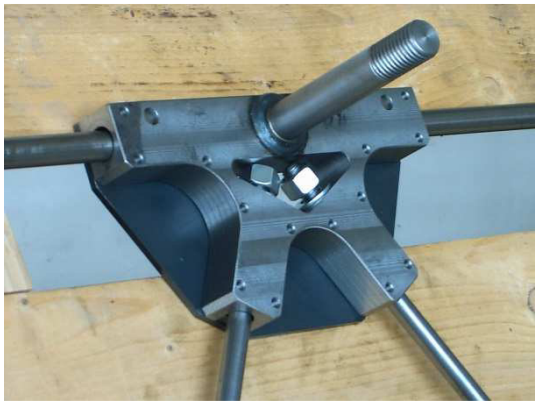
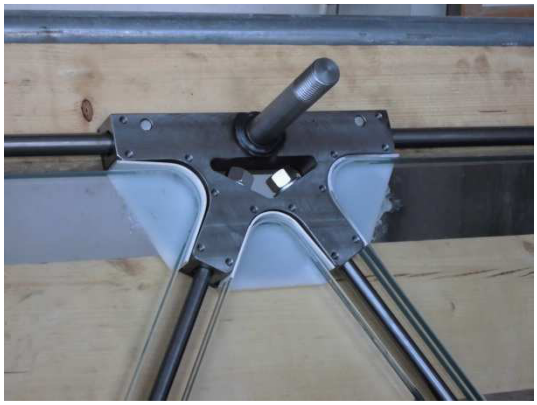
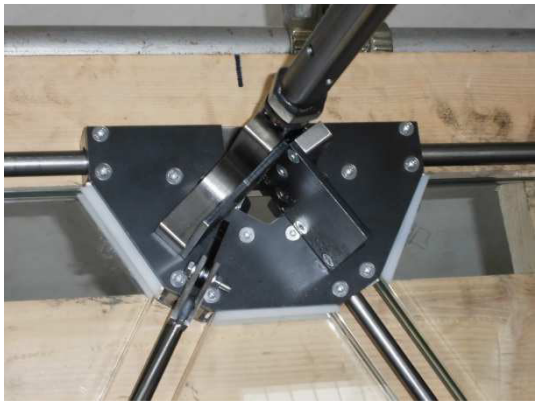

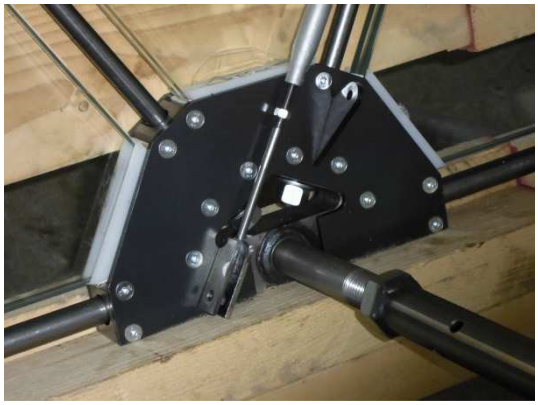



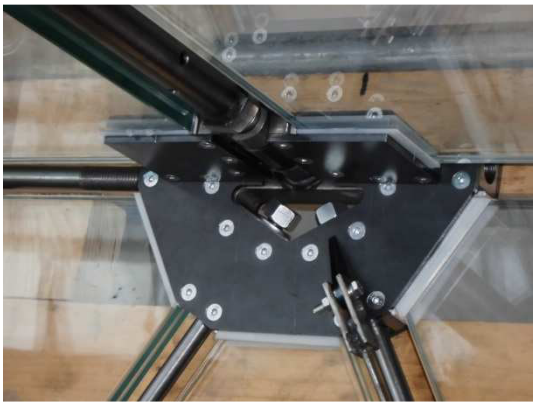
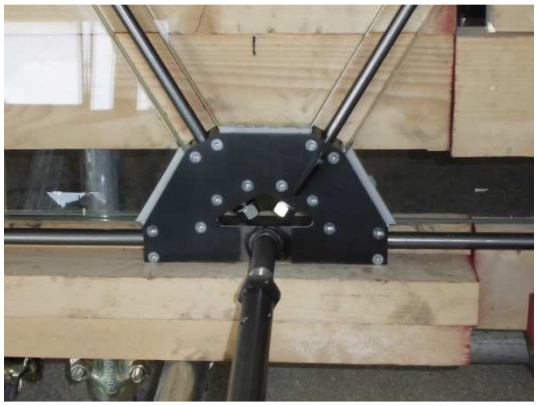




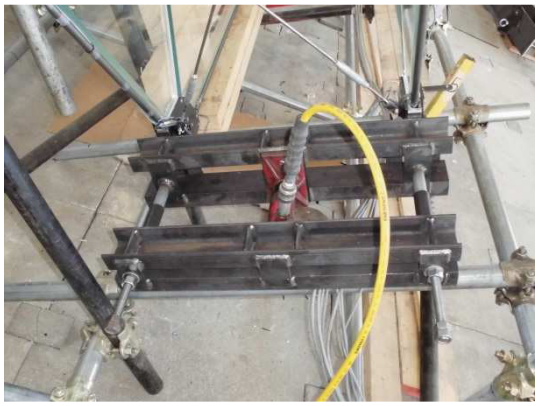

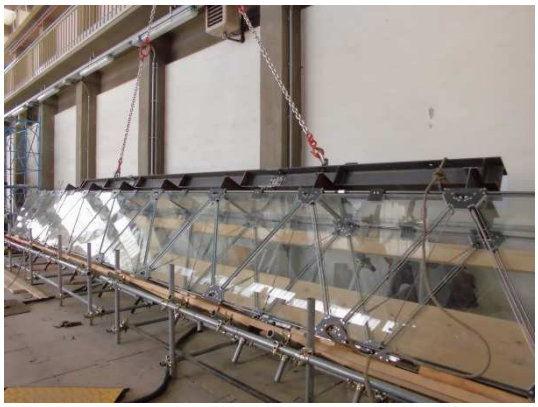

Photographs of the top-end joints

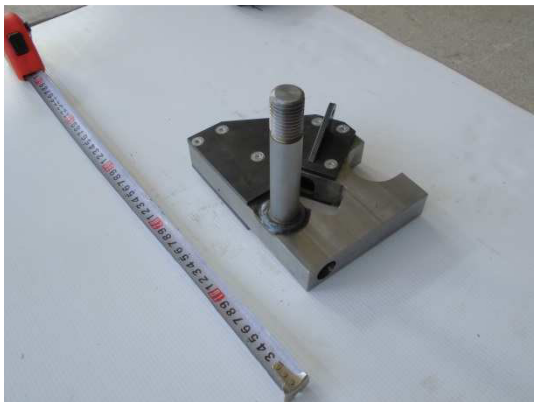



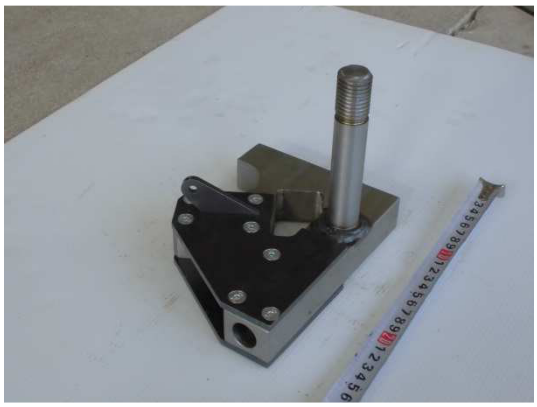


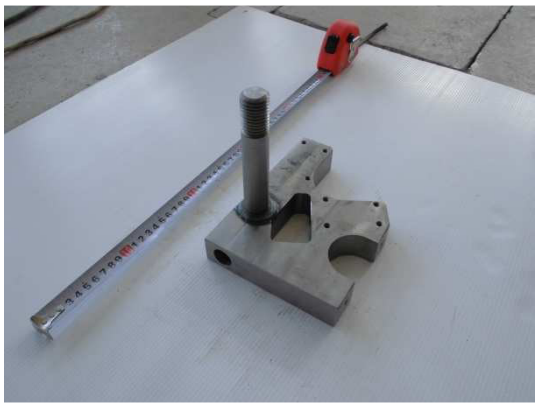


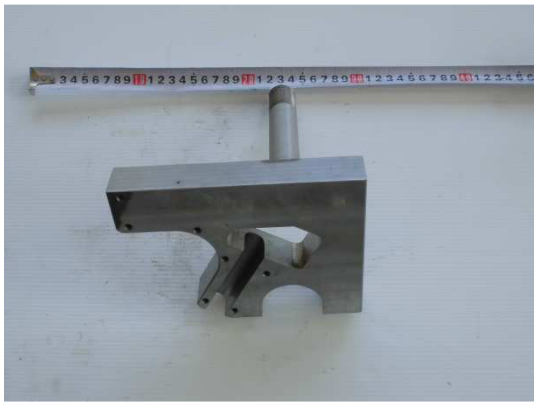


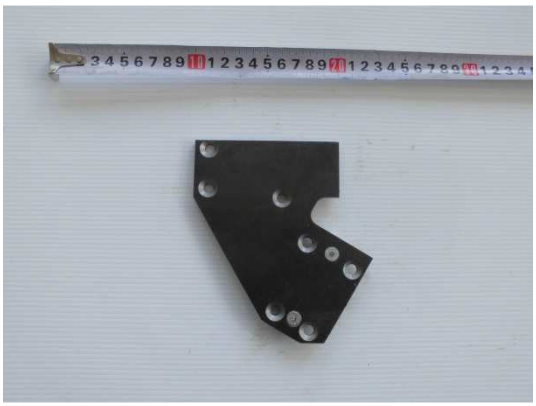


Photographs of the bottom-end joints


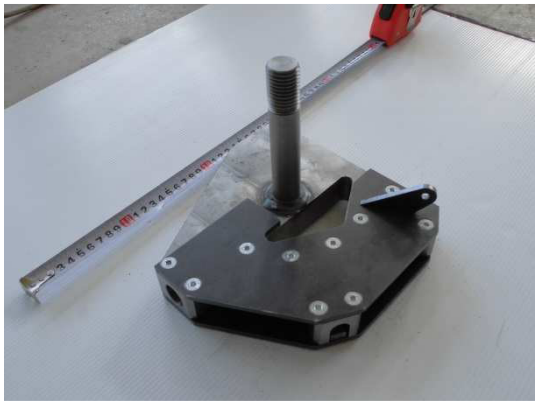
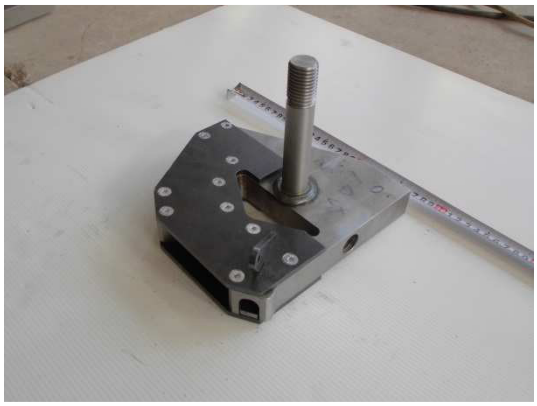
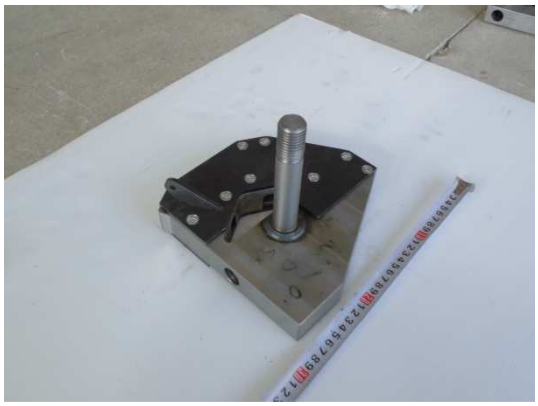
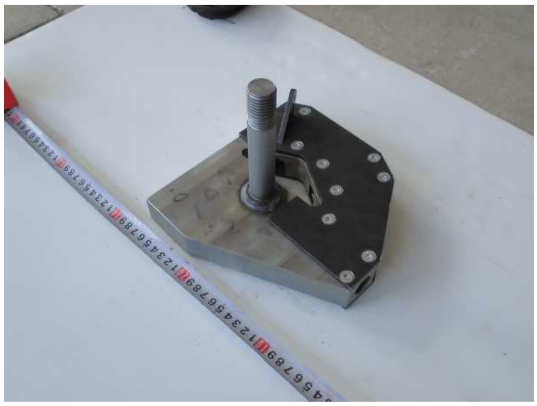
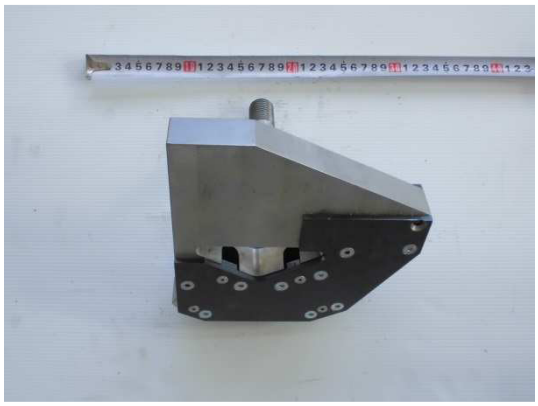





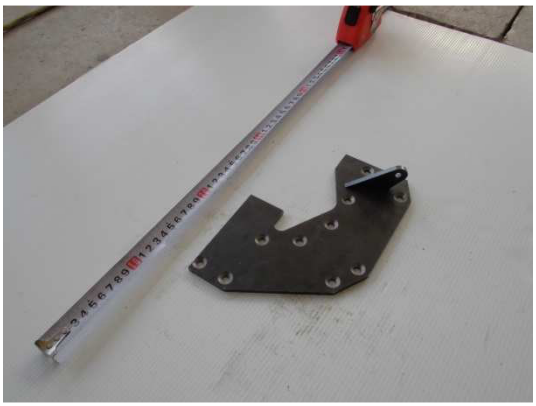


Photographs of the central joints





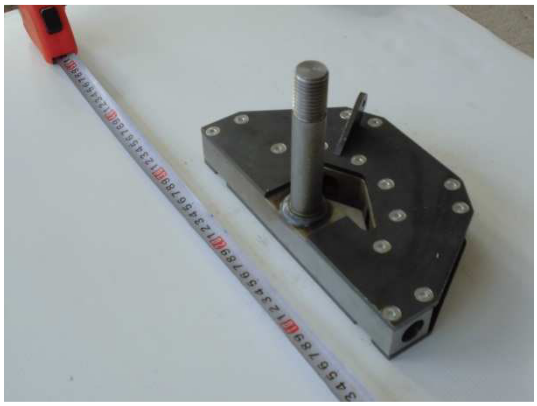


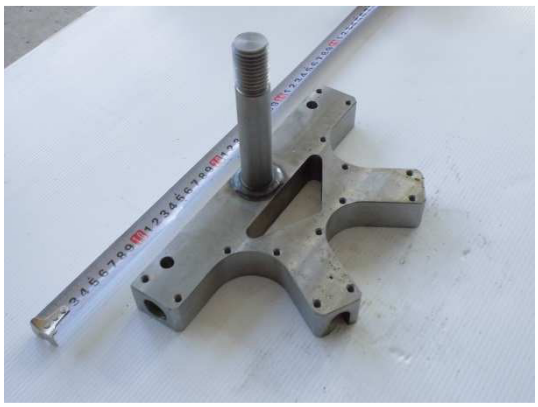








Photographs of the pinned connections

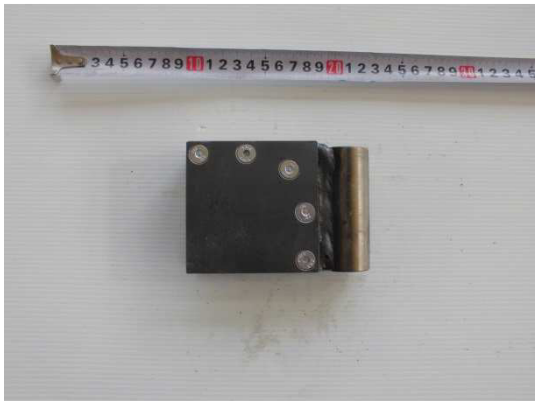


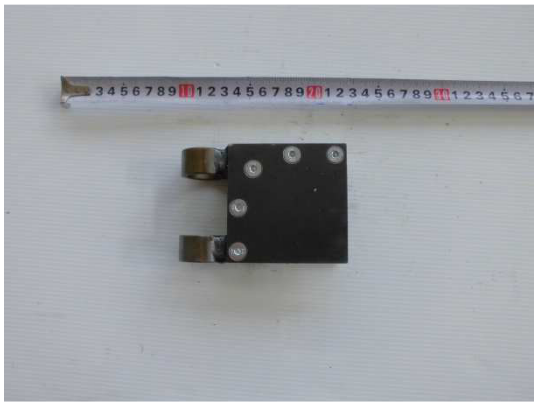




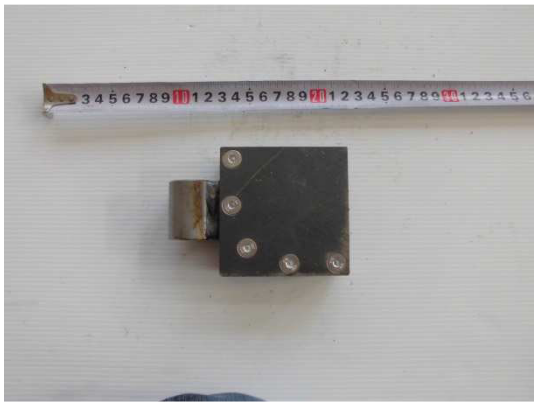
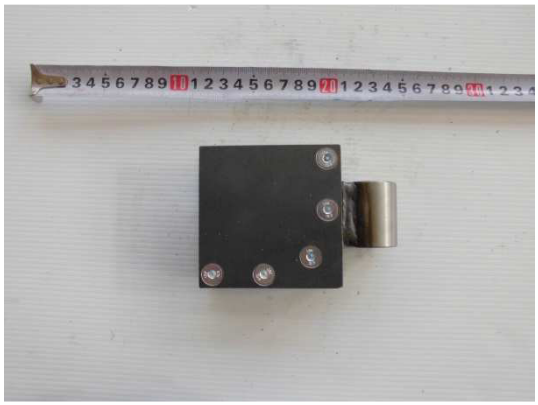




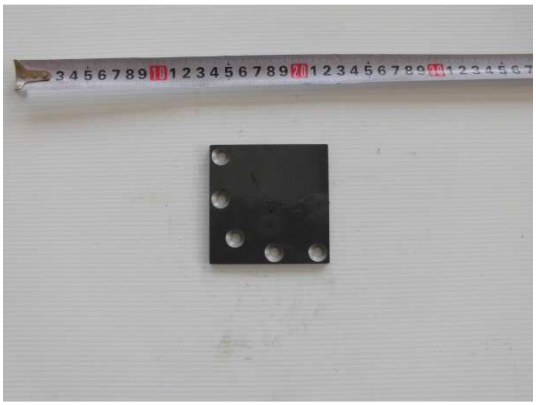

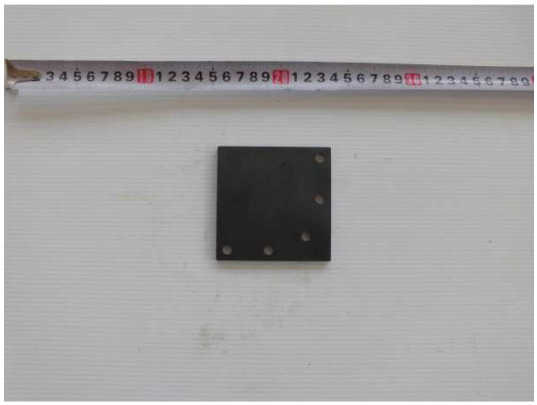

Photographs of the joint-to-joint connections

Photographs of the friction – grip connections








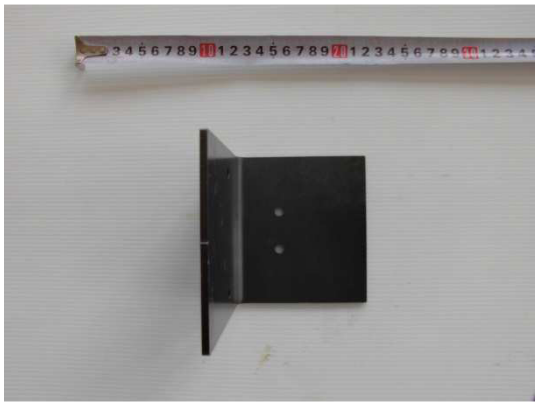

Photographs of the intermediate elements

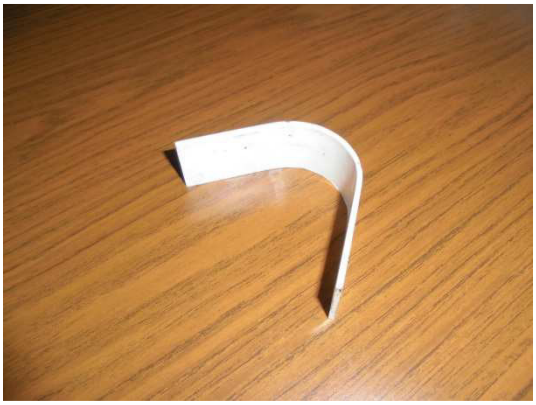

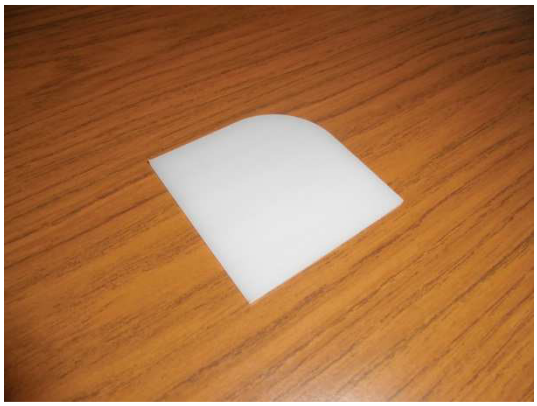

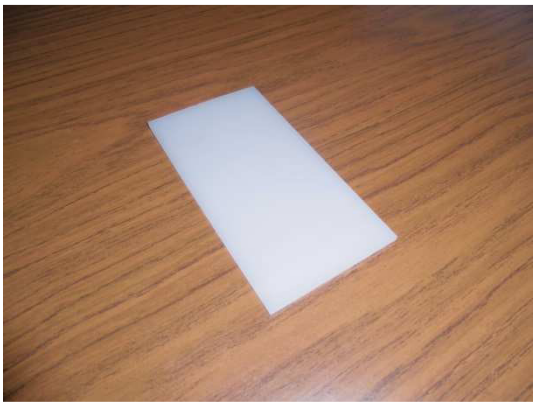

Appendix III Technical drawings

The following table lists the technical drawings made during the design process of the 12 m prototype. The technical drawings are appended to this dissertation.

Drawing Number	Drawing Title	Size	Scale
1	General views	A1	1:16 – 1:20
2	Details 1-2	A1	1:2
3	Details 3-4	A1	1:2
4	Details 5-6	A1	1:2
5	Details 7-8	A1	1:2
6	Details 9-10-11	A1	1:2
7	Details 12-13-14	A1	1:2
8	Details 15-16-17-18	A1	1:2
9	Detail 19	A3	1:2
10	Details 20-21	A3	1:2 – 1:5
11	Assemblies 1-10	A1	1:2
12	Part 1	A1	1:1
13	Part 2	A1	1:1
14	Part 3	A1	1:1 – 1:2
15	Part 4	A1	1:1 – 1:2
16	Part 5	A1	1:1
17	Parts 6-7	A1	1:1
18	Parts 8-9	A1	1:1
19	Parts 10-11	A1	1:1
20	Parts 12-13	A1	1:1
21	Parts 14-15-16	A1	1:1 – 1:2
22	Part 17	A2	1:1
23	Parts 18-23	A1	1:1
24	Parts 24-25	A2	1:1
25	Part 26	A2	1:1
26	Part 27	A2	1:1
27	Part 28	A2	1:1
28	Part 29	A2	1:1
29	Part 30	A2	1:1
30	Part 31	A4	1:1
31	Bars	A2	1:2 – 1:10
32	Aluminium elements	A3	1:1
33	Polyethylene elements	A3	1:1
34	Triangular glass	A3	1:1 – 1:5
35	Rectangular glass	A3	1:1 – 1:5

Table III.3 Technical drawings.

References

ABAQUS, 2010. *Getting Started with Abaqus.* s.l.:Dassault Systèmes.

ABAQUS, 2012. *Analysis User's Manual.* s.l.:Dassault Systèmes.

Agnetti, S. & Speranzani, E., 2014. Hybrid steel-fibre reinforced glass beams - Experimental and numerical analysis. *Challenging Glass 4 & Cost Action TU905 Final Conference,* pp. 211-218.

Belis, J., Callewaert, D., Delincé, D. & Van Impe, R., 2009. Experimental Failure investigation of a hybrid glass/steel beam. *Engineering Failure Analysis,* 16(4), pp. 1163-1173.

Bennison, S. J., Jagota, A. & Smith, C. A., 1999. Fracture of Glass / Poly(vinyl butyral) (Butacite®) Laminates in Biaxial Flexure. *Journal of the American Ceramic Society,* 82(7), pp. 1761-1770.

Bennison, S. J., Quin, M. H. X. & Davoes, P. S., 2008. High-performance laminated glass for structurally efficient glazing. *Innovative Light-weight Structures and Sustainable Façades, Hong Kong..*

Bos, F. et al., 2005. The Joints for the All Transparent Pavilion. *Glass Processing Days 2005.*

Bos, F. et al., 2005. Designing and Planning the World's Biggest Experimental Glass Structure. *Glass Processing Days 2005.*

Bucak, O. et al., 2009. Bonded steel glass hybrid beams. *Glass Performance Days 2009,* pp. 318-320.

Cagnacci, E., Orlando, M. & Spinelli, P., 2009. Experimental campaign and numerical simulation of the behaviour of reinforced glass beams. *Glass Performance Days 2009,* pp. 484-487.

Cruz, P. & Pequeno, J., 2008a. Structural Timber-Glass Adhesive Bonding. *Challenging Glass, conference on architectural and structural applications of glass,* pp. 205-214.

Cruz, P. & Pequeno, J., 2008b. Timber-Glass Composite Beams: Mechanical Behaviour & Architectural Solutions. *Challenging Glass, conference on architectural and structural applications of glass,* pp. 439-448.

D'Haene, P. & Savineau, G., 2007. Mechanical properties of laminated safety glass – FEM study. *Glass Performance Days 2007.*

EN 10025-2:2004, 2004. *EN 10025-2:2004 Hot rolled products of structural steels - Part 2: Technical delivery conditions for non-alloy structural steel,* s.l.: s.n.

EN 10277-2:2008, 2008. *EN 10277-2:2008: Bright steel product – Technical delivery conditions – Part 2: Steels for general engineering purposes,* s.l.: s.n.

EN 1993-1-1:2005, 2005. *EN 1993-1-1:2005: Eurocode 3 - Design of steel structures – Part 1-1: General rules and rules for buildings,* s.l.: s.n.

EN 1999-1-1:2007, 2007. *EN 1999-1-1:2007: Eurocode 9 - Design of aluminium structures – Part 1-1: General structural rules,* s.l.: s.n.

EN 572-1:2004, 2004. *EN 572-1:2004: Glass in building – Basic soda lime silicate glass products – Part 1: Definitions and general physical and mechanical properties,* s.l.: s.n.

Feldmann, M., Abeln, B. & Baittinger, M., 2010. Analysis of bonded hybrid steel-glass-beams by small scale tests. *Challenging Glass 2,* pp. 249-258.

Feldmann, M. et al., 2014. *Guidance for European Structural Design of Glass Components. Support to the implementation, harmonization and further development of the Eurocodes - Joint Research Centre – Scientific and Policy Report, European Commission.* Luxembourg: S. Dimova, A. Pinto, M. Feldmann, S. Denton.

Freytag, B., 2004. Glass-Concrete Composite Technology. *Structural Engineering International,* 14(2), pp. 111-117.

Froli, M. & Lani, L., 2008. Strutture duttili in vetro. *Nuova Finestra,* Issue 336, pp. 106-109.

Froli, M. & Lani, L., 2010. Glass Tensegrity Trusses. *Structural Engineering International,* 20(4), pp. 436-441.

Froli, M. & Mamone, V., 2013a. Le travi TVT in vetro armato precompresso vincono la sfida delle grandi luci. *Rivista del vetro,* Issue 4, pp. 22-30.

Froli, M. & Mamone, V., 2013b. Una trave ibrida precompressa in vetro-acciaio di luce 12 metri. *Costruzioni Metalliche,* Issue 6, pp. 55-64.

Haldimann, M., Luible, A. & Overend, M., 2008. *Structural Use of Glass - SED 10.* Zürich: IABSE-AIPC-IVBH.

Hamm, J., 2001. Development of Timber-Glass Prefabricated Structural Elements. *Innovative Structures and Bridges,* pp. 119-124.

Jordão, S. et al., 2014. Numerical modelling of a laminated glass beam reinforced with pre-stressed cables. *Challenging Glass 4 & Cost Action TU905 Final Conference,* pp. 253-260.

Kozlowski, M., Serrano, E. & Enquist, B., 2014. Experimental investigations on timber-glass composite I-beam. *Challenging Glass 4 & COST Action TU0905 Final Conference,* pp. 261-268.

Kreher, K., Natterer, J. & Natterer, J., 2004. Timber-Glass-Composite Griders for a Hotel in Switzerland. *Structural Engineering International,* 14(2), pp. 149-151.

Louter, 2011. *Fragile yet Ductile,* Zutphen: Christian Louter.

Louter, C. et al., 2005. Reinforced Glass Cantilever Beams. *Glass Processing Days 2005,* pp. 430-434.

Macfarlene, T., 1999. Construction Details for Structural Glass Assemblies. *Glass Processing Days,* pp. 474-476.

Mamone, V., 2011. *Progetto di una trave presollecitata di luce 12 metri in sistema misto vetro-acciaio,* Pisa: Master Thesis, Faculty of Engineering, University of Pisa (supervisors M. Froli & G. Masiello).

Netusil, M. & Eliasova, M., 2010. Experimental and numerical analysis of glued steel-glass joints. *Challenging Glass 2,* pp. 269-276.

O'Callaghan, J., 2012. Adventures with Structural Glass. *Glass Performance Days 2012.*

Ølgaard, A., Nielsen, J. H. & Olesen, J. F., 2009. Design of Mechanically Reinforced Glass Beams: Modelling and Experiments. *Structural Engineering International,* 19(2), pp. 130-136.

Palumbo, D., Palumbo, M. & Mazzucchelli, M., 2005. A New Roof for the XIIIth Century “Loggia de Vicari” (Arquà Petrarca – PD – Italy) Based on Structural Glass Trusses: a Case Study. *Glass Processing Days 2005.*

Trösch, E. & Kassnel-Henneberg, B., 2013. Load-bearing behaviour of splice-laminated glass beams for wide spans. *COST Action TU0905 Mid-term Conference on Structural Glass,* pp. 77-91.

Ungermann, D. & Preckwinkel, E., 2010. Structural Behaviour of Hybrid Steel-Glass Beams. *Challenging Glass 2,* pp. 485-496.

Van Duser, A. & Jagota, A. B. S. J., 1999. Analysis of glass/polyvinyl butyral laminates subjected to uniform pressure. *Journal of Engineering Mechanics,* 125(4), pp. 435-442.

Veer, F. A. et al., 2003. Spanning Structures in Glass. *Glass Processing Days 2003,* pp. 78-81.

Veer, F. A. et al., 2003. Composite Glass Beams, the Third Chapter. *Glass Processing Days 2003.*

Weller, B. & Engelmann, M., 2014. Deformation of Spannglass beams during post-tensioning. *Challenging Glass 4 & Cost Action TU905 Final Conference,* pp. 285-294.

Weller, B., Meier, A. & Weimar, T., 2010. Glass-Steel Beams as Structural Members of Façades. *Challenging Glass 2,* pp. 517-524.

Wellershoff, F. & Sedlacek, G., 2003. Structural Use of Glass in Hybrid Elements: Steel-Glass-Beams, Glass-GFRP-Plates. *Glass Processing Days 203,* pp. 268-270.

Wellershoff, F., Sedlacek, G. & Kasper, R., 2004. Design of joints, members and hybrid elements for glass structures. *Proceedings of ISAAG 2004.*